UNDERSTANDING

THE MECHANICAL BEHAVIOR OF

PARTICULATE REINFORCED METAL MATRIX COMPOSITES

A Dissertation

Presented to

The Graduate Faculty of The University of Akron

In Partial Fulfillment

of the Requirements for the Degree

Doctor of Philosophy

Meslet Al-Hajri

August, 2003

UMI Number: 3098476

Copyright 2003 by

Al-Hajri, Meslet H.

All rights reserved.

UMI®

UMI Microform 3098476

Copyright 2003 by ProQuest Information and Learning Company.

All rights reserved. This microform edition is protected against

unauthorized copying under Title 17, United States Code.

ProQuest Information and Learning Company
300 North Zeeb Road
P.O. Box 1346
Ann Arbor, MI 48106-1346

UNDERSTANDING

THE MECHANICAL BEHAVIOR OF
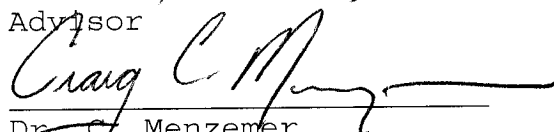
PARTICULATE REINFORCED METAL MATRIX COMPOSITES

Meslet Al-Hajri

Dissertation

Approved:

_____
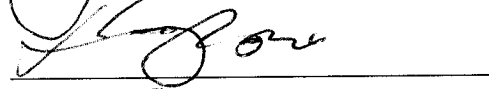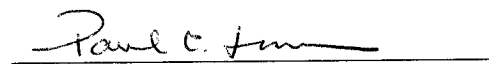Dr. T. Srivatsan
Advisor

_____
Dr. C. Menzemer
Committee Member

_____
Dr. X. Gao
Committee Member

_____
Dr. P. Lam
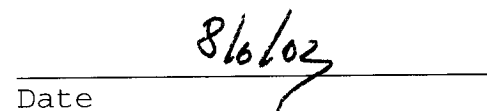Committee Member

_____
Dr. S. Jana
Committee Member
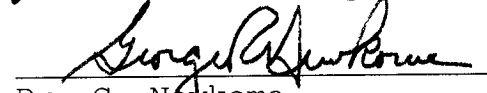
Accepted:

_____
Dr. C. Batur
Department Chair

_____
Dr. G. Haritos
Dean of the College

_____
Dr. G. Newkome
Dean of the Graduate School

8/6/02
_____
Date

ii

ABSTRACT

Particulate reinforced metal matrix composites (PMMCs) are beginning to make significant contributions in the industries of aerospace, automotive and consumer-related products. Such advances have created an inescapable need for establishing an understanding of the inter-relationship between composite microstructure and mechanical behavior.

In the present study, three kinds of PMMCs were chosen for an assessment of their mechanical performance in view of potential applications in ground transportation, automobile, aerospace and high-performance goods. The aluminum alloys chosen were the precipitation hardened Al-Cu-Mg and Al-Zn-Mg-Cu system because of their promising mechanical properties. The magnesium alloy chosen is based on the binary Mg-6%Zn system. The reinforcement chosen was silicon-carbide (SiC) particulates. To facilitate a better understanding of the mechanical behavior of the composites, the initial microstructure was examined by optical and transmission electron microscopy (TEM). The fatigue and final fracture behavior of aluminum alloy 2009 metal

iii

matrix composite and Mg-6%Zn magnesium matrix composite were studied at both ambient temperature (27 °C) and elevated temperature of (150 °C). The fatigue behavior of 7034 aluminum matrix composite was also examined in the under-aged (UA) and peak-aged (PA) conditions at both ambient (27 °C) and elevated temperatures (120 °C).

Tensile tests were conducted to determine the basic mechanical properties, and microstructural examination was performed to characterize the initial microstructure of the material. Applying the basic theories governing high and low cycle fatigue behavior of common metals and alloys, the fatigue exponents and constants were determined from the experimental data. Results of the study demonstrate the applicability of traditional fatigue analyses for particulate-reinforced composites.

Also examined, with aid of finite element simulations using ABAQUS software and the periodical unit cell model, was the intrinsic influence of particulate distribution and clustering in dictating the mechanical behavior of discontinuously-reinforced aluminum metal matrix composites. For cyclic fatigue, two types of modeling schemes were evaluated. The fatigue damage evolution model is used to predict the cyclic-stress controlled fatigue

iv

response. In the last section the methodology and potential for incorporating the parameters obtained from the experimental study for analyzing the cyclic-plastic strain controlled response is presented.

v

ACKNOWLEDGEMENTS

There are numerous people who were instrumental in assisting me to finally complete this degree.

I sincerely thank the committee chairman and my advisor Dr. T. S. Srivatsan for his guidance and support during my research. His time and effort in guiding the direction of this research was indispensable in the completion of this dissertation.

I would also like to thank the committee members Dr. T. S. Srivatsan, Dr. X. Gao, Dr. P. Lam, Dr. A. Prakash, and Dr. R. Shemenski from the Department of Mechanical Engineering, Dr. C. Menzemer from the Department of Civil Engineering and Dr. S. Jana from the Department of Polymer Engineering for having faith in my abilities and for exercising infinite patience and encouragement.

My sincere appreciation extends to Dr. Vijay Vasudevan from The University of Cincinnati. The use of his laboratory greatly aided in the completion of this work

Finally, special grateful to the two moons in my life my parents for their incessant encouragement.

vi

TABLE OF CONTENTS

Page

viii

x

xi

LIST OF TABLES

LIST OF FIGURES

xiv

xv

xvi

xxiii

xxv

xxvi

CHAPTER I

INTRODUCTION

Driven initially by the demand for high performance
military and space applications, discontinuously-reinforced
metal matrices (DRMMCs) have engendered considerable
scientific and technological interest in the time spanning
the last two decades. Also, the need for satisfying high
fuel-economy goals in the automobile and ground
transportation industries is a major challenge, which metal
matrix composites, based on lightweight alloys, will play a
significant role. Classes of metal-matrix composites,
which have grown in stature to emerge and attract
attention, are both the magnesium and aluminum alloy metal
matrices discontinuously-reinforced with silicon carbide
particulates (SiC_p). The presence of SiC_p in a metal matrix
exerts an influence on crack growth, i.e., both crack
initiation and crack or damage propagation, and final
fracture behavior. The influence on both crack initiation
and growth, or damage propagation, is governed by the
conjoint and mutually interactive influences of matrix

1

composition, microstructure, geometrical constitution, processing conditions, and applied cyclic stress and strain intensity ranges. In fact, presence of discontinuous silicon carbide particle reinforcement in a ductile metal matrix tends to alter the precipitation kinetics of the material during artificial aging, which exerts an appreciable influence on the mechanical behavior and fracture response characteristics.

While few studies have focused on establishing an understanding of the influence of particulate reinforcements on matrix microstructure and monotonic response, the fatigue database and concurrent fracture behavior for particulate-reinforced metal matrix composites is limited and there does exist a critical need to examine and understand this aspect of mechanical characterization. Overall, the fatigue properties of metal-based alloys are sensitive to changes in intrinsic microstructural features [1]. Microstructural features also exert an appreciable influence on fracture behavior. Therefore, this certainly necessitates a critical need to study the cyclic fatigue and fracture characteristics.

The primary objectives of this research endeavor were to evaluate the influence of discontinuous silicon carbide

particulate (SiC$_p$) reinforcements on tensile deformation, cyclic high-cycle and cyclic low-cycle fatigue properties and fracture (quasi-static and cyclic) behavior of: (a) aluminum-copper-magnesium alloy (AA2009), (b) aluminum-zinc-magnesium- copper alloy (AA7034) and (c) magnesium-zinc alloy (Mg-6%Zn). The high-cyclic and low-cycle fatigue characteristics and final fracture behavior of the composites are discussed in light of concurrent and mutually interactive influence of (a) composite microstructural effects (heat treatment-aging condition), (b) deformation characteristics of the composite constituents, (c) test temperatures (ambient and elevated), and (d) nature of loading.

Also examined with the aid of finite element analysis using the ABAQUS software and the periodical unit cell approach, was the role of particulate distribution and clustering in governing the mechanical behavior of particulate-reinforced metal matrix composites. For cyclic fatigue, two types of modeling schemes were examined. The fatigue damage evolution model was used to predict the cyclic-stress controlled fatigue response. Also highlighted is the methodology and promise in incorporating the fatigue

test parameters obtained from the experimental

investigation into simulations for cyclic-plastic strain

controlled response.

CHAPTER II

REVIEW OF THE LITERATURE

2.1. Metal Matrix Composites (MMCs)

The development of metal matrix composites (MMCs) has reflected the need to achieve property combinations beyond those attainable in monolithic metals. Thus, tailored composites resulting from the addition of reinforcements to a metal tend to provide enhanced specific stiffness, increased specific strength, improved fatigue and wear resistance, coupled with desired thermal characteristics (example: reduced thermal expansion coefficient and conductivity) in the resulting metal matrix composite (MMC) [1-7].

The choice of a matrix alloy for a MMC is dictated by several considerations. Of particular importance is whether the resultant composite is to be continuously or discontinuously-reinforced. The use of continuous fibers as reinforcement results in transfer of load to the reinforcing filaments and the composite is essentially governed by fiber strength. On this basis, lower strength,

5

more ductile, and tougher matrix alloys may be utilized for continuously-reinforced MMCs. For discontinuously-reinforced MMCs, the matrix essentially governs composite strength. Thus, choice of the matrix is often influenced by considerations of required composite strength and/or performance. This necessitates the need for having high strength matrix alloys.

Additional considerations in the choice of the metal matrix include:

(a)   potential reinforcement/matrix reactions, either during processing or while in service, that might result in degraded composite performance;

(b)   thermal stresses due to thermal expansion mismatch between the reinforcements and the matrix

(c)   the influence of matrix fatigue behavior on the cyclic response of the composite.

Indeed, the behavior of MMCs under cyclic loading conditions is an area requiring special consideration. For those MMCs intended for use at elevated temperatures, an additional consideration is the difference in

melting temperatures between the matrix and the reinforcement phase [2].

The reinforcement materials for metal matrix composites (MMCs) are second-phase additions to a metallic matrix that result in net property improvement, such as, improvement in toughness, enhanced fatigue resistance, improved wear characteristics and marked increase in stiffness and strength [3-6]. Generally, most reinforcement materials for metal matrix composites (MMCs) are ceramics (oxides, carbides, and nitrides), which are characterized by their high strength and stiffness at both ambient and elevated temperatures. Examples of commonly used reinforcements are silicon carbide (SiC), alumina (Al_2O_3), titanium boride (TiB_2), boron carbide (B_4C), and graphite. For aluminum alloys, alumina (Al_2O_3) is less reactive than silicon carbide (SiC) and is the preferred choice [6-10].

Reinforcements can be divided into two major groups, discontinuous and continuous. Fiber reinforcements may be either the continuous or the discontinuous type [3]. Normally, fibers tend to enhance strength in the direction of orientation. Low strength in the direction perpendicular to fiber orientation is characteristic of continuous fiber-reinforced MMCs. Particulate-reinforced MMCs, on the other

hand, display near isotropic characteristics [4]. The role of the reinforcing phase varies with the type chosen for structural MMCs. In particulate and whisker-reinforced MMCs, the matrix is the major load-bearing constituent [5]. The exact role of the reinforcing phase is to strengthen and stiffen the metal matrix by imposing constraints on matrix deformation [5]. The restraint or constraints on deformation is a function of the interparticle spacing-to-diameter ratio [6]. In continuous-fiber-reinforced MMCs, the reinforcement is the principal load-bearing constituent, while the metallic matrix serves to bond the reinforcement and facilitates transfer and distributes of the load. However, the cost of achieving property improvements remains a challenge in many potential continuous fiber-reinforced MMCs applications [7].

2.2. Discontinuously Reinforced Metal Matrix Composites

Discontinuously-reinforced metal matrix composites (DRMMCs) are highly versatile engineering materials with unique combinations of strength, stiffness, and affordability, as well as an ability to be processed and finished using conventional metal working techniques. Besides, it has good wear and corrosion resistance [7-12]. DRMMCs technology has matured to the point where components

are now being produced for aircraft structures, gas turbine engines, automobiles, electronics and even spacecraft [7-12]. Most light-weight alloy metal matrix composites in use today are particulate-reinforced. The cost efficiency in using mass production technologies for particulate-reinforced metal matrices stands out in aiding its selection and use when compared to the continuously-reinforced counterpart.

2.3. Microstructural Characteristics of Metal-Matrix Composites

2.3.1. Aluminum alloy-based composites

Wide ranges of aluminum alloys in various tempers have been chosen as the matrix material for MMCs. The density of most aluminum alloys is near that of pure aluminum, approximately 0.1 lb/in^3. Pure aluminum melts at 660 °C. This relatively low melting temperature, in comparison to most other candidate matrix metals, facilitates processing of aluminum-based MMCs by (a) solid-state routes, such as powder metallurgy [8], and (b) traditional casting techniques [5]. The designation schemes for wrought alloys are based on the major alloying additions. Heat treatable refers to those alloys that may be strengthened by thermal treatment [3]. Wrought alloys belonging to the 2XXX, 6XXX

and 7XXX series are generally heat treatable, and include

alloys containing lithium. (e.g., some 8XXX alloys). A

typical heat treatment operation at room and elevated

temperatures includes solution heat treatment, quenching in

a liquid medium and subsequent aging. A temper designator

is appended to the alloy designation to describe the

resulting condition of heat treatment. Thus, "T4" refers to

material allowed to naturally age at room temperature

following solution heat treatment and quenching in cold

water, while "T6" describes artificial aging to peak

strength. The addition of reinforcements (especially

particulates and whiskers) has been shown to have a

significant influence on the aging response of the matrix

composition for many discontinuously-reinforced matrices.

The aging response may be either accelerated or retarded

and the effect is both material and process specific [9].

For this reason the aging treatment for a MMC with a heat

treatable matrix alloy differs significantly from that of

the unreinforced metal matrix [10].

Among the available aluminum alloys the precipitation

hardenable alloys, belonging to Al-Cu-Mg and Al-Zn-Mg-Cu,

families are of special interest. They rely on the

precipitation of fine coherent precipitates and dispersoids

for strengthening. The morphology and distribution of the second-phases in the metal matrix dictates mechanical properties and environmental response of the material. The microstructure of the material is controlled by heat treatment and the material may be produced in a variety of microstructural conditions, or tempers, which facilitates specific design requirements to be met [1].

The age-hardening behavior of discontinuously-reinforced aluminum alloy metal matrix composites has been a subject of great interest both from scientific and technological view-points [11]. The mechanism of age hardening responsible for strengthening is based on the formation of intermetallic compounds through the decomposition of a metastable supersaturated solid solution (αsss) obtained by solution treatment and quenching [11]. Since interactions between the αsss decomposition products and dislocations are primarily responsible for strengthening, a knowledge of the decomposition process is important for achieving technical development and resultant improvement [1].

The precipitation sequence for hardening of Al-Cu-Mg alloy is [12]

$$\alpha\text{sss} \rightarrow \text{GPzone} \rightarrow \theta^{//} \rightarrow \theta^{/} \rightarrow \theta\text{-Al}_2\text{Cu)} \qquad (2.1)$$

$$\alpha sss \rightarrow \text{GPzone} \rightarrow (S^{//}) \rightarrow S^{/} \rightarrow S\text{-}Al_2CuMg) \quad (2.2)$$
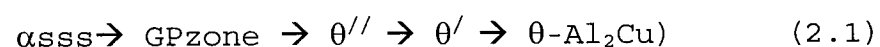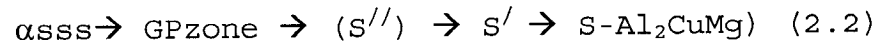
In equation (2.1) where GPzone refers to the (Cu) Guinier-Preston zones, $\theta^{//}$ and $\theta^{/}$ are the metastable Al_2Cu phase, and θ is the equilibrium Al_2Cu phase [2]. In equation (2.2) GPzone the (Cu/Mg) Guinier-Preston-Bagariastkij zones, $S^{//}$ and $S^{/}$ are the metastable Al_2CuMg phases, and S is the equilibrium Al_2CuMg phase [2].

The aging sequence observed in both the unreinforced alloy and the composite of the Al-Zn-Mg-Cu alloy is [13]:

$$\alpha sss \rightarrow \text{GPZ} \rightarrow \eta^{/} \rightarrow \eta (MgZn_2) \quad (2.3)$$
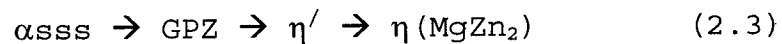
where αsss is the (supersaturated solid solution), GPzone coherent spherical Guinier-Preston zones, $\eta^{/}$ is semi-coherent transition phase and η is the incoherent equilibrium $\eta (MgZn_2)$ phase, shown in Figure 2.1 [13].

To achieve superior mechanical properties in MMCs, it is essential to form adequate interfaces, which tend not to degrade the reinforcement during fabrication, but will retain overall structural stability in both corrosive environments and at elevated temperatures [14]. As a result, composite interfaces will play an important role in determining the resultant of the metal-based composite properties. According to various theoretical and

$$SSSS \rightarrow GP\ zones \rightarrow \eta'\ (MgZn_2) \rightarrow \eta\ (MgZn_2)$$
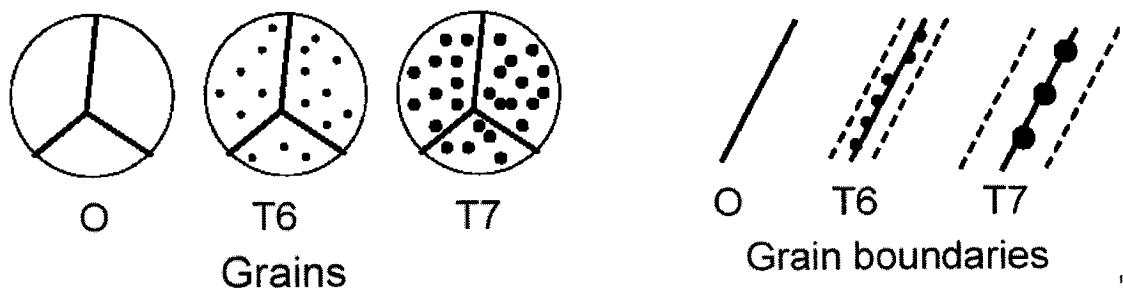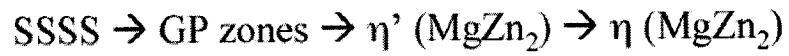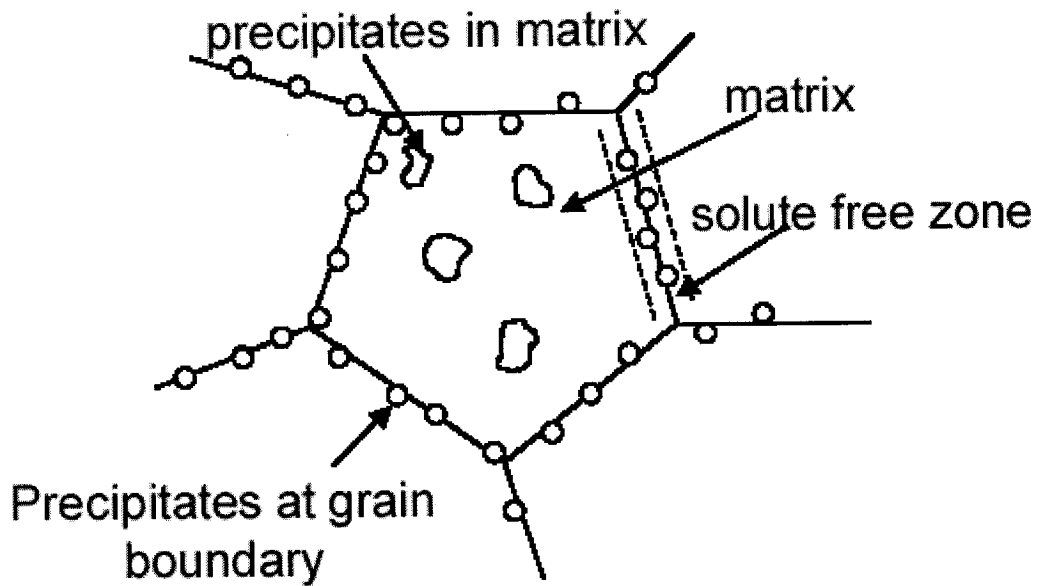
Figure 2.1:Precipitation configuration mechanisms for the Al-Zn-Mg-Cu alloy at different aging conditions.

experimental studies, SiC reacts with aluminum to form Al_4C_3 and Si according to the reaction.

$$4Al + 3SiC \rightarrow Al_4C_3 + 3Si \qquad (2.4)$$
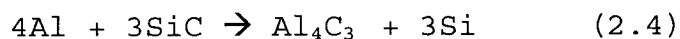
In general, a frequent problem encountered in fabricating aluminum alloy-based composites reinforced with silicon carbide (SiC), boron carbide (B_4C), titanium carbide (TiC), is the formation of Al_4C_3 at the carbide/matrix interfaces as a result of interfacial reactions between the aluminum metal matrix and the reinforcing carbides. Al_4C_3 is known to be very brittle and unstable, resulting in degradation of mechanical properties of the composites [15]. In addition, due to the hydrophilic nature of Al_4C_3, composites containing Al_4C_3 are sensitive in corrosive environments [16]. Therefore, formation of Al_4C_3 during composite material fabrication has to be either avoided or minimized. Methods used to avoid the formation of Al_4C_3 or to obtain desired interfaces in SiC/Al composites, are (a) addition of silicon to the matrix [16], (b) coating of SiC [17], and (c) passive oxidation of SiC [16]. In a comparison study, Weiland and co-workers [18] found the particulate-matrix interface in a SiC particulate-reinforced 2014 aluminum alloy to be defined. There was no evidence of pore formation, and no reactions between the metal matrix and

the reinforcing phase during production and subsequent heat treatment. Moreover, since increased precipitate concentration was not observed at the interfaces, it was concluded that the interface itself did not contribute appreciably to the aging behavior of the composite. Jae-chul and co-workers [19] observed the extent of interfacial reactions in 2024/SiC$_p$ composites to be dependent on processing temperature. Almost no interfacial reaction occurred in a spray formed composite, while significant amounts of interfacial reactions were observed to occur in a powder metallurgy (P/M) hot pressed, thixoformed, and compocast composites [19].

The nature of the change in kinetics and magnitude of hardening during aging of these composites depend on various factors. H. J. Rack and co-workers [20] reported that reducing the magnesium content from 1.63 wt% to 1.34 wt % resulted in a decrease in peak hardness of the metal matrix composites. A similar effect was observed when the copper content was decreased from 4.6 wt% (2124 aluminum alloy) to 3.7 wt% (2048 aluminum alloy).

An increase in dislocation density depends upon size of the reinforcing phase. As the particle size increases for a constant volume fraction, the inter-particle spacing

increases and the dislocation density due to the

coefficient of thermal expansion mismatch decreases [21].

Particle size and inter-particle spacing are related by the

expression [21]:

$$\lambda = \left(\left(\pi / 6 f \right)^{0.5} - 2/\pi \right) \cdot D \qquad (2.5)$$

where, λ = mean edge to edge free path, f = volume fraction

of particulate reinforcement and D = size of reinforcement.

An Al-Cu-Mg alloy reinforced with SiC particulate of ~1 μm

size revealed superior aging behavior in comparison with

composites containing coarser SiC particulate

reinforcements (~12 μm and ~65 μm) [22]. The required time

to reach peak hardness decreased with a decrease in the

size of the SiC particulate reinforcing. This was

attributed to faster diffusion of solutes in the matrix due

to enhanced dislocation density. Sannino and co-workers

[23] found the reinforcement in a 2xxx aluminum

alloy/silicon carbide particulate composite to have an

influence on both precipitation hardening behavior and

aging kinetics. Decreasing the particulate size decreased

the hardening rate during under-aging (UA). However, peak-

aged (PA) and over-aged (OA) conditions were not

appreciably influenced. The aging sequence of 2009

aluminum involves either two or three stages depending upon

the size of the reinforcing SiC particulates. Initial

aging of 2009/SiC consists of GPBI zone formation from a

supersaturated Al-Cu-Mg solid solution (SSSS). During this

stage, the hardness increases with a decrease in

particulate size. The extent of (SSSS) $\rightarrow$ GPB I

transformation decreases as size of the reinforcing

particulate decreases [23]. A decrease in GPB I zone

formation during aging of the smaller (4 µm) particulate-

reinforced metal matrix composite provided evidence that

size of the SiC influences vacancy supersaturation in the

as-quenched 2009 Al-20 vol% SiC particulate (2009/SiC/20p)

composites [23]. The decrease in vacancy supersaturation

was attributed to an increase in particulate

(SiC)/(aluminum alloy) metal matrix interfacial surface

area with decreasing SiC particulate size [23]. The

interfaces served as vacancy sinks during quenching.

Continued aging involved a transition for metal matrices

containing larger reinforcements of GPB I zones to GPB II-

dislocation complexes. For smaller reinforcing

particulates, the first stage of age hardening is absent

and the formation of GPB II-dislocation complexes occurs

directly. Finally, the third stage of age hardening,

common to all particulate sizes for 2009/SiC MMCs, consists

of heterogeneous nucleation of S'/S and GPB II $\rightarrow$ S'/S transformation [23].

It has been shown that work hardening in metal matrix composites is related primarily to particle volume fraction (f_p) and matrix shear modulus [24], the effect of which is considered to be constant for one alloy. Davies [25] examined the CW67 alloy (of composition in weight percent%: 8.99Zn, 2.47Mg, 1.47Cu, 0.1Zr, and 0.1 of each Fe, Ni and Si, the balance being Al) blended with silicon carbide particulates having a mean size of 5 μm and four volume fractions (10 vol%, 15 vol%, 20 vol% and 25 vol%). The aging kinetics for the high volume fraction material was quite different from the aging kinetics for the unreinforced counterpart and for the CW67/SiC/10p. Moreover, precipitation in the CW67/SiC/20p was found to occur primarily on dislocations. This is because of the increased dislocation density and the concomitatant paucity of vacancies present [13]. The precipitates so formed have little influence on strengthening.

The method of processing the composite has a significant impact on microstructure. Dutta and co-workers [26] reported the aging kinetics in cast materials to be considerably slower than in the powder metallurgy processed

counterpart. Around the same time, Weiland and co-workers [18] have shown that the kinetics of precipitation in a SiC particulate reinforced 2014 aluminum alloy and a reference powder having the same composition to differ substantially. The difference was ascribed to thermal misfit stresses in reinforced metal matrix composites, which are not present in the powder. Jae-chul and co-workers [19] evaluated the aluminum metal matrix composites $2024/SiC_p$ fabricated using the techniques of spray forming, P/M hot pressing, thixoforming, and compocasting. The results revealed that processing temperature employed in spray forming is significantly lower than the transition temperature determined for the composite. They concluded, that spray forming can be considered to be an adequate processing technique for fabricating wrought Al/SiC_p composites [19].

In reinforced metal matrices, it is recognized that the matrix alloy does not necessarily respond to heat treatment in a manner identical to that of the unreinforced counterpart. Consideration should be given to the possible influence of reinforcing particulates, and whiskers on the structure of the heat-treated matrix and resultant properties [10]. Several researchers [27-31] have found a substantial influence of reinforcement on aging kinetics,

precipitation behavior, and dissolution kinetics. It was shown that the heat-treatment response of a reinforced alloy is significantly different from an unreinforced counterpart. However, Harris and co-workers [28] found that SiC additions had no influence on room-temperature aging response of aluminum alloy based composites compared to the unreinforced counterpart. McDanels and co-workers [29] found high strength matrix alloys to benefit proportionally less from the addition of a ceramic reinforcement than lower strength counterparts. The reason for different aging kinetics in metal matrix composites (MMCs) is that they contain a high dislocation density compared to the unreinforced alloy, generated to relieve the thermal stresses produced during cooling. A high dislocation density contributes positively to altering the aging kinetics by either enhancing the diffusion rates of elements within the matrix or by providing preferential sites for precipitate nucleation [30]. However, in some cases, high dislocation densities tend to reduce the age-hardening rates of the composite by effectively removing the quenched-in vacancies, which are an important constituent in the early stages of Guinier-Preston (GP) zone formation [31].

2.3.2. Magnesium alloy-based composites

Magnesium is the lightest of the structural metals, i.e. approximately 35% lighter than aluminum but more active in a corrosive environment. The corrosion resistance of magnesium alloys has been greatly improved by increasing its purity level [32-42]. However, the strength is rather low at the elevated temperatures. Conventional alloying practice cannot ensure the attainment of certain properties and to achieve these particulate reinforcements need to be used. The candidate reinforcement materials are aluminum oxide (Al_2O_3) and silicon carbide (SiC). The greater stability of Al_2O_3, compared to SiC, in an aluminum metal-matrix is reversed for magnesium matrices. Magnesium metal-matrix composites are being developed to essentially have the same properties as those provided by aluminum metal-matrix composites (MMCs), namely: (a) high stiffness, (b) light weight, and (c) low coefficient of thermal expansion (CTE).

Ceramic particulates, when added to a metal alloy, tend to increase the dislocation density in the metal matrix upon quenching from the solutionizing temperature [32]. These dislocations in a precipitation hardenable alloy can have two effects on the matrix: (1) it gives rise

to simple dislocation strengthening, and (2) they can act as heterogeneous sites for the nucleation of strengthening precipitates during subsequent aging treatments. The latter in turn can alter precipitation kinetics, and thus precipitation hardening, of the metal-matrix composite [1].

The nucleation behavior of the primary phase on reinforcement particles in magnesium alloy based metal-matrix composites is fairly well studied [33,34]. Mikucki and co-workers [33] reported that the presence of SiC particles tends to refine the matrix microstructure of the magnesium alloy to varying extent depending on the processing. Recently, Mg-Al-Zn alloy (AZ91)/SiC$_p$ composites were prepared using a liquid mixing and casting process. The melts were prepared in an electric resistance furnace using a steel crucible and a SF$_6$/CO$_2$ gas atmosphere. Luo and co-workers [34-35] observed grain refinement in magnesium metal matrix composites is the result of two separate processes: nucleation and growth. In the AZ91/SiC/10p metal-matrix composite, the observed grain refinement (67%) is the combined effect of enhanced heterogeneous nucleation and restricted grain growth during solidification. In the AZ91/SiC/0.5p metal-matrix composite, the grain refinement (37%) was attributed to a heterogeneous nucleation

mechanism [36]. These researchers also found the SiC particulates to be thermodynamically stable in pure magnesium and no reaction products were found at the pure magnesium/SiC interfaces. In the SiC reinforced AZ91 alloy, however, particulate/matrix interface reactions are evidenced by the presence of the Mg_2Si phase and complex reaction products containing magnesium (Mg), silicon (Si), aluminum (Al), carbon (C), and oxygen (O) on the surface of SiC particles. Saravanan and co-workers [37] used the conventional stir casting process for fabrication of a pure magnesium-30% vol. SiC metal matrix composite without the use of flux or SF_6/CO_2 protective gas atmosphere. There is no marked difference in the dendrite arm spacing/cell size of the composite compared to pure magnesium. Distribution of SiC particles was not completely uniform in the as-cast composite. Also, there were no reaction products at the interface [37]. Using the technique of disintegrated melt deposition Gupta and co-workers [38] revealed the presence of minimal porosity and completely recrystallized matrix in a Mg/SiC composite. Concurrently, a uniform distribution of the SiC particulates and Mg/SiC interfacial integrity were also realized. The presence of SiC particulates

resulted in a reduction in the CTE value of the magnesium

alloy metal matrix.

The magnesium-zinc alloys exhibit the most marked age

hardening response among the magnesium-based alloys.

Mingyuan and co-workers [39] reported that addition of

boron carbide particulates (B_4C_p) and silicon carbide

whiskers (SiC_w) affects the artificial aging behavior of

ZK60-based composite with respect to the monolithic

counterpart. The formation of the β' ($MgZn_2$) phase is

considerably accelerated. Also, the amount, growth rate

and stability of the precipitates near the reinforcement-

matrix interfaces increased [39]. The age hardening

efficiency of the composite is the same as that of the

monolithic alloy. Accelerated aging was also reported for

a SiC particle-reinforced Mg-6%Zn composite where

appreciable hardening takes place at shorter times and

lower temperatures [40]. The interfacial reactions in the

composite were examined to get an insight into the nature

of reinforcement/matrix interfaces [41]. Experimental

results of the (SiC_w and B_4C_p)/ZK60A hybrid composite

revealed that SiC_w did not make a direct contribution to the

interfacial reaction, since it did not take part in the

reaction. However, the surface of B_4C_p was oxidized during

fabrication of the composite, resulting in the formation of magnesium oxide (MgO) and magnesium boride (MgB_2). Thus, SiC_w is more stable than B_4C_p in the (SiC_w and B_4C_p)/ZK60A hybrid composite [41]. To eliminate shrinkage defects in metal-matrix composites and improve the metal matrix-reinforcement interface bond strength Lianxi and co-workers [42] have modified the squeeze casting process. The two-step squeeze casting procedure is an effective route for fabrication of magnesium matrix composites. In particular, the process has advantages over conventional squeeze casting in two ways. The first being deformation of the preform during casting is reduced to a very low level, thus ensuring an as-designed reinforcement volume fraction of the composite. The second is a possible entrapment of gases coupled with oxidation of the magnesium alloy melt, during conventional squeeze casting, is effectively avoided due to a steady infiltration under very low pressure prior to high pressure squeezing [33].

2.4. Manufacturing Processes for Metal-Matrix Composites

The primary industrial-manufacturing processes can be classified as shown in Figure.2.2 to be, liquid phase, solid state and gaseous state. In particular, some of the processing routes are more expensive than others. Liquid
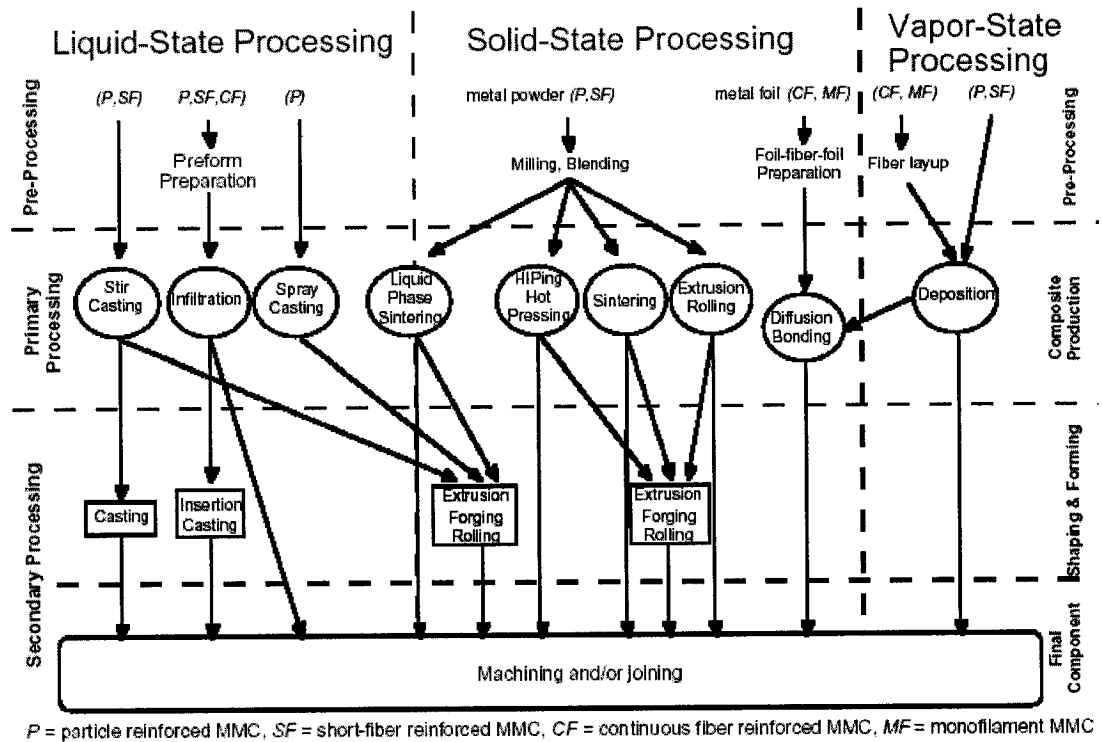
Figure 2.2:Overview flow chart of processing routes for
metal matrix composite [5].

phase processing, which is a lowest cost route is characterized by an intimate interfacial contact and strong bonding, but with the formation of a brittle interfacial layer. Solid-state processes include powder blending followed by consolidation, diffusion bonding and vapor deposition. Liquid phase processes include squeeze casting and squeeze infiltration, spray deposition, slurry casting (compocasting), and reactive processing (in-situ composites). The individual composite production operations are briefly outlined below under these groups.

2.4.1. Liquid State Processing

2.4.1.1. Slurry casting

Liquid metal is stirred as solid reinforcement particles are added to the melt to produce a slurry. Stirring continues as the melt is cooled until the metal itself becomes semi-solid and traps the reinforcement particles in a uniform dispersion. Further cooling and solidification then takes place without additional stirring. The slurry is transferred directly to a shaped mold prior to complete solidification, or is allowed to solidify in billet or rod shape so that it can be reheated to form a slurry for further processing by techniques of die-casting [43].

2.4.1.2. Reactive processing

There are several different processes that would fall under this category. Directional solidification of eutectics in which one of the phases solidifies in the form of fibers is one such process. Inherent limitations in the nature and volume fraction of the reinforcement and the morphological instabilities associated with thermal gradients have resulted in a decrease in interest in these types of composites. Exothermic reactions, such as direct metal oxidation, are one family of processes for the production of in-situ composites. A major advantage for use of this class of composites is that the in-situ reaction products are thermodynamically stable [44].

2.4.1.3. Squeeze casting and squeeze infiltration

Porous preforms of reinforcement material are infiltrated by molten metal under pressure to produce metal-matrix composites. Reinforcement materials include: (a) carbon, (b) graphite, and (c) ceramics, such as: oxides, carbides, or nitrides. Reinforcement forms include: (i) continuous fibers, (ii) discontinuous fibers, and (iii) (iii) particulates. Most commonly metals used include aluminum, magnesium, copper, and silver. The volume fraction of reinforcement in the metal-matrix composites

varies from 10 to 70% vol depending on the particular application for the material.

Generally, the preform, which is shaped to match the contours of the mold, is not wetted by the molten metal and must be infiltrated under pressure. In squeeze casting, a hydraulically activated ram applies a controlled pressure to the molten metal to attain infiltration of the preform without damaging it. Infiltration may or may not be vacuum assisted. Once infiltration is complete, a high pressure is applied to eliminate shrinkage porosity that occurs when the liquid metal contracts as it transforms to the solid state. This complete consolidation, or absence of porosity, provides the squeeze cast metal-matrix composite with excellent mechanical properties.

2.4.1.4. Spray deposition

A number of processes have evolved under this category in which a stream of metal droplets impinge on a substrate in a manner as to build up a composite [45]. If the choice of reinforcement is particulates, it can be fed into the spray. The techniques employed fall into two distinct classes:

(a)   depending on whether the droplet stream is produced from the molten bath (for example, the Osprey process), and

(b)   continuous feeding of cold metal into a zone of rapid heat injection (for example, the thermal spray process).

In general, spray deposition methods are characterized by rapid solidification, low oxide contents, and significant porosity levels [45]. Depositions of this type are consolidated to full density during subsequent processing.

2.4.2. Solid State Processing

2.4.2.1. Powder blending and consolidation

Powder blending and consolidation is a commonly used method for preparation of discontinuously-reinforced MMCs. In this process, powders of the metallic matrix and reinforcement are first blended and fed into a mold of the desired shape. Blending is carried out either in the dry or in liquid suspension. Pressure is then applied to further compact the powders (cold pressing). The compact is then heated to a temperature, which is below the melting point but high enough to develop significant solid-state diffusion (sintering). After blending, the mixture is consolidated by hot pressing or hot isostatic pressing

(HIP) to obtain a high density product. The consolidated composite is then available for secondary processing. Achieving a homogeneous mixture during blending is a critical factor because the discontinuous reinforcement tends to persist as agglomerates with interstitial spaces too small for penetration of matrix particles [8].

2.4.3. Vapor State Processing

2.4.3.1. Vapor deposition

Prominent among the vapor deposition techniques for fabrication of metal matrix composites is electron beam/physical vapor deposition (EB/PVD). The process essentially involves continuous passage of fiber through a region of high partial vapor pressure of the metal to be deposited, where condensation takes place so as to produce a relatively thick coating on the fiber. The vapor is produced by directing a high power (~10kW) electron beam onto the end of a solid bar feedstock. Distinct advantage of this technique is that a wide range of alloy compositions can be used. Most importantly, an advantage worth noting is that there is little or no mechanical disturbance of the interfacial region, which can be quite significant when the fibers have a diffusion barrier layer or a tailored surface chemistry. Final fabrication of the

composite is completed by assembling the coated fibers into a bundle or array and consolidating in a hot press or hot isostatic pressing (HIP) operation [46].

2.5. Mechanical Properties of Metal-Matrix Composites

The behavior of discontinuous MMCs is largely controlled by the load transfer capability, which is directly linked to the quality of the interface, by hardening of the matrix and resultant stress accommodation capability. This is directly dependent on an understanding of the complex and correlated microstructural parameters, such as: (a) dislocation density, and (b) precipitation state. An obvious effect of the reinforcement on properties of the matrix is observed in the mechanical properties. A uniform distribution of the reinforcement in matrices of metal matrix composites results in a significant improvement in yield strength, or flow stress, and even ultimate tensile strength by as much as 60% over the unreinforced counterpart. The reinforcement generally has a brittle nature, which degrades the overall ductility as well as fracture toughness of the metal-base alloys [47].

2.5.1. Tensile Properties

2.5.1.1. Aluminum matrix composites

The effect of heat treatment and size of particulate the reinforcement on tensile fracture of SiC_p-reinforced aluminum alloy was studied by Singh and co-workers [48]. They found the dominant mode of microscopic failure to change from particulate fracture in the underaged (UA) material to failure at and near the particle/matrix interfaces, and failure in the matrix for an over-aged (OA) condition. However, Lewandowski and co-workers [49] found the effect of matrix microstructure (UA versus OA) on macroscopic tensile ductility was negligible, while the remaining uniaxial tensile properties were similarly negligibly affected by drastic changes in microstructure. Vedani and co-workers [50] demonstrated the tensile deformation of the 2014/SiC composite to occur along the entire gauge length and tended to localize immediately prior to fracture. The differences found between the UA and the OA treated composite was due to the fact that uniform deformation was predominant for the under-aged condition whereas for the peak-aged material, localization of strain contributed a significantly to the total elongation. Similar considerations were also drawn from an

estimation of the number of fractured particulates. In the "T6" temper a larger fraction of the broken SiC particulates were found close to the final fracture region.

Matrix alloy is one of the key microstructural variables, which influences the mechanical properties of a material. Stronger matrix alloys tend to produce stronger composites, although an increase in strength due to presence of particulate reinforcements tends to be less when high strength matrix alloys are used. In the case of the highest strength matrix alloys, the particulate reinforcement has been observed to cause a reduction in strength [51].

It is generally found that size of the reinforcing SiC_p does influence the tensile behavior of the composite. Zhang and co-workers [52] observed that the composite containing a smaller particle size (7 μm) had a higher plastic flow stress when compared to the composite with a larger particle size (14 μm). In addition, a larger particle size results in a lower strain to failure and even low fracture strength. This is primarily because they are more likely to contain flaws of a critical size [53]. It is likely that when the applied stress reaches the yield stress of the matrix material, most of the reinforcing particles will

still be intact. For the case of smaller reinforcing particulates the thermal residual stresses will be greater, but so will potential strengthening contributions due to dislocation density and grain size [1]. Hence, actual stress on a matrix will be less than the yield stress and the matrix will not yield until greater stresses are applied, and internal damage begins to accumulate. This would lead to an observed increase in yield stress and tensile strength of the composite materials.

The yield stress and tensile strength tend to increase, and toughness and ductility decrease with increasing volume fraction of reinforcing particulates [29]. However, properties of the silicon carbide particulate (SiC_p) reinforced metal-matrix composites have been found to be strongly dependent on both the processing technique and subsequent thermo-mechanical treatments [54]. For the highest volume fraction composite, the tensile yield strength values decreased for the peak-aged and over-aged conditions whereas in the solutionized condition an increase was observed [54].

2.5.1.2. Magnesium matrix composites

The additions of ceramic reinforcements led to considerable improvements in the mechanical properties of

magnesium-based composites [55]. Luo and co-workers [35] examined the strain-hardening behavior of AZ91/ SiC composites prepared by the liquid mixing and casting processes. They showed the strain-hardening rate during plastic deformation of the composite is higher than that of the AZ91 matrix alloy, while differences between the strain-hardening rates of the two materials decreases with an increase in plastic strain. In comparison with the aluminum (7XXX)/SiC$_p$ composites, the magnesium/SiC$_p$ composite behaves differently during deformation and fracture. In aluminum alloy-based composite, in which cracking of the reinforcing SiC particle is the predominant type of damage occurring during fracture of the material, the AZ91/SiC$_p$ composite shows more matrix cracking of the matrix but less cracking of the reinforcing particulates.

Martin and co-workers [55] examined the magnesium composite reinforced with SiC particulates and subject to various heat treatments. They reported that the addition of SiC particulates led to an increase in the elastic modulus by 62%, and tensile strength of the composite in the artificially aged condition was better than the artificially aged unreinforced counterpart. The composite exhibited a strong response to the two-step artificial

aging treatment, which increased both the yield and tensile strengths over that of the as-received material. However, the strain-to-failure and fracture toughness of the composite were very low. They attributed this to the presence of abundant porosity coupled with the formation of microscopic-cracks in the matrix because of large strain gradients, which are developed around the particulate reinforcements during plastic deformation and cannot be accommodated.

The overall fracture toughness of a magnesium alloy metal matrix composite depends on the extent of heavily strained region (plastic zone) ahead of the crack tip that is a function of both yield strength and modulus of elasticity [48]. It is also dependent upon size [51] and volume fraction of the reinforcing particulates [54]. Chua and co-workers [56] investigated the influence of particle size on the mechanical properties of $AZ91/SiC_p$ composites. There was little difference in the yield and tensile strength of the 15 μm and 25 μm SiC_p. However, the 50 μm particulates possessed a significantly lower 0.2% yield and tensile strength.

Using the spray processing type techniques, disintegrated melt deposition (DMD) by Gupta and co-workers

[38] revealed that an increase in weight percentage of SiC particulates led to an increase in microhardness of the metallic matrix coupled with an increase in overall hardness of the composite material. They pointed out that the increasing presence of SiC particulates in the magnesium matrix did not affect 0.2% yield strength but reduced the tensile strength, ductility and work for fracture. The elastic modulus increased as the weight percentage of SiC particulate increased.

2.5.2. Fatigue mechanism

2.5.2.1. Aluminum matrix composites

Several studies have shown that the stress-controlled fatigue lives of particulate-reinforced aluminum composites are superior to those of unreinforced matrix material [57-62]. These improvements were attributed to the higher stiffness of the composites [57]. However, at high-applied stresses fatigue resistance of composites is inferior to the unreinforced alloy. Also, at high stresses the plastic strains are noticeably lower in the composite than in the unreinforced counterpart, the cyclic ductility is also lower, as is the resistance to crack initiation. There are many microstructural variables influencing the fatigue properties of composites. Typically, these include: (a)

particulate size, (b) particulate volume fraction and (c) their distribution in the extruded MMCs [58-61].

The influence of different sizes of SiCp on the cyclic stress response of Al-Cu-Mg alloy matrix composites has also been studied [59]. The study of cyclic fatigue revealed a strong dependence on size of the reinforcement. Finer size of SiC_p reinforcements in Al-Cu-Mg alloy matrix composite had a higher degree of cyclic hardening. Tokaji and co-workers investigated the 2024/SiC_p composites having particle sizes of 5 μm, 20 μm and 60 μm. They reported the fatigue strength to increase with a decrease in particle size [60]. The addition of 5 μm SiC particles led to higher fatigue strength than the unreinforced alloy. The composite with 20 μm SiC particles exhibited higher strength than the unreinforced counterpart at high stress levels [60]. However, the improvement tended to diminish with a decrease in stress level coupled with slightly reduced fatigue strength at low stress levels. For the composite with 60 μm SiC particles, the fatigue strength was the same as that of the unreinforced alloy at high stress levels but significantly reduced at lower stress levels.

An increase in fatigue strength resulting from an addition of reinforcement material depends on both

fabrication processes and fabrication defects. Powder

processed-and-extruded, where processing imperfections have

presumably been minimized, have significantly improved the

fatigue strength of aluminum alloy-based MMCs [46-57].

However, in many cast materials, casting-related defects

such as, porosity, are inherent features of the

microstructure. These defects have a deleterious effect on

overall fatigue properties [61].

2.5.2.2. Magnesium matrix composites

Cyclic strain hardening was observed in the solution

heat-treated condition of the magnesium alloy based

composites, whereas the cyclic fatigue behavior was stable

after aging at elevated temperature [55]. The amount of

cyclic hardening in the T4 temper was moderate for the

magnesium alloy based composites compared to the aluminum

alloy based counterpart.

The effect of changes in reinforcement volume fraction

and reinforcement (silicon carbide particulates) size has a

significant influence on fatigue behavior of magnesium

alloy based composites. Vaidya and co-workers [62] carried

out a study on the AZ91D composite. In their study they

found the addition of SiC_p to increase both strength and

elastic modulus of the AZ91D composite, with higher

strengths resulting from use of finer reinforcement (15 μm versus 52 μm). Reinforcing with either 20 or 25 vol.% of 15 μm SiC$_p$ provided improved performance with respect to monolithic AZ91D, while fatigue life of the composites containing 52 μm SiC$_p$ was inferior to both the monolithic AZ91D alloy and AZ91D containing 15 μm SiC$_p$. A large percentage of cracked SiC$_p$ were found both on the fracture surface as well as beneath the fracture surface for the composites containing 52 μm SiC$_p$ [62].

2.6. Modeling The Mechanical Performance

Modeling of metal matrix composites provides way of predicting effective properties of the composite. The stress-strain behavior of ductile solids under a uni-axial load, including the flow characteristic of the composites was modeled using the Ramberg-Osgood equation:

$$\varepsilon = \sigma/E + \alpha(\sigma/\sigma_o)^m = \sigma/E + (\sigma/H)^{1/n} \qquad (2.6)$$

where σ is the stress, σ_o is the yield strength, m is the inverse of strain hardening exponent (n), α is a constant, and H is the strength coefficient.

Different models exist for the elastic behavior of MMCs. All models are based on the assumption of perfect and intact reinforcement. The Young's modulus follows the rule

of mixture (ROM) theory for particulate composites, and is

given by the Tsai-Halpin equation [63]:

$$E_c = \left(E_m\left(1 + 2 \cdot s \cdot q \cdot f_p\right)\right)/\left(1 - q \cdot f_p\right) \qquad (2.7)$$

$$q = \left(E_P/E_m - 1\right)/\left(E_P/E_m + 2s\right) \qquad (2.8)$$

E, is the elastic modulus, f = volume fraction, and s = the

aspect ratio of the reinforcement. The subscripts m and p

refer to matrix and reinforcement. These semi-empirical

models are widely used due to their simplicity. The elastic

modulus of a composite is estimated from the model proposed

by Hashim and co-workers [64]:

Upper bound:

$$E_c = E_m f_m + E_p f_p \qquad (2.9)$$

Lower bound:

$$E_c = E_m(E_m f_p + E_p(f_p + 1))/(E_p f_m + E_m(f_p + 1)) \qquad (2.10)$$

Where the c, m and p refer to the composite, the matrix and

the reinforcement (particulate) respectively.

The Finite Element Analysis (FEA) has been extensively

used to calculate/estimate the direct strengthening effects

in composites [65].

2.6.1. Fatigue life estimation models

The nominal stress approach has been widely used for

the study of premature failures of components when

subjected to fluctuating loads. Traditionally, the
magnitude of the observed cyclic stresses were less than
the tensile elastic limit and with fatigue lives, greater
than 100,000 cycles. This pattern of behavior is known as
"high-cycle fatigue" (HCF). As duty (usage) cycles have
become more severe and components more complicated, a more
diverse pattern to characterize fatigue behavior has
emerged. In this regime, the cyclic loads are relatively
larger, having significant amounts of plastic deformation
associated with them and resultant short fatigue lives.
This type of behavior is commonly referred to as "low-cycle
fatigue" (LCF) or more recently strain-controlled fatigue
[66]. A number of years ago, Basquin observed the stress-
life data can be represented by a straight line
relationship when plotted using log scales. The
relationship is expressed in terms of true stress as:

$$\sigma_a = \sigma_f' \cdot (2N_f)^b \qquad (2.11)$$

where: (a) σ_a is the true cyclic stress amplitude, (b) σ'_f
is the regression intercept called fatigue strength
coefficient, (c) $2N_f$ number of reversals-to-failure, and
(d) b is the regression slope called the fatigue strength
exponent. σ'_f and b are considered as material properties
with the fatigue strength coefficient (σ'_f) being

approximately equal to the monotonic fracture stress (σ_f) and b varies between (-0.05) and (-0.12). The Basquin equation is rewritten in terms of elastic strain amplitude:

$$\varepsilon_e = \sigma_a / E = (\sigma'_f / E) \cdot (2N_f)^b \qquad (2.12)$$

where: ε_e is the elastic strain amplitude and E is the modulus of elasticity.

In the 1950s, Coffin and Manson [67] independently proposed the plastic strain component of a fatigue cycle to be related to fatigue life by a simple power law:

$$\varepsilon_p = \varepsilon'_f \cdot (2N_f)^c \qquad (2.13)$$

where: ε_p is the plastic strain amplitude, ε'_f is the regression intercept called the fatigue ductility coefficient, and c is the regression slope called the fatigue ductility exponent. ε'_f and c are considered to be material properties, with the fatigue ductility coefficient (ε'_f) being approximately equal to the monotonic fracture strain (ε_f) and c varies between (-0.5) and (-0.8).

The total is the sum of elastic and plastic strain amplitude, and can be obtained by summing together the Basquin and the Coffin-Manson components.

$$\varepsilon_t = \varepsilon_e + \varepsilon_p \qquad (2.14)$$

$$\varepsilon_t = (\sigma'_f / E) \cdot (2N_f)^b + \varepsilon'_f \cdot (2N_f)^c \qquad (2.15)$$

2.6.2. <u>Unit cell models</u>

A calculation of the strengthening effect in composites is usually based on the unit cell model, in which one or more reinforcement particles is embedded in the matrix, so as to simulate a composite material having a periodic array of reinforcements. A periodic arrangement of particles having the shape of a unit-cylinder, truncated-cylinder, double-cone and sphere may be simulated using the appropriate boundary conditions [68]. Such an analysis is independent of both the physical dimensions of the unit cell and the reinforcement, but is based on volume fraction of the reinforcing phase, severity of load transfer and stress triaxialty resulting from the presence of a second phase. While the unit cell analysis is independent of inclusions and unit cell size, some size dependence has been noted from experimental tests [47,68]. The unit cell approach is useful for studying the effects of reinforcement volume fraction, reinforcement particle shape, reinforcement particle distribution, load orientation, matrix and inclusion material properties, and damage, such as: (a) particle cracking, and (b) interface debonding [47]. The two-dimensional axisymmetric unit cell [69] and three-dimensional rectangular unit cell [65] are

the most popular. McMeeking and co-workers [70] used axisymmetric unit cells for a spherical and equiaxed cylinder to study the influence of residual stress in a SiC particulate reinforced aluminum alloy based composite. Jain and co-workers [71] analysed residual stresses in an annealed 6061 aluminum alloy reinforced with SiC particles using a three dimensional finite element analysis. Descriptions of composites are based on the periodic unit-cell approaches or embedded cell methods. In this method, the material is simulated by a model consisting of a core, similar to a unit cell, containing separate representation of the matrix and reinforcing particles. This core surrounded by an outer region with homogenized material properties of the composite. For particulate-reinforced MMCs the results contained in the literature showing how the periodic unit cell methodology has been successfully used to study loading behavior in materials, based on models used for idealized and regular microstructural geometries [72]. Models of this type have also been used by Llorca and co-workers [47] to study the influence of cyclic loading. The unit cell model provides an accurate estimate of global mechanical properties while concurrently

providing an indication of the micro-mechanical stress-strain distributions around the reinforcement phase.

The finite element method-based studies of: (a) Llorca and co-workers [82], and (b) Christman and co-workers [65] are involved with deformation analysis of a unit cell, with the metal matrix and reinforcing phase having a certain geometrical arrangement that represents particle local inhomogeneity (clustering) in the composite matrix, i.e., the distances between two or three adjacent reinforcements were shortened. Because of the geometrical arrangement, the clustering is restricted to interactions between two or three particles and/or short fibers. Repetition of unit cells in space implies that the composite consists of uniformly distributed clusters. Each cluster contains two or three reinforcing particles. They reported that the influence of clustering of the reinforcement on the stress-strain response is not significant for the composites reinforced with particulates having a unit aspect ratio. Christman and co-workers [65] showed, purely on the basis of finite element simulations of deformation of metal matrix composites, that uniformly distributed aligned cylindrical particles present more effective reinforcements than spherical particles.

2.6.3. Micromechanical models

Micromechanical unit cell modeled using finite element method is a valuable tool in the analysis and study of the failure behavior of metal matrix composites [68]. This method allows for quantification of the interaction between the mechanisms of: (1) reinforcement fracture, (2) matrix-reinforcement interfacial debonding, and (3) ductile failure. Microscopic voids already exist in metals prior to plastic deformation. They nucleate during deformation as a result of the presence of coarse second-phase inclusions in the metal matrix. The ductile failure mechanism in most structural metals involve: (i) nucleation of voids due to failure by fracture of the particle-matrix interface, and (ii) failure of the reinforcement particle by cracking or micro-cracking. The microvoid nucleation strain is often exceeded, for a given set of particles in a plastically deforming metal matrix, and continuing plastic flow will facilitate growth of the microscopic-voids to a size that exceeds the size of the existing holes. Also, coalescence of the microscopic-cracks and linking of neighboring voids results in a decrease in load carrying capacity of the material [73].

Micromechanical approaches using local failure criteria provide information about the influence of inhomogeneities on the initiation and evolution of local damage. Applying suitable homogenization and averaging theorems, they contribute to the prediction of overall behavior of the material. The Gurson [74] model was derived based on the theory of homogenization (transition from microscopic-to-macroscopic properties) and limit-analysis of a rigid-ideal plastic hollow sphere (representing a typical cell-element in a porous ductile medium) when subjected to arbitrary loading. Tvergaard [75] introduced a parameter into the model to account for interactions between voids and to get a better fit with the results. To account for coalescence of the micro-voids, which occurs during the later stages of ductile deformation, Tvergaard and Needleman [76] proposed to replace the true porosity in the yield criterion by a larger fictitious one. Thomson [73,77] proposed a model that is capable of simulating the intrinsic ability at predicting void coalescence. Tvergaard [78] developed the cohesive zone model, where the crack path is prescribed and presented for a thin layer of material having its own constitutive relation (traction-separation law). The

relation is such that with increasing crack opening, the traction reaches a maximum and then decreases. Eventually, the traction vanishes and complete decohesion occurs. Siegmud and co-workers [79] studied the inter-relationship between the model of crack growth based on void nucleation and coalescence: (a) the Gurson-Tvergaard-Needelman model, and (b) cohesive zone model. Xia and co-workers [80] developed a computational cell methodology, where crack propagation occurred because of void growth in front of the crack tip. Void growth is confined to a layer, the thickness of which is equal to the mean distance between inclusions, which causes void initiation. The layer consists of cubic cells, each cell containing a cavity of a given size. The void growth in each cell is described by the Gurson-Tvergaard model. When void volume fraction is removed the crack grows. Using the cohesive zone models or computational cell methodology together with unit cells placed in front of a growing crack allows studying the mechanisms of crack growth and the influence of material structure on crack propagation. Anderson [81] simulated crack propagation by mechanisms of void growth and coalescence ahead of a crack tip. He used an axisymmetric cylindrical unit cell from a rigid-perfectly plastic

material, having a spherical void, and varied the ratio between size of the void and radius of the cell. He found the dissipation of energy during void growth, per unit of fracture surface, was proportional to the distance between voids.

CHAPTER III

MATERIALS SELECTION

3.1. 2009 Aluminum Matrix Composite

The DRA MMC material selected for investigation in this study was based on Al-Cu-Mg matrix alloy, designated by the Aluminum Association as AA2009. This matrix alloy system was chosen since it provides excellent combinations of strength and damage tolerance. The nominal chemical composition (in weight percent) of the matrix alloy is given in Table 3.1. The reinforcement used was silicon carbide particulates (referred to as SiC_p), 15 percent by volume. The material was produced and made available by [DWA Aluminum Composites (Chatsworth, CA, USA)]. Details of the processing technique (both primary and secondary) are considered to be proprietary by the manufacturer. The 2009/SiC/15p MMC was provided as an extruded billet in the T42 condition.

52

Table 3.1: Nominal chemical composition of aluminum alloy 2009 (in weight percent).

	Elements				
Alloy	Cu	Mg	Fe	Si	Al
2009	3.7	1.30	0.05	0.16	Balance

3.2. 7034 Aluminum Matrix Composite

The aluminum alloy MMC used in this research investigation was made using the spray processing technique and provided as an extruded billet by the [Air Force Materials Laboratory (Dayton, Ohio, USA)]. A practical limit of about 8% wt of zinc is imposed for conventional cast materials because of inherent foundry problems such as solute macro-segregation and cracking. The spray deposition technique enables the level of zinc in the alloys to be increased. This increases the volume fraction of hardening precipitates, thus facilitating an improvement in strength. Zirconium was added to form small coherent dispersions, which control recrystallisation and grain growth. The nominal chemical composition (in weight percent) of the matrix alloy is given in Table 3.2. The billet was obtained by extruding the consolidated sample through a standard shear-face die. The as-received billet was subject to the following heat treatment:

(a) solution heat treated at 490 °C for 4 hours,

(b) immediately quenched in cold water, and

(c) artificially aged at the following temperatures:

(1) 120 °C for 30 minutes to get the under-aged (UA) condition, and

Table 3.2: Nominal chemical composition of aluminum alloy 7034 (in weight percent).

			Elements		
Alloy	Zn	Mg	Cu	Zr	Al
7034	11.05	2.19	1.06	0.19	Balance

(2) 120 °C for 24 hours to get the peak-aged

condition.

The composites are referred to henceforth in this study as

7034/SiC/15p-UA and 7034/SiC/15p-PA.

3.3. Mg-6%Zn Matrix Composite

Elemental magnesium was melted in a stainless steel

crucible. The melt was prevented from burning by using a

protective atmosphere of carbon dioxide, air and SF_6 [83]. A

nominal 6.0 weight percent of zinc was added to the melt.

This was followed by the addition of 600 grit silicon

carbide (SiC) particulates to the molten magnesium-zinc

alloy using proprietary techniques. The molten composite

material was cast into billets. A stainless steel impeller

continuously stirred the composite melt so as to keep the

SiC particulates in motion and away from suspension. Prior

to extrusion, the composite billet was homogenized at 672 °K

for 4 hours followed by quenching in water. The billet was

extruded into a solid rod using classical extrusion

techniques that are employed for conventional magnesium

alloys. The reduction ratio used was 60:1. The

manufacturer [Dow Chemical Company (Freeport, Texas, USA)]

considers precise details of the primary processing and

secondary processing treatment to be proprietary. The

Z6/SiC/20p MMC was provided in the as-extruded condition

(F).

CHAPTER IV

EXPERIMENTAL TECHNIQUES

4.1. Microstructure Characterization

Metallographic samples were cut from the as-received composite extrusion, mounted in bakelite and wet ground on 320, 400 and 600 grit SiC impregnated emery paper, using copious amounts of water as lubricant. The mounted and ground samples were mechanically polished using a one-micron alumina-powder suspended in distilled water. Fine polishing to mirror finish was achieved using 0.5-micron diamond paste. Reinforcement morphology and distribution in the metal matrix, and other intrinsic microstructural features were examined in an optical microscope and photographed using bright-field illumination technique.

4.2. Specimen Preparation

Blanks of length 150 mm were cut from the as-received composite extrusions using a diamond-coated blade. Smooth cylindrical test specimens (6.25-mm gage diameter and 25-mm gage length) were machined from the blanks using diamond tooling. The specimens were machined with the stress axis

58

parallel to the extrusion direction and conformed to specifications in ASTM Standard E8-93 [84]. The length-to-diameter ratio of the mechanical (fatigue) test specimen was chosen so as to minimize buckling during stress-amplitude-controlled and strain-amplitude controlled cyclic deformation. To minimize the effects of surface irregularities and finish, the test specimen surface was prepared by mechanically polishing the gage section using progressively finer grades of silicon carbide impregnated emery paper and then finish polished using 0.5 micron alumina powder suspended in distilled water so as to obtain a mirror-like finish that is free of all circumferential scratches and surface machining marks.

4.3. Mechanical Testing

4.3.1 Tensile Tests

The tensile and cyclic fatigue tests were performed on a fully automated, closed-loop servo-hydraulic test machine (INSTRON) equipped with a 10,000 kg (98 KN) load cell. The tests were conducted in controlled laboratory air environment [Relative Humidity of 55%] at both ambient temperature (27 °C) and at an elevated temperature. Tensile tests were conducted in accordance with procedures outlined in ASTM E-8 at a strain rate of 1×10^{-4}/sec using a 12.5 mm

gage length extensometer to measure strain, using rubber bands for the ambient temperature tests and steel springs for the elevated temperature tests. Reduction in area was measured at the fractured surfaces of the deformed and failed specimen using a micrometer.

In view of the limited tensile ductility, cyclic stress resistance and resultant high-cycle fatigue (HCF) life of the alloy at ambient temperature (27 °C), the stress amplitude-controlled high-cycle fatigue tests were also conducted at an elevated temperature.

4.3.2 Cyclic-Stress Controlled Tests

The high cycle fatigue tests were conducted in accordance with ASTM Standard E-466 [85]. The elevated temperature chosen corresponded to:

    (a)   The maximum temperature limit of the environmental chamber unit for the Mg-6%Zn metal-matrix composite, and

    (b)   To the aging temperatures of aluminum alloys AA2009 and AA7034.

The elevated temperature tests were conducted in an Environmental Chamber unit (Instron Model: 3111). The temperature was controlled with the aid of a temperature controller unit in conjunction with a thermocouple. The

thermocouple was fixed onto the surface of the specimen. Maximum temperature variation was well within 3 $^\circ$C of the set-point temperature over the entire duration of the test. Before each test, the specimen was maintained at the test temperature for 30 minutes to achieve stability with the environment. The fatigue tests were conducted at constant cyclic frequency of 5 Hz and at stress ratios [R = $(\sigma_{min})/(\sigma_{max})$] of 0.1 and -1.0. The number of cycles to cause complete failure or separation is taken as fatigue life (N_f).

4.3.3 Cyclic-Strain Controlled Tests

Low cycle fatigue tests were conducted in the axial total strain-amplitude control mode under fully reversed, push-pull, tension-compression loading. The low cycle fatigue tests were conducted in accordance with ASTM Standard E-606 [86]. For each individual test, the test machine was programmed to maintain a constant nominal strain rate of 1 x 10^{-3} s^{-1}. The test command signal (strain function) was a triangular waveform, and the mean strain was zero. All total-strain- amplitude-controlled $(\Delta\varepsilon_T/2)$ cyclic fatigue tests were initiated in tension. An axial 12.7 mm clip-on extensometer was attached to the test specimen, using rubber bands for the purpose of monitoring

total strain-amplitude during fully reversed strain
amplitude-controlled fatigue tests, such that the magnitude
of negative strain equals the magnitude of positive strain
(R_ε = $\varepsilon_{min}/\varepsilon_{max}$ = -1). The controlled variable is total strain
amplitude ($\Delta\varepsilon_T/2$) and the LCF tests were performed over a
range of total strain-amplitudes ($\Delta\varepsilon_T/2$). The extensometer
was calibrated prior to the initiation of each cyclic
fatigue test. The tests were conducted in controlled
laboratory air environment at ambient temperature [27 ^{o}C]
(relative humidity of 55%) and at an elevated temperature.
The stress and strain data for each fatigue cycle were
recorded on a PC-based data acquisition system. The number
of cycles to failure (N_f) or separation is taken as fatigue
life.

4.4 Failure-Damage Analysis

4.4.1 Scanning Electron Microscopy (SEM)

Fracture surfaces of the tensile and cyclically
deformed test samples were examined in a scanning electron
microscope (SEM) to: (a) determine the macroscopic fracture
mode, and (b) characterize the fine-scale topography and
establish the microscopic mechanisms governing fracture.
The distinction between macroscopic mode and microscopic

fracture mechanisms is based on the magnification level at which the observations are made. The macroscopic mode refers to the nature of failure, while the microscopic mechanism relates to the local failure processes (microvoid formation, coalescence, and nature and intensity of cracking). Samples for SEM observation were obtained from the failed specimens by sectioning parallel to the fracture surface. Matching fracture surfaces were viewed in many cases in order to determine the presence of fractured SiCp on both halves of the specimen.

4.4.2 Transmission Electron Microscopy (TEM)

Samples for Transmission Electron Microscopy (TEM) were first cut with a low-speed cutting saw and mechanically pre-thinned on both sides, to a thickness of less than 1 mm. Thin foils for TEM investigation were prepared from disks 3 mm in diameter that were cut, ground and subsequently thinned to a thickness of 0.15 mm. electrolytically double jet thinned in a Struers Tenupol unit. The electrolyte was 30% nitric acid and 70% of methanol, used in methanol solution maintained at a temperature -40 °C (this minimizes the heat of reaction on the specimen and prevents vaporization of the electrolyte) and Voltage = 20 V. After perforation the thin foils were

rinsed, first in methanol and then in ethanol. For examinations in a TEM, a 200 kV Phillips CM20 microscope was used at an operating voltage of 120 kV with a double tilt specimen holder to facilitate the two tilting axes.

CHAPTER V

RESULTS AND DISCUSSION

5.1. 2009 Aluminum Matrix Composite

5.1.1. Initial Microstructure

The optical micrographs illustrating the microstructure of the 2009/SiC/15p-T42 composite, in both the longitudinal (extrusion) and transverse orientations of the extruded billet, are shown in Figure 5.1. The SiC_p reinforcement phase, in the 2009 aluminum alloy metal matrix, were of near-uniform size. However, very few of the SiC particles were found to be irregularly shaped and these were dispersed randomly through the metal matrix. At regular intervals a clustering or agglomeration of the reinforcing SiC_p was observed in the longitudinal orientation of the billet. An agglomerated site consisted of a few larger SiC particles intermingled with smaller, uniform and more regularly shaped particles. No attempt was made, in this research study, to determine the particle size distribution for the 2009/SiC/15p-T42 MMC material. The matrix of the composite revealed very fine grains

65
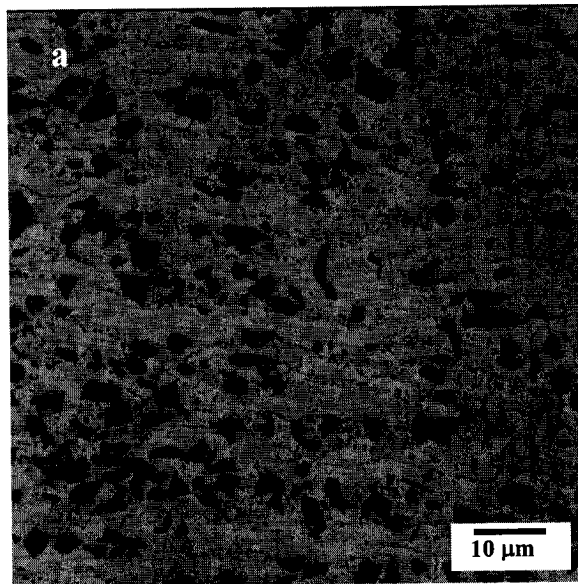
Longitudinal orientation
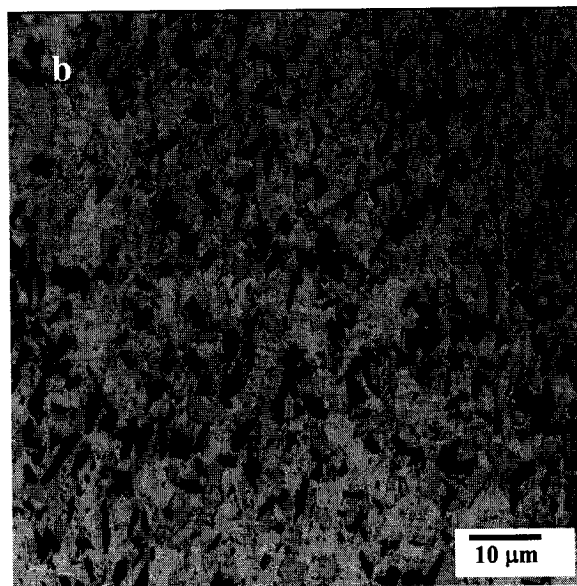
Transverse orientation

Figure 5.1: Optical micrographs showing microstructure of the 2009/SiC/15p-T42 Composite: (a) Longitudinal orientation, (b) Transverse orientation.

following etching of the polished surfaces with Keller's

reagent (a solution mixture of nitric acid, hydrofluoric

acid and distilled water) and observing in an optical

microscope using bright field illumination (i.e. < 1000X).

Transmission electron microscopy observations revealed

the presence and near uniform distribution of the needle-

shape S' (Al_2CuMg) phase (Figure 5.2a). High magnifications

revealed a distribution of the θ' precipitates in the grain

interior (Figure 5.2b). The coarse second-phase particles

were found decorating the high angle grain boundaries

(Figure 5.2c). Precipitate free zones (PFZ's) were not

found at and along the grain boundaries of the 2009/SiC/15p

composite (Figure 5.2d). Clustering of the second-phase

particles was seldom observed. A majority of large and

intermediate-size second-phase particles were also found

located within the grain interior (Figure 5.3).

5.1.2. Tensile Behavior

The tensile properties of the 2009/SiC/15p-T42 MMC, at

the two test temperatures, are summarized in Table 5.1.

The results presented are the mean values based on

duplicate tests. Test results reveal only a marginal

decrease in elastic modulus with an increase in test

temperature. The value of elastic modulus of the 2009/SiC_p
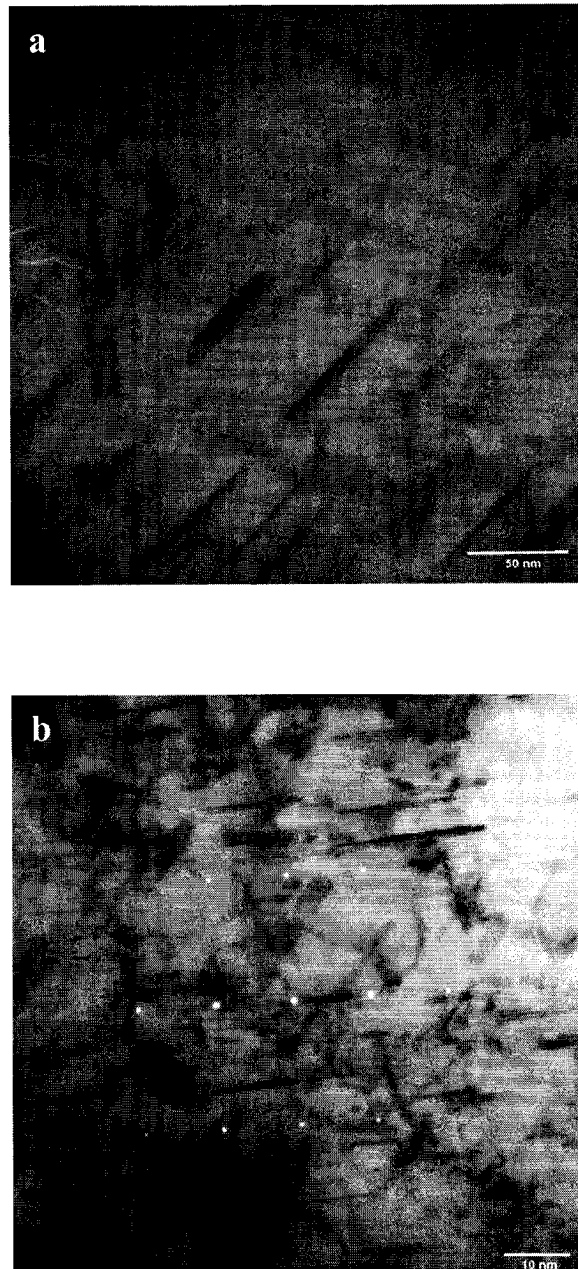
Figure 5.2: Bright filed transmission electron micrographs
of the 2009/SiC/15p-T42 composite showing:(a)
Needle shaped S' (Al$_2$CuMg) precipitates. (b)
Distribution of the θ' in the grain interior.
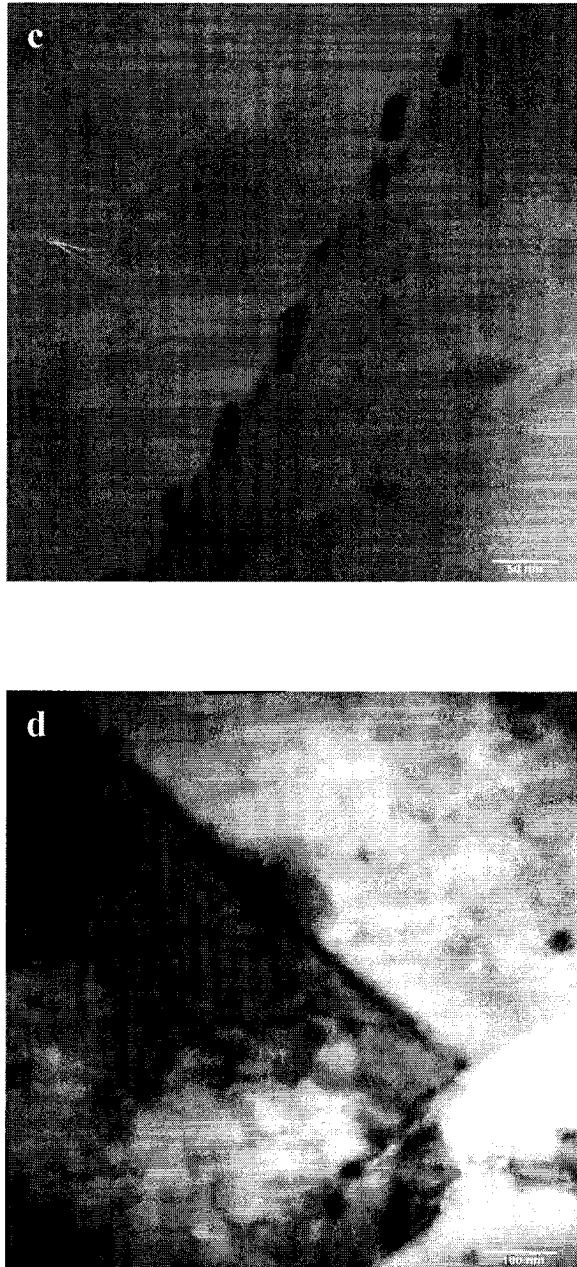
Figure 5.2(Cont.): Bright filed transmission electron
micrographs of the 2009/SiC/15p-T42 composite
showing: (c) Coarse second phase particles at the
grain boundary and (d) Absence of precipitate
free zone at the grain boundary.
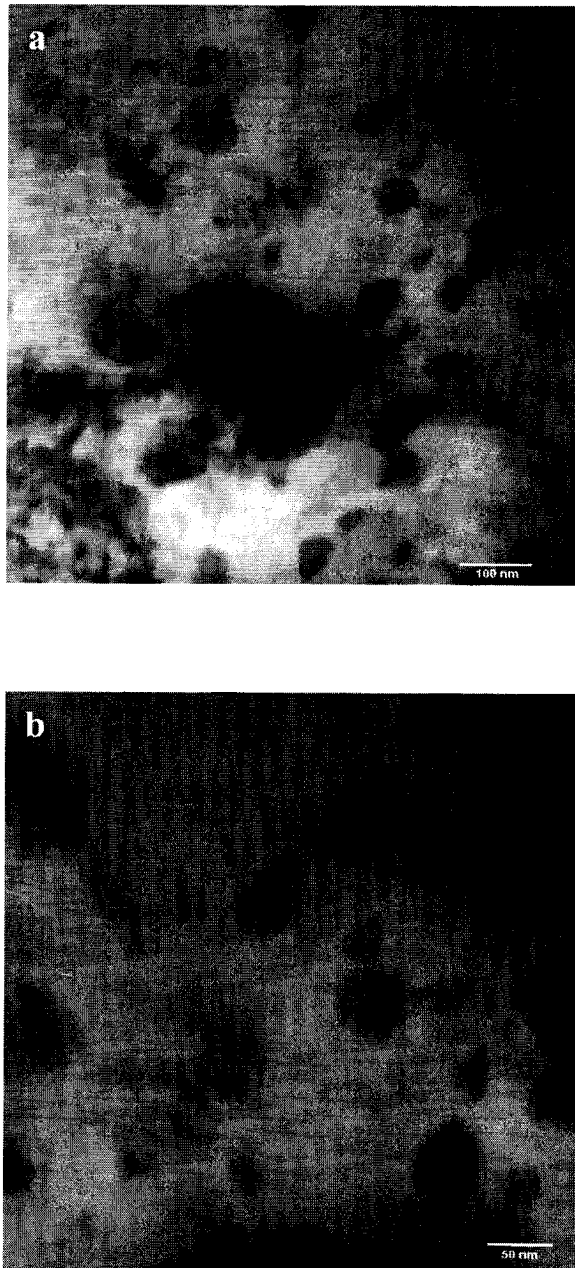
Figure 5.3:Bright filed transmission electron micrographs
        of the 2009/SiC/15p-T42 composite showing
        distribution of large and intermediate size
        second-phase particles in the grain interior (a)
        Low magnification and (b) High magnification.

Table 5.1: Uniaxial tensile properties of the
2009/SiC/15p-T42 composite.

Test Temperature (°C)	Elastic Modulus (GPa)	Yield Strength		UltimateTensile Strength		$\frac{YS}{UYS}$ (%)	Elongation (%)	Reduction In Area (%)
		MPa	(Ksi)	MPa	(Ksi)			
27	100.0	367	(53.2)	537	(77.8)	68.3	9.3	9.2
150	91.0	360	(52.0)	464	(67.2)	78.0	10.0	10.0

composite was provided as an output of the tensile stress program by the computer control console of the servohydraulic materials test machine (INSTRON: Model 8500 Plus). This value was checked for both accuracy and consistency by measuring the slope of the initial region of the stress-strain curve, below the elastic limit. The ambient temperature elastic modulus of the 2009/SiCp/15p-T42 composite is 100 GPa, which is 50 percent more than the elastic modulus of the matrix alloy with no SiC_p reinforcement (70 GPa), that is, the unreinforced aluminum alloy metal matrix.

The decrease in yield strength, which is defined as the stress required at a plastic strain of 0.2%, due to an increase in test temperature was only marginal for this 2009/SiC_p MMC. The matrix alloy with 15vol.% SiC_p had a 2% lower yield strength at the higher test temperature. The ultimate tensile strength of the composite is significantly higher than the yield strength indicating the occurrence of work hardening past yielding. The ultimate tensile strength followed the same trend as the yield strength of the 2009/SiCp composite. The degradation in ultimate tensile strength due to an increase in test temperature was as high as 14.0%.

Whereas, the yield strength and ultimate tensile strength of the 2009/SiCp15p-T42 composite show a decrease with an increase in test temperature, the ductility of the composite, quantified both by tensile elongation (ε_f) over 12.7 mm gage length and reduction-in-area (RA) increases. The increase in tensile elongation (ε_f) with an increase in test temperature from 27 °C to 150 °C is as high as 7.5%. An increase in test temperature increased the reduction-in-area of the composite by 8.0%.

The manner in which the reinforcing ceramic (SiC) particulates affect the tensile strength of the aluminum alloy composite can be best described in terms of work hardening. Beyond macroscopic yield a power law represents the stress versus strain curve. It is expressed by the equation:

$$\sigma = k \cdot (\varepsilon_p)^n \qquad (5.1)$$

Where K is the monotonic strength coefficient (intercept at plastic strain, $\varepsilon_p = 1$) and n is the work hardening or strain-hardening exponent. The monotonic stress-strain curves at the two temperatures are shown in Figure 5.4. An increase in test temperature is observed to have little to no influence on the monotonic strain-hardening exponent (n) of the 2009/SiC/15p-T42 composite.
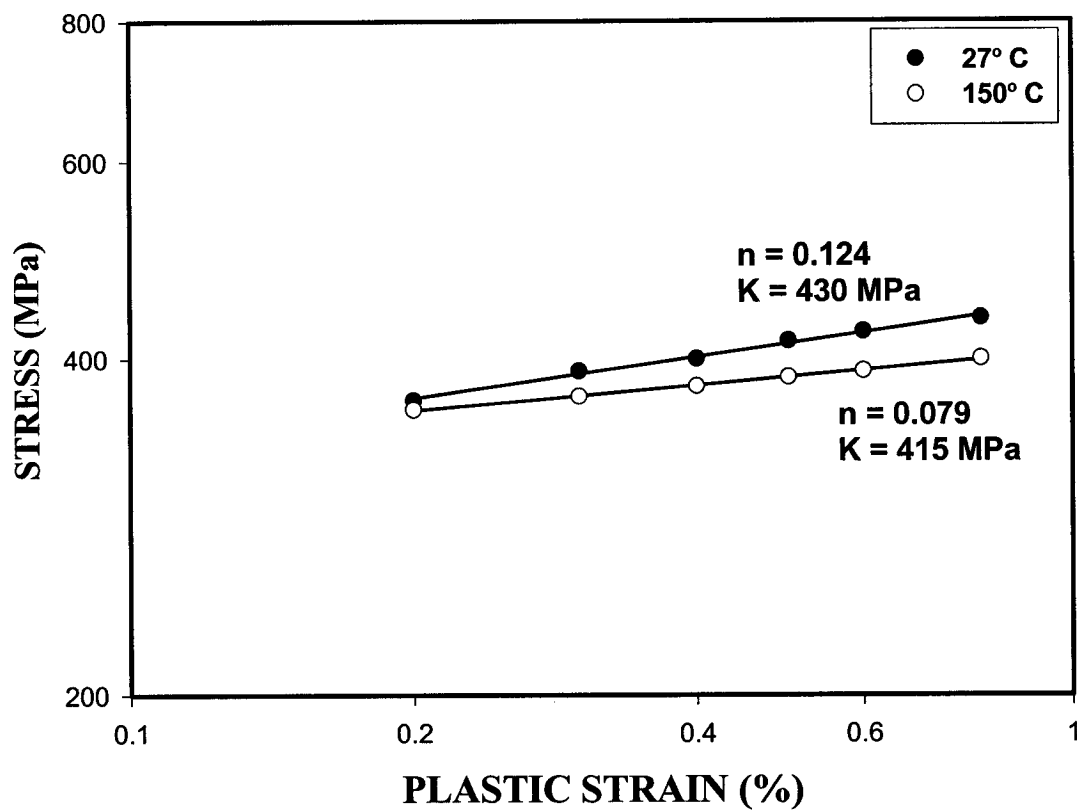
Figure 5.4: Comparison of the monotonic stress-strain
curves for the 2009/SiCp composite at the two-
test temperature.

In this 2009/SiC/15p-T42 composite, with large coefficient of thermal expansion (*CTE*) mismatch between the aluminum alloy metal matrix and the reinforcing (SiC) ceramic particulates, the plastic deformation of the ductile aluminum alloy metal matrix, in the presence of the discontinuous SiC particulates reinforcement, is non-uniform, i.e., heterogeneous, primarily due to the hard, brittle and elastically deforming particles resisting plastic flow of the soft and ductile aluminum alloy metal matrix. The plastic deformation-induced dislocations, or slip dislocations, would become dominant when the plastic strain exceeds the thermal mismatch strain and the two effects would eventually act in synergism so that they can be lumped together. The increased yield strength ($\Delta\sigma_y$) of the matrix of this SiC_p reinforced 2009 aluminum alloy MMC, due to disloction generation and accumulation, and assuming the dislocations are uniformly dispersed in the metal matrix, can be estimated using the equation:

$$\Delta\sigma_y = \alpha \cdot G \cdot b \cdot (\rho^{1/2})$$
(5.2)

Where $\Delta\sigma_y$ is increase in yield strength of the composite over that of the unreinforced matrix alloy (aluminum alloy 2009), G is the shear modulus (GPa) of the metal matrix, b is the Burgers vector, ρ is the increase in dislocation

density of the composite matrix over that of the unreinforced matrix density, and α is a constant and is equal to 1.25 for aluminum [87]. Generation of dislocations due to mismatch in coefficient of thermal expansion (CTE), in discontinuous whisker-reinforced and aligned continuous fiber-reinforced metal matrices, has been found and documented by other investigators [88-89]. Taya and Mori [15] and Mochida and co-workers [90] have shown that the punching of dislocations generated by CTE mismatch strain in a particulate-reinforced MMC is sufficiently extensive to cover most of the matrix domain. The dislocations generated by the CTE mismatch strain can at best be considered as an example of geometrically necessary dislocations defined by Ashby [91]. The "geometrically necessary" dislocations occur in order to permit compatible deformation in a system having geometrical constraints such as the hard and brittle SiC particles, which deform elastically while the surrounding 2009 aluminum alloy metal matrix is soft and ductile and undergoes plastic deformation [92]. The "geometrically necessary" dislocations become essential when deformation occurs without the formation of voids around the reinforcing SiC particulates. These dislocations

contribute to the dislocation density in the composite matrix.

The increase in flow stress of the discontinuous ceramic particulate-reinforced aluminum alloy metal matrix over the unreinforced matrix alloy is proportional to the CTE mismatch strain if the dislocations generated by CTE mismatch strain are dominant. The mismatch strain (ε_α) induced in the particle is [93]:

$$\varepsilon_\alpha = (\alpha_p - \alpha_m) \cdot \Delta T \qquad (5.3)$$

Where:

(a) α_p and α_m are coefficient of thermal expansion of the ceramic particle (SiC_p) and the matrix (aluminum 2009) respectively, and both the matrix and the particle are assumed to be isotropic in stiffness and *CTE*.

(b) ΔT is the net temperature (T_o - $T_{ambient}$) change when the SiC particulate-reinforced aluminum alloy metal matrix is quenched from an elevated temperature (say T_o).

Based on the results obtained in this study, the contributions to strengthening of the 2009 aluminum alloy arises from the mutually competitive influences of the following mechanisms:

(1) The dislocations, which are introduced during processing, are not completely annihilated by the solution heat treatment during the T42 processing treatment. Consequently, they become trapped at the reinforcing SiC particulates resulting in local regions of high dislocation density; that is, the density is higher near the reinforcing SiC particulate or the reinforcement-matrix interfaces [1].

(2) Strengthening due to large differences in thermal coefficients of expansion between constituents of the composite, i.e., aluminum alloy and the reinforcing SiC, resulting in misfit strains due to differential thermal contraction at the Al/SiC interfaces. The misfit strain and concomitant misfit stresses generate dislocations. The increased dislocation density generated to accommodate the misfit strains provides a positive contribution to strengthening of the 2009/SiC$_p$ composite matrix.

(3) Strengthening arising from constrained plastic flow and triaxiality in the ductile 2009 aluminum alloy matrix due to the presence of the discontinuous particle (SiC$_p$) reinforcements [93-95]. As a result of the elastically deforming SiC particles resisting the

plastically deforming metal-matrix, an average internal stress or back stress (σ_b) is generated.

(4) A small contribution from dispersion strengthening caused by the presence of reinforcing SiC_p in the 2009 aluminum alloy metal matrix and thus the additional stress required for slip dislocations to by-pass a reinforcing SiC particle.

5.1.2.1. Tensile Fracture

The tensile fracture surfaces are helpful in elucidating microstructural effects on the ductility and fracture properties of the 2009/SiC/15p-T42 composite. It is fairly well established that the fracture of unreinforced alloys is associated with events of void nucleation and growth, with the nucleation essentially occurring at the coarse constituent particles present in the microstructure [96,97]. The 2009/SiC/15p composite examined exhibited limited ductility, on a macroscopic scale, with fracture occurring normal to the tensile stress axis. However, microscopic examination of the fracture surfaces, at high magnifications, revealed features reminiscent of locally ductile and brittle mechanisms. Representative fractographs of the tensile fracture

surfaces, at the two test temperatures, are shown in

Figures 5.5-5.8.

5.1.2.1.1. Test Temperature = 27 °C

On a macroscopic scale the fracture surfaces of this

composite were flat, but relatively rough when viewed on a

microscale (Figure 5.5a). The fracture surfaces revealed

fractured and/or decohered particles (Figure 5.5b)

surrounded by ductile regions described as "tear ridges".

Few tear ridges were evident on the fracture surface

(Figure 5.5c). The matrix of the 2009/SiC/15p-T42

composite was covered with a population of fine microscopic

voids. The voids were intermingled with isolated regions

of dimple rupture (Figure 5.5d). The constraints in

mechanical deformation caused by the hard, brittle and

elastically deforming SiC_p in the soft, ductile and

essentially plastically deforming aluminum alloy metal

matrix coupled with the development of a triaxial stress

state in the matrix aids in limiting flow stress of the

composite microstructure and is conducive for both void

initiation and growth. As direct consequence of the

deformation constraints induced by the elastically
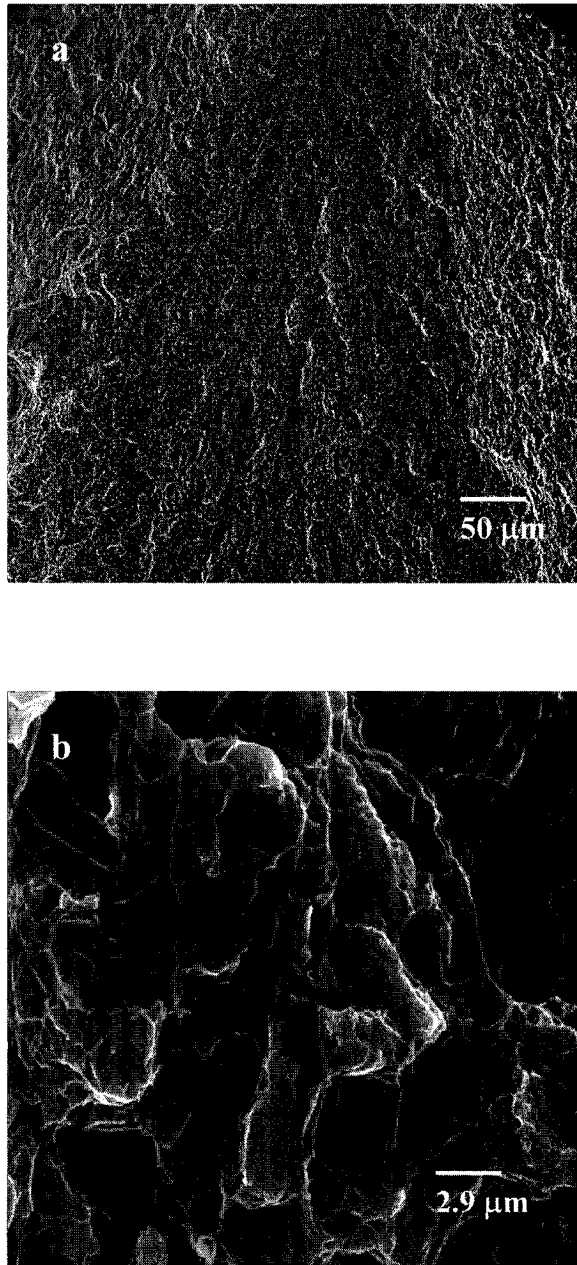
Figure 5.5: Scanning electron micrographs of the tensile
          fracture surface of the 2009/SiC$_p$ composite at
          ambient temperature (27 °C), showing: (a) overall
          morphology, and (b) cracked and decohered SiC
          particulates.
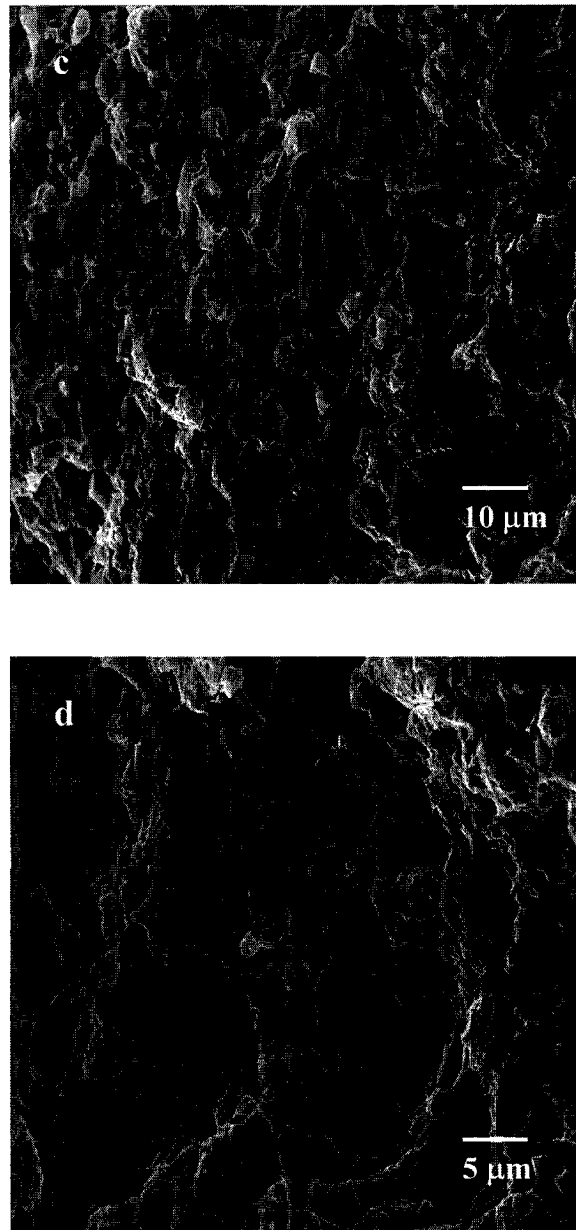
Figure 5.5(cont.):Scanning electron micrographs of the
              tensile fracture surface of the 2009/SiC$_p$
              composite at ambient temperature (27 °C),
              showing:(c) ductile tear ridges, and (d) pockets
              of shallow dimples.

deforming SiC particulate reinforcements, a higher applied stress is required to initiate plastic deformation in the adjoining matrix. This translates to a higher elastic constant and yield strength of the 2009/SiC/ 15p-T42 composite [92].

5.1.2.1.2. Test Temperature = 150 $^{\circ}$C

On a macroscopic scale the overall fracture surface morphology was flat and normal to the far field stress axis. At higher magnifications the microscopic fracture was rough (Figure 5.6a) comprising a large population of fine microscopic voids and regions covered with ductile tear ridges (Figure 5.6b). The matrix of the composite was covered with random isolated pockets of shallow dimples (Figure 5.6c) coupled with microscopic cracking in the matrix and cracked SiC particulates (Figure 5.6d), features reminiscent of locally brittle failure. Basically little difference was observed on the microscopic fracture surface features at the two temperatures.

5.1.2.2. Mechanisms Governing Fracture Behavior

Under the influence of a far-field tensile load, the fine microscopic voids appeared to have undergone limited growth confirming a possible contribution from particle
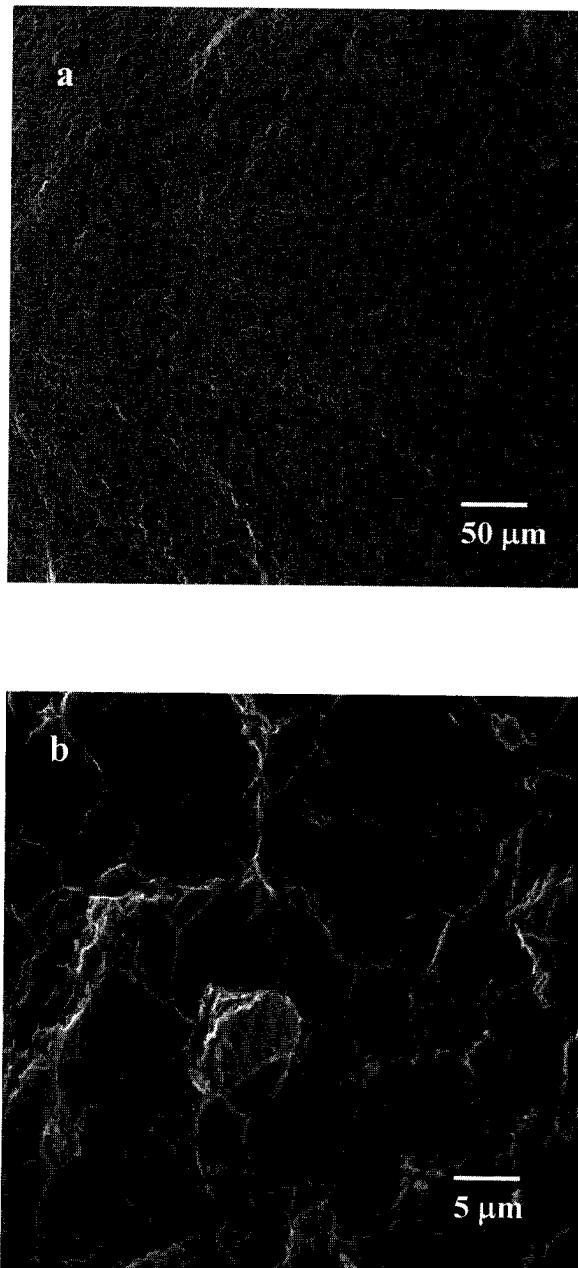
Figure 5.6:Scanning electron micrographs of the tensile
fracture surface of the 2009/SiC$_p$ composite at
150 °C, showing: (a) overall morphology, and (b)
a population of microscopic voids and tear
ridges.
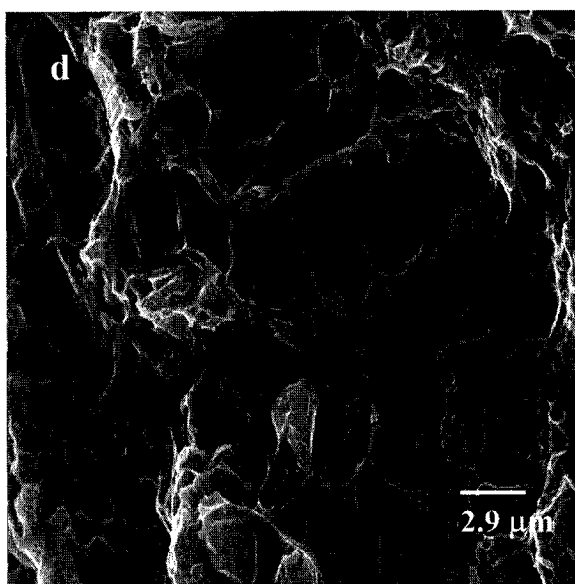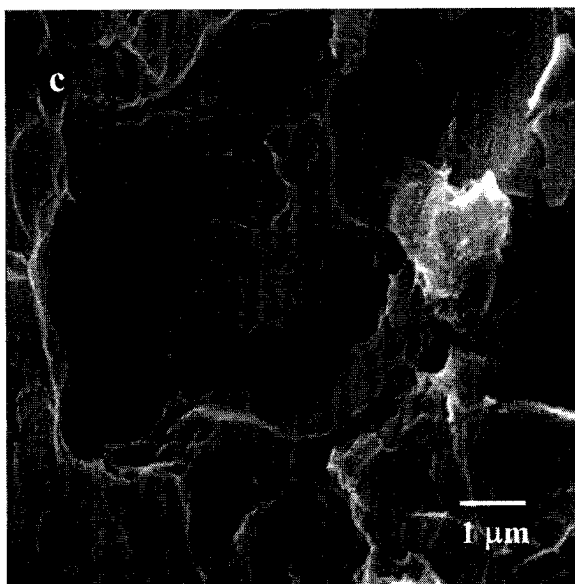
Figure 5.6(cont.): Scanning electron micrographs of the
          tensile fracture surface of the 2009/SiC_p
          composite at 150 °C, showing: (c) microscopic
          cracking at matrix-particulate interfaces and
          cracked SiC particle, and (d) shallow dimples
          covering the transgranular fracture surface.

constraint-induced triaxiality on failure of the composite

matrix. Particle failure is governed by the conjoint

influence of local plastic constraints, particle size and

agglomeration [82]. The local plastic constraints are

particularly important for the larger-sized particles and

particle clusters during composite fracture [58,98].

Examination of the tensile fracture surfaces revealed that

damage associated with fracture to be highly localized at

the discontinuous SiC_p reinforcement with little evidence of

void formation away from the fractured SiC particle (Figure

5.6c). Fracture of the SiC_p was observed to be greater in

regions of particle clustering due to enhanced local

stresses resulting from restriction of plastic deformation

(Figure 5.7). The intrinsic brittleness of the reinforcing

SiC_p and the propensity for it to fracture, due to localized

deformation, results in particle cracking being the

contributing damage mode. Furthermore, assuming the

aluminum alloy metal matrix/SiC_p interfaces to be strong the

triaxial stresses generated during far-field tensile

loading favors limited growth of the microscopic voids in

the matrix of the composite. The limited growth of voids

during far-field tensile loading coupled with lack of their

coalescence and thus inhibiting the dominant fracture mode
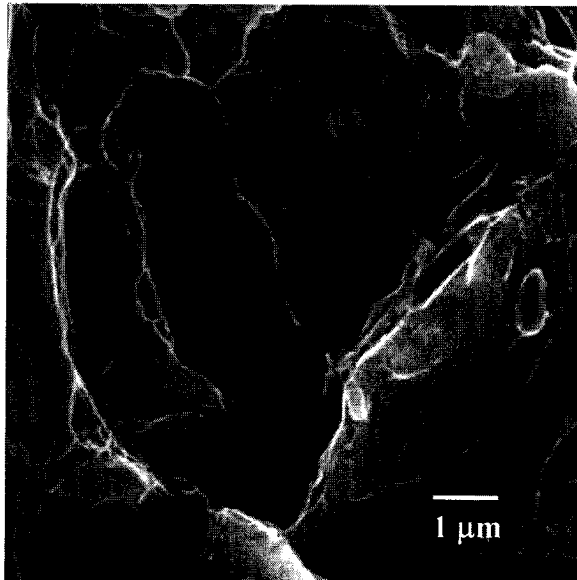
Figure 5.7: Scanning electron micrographs of the tensile
fracture surface showing an agglomeration of
reinforcing SiC particulates.

to be ductile failure for this 2009/SiC/15p-T42 composite clearly indicates that the plastic deformation properties of the 2009 aluminum alloy are significantly altered by the presence of reinforcing SiC_p. Very few of the fine microscopic voids coalesce and the halves of these voids are the shallow dimples observed covering the transgranular fracture surface (Figure 5.6d). The lack of formation of ductile dimples, as a dominant fracture mode, is attributed to the constraints on plastic flow in the composite matrix caused by the presence of the discontinuous SiC_p reinforcement and not due to limited ductility of the aluminum alloy [51]. The constraints in plastic flow favors the formation of fine tear ridges between the reinforcing SiC particulates. With an increase in strain, during tensile deformation, the larger-sized particles fracture first, followed by fracture of the smaller-sized particles. An observation consistent with recent studies, which found the number of cracked particles to increase with increasing stress as well as an increase in the plastic zone size ahead of a crack tip [49,99]. In regions of clustering of the reinforcing SiC particulates, or agglomeration, the short interparticle distance facilitates linkage between neighboring voids and microscopic cracks as

a direct result of decreased propagation distances between the cracked SiC particles (Figure 5.8). Based on an observation of the fracture surface, it is seen that the fracture plane of cracked SiC particles is essentially perpendicular to the loading axis, suggesting the importance of the tensile stress in inducing particle fracture. Failure of the reinforcing SiC particles both by cracking and decohesion at interfaces is responsible for the inferior ductility of this 2009/SiC/15p-T42 composite [100].

The overall "damage" resulting from uniaxial straining of the 2009/SiC/15p-T42 is due to the conjoint action of the two mechanisms: (1) Damage associated with the discontinuous SiC_p reinforcement, such as failure of the particulate by cracking and decohesion at the SiC particle-aluminum alloy metal matrix interfaces, and (2) lattice damage arising from point defects, dislocations and residual stress effects associated with presence of discontinuous SiC particles [63].

For the SiC particles to fracture completely, they must be loaded to their fracture stress. This is achieved globally by the tensile stress and locally by shear loading through the particulate-matrix interfaces. The extent of
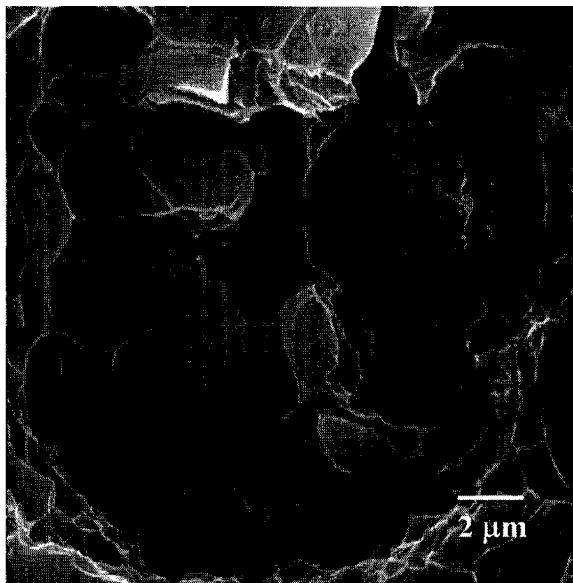
Figure 5.8: Scanning electron micrograph of the tensile
fracture surface showing cracked SiC particles.

particle loading by shear mechanism is dependent on the aspect ratio of the reinforcing SiC_p. For the case of symmetrically packed particles in a metal matrix, the aspect ratio (S_s) for maximum loading is [63]:

$$S_s = \sigma_{SiC} / \tau_i \qquad (5.4)$$

Where σ_{SiC} is the strength of the particle and τ_i is the interfacial shear strength. The strength of monolithic SiC is around 2000 MPa (290 Ksi) and assuming that $\tau_i = \sigma_m/2$, where σ_m is the maximum stress achieved in the aluminum alloy matrix (about 500 MPa), the critical aspect ratio is about 8. The shear mechanism approach ignores any end-loading effects, which would exert additional stress on the SiC particle. A careful observation of the tensile fracture surfaces revealed less than 30% of the reinforcing SiC particles had fractured. This indicates that not all of the SiC particles were loaded to their fracture stress suggesting the importance and role of SiC particulate distribution in the metal-matrix [101].

For this SiC particulate-reinforced 2009 aluminum alloy matrix, the damage is associated with the reinforcing SiC particulates, in the form: (a) cracking and decohesion at the interfaces, (b) tear ridges, and (c) fine microscopic voids, which have formed around the cracked SiC

particles. The fracture initiates by cracking of the SiC_p coupled with decohesion of the matrix surrounding and between the SiC particles. Few voids generated by particle cracking did not grow extensively in the tensile stress direction, which is generally the case in ductile fracture of unreinforced 2XXX-series aluminum alloys [102]. The lack of extensive void growth in this SiC particulate-reinforced 2009 metal matrix suggests that the overall fracture strain be critically controlled by both the void nucleation strain and linkage strain [92].

5.1.3. Cyclic-Stress Controlled

Many practical applications for the DRA MMCs involve cyclic loading, and therefore the cyclic fatigue properties and fracture characteristics are needed and of interest. Since the fatigue properties of aluminum alloys are sensitive to microstructure, the overall resistance of a DRA MMC to both fatigue crack initiation and fatigue crack growth will exhibit different sensitivity to microstructure. Also, a change in intrinsic microstructural features of the composite can exert an appreciable influence on fracture behavior. The objective of this section is to examine the conjoint influence of composite microstructure and test parameters, to

specifically include nature of loading and test

temperature, on high cycle fatigue resistance and fracture

behavior of an Al-Cu-Mg alloy reinforced with fine

particulates of silicon carbide. The cyclic fatigue life

and resultant fracture behavior of the composite are

discussed in light of the synergistic influences of

composite microstructure effects, nature of loading (stress

ratio), test temperature, magnitude of maximum stress and

the nature and role of microscopic cracks. The high cycle

fatigue response of this MMC is addressed in an attempt to

substantiate its use in load-critical and fatigue-critical

applications.

5.1.3.1. High Cycle Fatigue Properties

Variation of maximum stress with fatigue life is shown

in Figure 5.9 and follows the general trend shown by most

non-ferrous metals and their composite counterparts.

5.1.3.1.1. Temperature Effects

An increase in test temperature was observed to have

no influence on high cycle fatigue life of the

2009/SiC/15p-T42 composite at a stress ratio of 0.1.

However, under fully reversed loading, i.e., at R = -1.0,

an increase in test temperature resulted in a noticeable
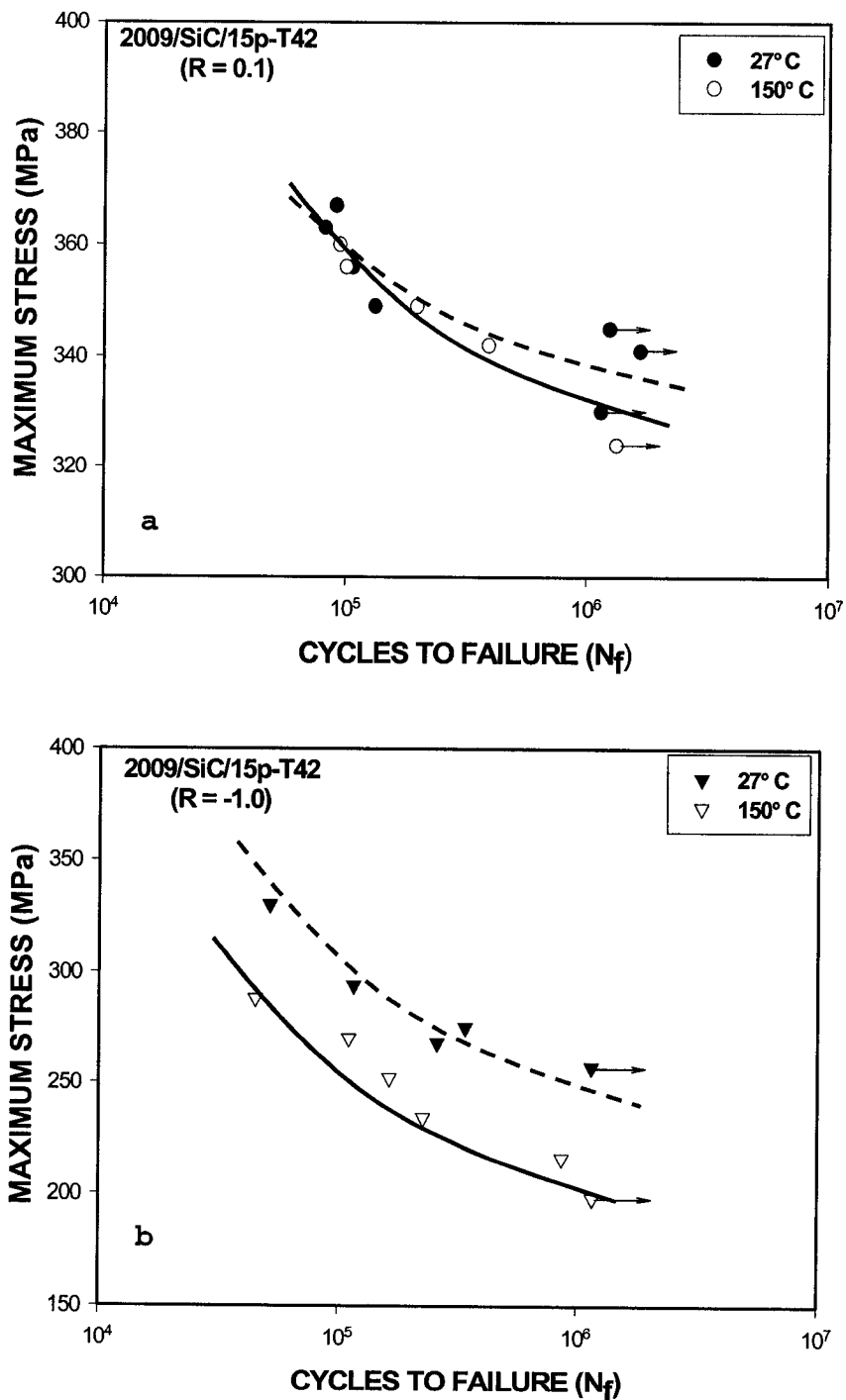
Figure 5.9:Influence of test temperature on variation of
maximum stress with cyclic fatigue life for the
2009/SiC/15p-T42 composite at load ratios of:
(a)   R = 0.1 and (b) R = -1.0.

degradation in cyclic fatigue life. The degradation at

equivalent values of maximum stress being of the order of

200%. In an attempt to better understand temperature

influences on cyclic fatigue behavior, the test data in

Figure 5.9 are replotted in terms of maximum elastic strain

in a manner suggested by Hassen and co-workers [103], where

the maximum elastic strain is the maximum stress normalized

by the elastic modulus at the temperature (Figure 5.10).

Based on maximum elastic strain a minimal improvement in

high cycle fatigue life at the elevated test temperature at

stress ratio of 0.1 (Figure 5.10a) is observed with no

appreciable influence of test temperature at stress ratio

of -1.0 (Figure 5.10b). In an attempt to rationalize the

influence of composite microstructure on cyclic fatigue

life, the test data in Figure 5.9 are re-plotted to take

into account the strengths (yield strength and ultimate

tensile strength) of the composite microstructure at the

two test temperatures. In Figure 5.11 the maximum stress

has been normalized by the uniaxial yield stress at the

temperature. At the stress ratio of 0.1 no appreciable

influence of microstructure of the 2009/SiC/15p-T42 MMC on

high cycle fatigue response is observed, while at the

stress ratio of -1.0 a noticeable degradation in fatigue
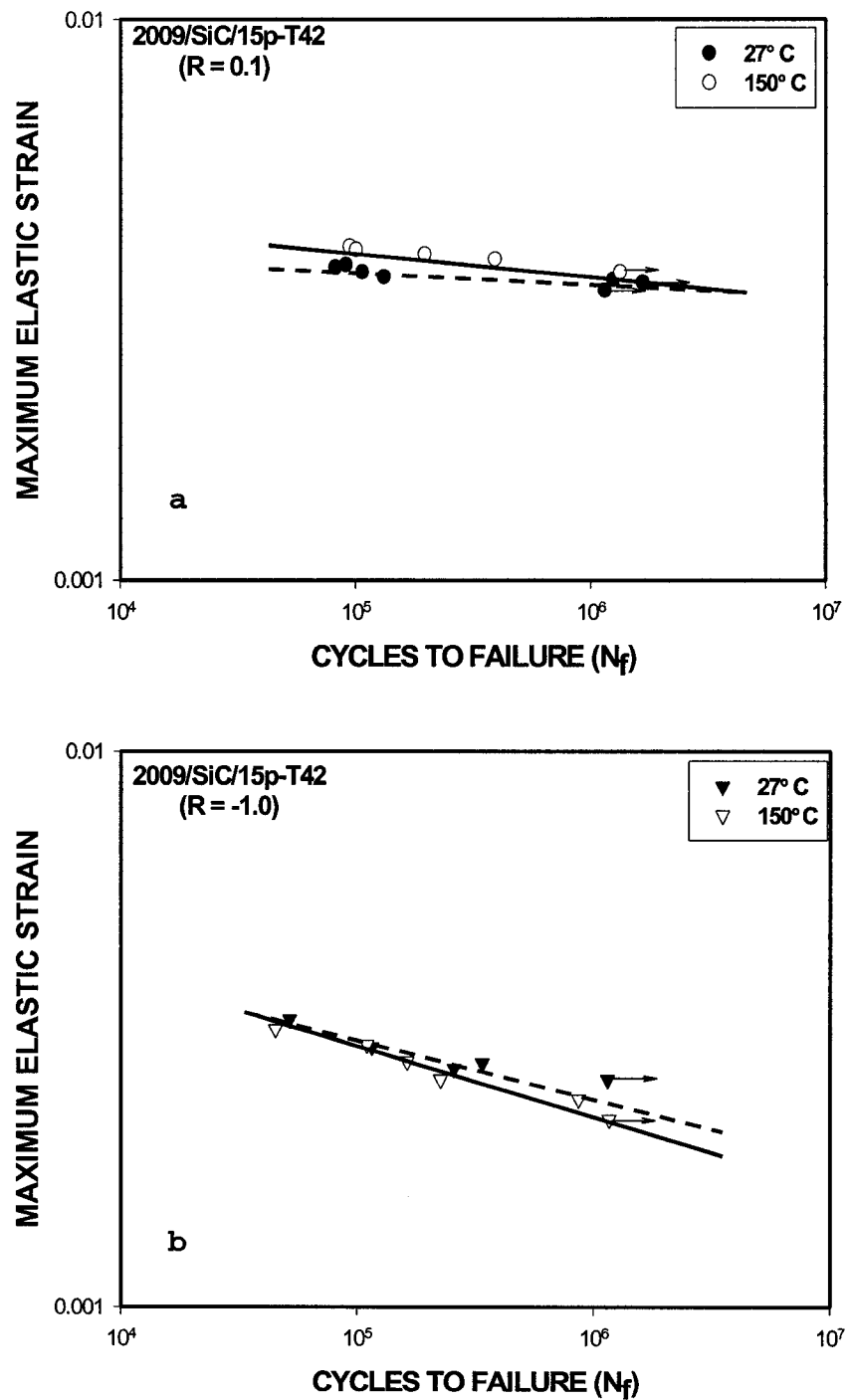
Figure 5.10: Influence of temperature on variation of maximum elastic strain with cyclic fatigue for the 2009/SiC/15p-T42 composite at load ratios of: (a) R = 0.1 and (b) R = -1.0.
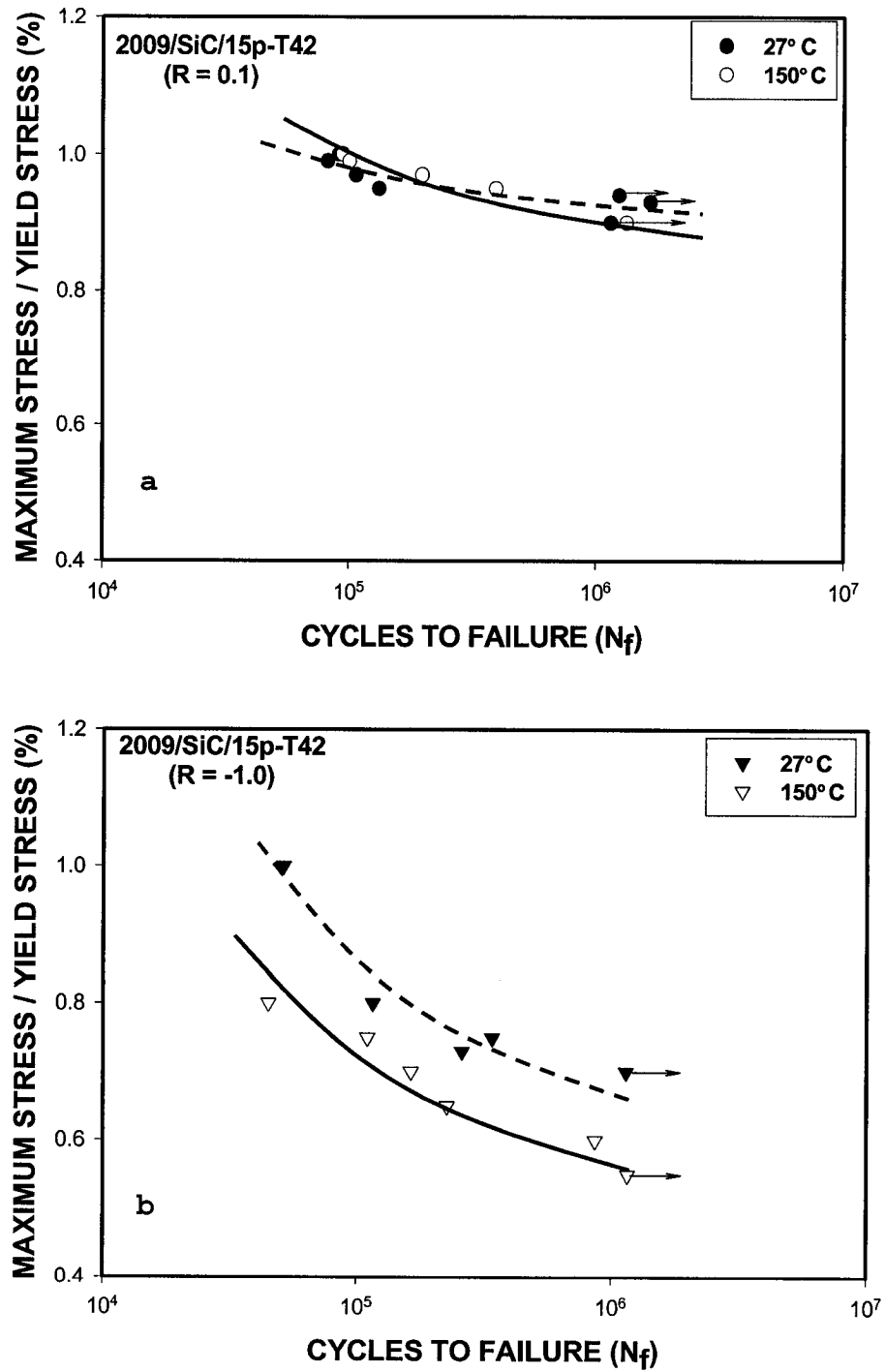
Figure 5.11: Variation of the ratio of maximum stress/yield
stress with fatigue life for the 2009/SiC/15p-
T42 composite at: (a) R = 0.1 and (b) R = -1.0.

resistance based on yield strength of the microstructure is evident. However, comparisons based on ultimate tensile strength (Figure 5.12) reveal a significant difference in high cycle fatigue response between the two test temperatures at the stress ratio of 0.1 and little to no influence of temperature at the lower stress ratio -1.0.

5.1.3.1.2. Stress Ratio Effects

At a given test temperature a decrease in stress ratio from 0.1 to -1.0 resulted in degradation in high cycle fatigue life. The degradation was consistent and around 200% for all values of maximum stress (Figure 5.13). The difference in high cycle fatigue response at the two stress ratios is readily apparent at the two test temperatures (27 °C and 150 °C).

5.1.3.2. Cyclic Fracture Behavior

Examination of the fracture surfaces of the cyclically deformed fatigue specimens, in JEOL scanning electron microscope, was done at (a) low magnifications to identify the regions of fatigue initiation and final fracture (overload), and (b) higher magnifications in fatigue region to identify both the nature and location of microscopic crack formation and damage initiation, (c) nature of
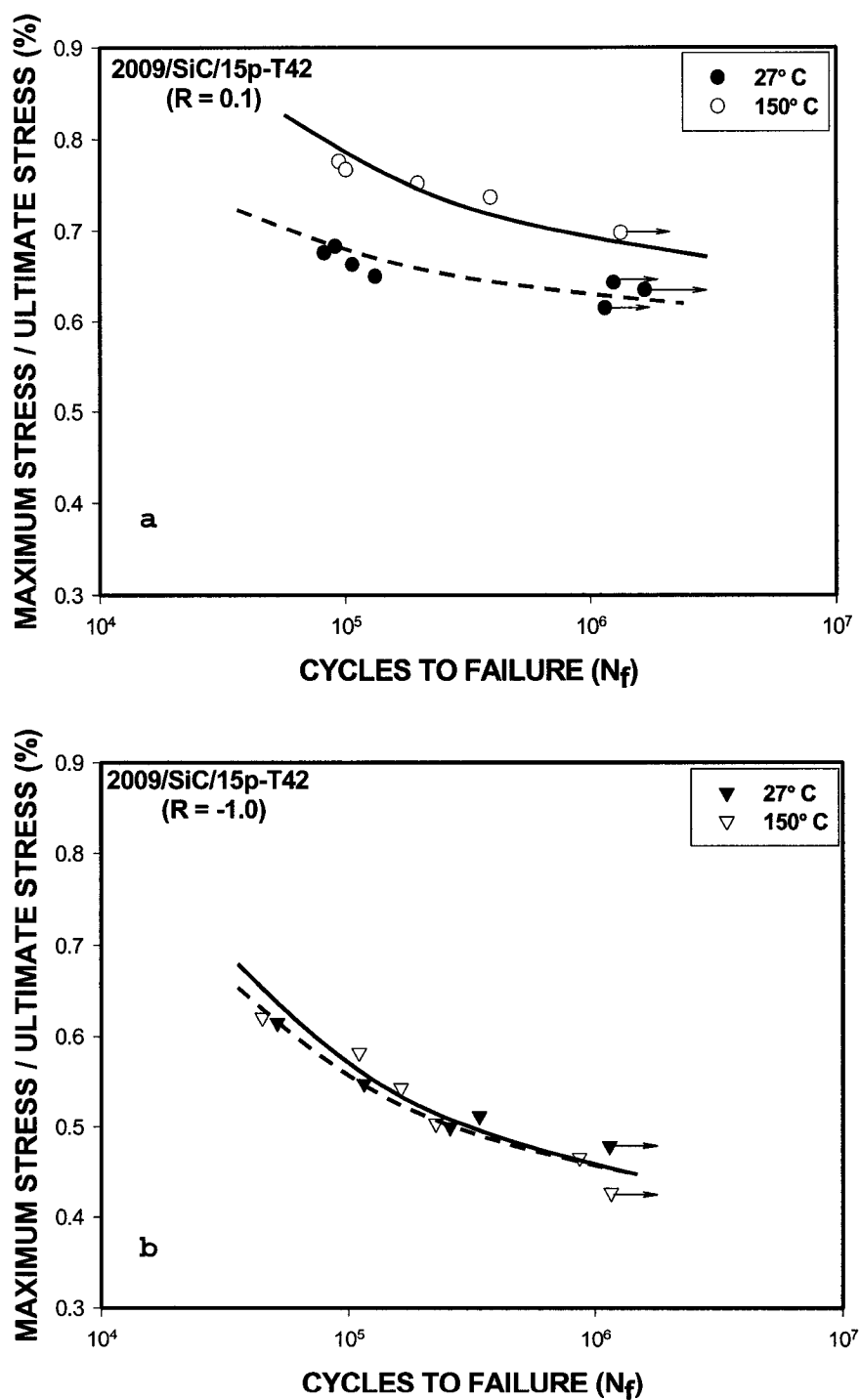
Figure 5.12: Variation of the ratio of maximum
stress/ultimate stress with fatigue life for
the 2009/SiC/15p-T42 composite at:
(a) R = 0.1 and (b) R = -1.0.
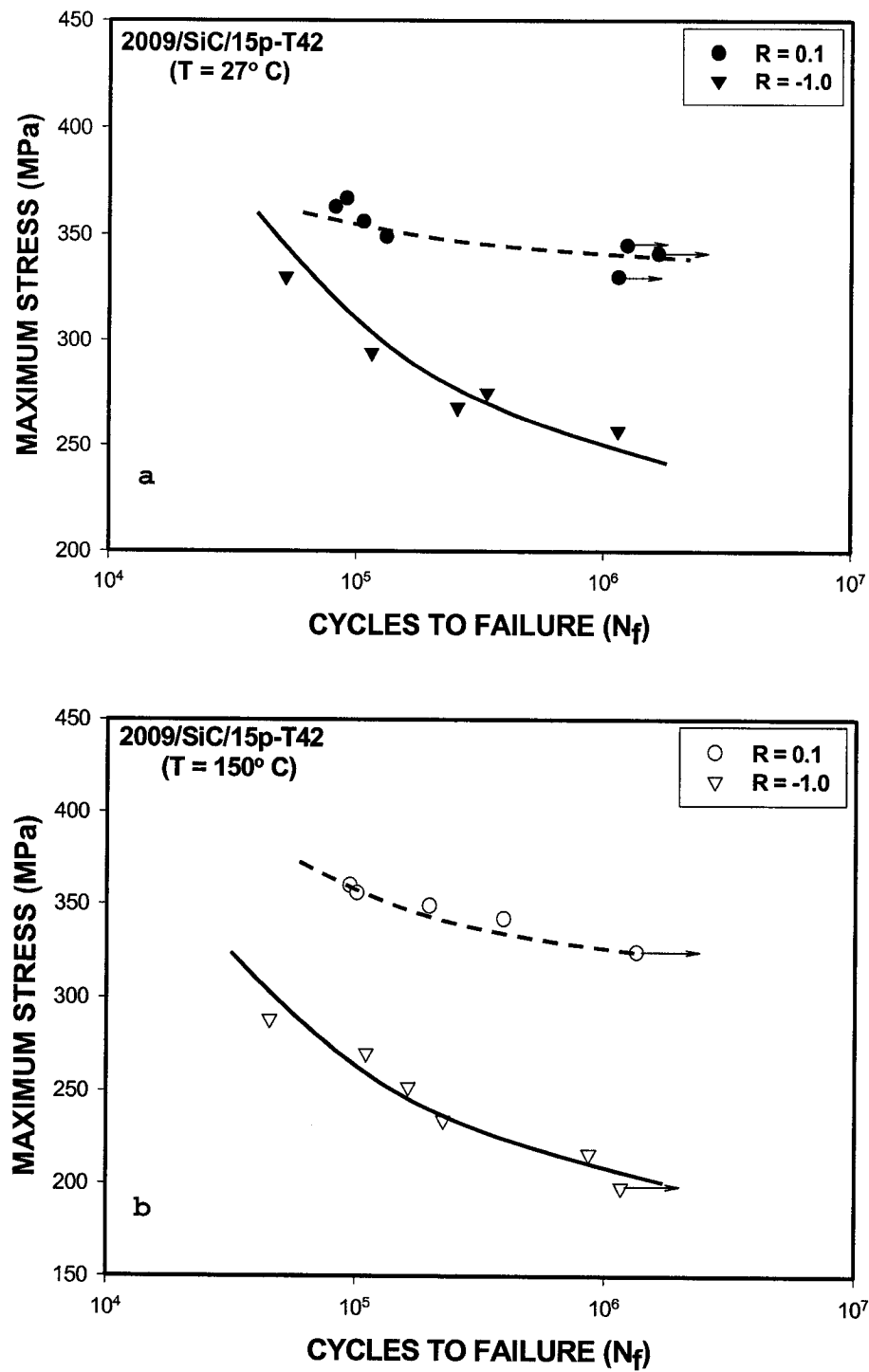
Figure 5.13:Influence of stress ratio (R = 0.1 versus R = -1.0) on cyclic fatigue response of the 2009/SiC composite at: (a) T = 27 °C and (b) T = 150 °C.

microscopic crack growth through the microstructure, and

(d) the overload region to identify the fine-scale fracture

features. At a given test temperature the fatigue fracture

surface features of the composite revealed near similar

topographies at the two load ratios (R = 0.1 and R = -1.0).

However, on a microscopic scale, the fatigue fracture

features were found to vary with maximum stress. Only

representative fractographs of the fatigue fracture surface

of the 2009/SiC/15p-T42 composite, cyclically deformed at R

= 0.1, are shown in Figures 5.14-5.18.

5.1.3.2.1. Test Temperature = 27 °C

For composite test specimen cyclically deformed at a

maximum stress of 349 MPa (N_f = *132,459 cycles*), the

macroscopic fracture behavior was normal to the far-field

stress axis comprising a small region of fatigue (slow and

stable crack growth) and a large portion of overload

(Figure 5.14a). Microscopic and/or high magnification

observations in the fatigue region revealed features

reminiscent of brittle, i.e., numerous microscopic cracks

and decohesion or separation at the metal matrix-SiC$_p$

reinforcement interfaces (Figure 5.14b), and locally

ductile (microscopic voids and shallow dimples) mechanisms

(Figure 5.14c). The microscopic cracks through the matrix
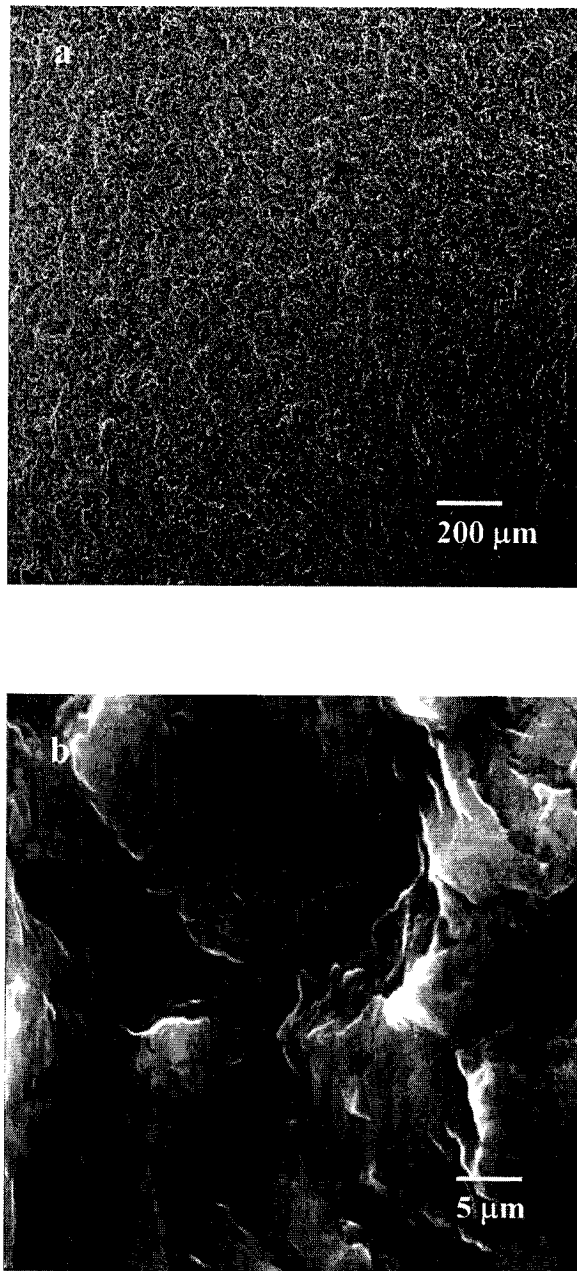
Figure 5.14:Scanning electron micrographs of the 2009/SiC/15p-T42 composite, cyclically deformed at 27 °C, at a load ratio of 0.1 and at a maximum stress of 349 MPa (N_f = 132,459 cycles), showing: (a) overall morphology, and (b) microscopic cracks and decohesion at matrix particle interfaces.
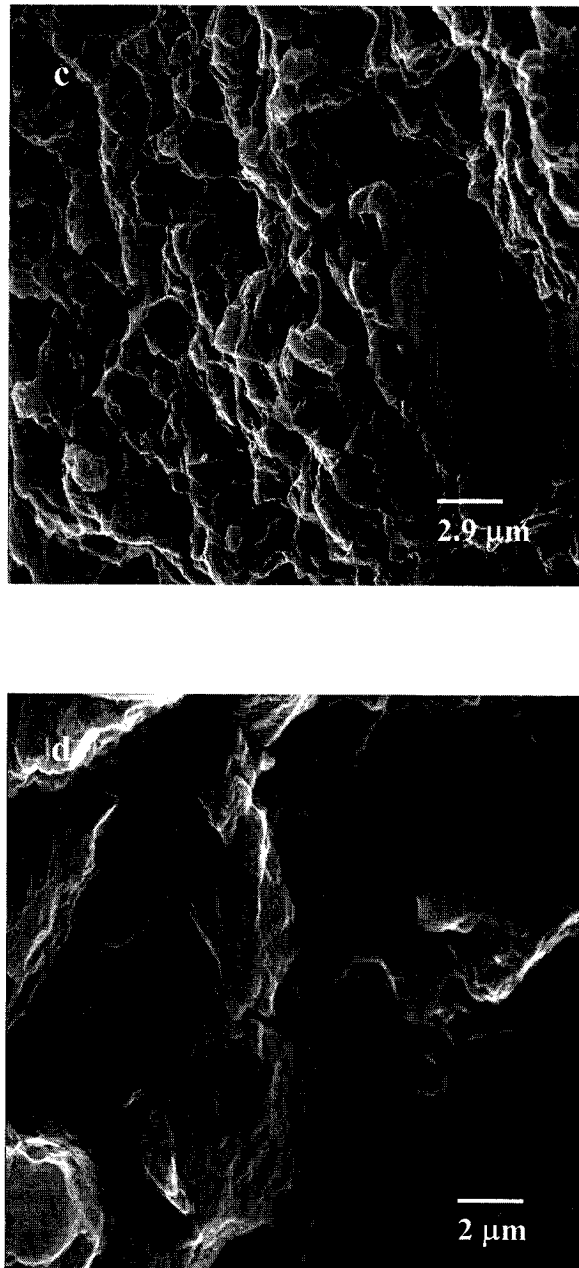
Figure 5.14 (cont.): Scanning electron micrographs of the
2009/SiC/15p-T42 composite, cyclically deformed
at 27 °C, at a load ratio of 0.1 and at a maximum
stress of 349 MPa (N_f = 132,459 cycles), showing:
(c) microscopic voids and shallow dimples, and
(d) macroscopic cracks and cracked SiC particle.

were surrounded by pockets of ductile tear ridges. Also

present in the region of slow and stable crack growth were

cracked SiC particles (Figure 5.14d) and isolated pockets

of shallow dimples. The test specimen cyclically deformed

at the higher maximum stress 367 MPa and resultant short

fatigue life ($N_f = 91,073\ cycles$) the macroscopic fracture

surface revealed distinct regions of fatigue and overload

(Figure 5.15a). High magnification observations in the

fatigue region revealed an array of coplanar microscopic

cracks (Figure 5.15b). Also observed was failure by

separation at the metal matrix-reinforcement particle

interfaces (Figure 5.15c) and ductile tear ridges, and

cracked SiC particles (Figure 5.15d). The overload region

was covered with a population of microscopic voids and

pockets of shallow dimples (Figure 5.16), features

reminiscent of locally ductile failure.

5.1.3.2.2. Test Temperature = 150 °C

Low magnification observations of the composite

specimen cyclically deformed at maximum stress of 342 MPa

and fatigue life (N_f) of 392,142 cycles revealed the

fracture surface to comprise distinct regions of fatigue

and overload (Figure 5.17a). The region of stable

microscopic crack growth was small. Key microscopic
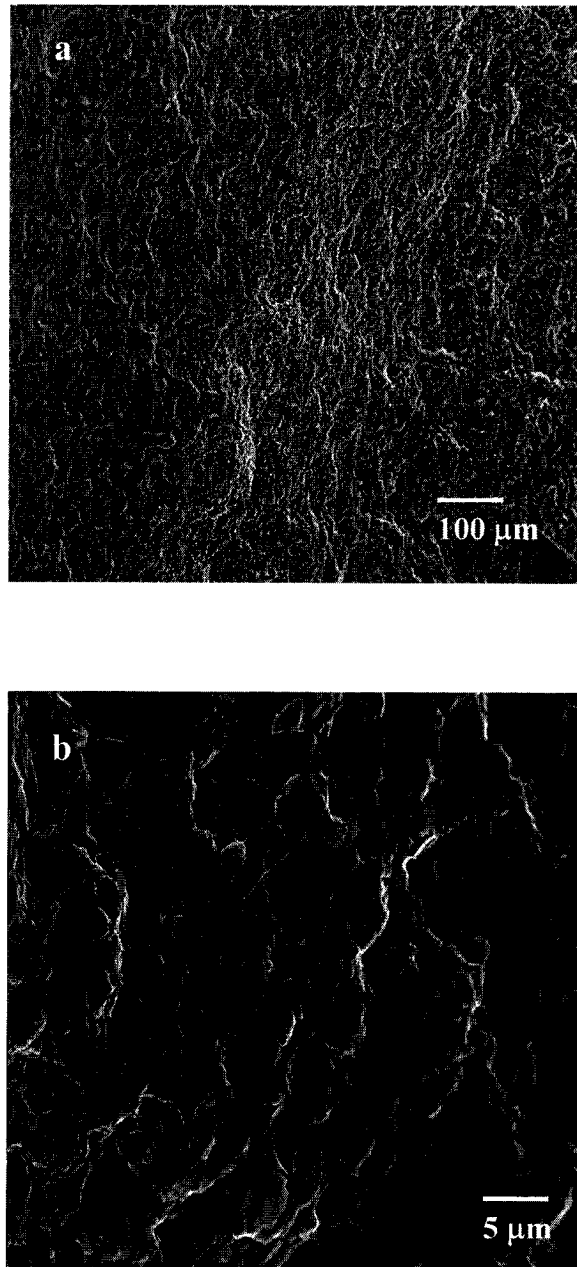
Figure 5.15: Scanning electron micrographs of the
2009/SiC/15p-T42 composite cyclically deformed at
a load ratio of 0.1 and maximum stress of 367 MPa
(N_f = 91,073 cycles), showing: (a) regions of
fatigue and overload, and (b) coplanar
microscopic cracks
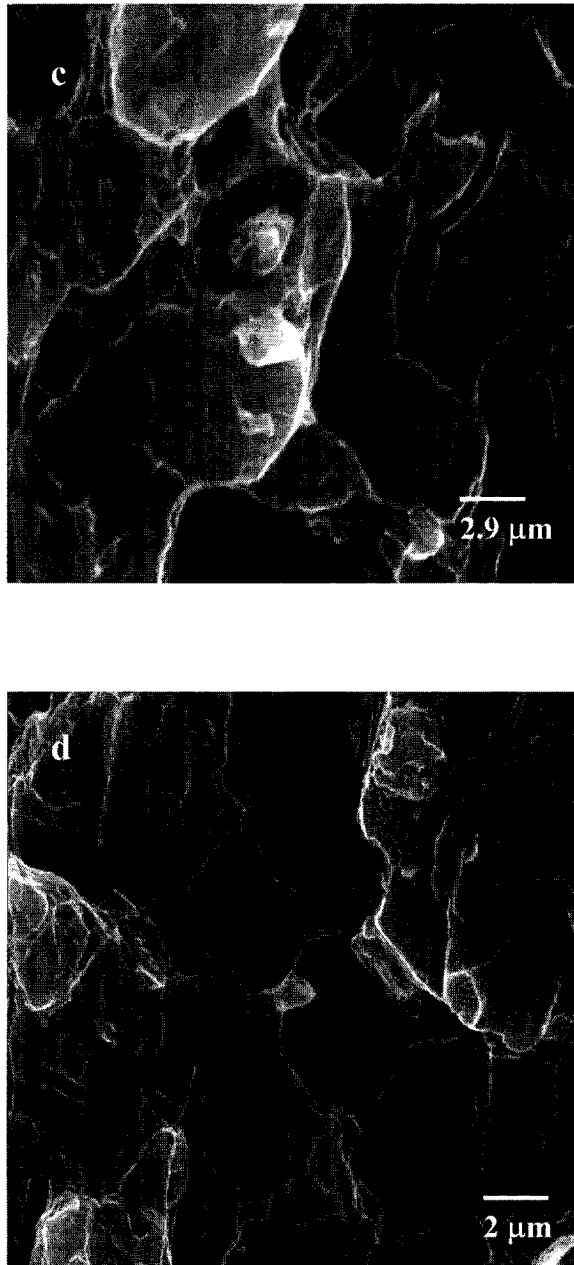
Figure 5.15 (cont.): Scanning electron micrographs of the
2009/SiC/15p-T42 composite cyclically deformed at
a load ratio of 0.1 and maximum stress of 367 MPa
(N_f = 91,073 cycles), showing: (c) cracked SiC
particulates and failure at the interfaces, and
(d) ductile tear ridges.
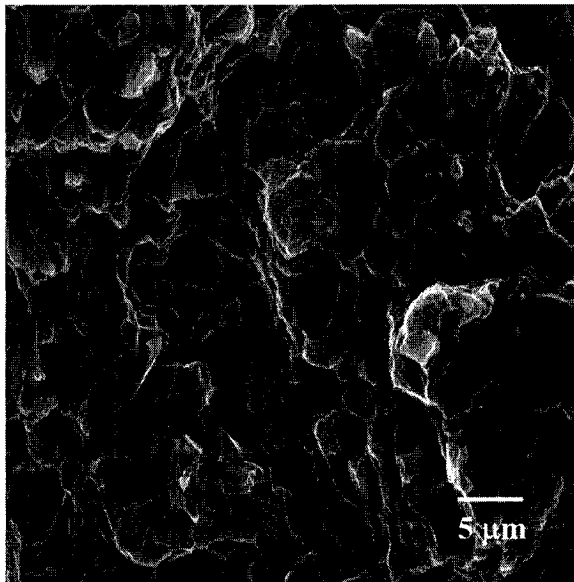
Figure 5.16: Scanning electron micrographs of the
2009/SiC/15p-T42 composite cyclically deformed at
a load ratio of 0.1 and maximum stress of 367 MPa
(N_f = 91,073 cycles) showing microscopic voids and
pockets of shallow dimples covering the overload
fracture region.

features observed in the fatigue region were: (a) failure

of the reinforcing SiC particulates through cracking and

presence of ductile tear ridges (Figure 5.17b), (b) growth

of the microscopic cracks by periodic deflection through

the matrix (Figure 5.17c). The overload region revealed

voids of varying size and shallow dimples features

reminiscent of locally ductile failure mechanisms (Figure

5.17d). The composite specimen deformed at the higher

maximum stress 360 MPa and resultant short fatigue life (N_f

= 94,265 cycles) revealed a fracture surface comprising

distinct regions of fatigue and overload (Figure 5.18a).

High magnification observations in the fatigue region

revealed the transgranular fracture regions to be flat and

featureless (Figure 5.18b) and covered with numerous

microscopic cracks (Figure 5.18c) and cracked SiC particles

(Figure 5.18d).

5.1.3.3. <u>Mechanisms Governing Cyclic Fracture</u>

The existence of a mismatch in strain carrying

capability between the hard, intrinsically brittle and

elastically deforming reinforcing SiC_p and the soft, ductile

and plastically deforming aluminum alloy metal matrix

becomes readily apparent during fatigue loading [37]. This

strain incompatibility promotes a concentration of stress
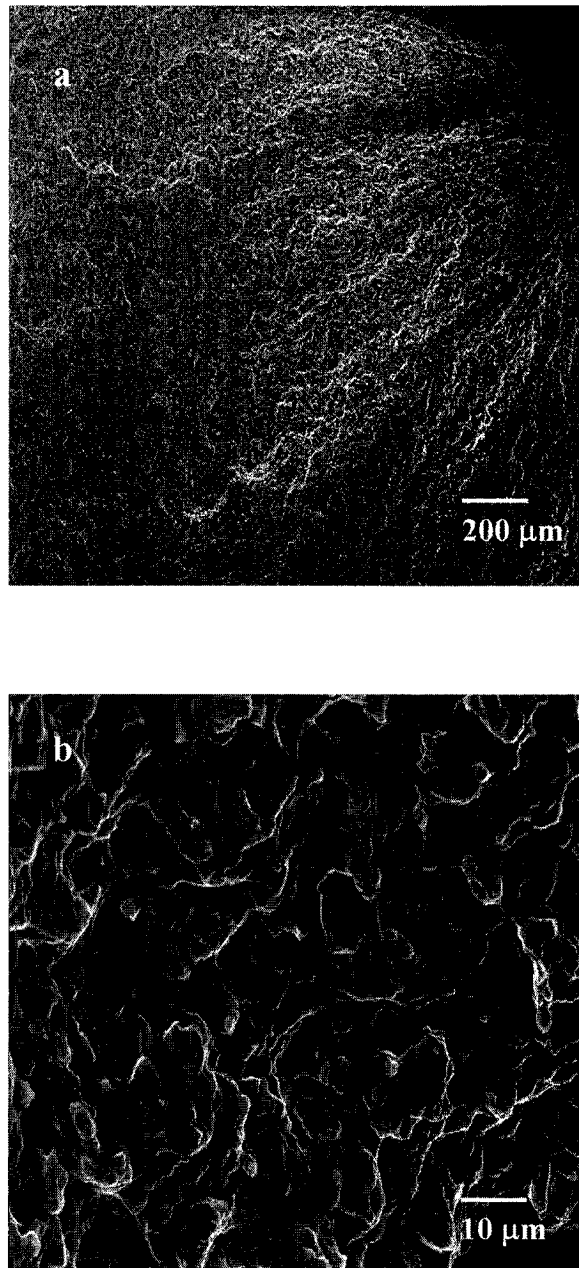
Figure 5.17: Scanning electron micrographs of the
2009/SiC/15p-T42 composite cyclically deformed at
150 °C at load ratio of 0.1 and at maximum stress
of 342 MPa (N_f = 392,142 cycles), showing: (a)
regions of fatigue and overload, and (b) ductile
tear ridges.
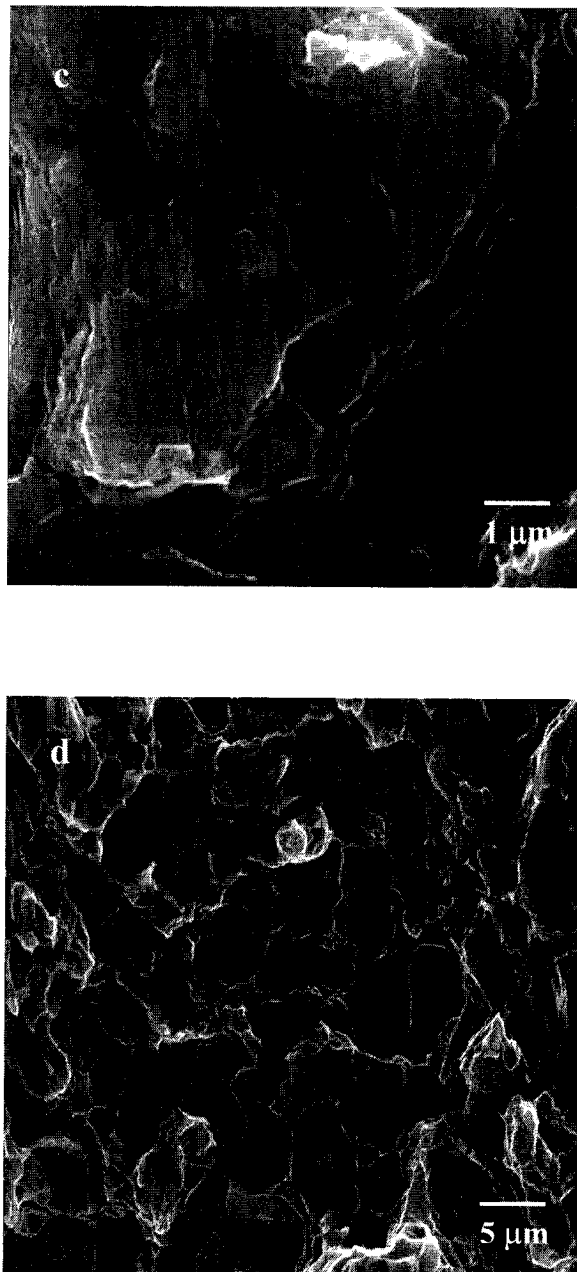
Figure 5.17 (cont.): Scanning electron micrographs of the 2009/SiC/15p-T42 composite cyclically deformed at 150 °C at load ratio of 0.1 and at maximum stress of 342 MPa (N_f = 392,142 cycles), showing: (c) microscopic crack propagation through the microstructure, and (d) voids of varying size and shallow dimples.
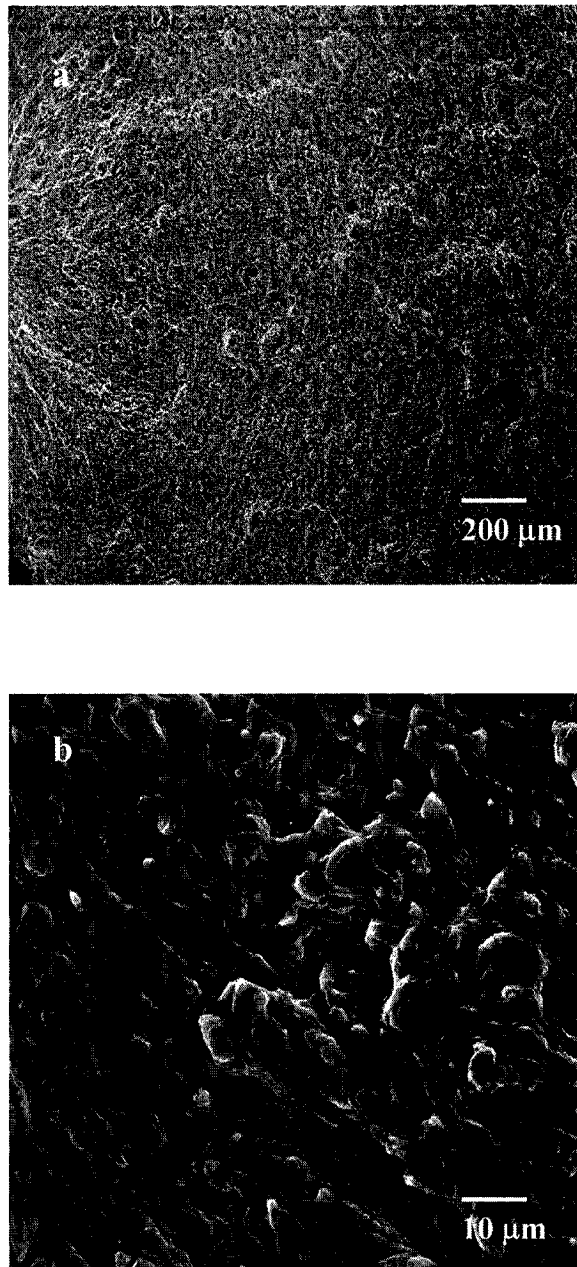
Figure 5.18: Scanning electron micrographs of the
2009/SiC15p-T42 composite cyclically deformed at
150 °C, at load ratio of 0.1 at a maximum stress
of 360 MPa (N_f = 94,265 cycles) showing: (a)
overall morphology showing two distinct regions
of fatigue and overall failure, and (b) numerous
microscopic cracks covering the transgranular
fracture region.
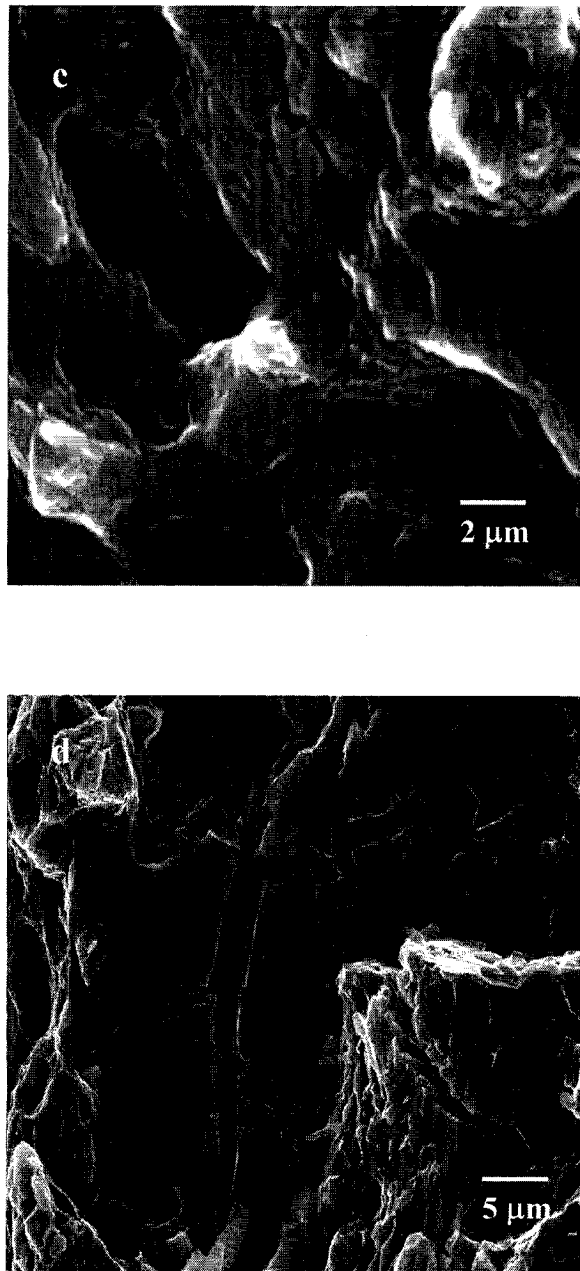
Figure 5.18 (cont.): Scanning electron micrographs of the 2009/SiC15p-T42 composite cyclically deformed at 150 °C, at load ratio of 0.1 at a maximum stress of 360 MPa (N_f = 94,265 cycles) showing: (c) high magnification of (b) showing morphology of a microscopic crack, and (d) microscopic cracks emanating from a macroscopic crack

to occur at and near the reinforcing SiC_p. When the local stress concentration exceeds a critical value it causes the reinforcement particle to crack and the adjacent matrix to fail by separation or decohesion. Failure through the conjoint influences of: (a) separation at the aluminum alloy matrix/reinforcing SiC particulate interfaces, or decohesion, and (b) cracking of the reinforcing SiC particulates dispersed through the aluminum alloy metal matrix, suggests the exacerbation of micro-plastic deformation in regions containing a high concentration or agglomeration of the reinforcing SiC and cracked SiC particulates. Concurrent failure of the reinforcing SiC_p and other coarse second phase particles (i.e., the constituent particles) in the composite microstructure is governed by the competing influences of: (1) local plastic constraints, (2) particle size, and (3) degree of agglomeration, all other factors being held constant. The local plastic constraints are particularly important for the larger sized particles and particle clusters during composite fracture [104].

The intrinsic brittleness of the reinforcing SiC particulates coupled with the propensity for it to fracture due to localized deformation results in both particulate

cracking and interfacial failure through debonding being the dominant damage modes. With continued cycling the microscopic cracks grow from one reinforcing SiC particle to another SiC particle. When the reinforcing SiC particles are positioned directly ahead of the advancing microscopic crack, propagation is temporarily arrested. The exacerbation of strain at the reinforcing SiC particles, lying well within the plastic zone of an advancing microscopic crack, is conducive for debonding with the plastically deformation metal matrix [82,92]. Extensive SiC particle cracking ahead of the microscopic cracks was not observed and is rationalized as being due to the relatively large size of the SiC_p reinforcement. Also, a careful observation of the cyclic fatigue fracture surfaces of the 2009/SiC/15p-T42 composite revealed that in excess of 50% of the reinforcing SiC_p had fractured during cyclic deformation [92,104]. This indicates that not all of the reinforcing SiC_p were loaded to their fracture stress providing direct evidence for: (a) the non-uniform distribution of SiC particulates in the 2009 aluminum alloy metal matrix, and (b) their orientation with respect to the applied stress axis. The situation of SiC_p particulate reinforcement failure through cracking and decohesion is

exacerbated by the mismatch strain and concomitant high compression stresses in the composite microstructure due to differences in the thermal expansion coefficient between the constituents of the composite, i.e., the SiC particulates and the 2009 aluminum alloy matrix [92,104]. Once formed, several of the microscopic cracks were observed to grow around the reinforcing SiC particles by linking with smaller microscopic cracks, which had formed at the interface. Few of the microscopic cracks eventually coalesce to become one or more macroscopic cracks. Since crack tip stress intensity, a function of the applied stress intensity (ΔK), are generally low in high-cycle fatigue (HCF), in comparison to low-cycle fatigue (LCF), the corresponding growth rates of the microscopic cracks during high-cycle fatigue are expected to be lower [104].

Micro-cracked areas were found both ahead of and near the tips of long cracks that were associated with regions of intense deformation. Crack propagation occurred by a process whereby coalescence of the fine microscopic cracks occurred through matrix failure ahead of the main crack tip [105]. Concurrently, the formation of addition microscopic cracks occurred ahead of the macroscopic crack tip [104]. There was some evidence of crack branching suggesting the

presence of damaged region ahead of the crack tip (Figure

5.18d). Such occurrence of damage suggests that the

reinforcing SiC particles are loaded by forces caused by

deformation of the metal matrix. Final fracture is

achieved by fast fracture through the matrix between the

reinforcing SiC particulates. Few of the voids generated

by cracking of the reinforcing SiC particulates did not

grow extensively in the tensile stress direction, which is

generally the case in ductile fracture of unreinforced 2XXX

series aluminum alloys [104,106]. The lack of extensive

void growth in this SiC particulate-reinforced 2009 metal

matrix suggests that the overall fracture strain is

critically controlled by both the void nucleation strain

and linkage strain [104,105].

5.1.4 Cyclic-Strain Controlled

Clearly the factors governing the cyclic plastic

strain response and the resultant low-cycle fatigue (LCF)

life and fracture properties of the composite

microstructure are far more complex than in the

unreinforced matrix material.

The objective of this section is to document the

influence of particulate reinforcement on the cyclic

strain-controlled fatigue response and final fracture

behavior of the 2009/SiC/15p-T42 composite. The results presented consider the following aspects: (a) the influence of discontinuous SiC particle reinforcement on cyclic stress response characteristics, cyclic stress-strain response characteristics. (b) influence of SiC reinforcement on cyclic strain resistance and cyclic fatigue life, and (c) the analysis of cyclic fracture behavior as a function of nature of loading, test temperature and composite microstructure effects.

This study on 2009 aluminum alloy MMC is considered novel since it attempts to relate the intrinsic mechanisms that enhance the resistance of the material to crack advance with the extrinsic mechanisms that tend to promote sub-critical crack growth.

5.1.4.1 Cyclic Strain Resistance

A measurable physical quantity during fully reversed strain-amplitude controlled cyclic deformation is plastic strain. Cyclic plastic strain produces a number of damaging processes, which affect the microstructure and resulting cyclic strain resistance and low-cycle fatigue life [107]. The progressive damage resulting from cyclic straining helps relate the cyclic fatigue life (N_f) to cyclic strain

amplitude $(\Delta\varepsilon/2)$ in a completely reversed $[R_\varepsilon = \varepsilon_{min}/\varepsilon_{max} = -1]$ total strain-amplitude $(\Delta\varepsilon_T/2)$ controlled fatigue test. The empirical relationship between plastic strain-amplitude $(\Delta\varepsilon_p/2)$ and the reversals-to-fatigue failure $(2N_f)$, the Coffin-Manson relationship, was determined for the LCF regime $[N_f < 10^4$ cycles] and predicts that [108,109]:

$$\Delta\varepsilon_p/2 = \varepsilon_f' (2N_f)^2 \qquad (5.5)$$

This relationship is plotted on bilogarithmic coordinates on the basis of cyclic plastic strain-amplitude $(\Delta\varepsilon_p/2)$ and number of reversals-to-fatigue failure $(2N_f)$:

$$ln (\Delta\varepsilon_p/2) = ln (\varepsilon_f') + c \, ln (2N_f) \qquad (5.6)$$

The best straight line fit for the Coffin-Manson plot or plastic strain amplitude-reversals-to-fatigue life curve is obtained by linear regression analysis. An extrapolation of the best fit is made to determine the value of cyclic plastic strain at $2N_f = 1$. This point on the plastic strain-fatigue life curve is the fatigue-ductility coefficient (ε'_f) and is related to cyclic ductility of the material. The slope of the plastic strain amplitude-reversals-to-fatigue life curve gives the fatigue-ductility exponent (C).

The effect of fully reversed strain cycling on LCF response of 2009/SiC/15p-T42 composite is shown in

Figure 5.19. The cyclic strain amplitude-reversals to fatigue life curve is viewed as an indication of the resistance of the composite microstructure to crack initiation and failure. Throughout LCF testing of the 2009/SiC/15p-T42 composite no evidence of specimen buckling was observed [111]. The elastic strain-amplitude-reversals to fatigue life curve is linear and the Basquin relationship is satisfied. The plastic strain-amplitude-reversals to fatigue life curve is linear and the Coffin-Manson relationship (Equation 5.5) can be used to determine the fatigue behavior in the LCF regime ($N_f < 10^4$ cycles). The values of LCF parameters that satisfy the Basquin and Coffin-Manson relationships are summarized. The value of fatigue-ductility exponent (c) is -0.4 and fall within the generally observed range (-0.7 to -0.2) for a large number of monolithic alloys [110]. The fatigue-ductility exponent (c) decreases from -0.4 at the elevated temperature (150 °C) to -0.59 at room temperature (27 °C). The fatigue ductility coefficient for this MMC is 5.9 % at 27 °C and 2.2 % at 150 °C, and does not accord well with the monotonic fracture ductility (ε_f).
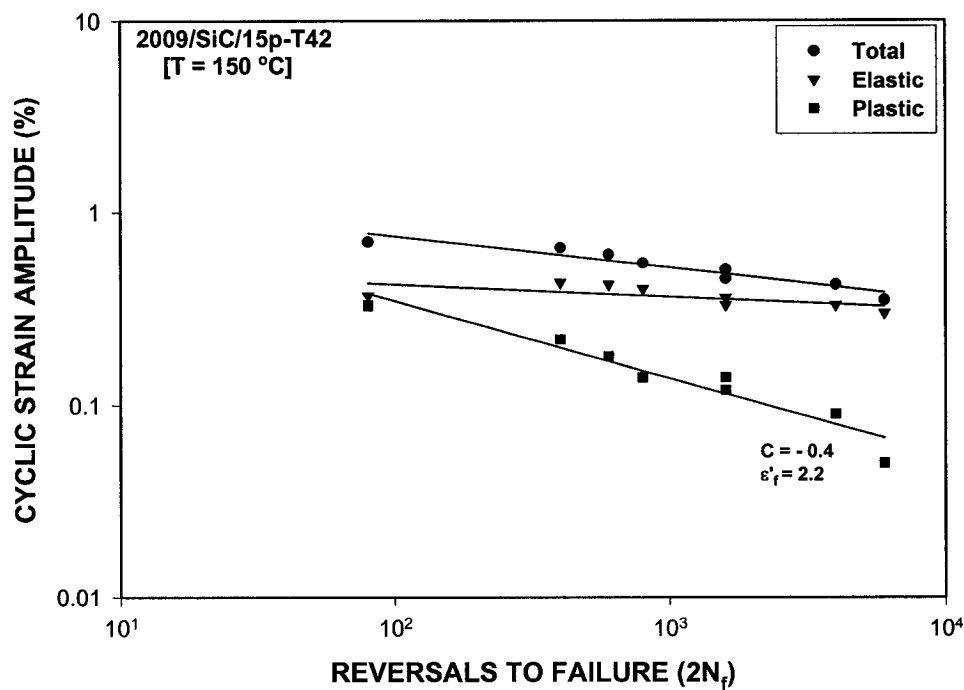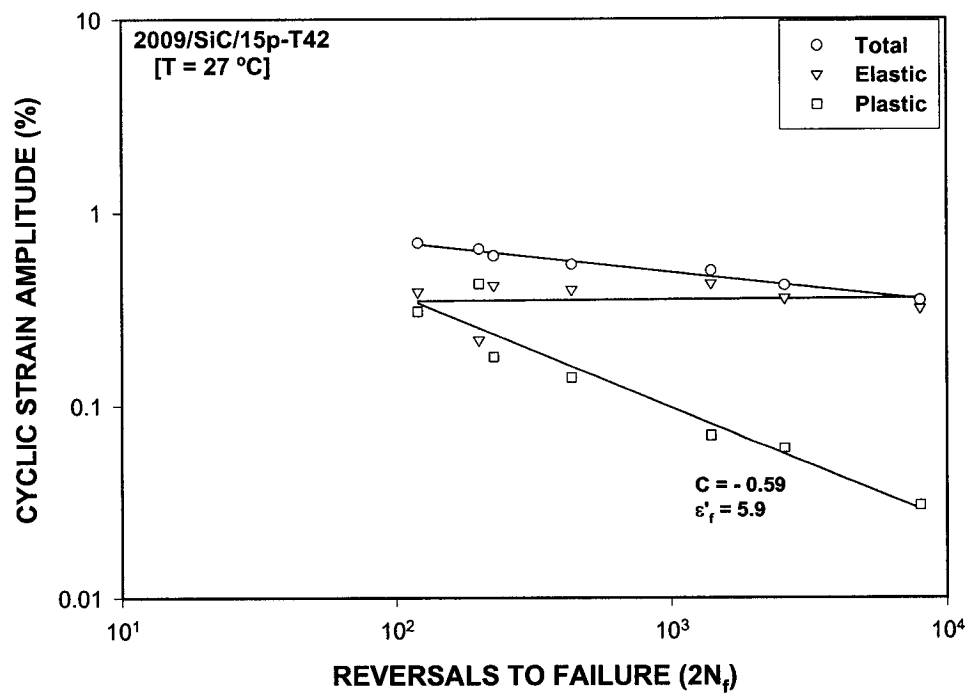
Figure 5.19: Cyclic strain amplitude-fatigue life response of the 2009/SiC/15p-T42 composite at: (a) 27°C, and (b) 150°C.

The influence of test temperature on plastic strain amplitude-reversals to fatigue life response is exemplified in Figure 5.20. At high cyclic plastic strain-amplitudes and resultant short low- cycle fatigue life there is little to no influence of test temperature on fatigue life. However, at equivalent lower cyclic plastic strain-amplitudes and resultant long fatigue life there occurs a 100-200 percent improvement in low-cycle fatigue life with an increase in test temperature from 27 °C to 150 °C. The observed improvement is consistent with a decrease in fatigue- ductility exponent (c) with an increase in test temperature. The plausible mechanisms responsible for the observed improvement in LCF life with an increase in test temperature are discussed in the following section.

Under total strain amplitude-controlled conditions, the elastic strains are much lower in the 2009/SiC/15p-T42 composite material than they would be in the unreinforced material (Alloy 2009). Thus, for a given total strain, the average plastic strain is significantly elevated in the composite material relative to the unreinforced metal matrix. The increased plastic strain dominates the development of fatigue damage resulting in a positive
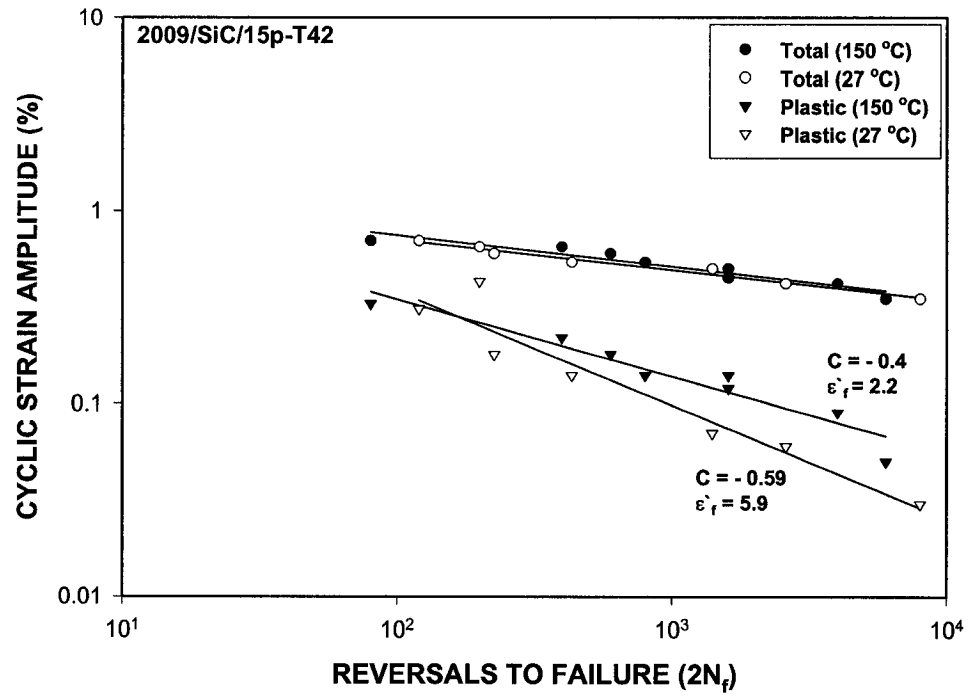
Figure 5.20: Comparison of the influence of test
temperature on plastic strain-fatigue life
response of the composite 2009/SiC/15p-T42.

contribution to the inferior cyclic strain resistance of

the composite microstructure when compared to the

unreinforced counterpart.

5.1.4.2 Cyclic Stress Response

The cyclic stress response curves, or cumulative glide

plots, showing variation of cyclic stress-amplitude with

the number of cycles, at fixed plastic strain-amplitudes,

illustrates the path taken by the composite material to its

final level of stress during fully-reversed total strain-

amplitude controlled cyclic deformation.

5.1.4.2.1 Test Temperature = 27 °C

The stress response curves for the 2009/SiC/15p-T42

composite are shown in Figure 5.21a. Since for a given

total strain amplitude the cyclic plastic strain amplitude

varied throughout testing, reaching a maximum value at the

minimum stress and a minimum value at the maximum stress,

the value at specimen half-life (N_f) is taken as the

reference. At all cyclic strain amplitudes the

2009/SiC/15p-T42 composite showed evidence of progressive

hardening from the onset of fully reversed deformation.

During the initial stages of cyclic straining, the

hardening effect, or increase in load carrying capability,
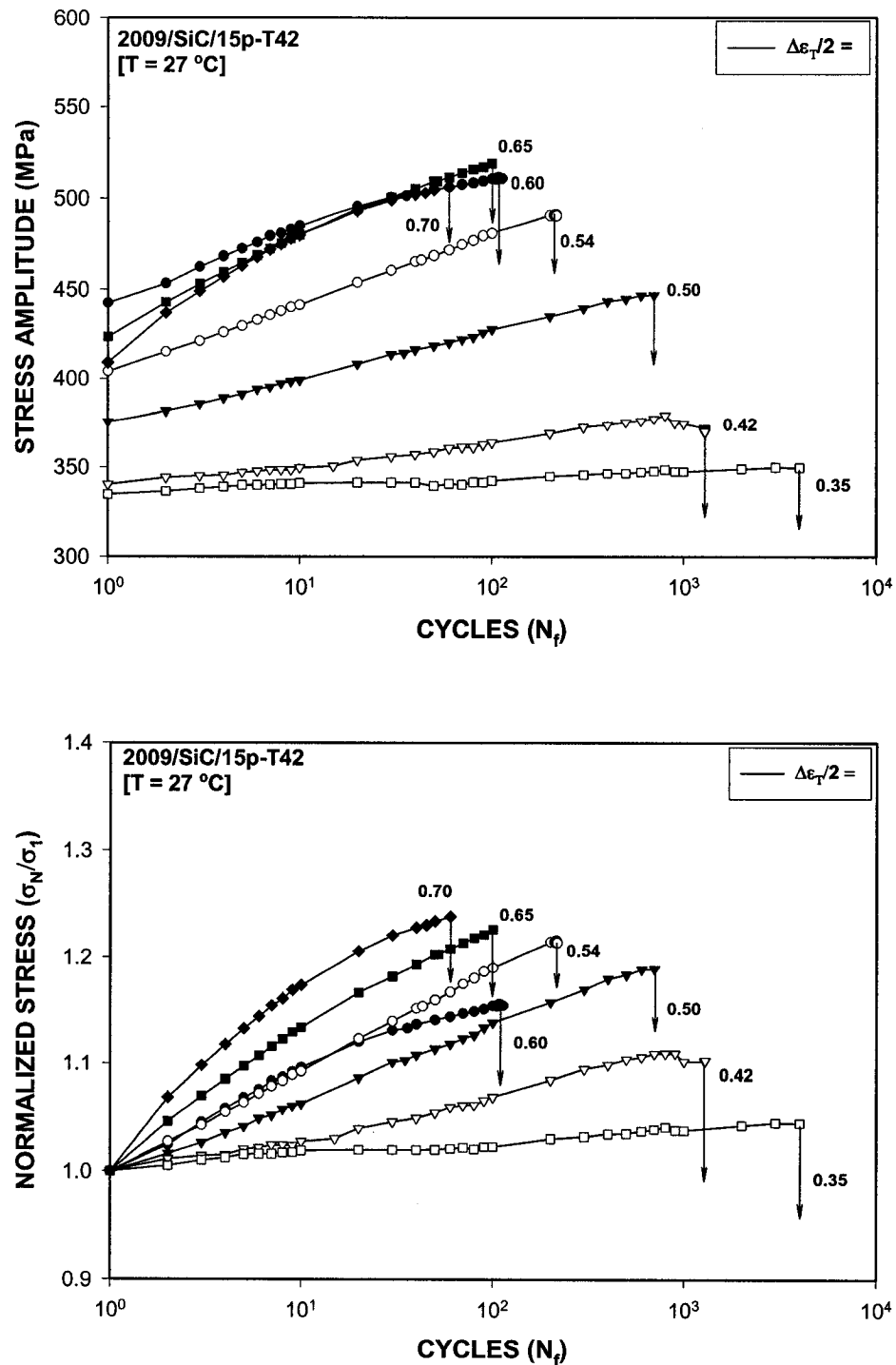
Figure 5.21: Cyclic stress response curves for the
2009/SiC/15p-T42 composite at 27 °C: (a) stress
amplitude versus cycles, and (b) normalized
stress with cycles.

was gradual and increased rapidly at the higher plastic strain amplitudes. The rapid increase in stress carrying capability is ascribed to the mutual interaction of dislocations with other dislocations and the reinforcing particulates. Variation of normalized stress with fatigue cycles reveals the hardening effect to be more pronounced at the higher cyclic strain amplitudes (Figure 5.21b)

5.1.4.2.2 Test Temperature = 150 °C

The stress response curves are shown in Figure 5.22a. At all cyclic strain-amplitudes this composite showed evidence of gradual hardening to failure. During the initial few cycles of fully reversed cyclic straining the hardening was rapid followed by a gradual decrease with continued cyclic straining. The rapid increase in stress, or load carrying capability, of the composite microstructure is attributed to the conjoint and mutually interactive influences of (a) an interaction of dislocations with each other, (b) interaction of dislocations with the reinforcing particulates and other intrinsic microstructural features [111]. As in the case of room temperature test the cyclic hardening at the higher test temperature an increased with increase in plastic strain amplitude. The overall degree of hardening,
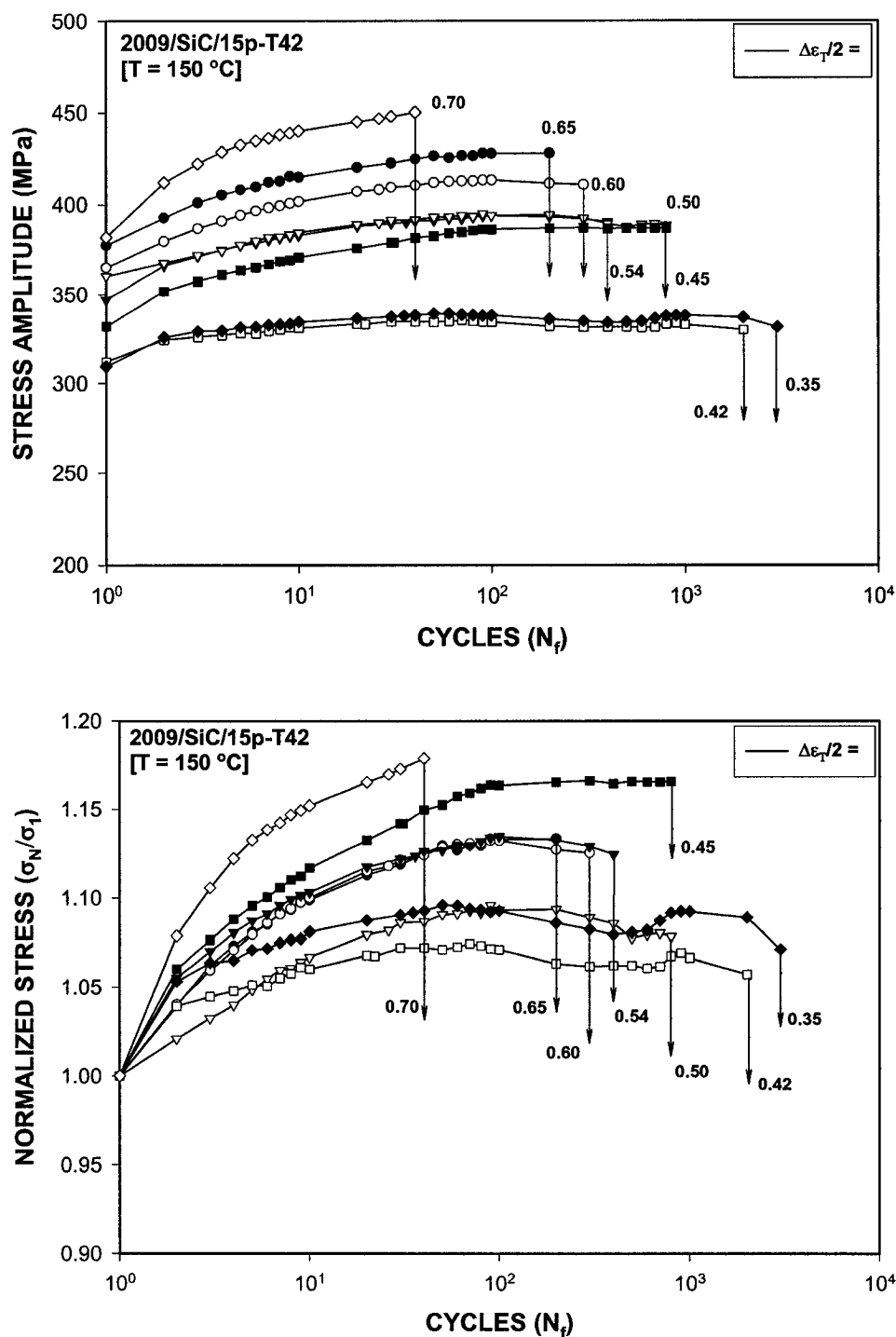
Figure 5.22: Cyclic stress response curves for the
2009/SiC/15p-T42 composite at 150 °C:
(a) variation of stress amplitude with cycles,
and (b) variation of normalized stress with
cycles.

established from the variation of normalized stress with fatigue cycles, of this aluminum alloy metal matrix was greater at the higher strain amplitudes and resultant short fatigue life than at the intermediate and lower cyclic strain amplitudes (Figure 5.22b).

The underlying mechanisms, which control the variation of cyclic stress amplitude during fully reversed strain-amplitude controlled cyclic straining, are dependent on both composite microstructure and cyclic strain range [107,111]. The plausible mechanisms governing stress response of this 2009/SiC/15p-T42 composite can be attributed to the mutually interactive influences of.

(a) An increase in the dislocation density already present in the composite matrix, during plastic deformation, by dislocation multiplication.

(b) An interaction of mobile dislocations with the reinforcing SiC particulates (Figure 5.23a) coupled with an initial interaction of the dislocations with the matrix strengthening precipitates (Figure 5.23b) and coarse second-phase particles, and interaction of dislocations at the grain boundaries (Figure 5.23c).
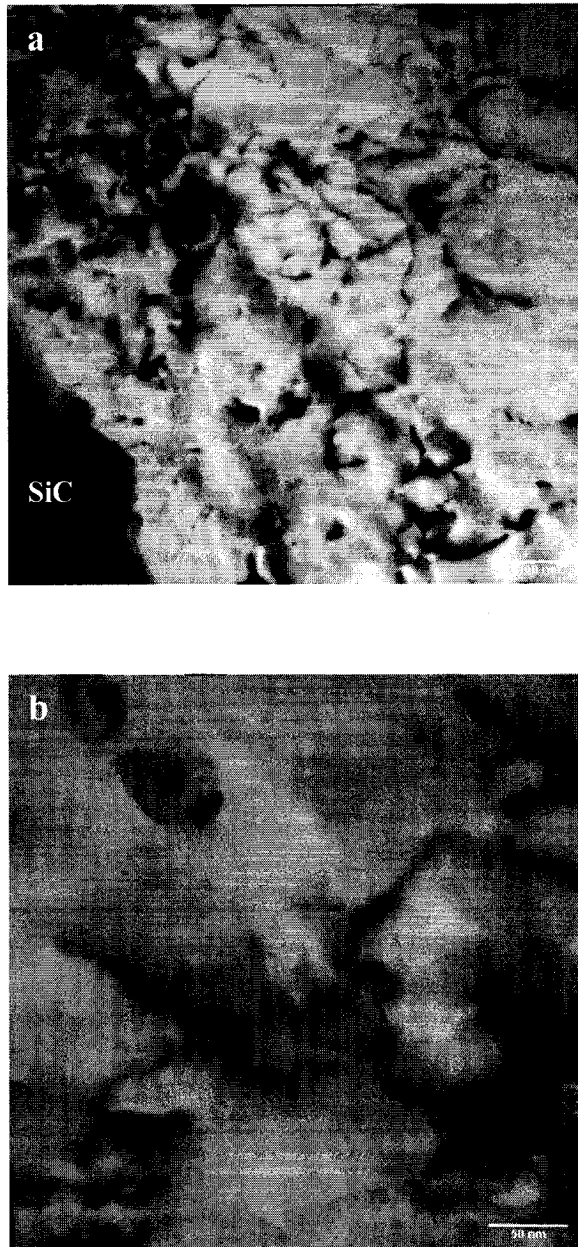
Figure 5.23: Bright filed transmission electron micrographs
of the cyclically deformed and failed
2009/SiC/15p-T42 composite samples showing:
(a) Dislocation-particulate interaction,
(b) Dislocation interaction with strengthening
precipitates.
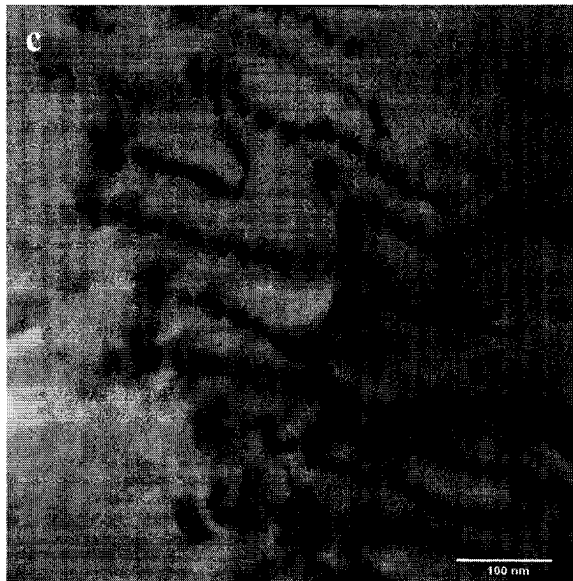
Figure 5.23 (Cont.): Bright filed transmission electron
     micrographs of the cyclically deformed and failed
     2009/SiC/15p-T42 composite samples showing: (c)
     Dislocation accumulation at the grain boundary.

(c) An increase in interaction of a moving dislocation with other dislocations.

5.1.4.3 Cyclic Stress versus Strain Response

When the composite material is subjected to prescribed cyclic total strain amplitude the resultant stress amplitude may change with continued cycling. The cyclic stress-strain response (*CSSR*), cyclic hardening and/or softening behavior is a measure of this transient response and is useful in designing microstructures and developing materials having improved cyclic fatigue resistance. Under fully-reversed, total strain amplitude-controlled ($\Delta\varepsilon_T/2$) cyclic straining, the resultant stresses developed in the composite matrix may be invariant during cycling, that is, they may remain stable, either increase (harden) or decrease (soften) with cycling. For the microstructure that cyclically hardens or softens, a stable stress, called the saturation stress, is generally taken at specimen half-life. The cyclic stress-strain curve is used to characterize the steady state behavior and is obtained by plotting the stabilized stress with applied plastic strain amplitude ($\Delta\varepsilon_p/2$), both taken at specimen half-life ($N_f/2$). Figure 5.24 reveals that the composite become harder or has higher cyclic strength at the higher test
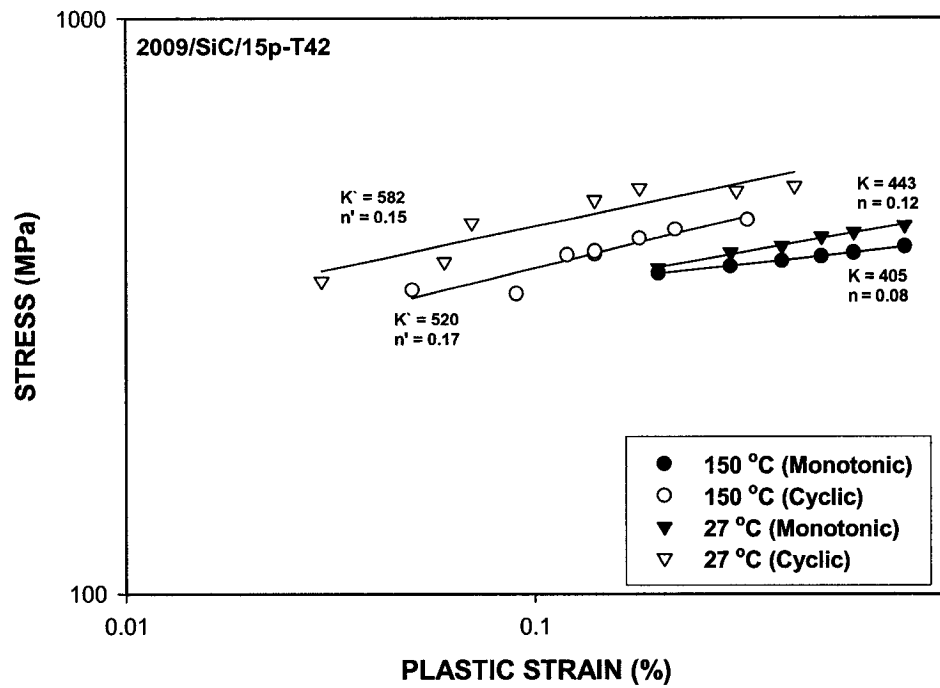
Figure 5.24: Comparison of the monotonic and cyclic stress
strain curves for the 2009/SiC/15p-T42
composite at the two temperatures 27 °C and
150 °C.

temperature (150 ^{o}C). The influence of SiC particulate reinforcement phase and test temperature on cyclic response and work hardening of the composite microstructure can be inferred from this figure. At a given test temperature the cyclic state is harder than the monotonic state. The influence on work hardening is important for an understanding of the effect of particulate reinforcement phase on cyclic deformation and strain-controlled fatigue response. The presence of SiC particulate reinforcements results in the development of localized stresses in the metal matrix around the reinforcing particles. The highly localized stresses contribute to work hardening of the composite microstructure. The concentration of localized stresses results from constrained deformation in the microstructure that occurs because of significant differences in elastic modulus of the discontinuous SiC particulate reinforcement phase and the continuous aluminum alloy (2009) metal matrix. The constraint results in the development of a triaxial stress state and steep stress gradients in the metal matrix around the reinforcing, particulates. The highly localized stresses lead to highly localized plastic deformation. As the stress in the metal

matrix increases, the volume of material that is

plastically deformed increases.

5.1.4.4 Cyclic Fracture Behavior

Examination of the cyclic fatigue fracture surface

features of the deformed 2009/SiC/15p-T42 composite

specimens, at a given test temperature, fracture surfaces

revealed near similar topographies, at high cyclic strain

amplitudes (short fatigue life), intermediate and low

cyclic plastic strain- amplitudes (long fatigue life).

However, on a macroscopic scale, the fracture surface

features were to found to vary with test temperature.

Representative fractographs of the fatigue fracture surface

features, at the two test temperatures, are shown in

Figures 5.25-5.30.

5.1.4.4.1 Test Temperature = 27 °C

Fatigue fracture of the metal-matrix composite was

inclined to the stress axis at both high cyclic strain

amplitude (Figure 5.25a) and low cyclic strain amplitude

(Figure 5.26a). Macroscopic, or low magnification

observations, revealed the fracture surface to be

essentially brittle (low cyclic ductility). The region of

stable crack growth was very small at both high plastic
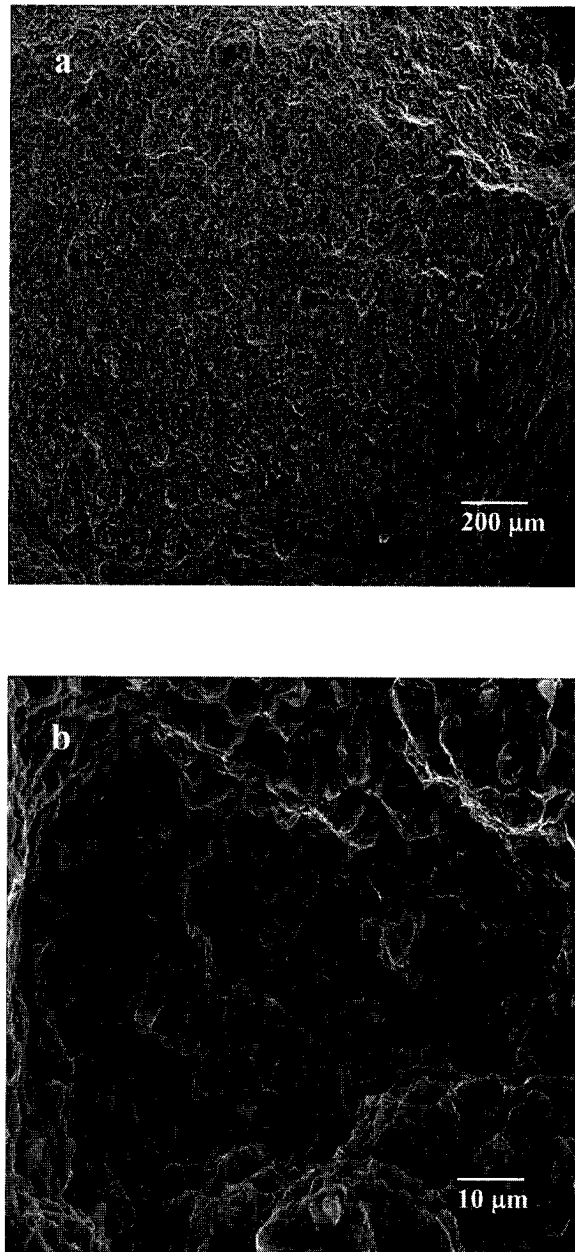
Figure 5.25: Scanning electron micrographs of the
2009/SiC/15p-T42 composite; cyclically
deformed at 27°C,at total strain amplitude of
0.70% (Fatigue Life = 60 cycles), showing: (a)
Overall morphology and (b) High magnification
of (a) showing crack growth region.

strain-amplitude (short fatigue life) and low plastic

strain-amplitude (long fatigue life). The stable crack

growth region was essentially flat (Figure 5.25b) with

isolated microscopic cracks and tear ridges (Figure 5.25c).

The microscopic cracks were in large numbers in the samples

deformed to failure at the lower cyclic strain-amplitudes

and resultant enhanced fatigue life (Figure 5.26b). The

region of fracture transition from stable crack growth to

unstable crack growth and coalescence was not distinct. The

region of unstable crack growth revealed evidence of: (a)

cracked particles (Figure 5.26d), (b) tear ridges and

dimples (Figure 5.26c), and (c) decohesion at matrix-

particulate interfaces (Figure 5.26c). The voids, of

varying size, were distributed randomly throughout the

fracture surface. The macroscopic and microscopic voids

were surrounded by cracked particulates and isolated

pockets of shallow dimples (Figure 5.26d). The constraints

induced by the presence of the hard, brittle and

elastically deforming SiC particulates, in the soft,

ductile and plastically deforming 2009 aluminum alloy

matrix, coupled with the resultant development of matrix

triaxiality influences cyclic flow stress of the

2009/SiC/15p-T42 composite during fully-reversed strain-
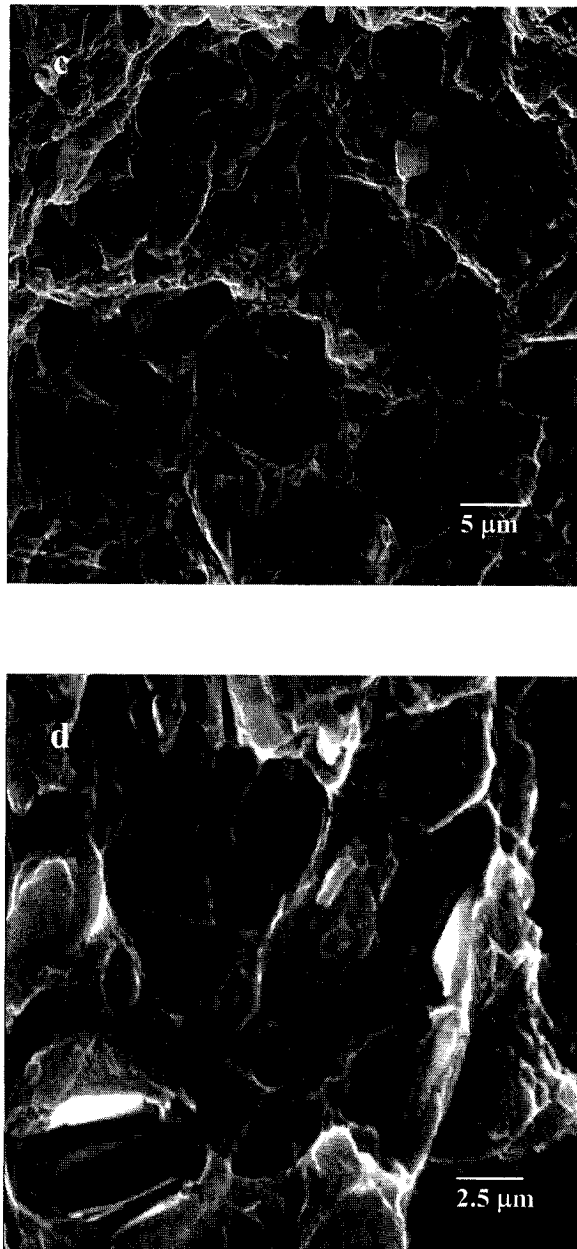
Figure 5.25 (Cont.): Scanning electron micrographs of the
2009/SiC/15p-T42 composite; cyclically deformed
at 27°C, at total strain amplitude of 0.70%
(Fatigue Life = 60 cycles), showing:
(c) Microscopic cracks and tear ridges and
(d) Cracked SiC particles.
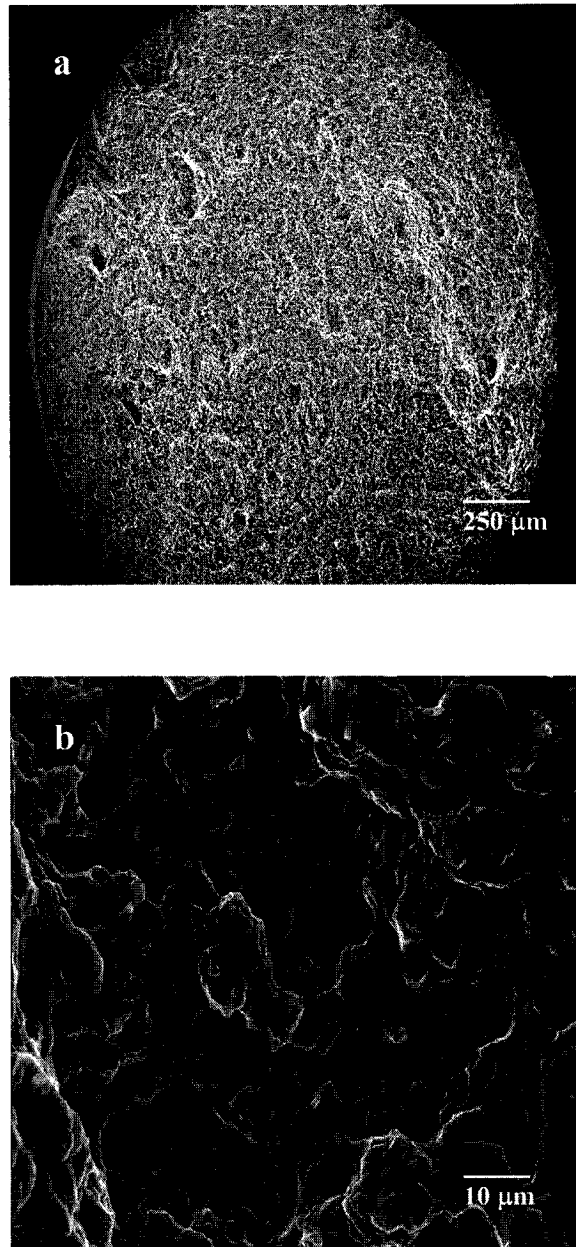
Figure 5.26: Scanning electron micrographs of the
2009/SiC/15p-T42 composite cyclically deformed
at 27°C, a total strain amplitude of 0.42%
(Fatigue Life: 1,293 cycles), showing: (a)
Overall morphology showing regions of fatigue
and overload and (b) Fine microscopic cracks
in composite matrix.
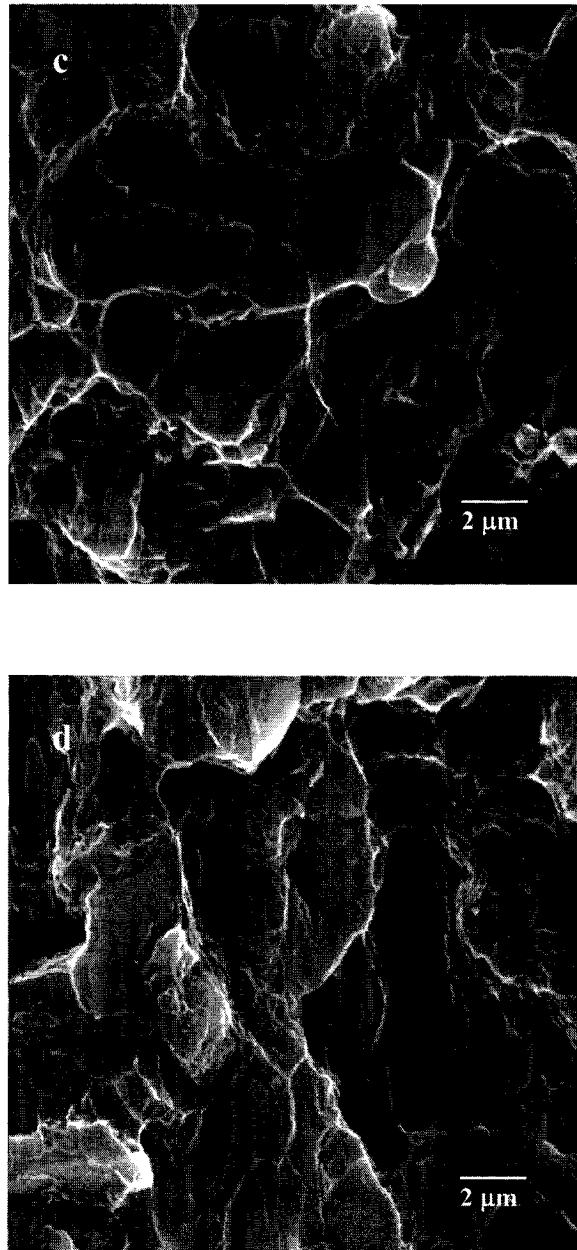
Figure 5.26 (Cont.): Scanning electron micrographs of the
        2009/SiC/15p-T42 composite cyclically deformed at
        27°C, a total strain amplitude of 0.42% (Fatigue
        Life: 1,293 cycles), showing: (c) Decohesion /
        failure at matrix-particulate interfaces and
        (d) Macroscopic and fine microscopic voids and
        shallow dimples.

amplitude controlled deformation. This in turn favors limited void growth.

5.1.4.4.2 Test Temperature = 150 °C

At this test temperature cyclic fatigue fracture was essentially similar at both high cyclic strain and low cyclic strain amplitudes. The region of crack initiation was very small (Figure 5.27a). A large portion of the fracture surface revealed evidence of. (a) microscopic cracks (Figure 5.27a), (b) tear ridges (Figure 5.27b), and (c) cracked particles and isolated pockets of shallow dimples (Figure 5.27d). At lower cyclic strain amplitudes and resultant long fatigue life microscopic observation of the fracture surface revealed: (i) evidence of brittle failure with multiple cracking of the reinforcing SiC particles (Figure 5.28b), and (ii) traces of ductile failure through the formation of isolated pockets of ductile dimples surrounding the tear ridges (Figure 5.28d).

The large mismatch in strain carrying capability that exists between the intrinsically brittle and elastically deforming reinforcing SiC particle and the plastically deforming aluminum alloy metal matrix results in a large concentration of stress both at and near the reinforcing particle causing the metal matrix in the immediate vicinity
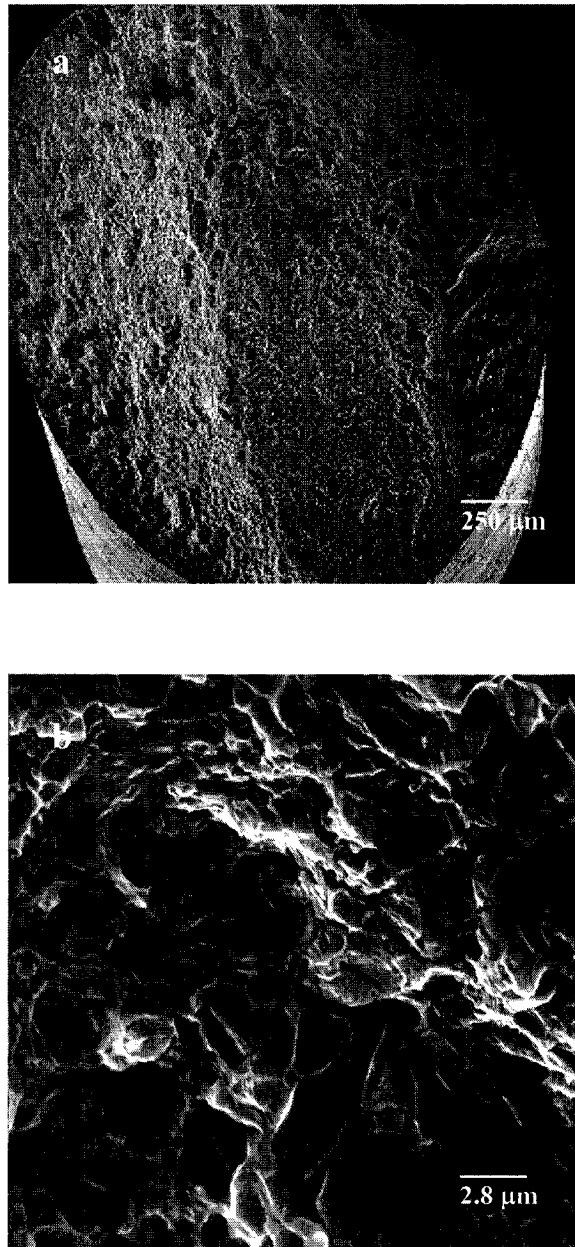
Figure 5.27: Scanning electron micrographs of the
2009/SiC/15p-T42 composite cyclically deformed
at 150°C at total strain amplitude 0.70 %
(fatigue life = 40 cycles), showing: (a)
Overall morphology showing regions of fatigue
and overload and (b) Microscopic cracks
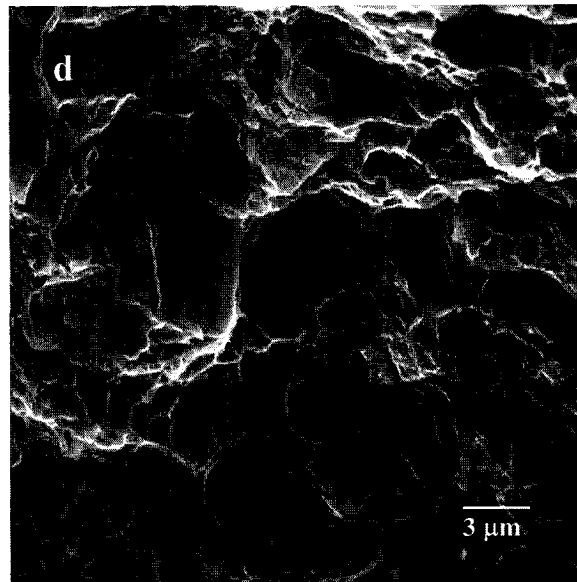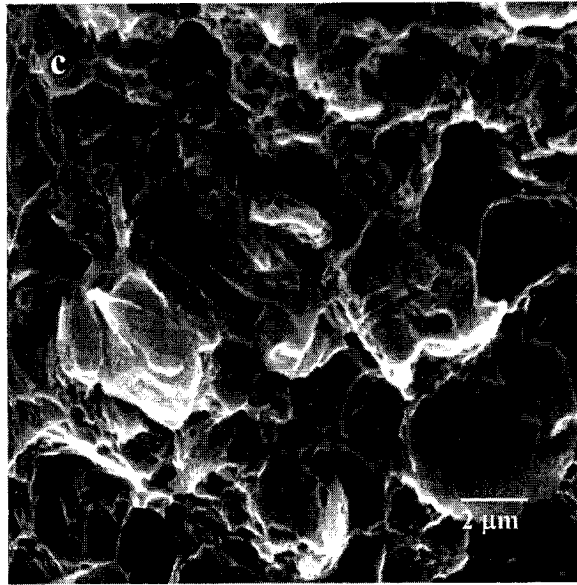
Figure 5.27(Cont.): Scanning electron micrographs of the
2009/SiC/15p-T42 composite cyclically deformed at
150°C at total strain amplitude 0.70 % (fatigue
life = 40 cycles), showing: (c) Microscopic crack
propagation through the tear ridges
microstructure (d) Cracked particles.
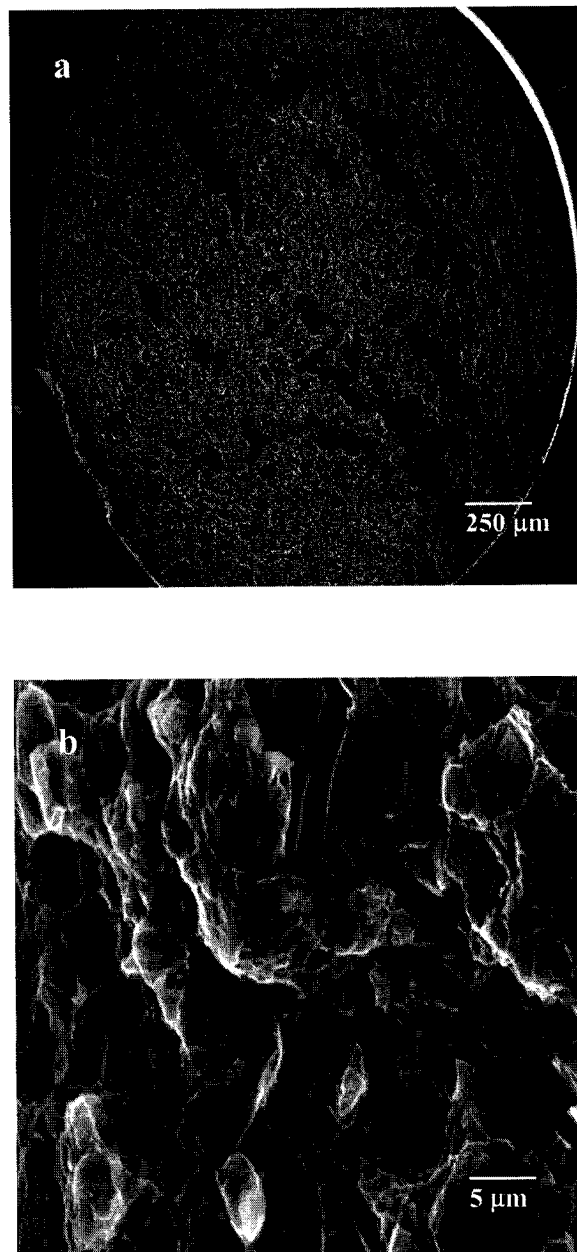
Figure 5.28: Scanning electron micrographs of the
2009/SiC/15p-T42 composite cyclically deformed
at 150°C at total strain amplitude 0.42%
(fatigue life = 2,000 cycles), showing: (a)
Overall morphology showing Regions of fatigue
and overload and (b) Cracked SiC particulate
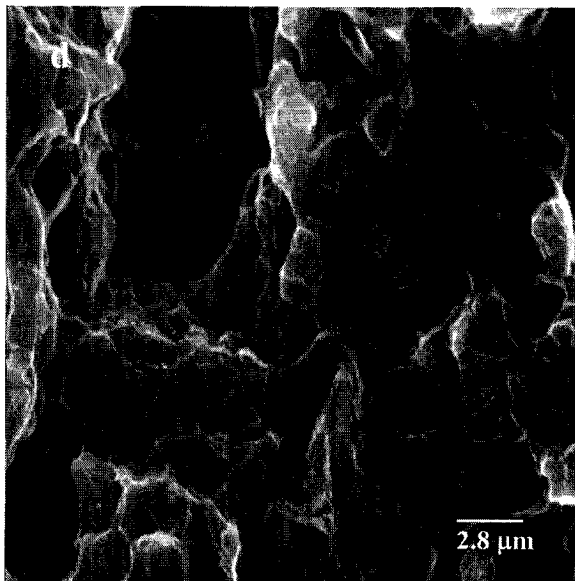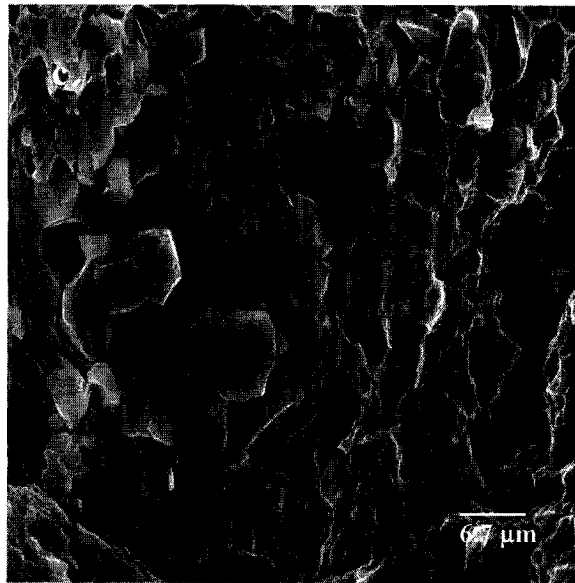
Figure 5.28 (Cont.): Scanning electron micrographs of the
2009/SiC/15p-T42 composite cyclically deformed
at 150°C at total strain amplitude 0.42% (fatigue
life = 2,000 cycles), showing: (c) Tear ridges
surrounded by shallow dimples and (d) Voids of
varying size and shallow dimples.

to fail. The decohesion and cracking of the reinforcing SiC particulates (Figure 5.29) suggests that local plastic strain dominates in regions containing a high volume fraction of the SiC particulates and is partially responsible for the degradation in cyclic strain resistance and fatigue life of this composite particularly at the lower test temperature. Cracking of a number of reinforcing SiC particles coupled with decohesion at the matrix-particulate interfaces was observed in regions of particulate clustering or agglomeration. This suggests the important role played by local plastic strain in governing damage initiation and propagation in this composite material. Furthermore, the short inter-particle distances associated with particulate clustering facilitate linkage between the neighboring voids as a direct result of decreased propagation distance between the cracked particulates. The coalescence of the fine microscopic voids results in pockets of shallow dimples on the fatigue fracture surface [111].

Overall damage to the composite microstructure by enhanced grain boundary degradation is ruled out since fractographic observations of samples deformed at the two temperatures (ambient and elevated) revealed that the
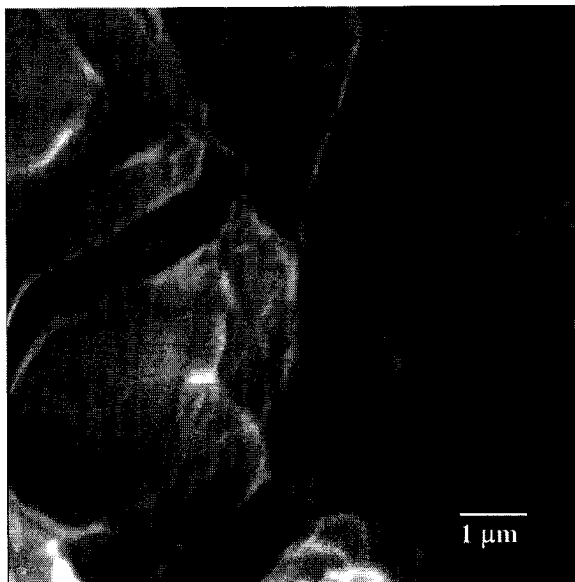
Figure 5.29: Scanning electron micrographs of the
2009/SiC/15p-T42 composite cyclically deformed
at total strain amplitude of 0.70% (fatigue
life = 60 cycles) showing cracked SiC
particulate and decohesion at the interfaces.

degradation in cyclic fatigue life with an increase in test temperature did not occur as a direct result of drastic change in overall fracture mode from brittle intergranular to ductile transgranular mode. The occurrence of plastic strain inhomogeneity as evidenced by planar deformation bands (Figure 5.30) and exacerbated by the presence of grain boundary particles (Figure 5.30c) is believed to be responsible for the intergranular cracking that is observed. Besides, the short time duration associated with each total strain amplitude controlled fatigue test, at the elevated temperature, is insufficient to cause any significant time dependent damage due to creep [111].

5.2. 7034 Aluminum Matrix Composite

The quasi-static response, cyclic stress amplitude controlled fatigue response and fracture behavior of aluminum 7034 discontinuously reinforced with silicon carbide (SiC) particulates were studied at room (27 °C) and elevated (120 °C) temperatures, in both the under-aged and peak-aged conditions, with the objective of documenting the influence of microstructure and temperature on tensile properties, cyclic fatigue test and intrinsic fracture behavior.
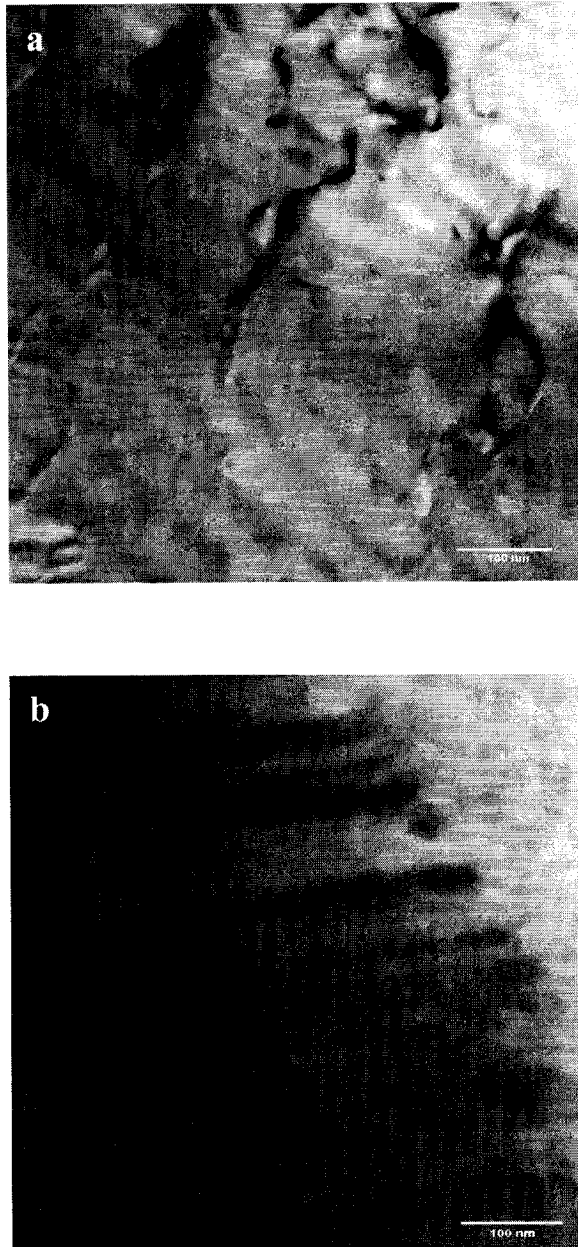
Figure 5.30: Bright filed transmission electron micrographs
of the 2009/SiC/15p composite showing: (a)
Planar deformation bands in the matrix of the
composite sample cyclically deformed at 27 °C,
(b) Planar deformation in sample deformed at
150 °C.
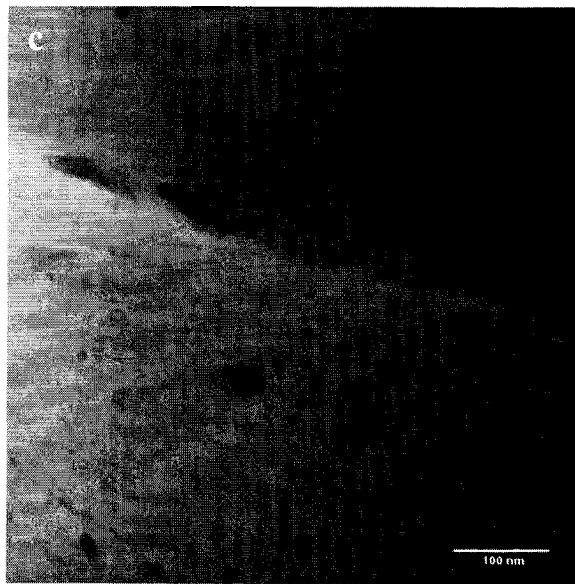
Figure 5.30(Cont.): Bright filed transmission electron
        micrographs of the 2009/SiC/15p composite
        showing: (c) Presence of coarse second phase
        particles at the grain boundary.

5.2.1. Initial Microstructure

The optical micrographs illustrating the microstructure of the 7034/SiC/15p-UA and 7034/SiC/15p-PA composites are shown in Figure 5.31. The SiC$_p$, in the 7034 metal matrix, were non-uniform in size, irregularly shaped and randomly dispersed. At regular intervals, a clustering or agglomeration of the SiC particulates, of varying sizes, was observed resulting in SiC particulate rich and SiC particulate depleted regions. An agglomerated site consisted of the smaller SiC$_p$ intermingled with few larger SiC$_p$. No attempt was made to determine the particle size distribution for the UA and PA microstructures.

The slightly differences in strength among these aging conditions can be elucidated the microstructure variation. The main strengthening mechanism in the 7034 alloy is precipitation hardening by structural precipitates formed during artificial aging (intermediate η' and equilibrium η (*MgZn$_2$*)). The spray deposition technique enables the zinc (*Zn*) content in the alloy to be increased. This increases the volume fraction of hardening precipitates, thus facilitating an improvement in strength.
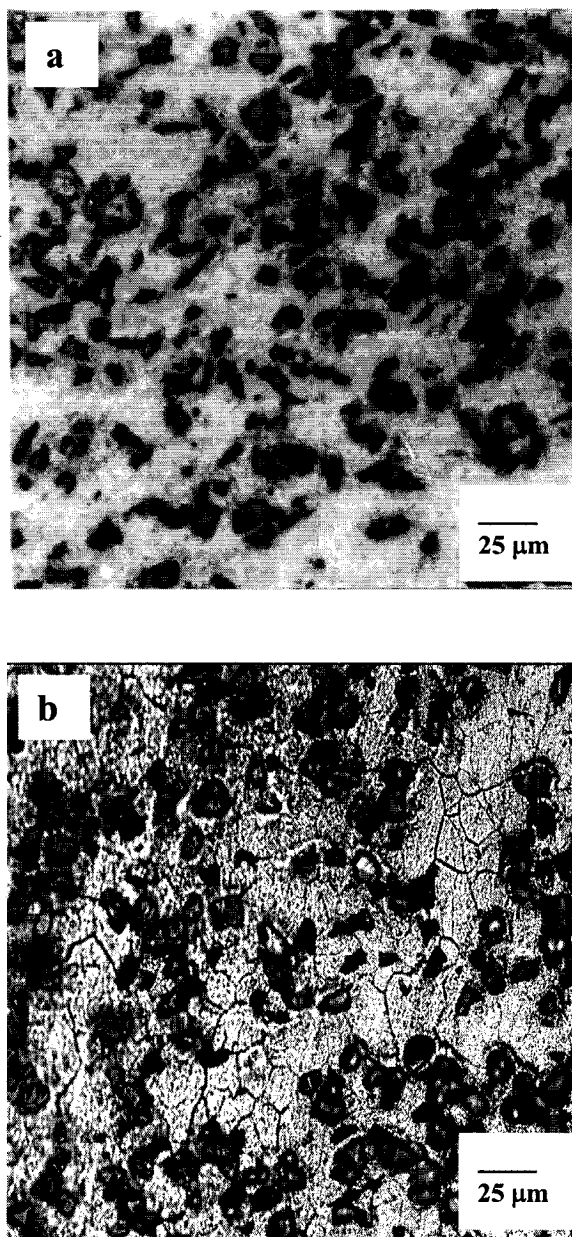
Figure 5.31: Optical micrographs showing the microstructure
of the 7034/SiC/15p composite for:
(a) under-aged (UA) and (b) peak-aged (PA).

The reasons for the improvement of the fatigue performance are due to the formation of a finer grain size and to the high volume fraction of intermetallic particles, which are finer size and coherent with the aluminum alloy metal matrix. The 7034-aluminum alloy utilizes zirconium (Zr) as the dispersoid-forming particle

The equilibrium precipitates are non-shearable particles that promote homogenous deformation through Orowan-type dislocation looping or bypassing of the precipitates. There was no appreciable difference in the size and the amount of precipitates observed in the two aging conditions Figure 5.32. Besides the fine precipitates, significantly coarse precipitates were observed in the aluminum alloy metal matrix Figure 5.32b.

Grain boundaries have an effect on short crack growth, with fine grain size being more resistant to short crack growth. Since transgranular fatigue crack can initiate along a localized slip band, which is induced by a local stress concentration, the grain boundaries act as barriers inhibiting the growth of short fatigue crack.

Precipitate free zones (PFZ's) are vacancy-depleted regions adjacent to a grain boundary decorated by equilibrium η precipitates Figure 5.33.
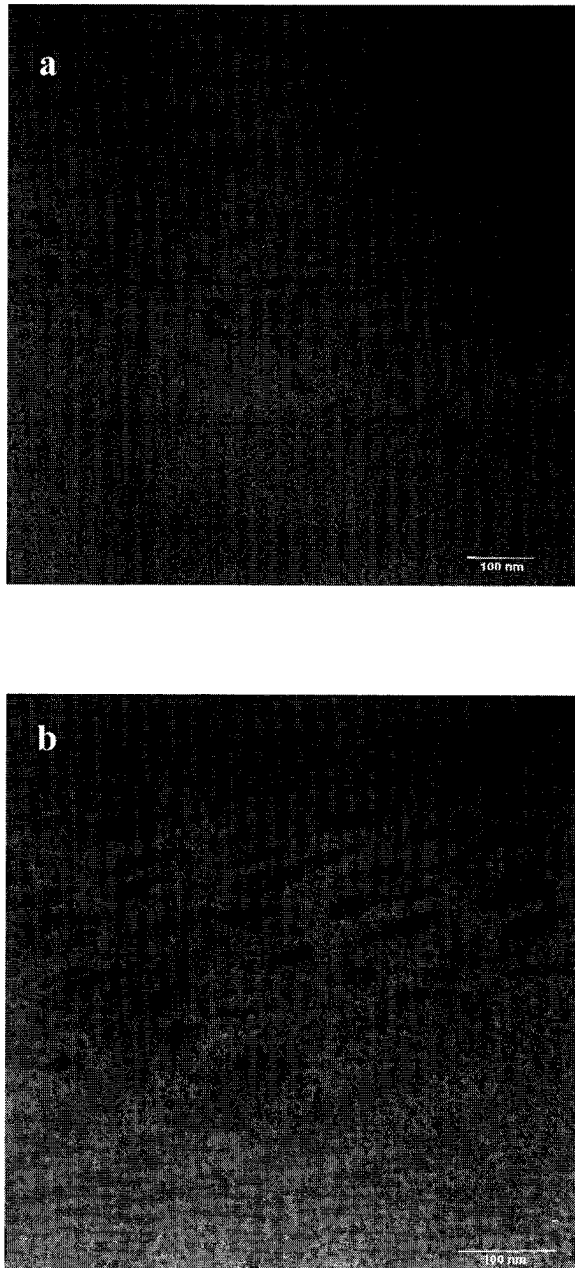
Figure 5.32:   Bright filed transmission electron
micrographs of the 7034/SiC/15p composite
showing a distribution of second phase
particles in the grain interior (a) Under-
aged condition (b) Peak-aged condition.
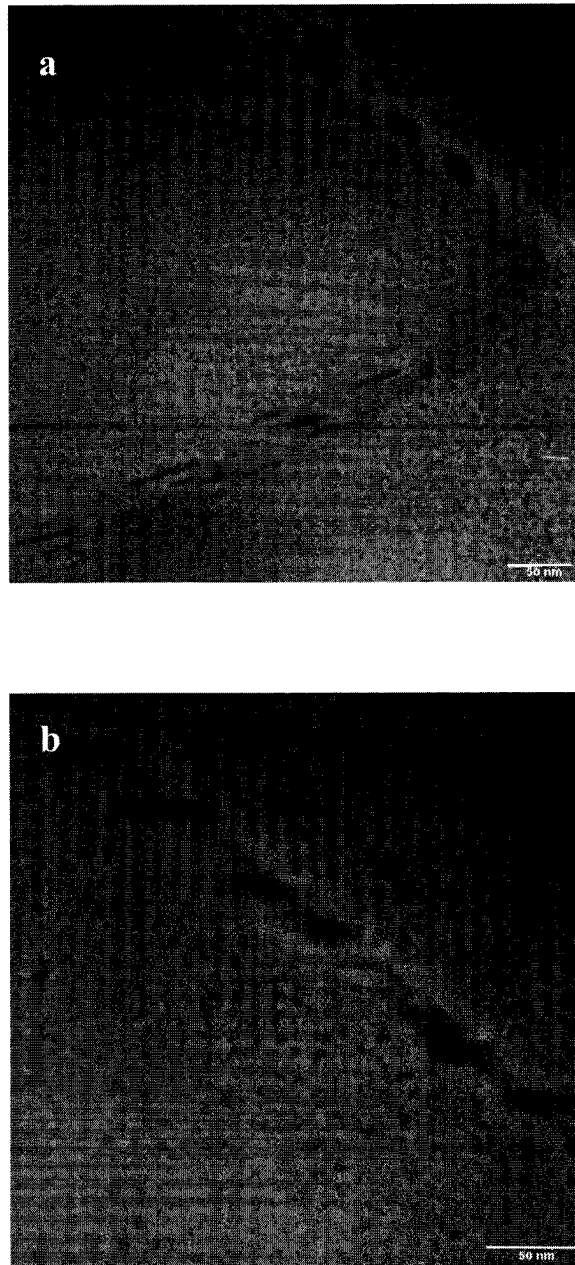
Figure 5.33:   Bright filed transmission electron micrographs of the 7034/SiC/15p composite showing precipitate free zones at the grain boundary decorated by precipitates η (a) Under-aged condition (b) Peak-aged condition.

Precipitate free zones result due to the preferential nucleation of precipitates at the grain boundary, due to the boundary lowering the surface and strain energies of the precipitates. Since the precipitate free zones are depleted of solute, they will be mechanically weaker than the matrix, which is conducive for strain localization, and preferential crack nucleation. In the presence of a PFZ, a material containing fine grain size will exhibit enhanced fatigue life than a large grain material. This is attributed to the increase in number of cycles required for crack initiation in fine-grained material. The fine grain material has shorter slip distance. The ratio of grain boundary precipitate size to width of the Precipitate free zones is used as a parameter to describe the susceptibility of a material to intergranular fracture. If the ratio is high, the properties of the grain interior are the dominant factor. However, when the ratio is low, the properties of the precipitate-free zone determine the intergranular fracture resistance. The width of the precipitate free zone for 7034-aluminum matrix is equal to 25 nm for both the under-aged (UA) and peak-aged (PA) conditions. This leads to improved fatigue crack initiation resistance.

5.2.2. Tensile Properties

The tensile properties are summarized in Table 5.2. Test results reveal that at the elevated temperature of 120 °C the elastic modulus of the 7034/SiC/15p-PA composite is marginally lower that at the ambient temperature (27 °C), and marginally higher for the 7034/SiC/15p-UA counterpart. The yield strength, defined as the stress corresponding to a plastic strain of 0.2 percent, decreased with an increase in test temperature for both the peak-aged (PA) and under-aged (UA) test samples. The observed decrease was as high as 13% for the 7034/SiC/15p-PA microstructure and only 9% for 7034/SiC/15p-UA counterpart. For both aging conditions the ultimate tensile strength (σ_{uts}) of the 7034/SiC/15p composite is marginally higher than the tensile yield strength (σ_{ys}) indicating that the work hardening rate past yielding is low. The ultimate tensile strength followed the same trend as the yield strength of the composite. The decrease in ultimate tensile strength with an increase in test temperature from 27 °C to 120 °C was around 11% for the 7034/SiC/15p-UA and 7034/SiC/15p-PA microstructures [112].

The ductility as measured by: (a) tensile elongation over a 12.7 mm gage length of the test specimen, and

Table 5.2:   The tensile properties of the 7034/SiC/15p
            composite**.

Aging Condition	Temperature (°C)	E (GPa)	Yield Strength (MPa)	Ultimate Tensile Strength (MPa)	Elongation (%)	Reduction-in-Area (%)
Under-aged (UA)	27	90	662	709	1.8	2.4
	120	86	574	604	2.5	5.1
Peak-aged (PA)	27	91	612	683	1.9	3.3
	120	90	562	611	1.9	4.0

** Results are the mean values based on duplicate tests.

(b) reduction in cross-sectional area, increased with an increase in test temperature. The increase was as high as 40% for the PA microstructure and only 3% for the UA microstructure. The reduction-in-cross sectional area increased with an increase in test temperature by as much as 110% for the 7034/SiC/15p-PA and only 25% for the 7034/SiC/15p-UA condition. The observed increase in strain-to-failure and reduction-in-area, with an increase in test temperature, is consistent with the degradation in strength of the composite at the higher test temperature.

5.2.2.1. Tensile Fracture Behavior

At both room (27 °C) and elevated (120 °C) test temperatures the 7034/SiC/15p composite exhibited essentially limited ductility, on a macroscopic scale, with fracture occurring on a plane normal to the far-field tensile stress axis. However, examination of the tensile fracture surfaces at higher magnifications revealed features reminiscent of locally ductile and brittle mechanisms. Representative fractographs of the tensile fracture surface of the 7034/SiC/15p-UA and 7034/SiC/15p-PA composites are shown in Figures 5.34 and 5.35.

5.2.2.1.1 Under-aged Condition

At both test temperatures the tensile fracture
surfaces of this microstructural condition was flat and
normal to the tensile stress axis when viewed on a
macroscopic scale but rough when viewed on a microscopic
scale (Figure 5.34a). The aluminum alloy metal matrix
revealed combinations of tear ridges (Figure 5.34b),
failure of the reinforcing SiC_p by cracking (Figure 5.34c)
and decohesion at the interfaces with the matrix (Figure
5.34c). Following the early initiation of damage,
subsequent accumulation, growth and eventual linkage in the
matrix resulted in brittle failure (Figure 5.34c). At the
higher test temperature the degree of particulate failure
through (a) cracking, and (b) decohesion at its interfaces
with the metal matrix increased (Figure 5.34d). The matrix
of this composite was covered with pockets of shallow
dimples. Multiple microscopic cracks were observed in
regions of particulate agglomeration, which is responsible
for the inferior ductility of the composite [112].

5.2.2.1.2 Peak-aged Condition

At ambient temperature (27 °C) the fracture surfaces
revealed the SiC particulates surrounded by ductile regions
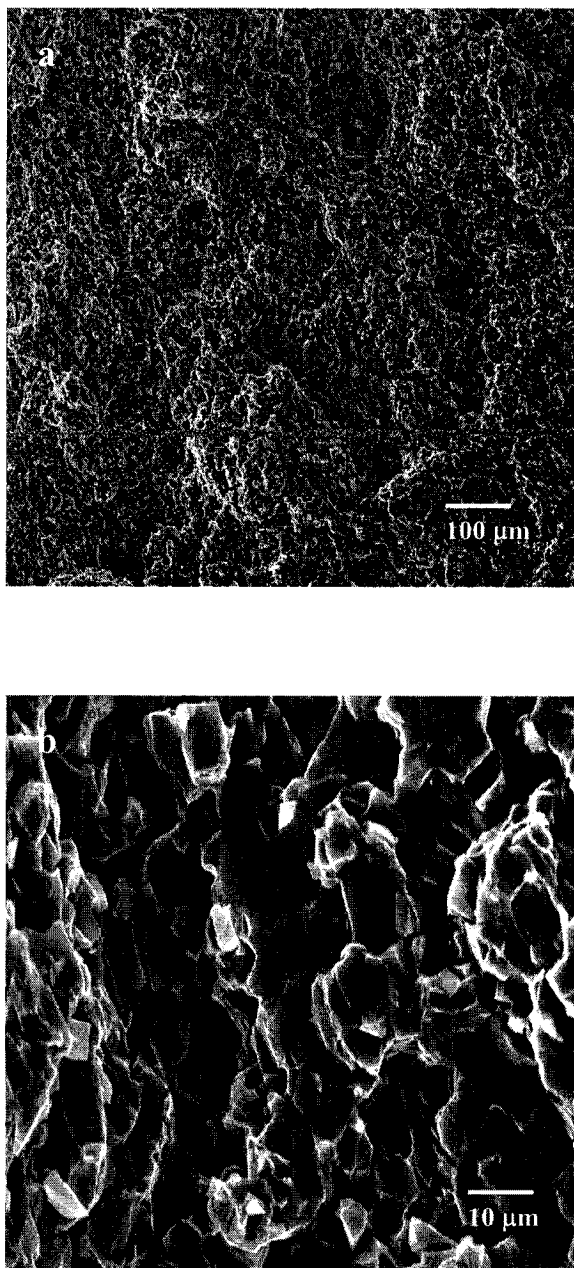
Figure 5.34: Scanning electron micrographs of the
7034/SiC/15p-UA composite deformed at 27 °C
showing: (a) overall morphology, (b) tear
ridges.
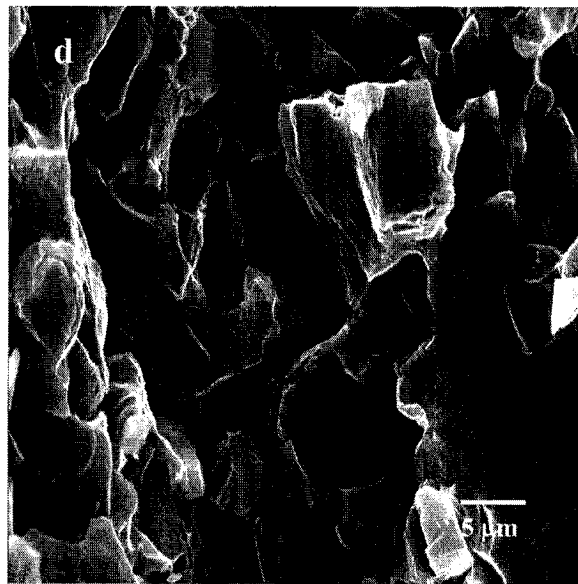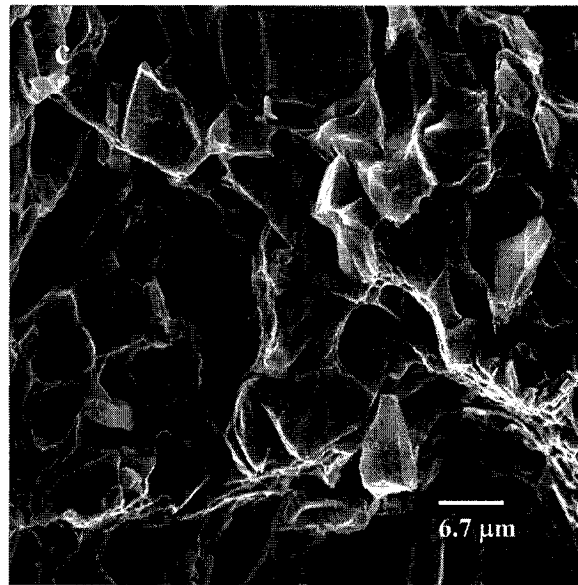
Figure 5.34 (Cont.): Scanning electron micrographs of the
7034/SiC/15p-UA composite deformed at 27 °C
showing: (c) cracked SiC particulates and
decohesion at matrix-particulate interfaces, (d)
microscopic features of fracture at 120 °C.

described as tear ridges (Figure 5.35b), particulate failure through cracking (Figure 5.35c) and decohesion or separation at the matrix-particulate interfaces (Figure 5.35d). No major difference in tensile fracture features was evident at the higher test temperature (120 °C). The matrix of the composite was covered with a population of microscopic voids of varying size and isolated pockets of shallow dimples. The submicrometer-sized dimples are indicative of the improved ductility of this composite at this temperature [112].

The constraints imposed on mechanical deformation by the presence of brittle and essentially elastically deforming SiC_p in a soft, ductile and plastically deforming 7034 aluminum alloy metal matrix and the resultant development of a local triaxial stress state, in the metal matrix, aids in limiting flow stress of the composite microstructure and thus favors: (a) void initiation and growth in the matrix, and (b) debonding at the matrix-SiC_p interfaces [112]. As a direct consequence of deformation constraints induced by the hard and brittle SiC_p reinforcements, a higher applied stress is required to initiate plastic deformation in the aluminum alloy metal matrix. This translates to a higher yield strength and
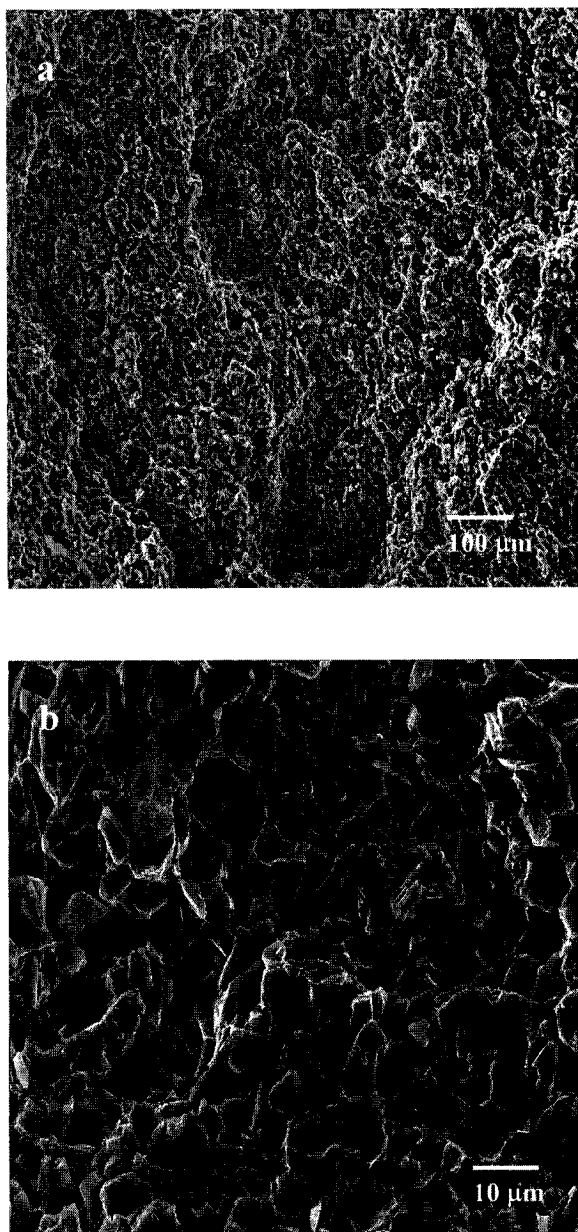
Figure 5.35: Scanning electron micrographs of the
7034/SiC/15p-PA composite deformed at 27 °C
showing: (a) overall morphology, (b) tear
ridges.
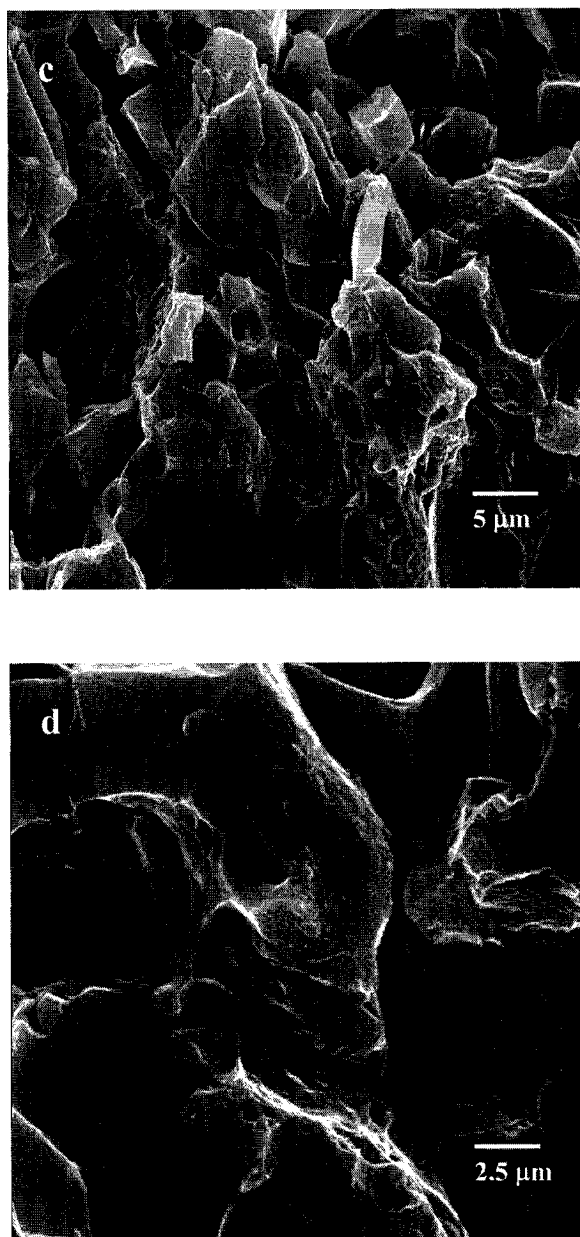
Figure 5.35 (Cont.): Scanning electron micrographs of the
7034/SiC/15p-PA composite deformed at 27 °C
showing: (c) cracked SiC particulates, and (d)
decohesion at matrix-particulate interfaces.

higher elastic modulus of the composite microstructure.

Under the influence of a far-field tensile load the voids

appeared to have undergone limited growth confirming a

possible contribution from particulate-constraints induced

triaxiality on failure of the composite matrix. The local

plastic constraints are particularly important for the

larger-sized SiC particulates and for SiC particulate

clusters during composite fracture [112-114]. Examination

of the fracture surfaces revealed damage to be highly

localized at the SiC reinforcing phase through: (a) cracked

particulates and (b) interfacial failure or decohesion.

This suggests that plastic strain becomes localized during

the early stages of tensile deformation. Few of the

microscopic voids, generated by cracking of the SiC

particulate, did not grow extensively in the tensile stress

direction, which is generally the case for ductile fracture

of unreinforced aluminum alloys [115]. The lack of

extensive void growth in this particulate-reinforced

aluminum alloy metal matrix also suggests that both void

nucleation strain and associated linkage strain critically

control fracture strain [112].

5.2.3. Cyclic-Stress Controlled

For a given aging condition a decrease in load ratio (R) from 0.1 to -1.0 was found to have a detrimental influence on cyclic fatigue life (Figure 5.36). At equivalent values of maximum cyclic stress the degree of degradation in cyclic fatigue life was in the range 200 to 300 percent. The degradation in cyclic fatigue life was more pronounced for the under-aged (UA) microstructure than the peak-aged (PA) microstructure. Also, for a given aging condition, increasing the load ratio resulted in higher fatigue strength (taken as the highest stress at which a composite specimen survived 10^6 cycles). The fatigue ratio, defined herein as the ratio of fatigue strength (taken as the stress at 10^6 cycles) to yield strength, was constant for both the under-aged (UA) and peak-aged (PA) composite microstructures.

In an attempt to examine the reasons for load ratio influences on cyclic fatigue behavior, the data in Figure 5.36 (a) and (b) have been replotted in terms of maximum elastic strain in a manner suggested by Haasen and co-workers [103], where maximum elastic strain is the maximum stress normalized by elastic modulus (Figure 5.37 (a) and (b)). For both aging conditions (UA and PA) it is seen a

degradation in cyclic fatigue life with a decrease in load ratio (R) from 0.1 to -1.0 is significant and a reflection of the variation of maximum stress with fatigue life. The degradation was being more significant for the under-aged microstructure. Also, for a given load ratio, variation of maximum stress with fatigue life reveals minimal to no influence of aging condition (i.e., UA versus PA) of the 7034/SiC/15p composite (Figure 5.38). This observation is consistent with the near identical yield strength (σ_{ys}) and ultimate tensile strengths (σ_{uts}) of the two microstructures. In order to rationalize the influence of microstructure of the composite, at a constant load ratio (R), on cyclic fatigue life, the test data in Figure 5.38 are replotted to take into account the strengths of the two composite microstructures. In Figure 5.39 the maximum stress has been normalized by the uniaxial yield stress, while in Figure 5.40 the maximum stress has been normalized by the ultimate tensile strength. For both cases, no appreciable influence of microstructure of the 7034/SiC/15p MMC on high cycle fatigue life is evident and conforms well to minimal strength difference for the two microstructures [116].
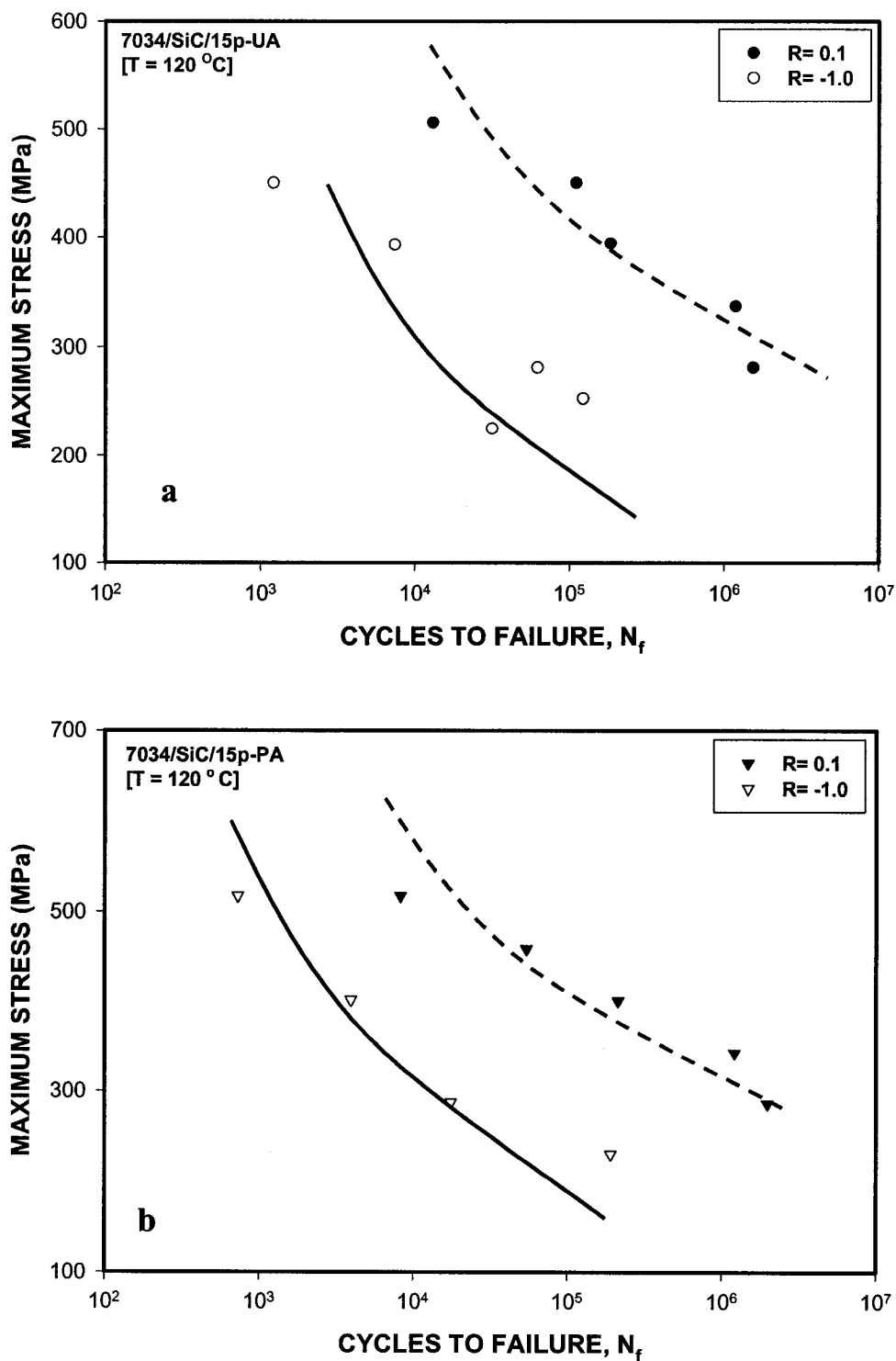
Figure 5.36: Variation of maximum stress with cyclic fatigue
life for the 7034/SiC/15p composite at load
ratios of R = 0.1 and R = -1.0:
(a) under-aged (UA) and (b) peak-aged (PA).
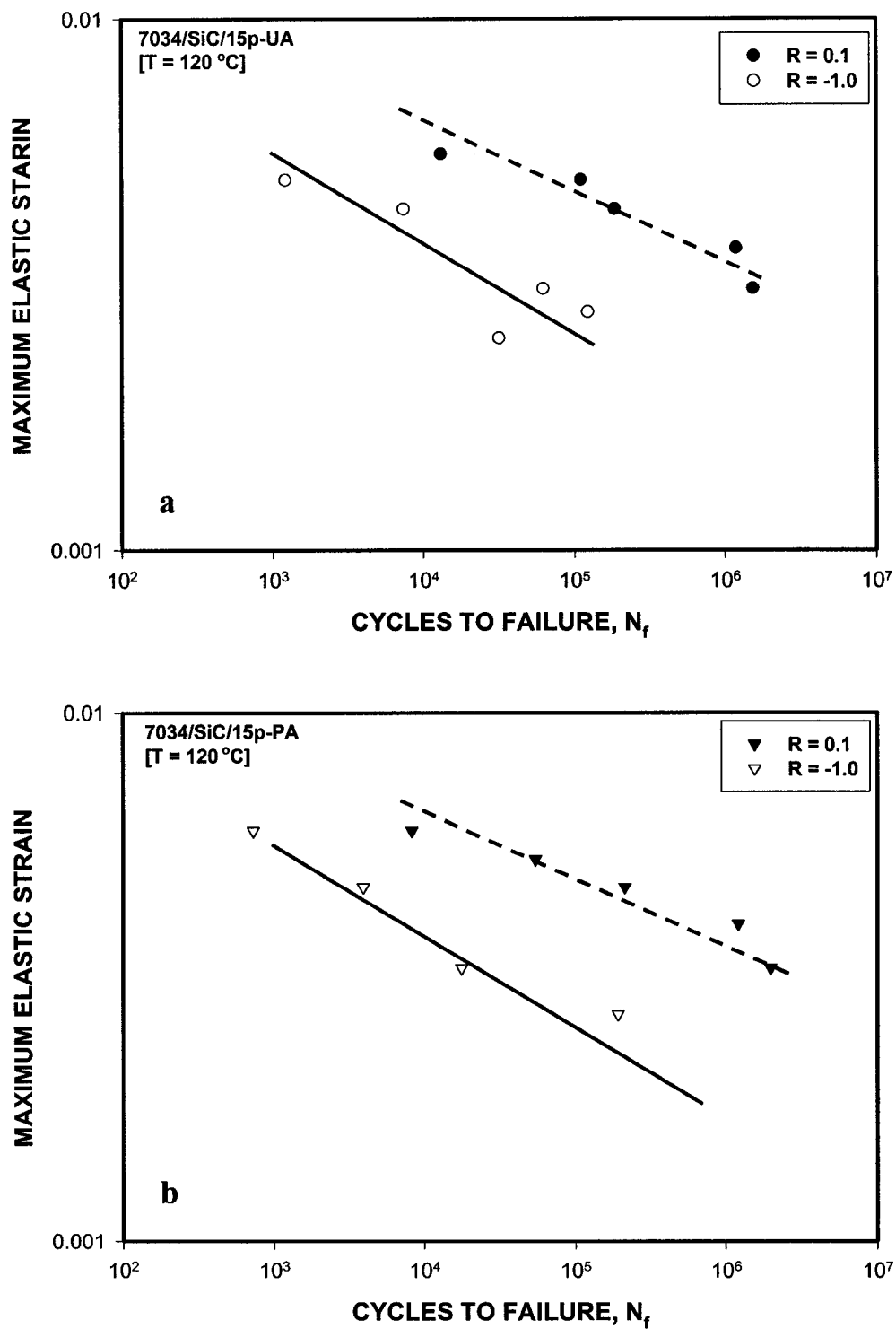
Figure 5.37: Variation of maximum elastic strain with cyclic
fatigue life for the 7034/SiC/15p composite at
load ratios of R = 0.1 and R = -1.0:
(a) under-aged (UA) and (b) peak-aged (PA).
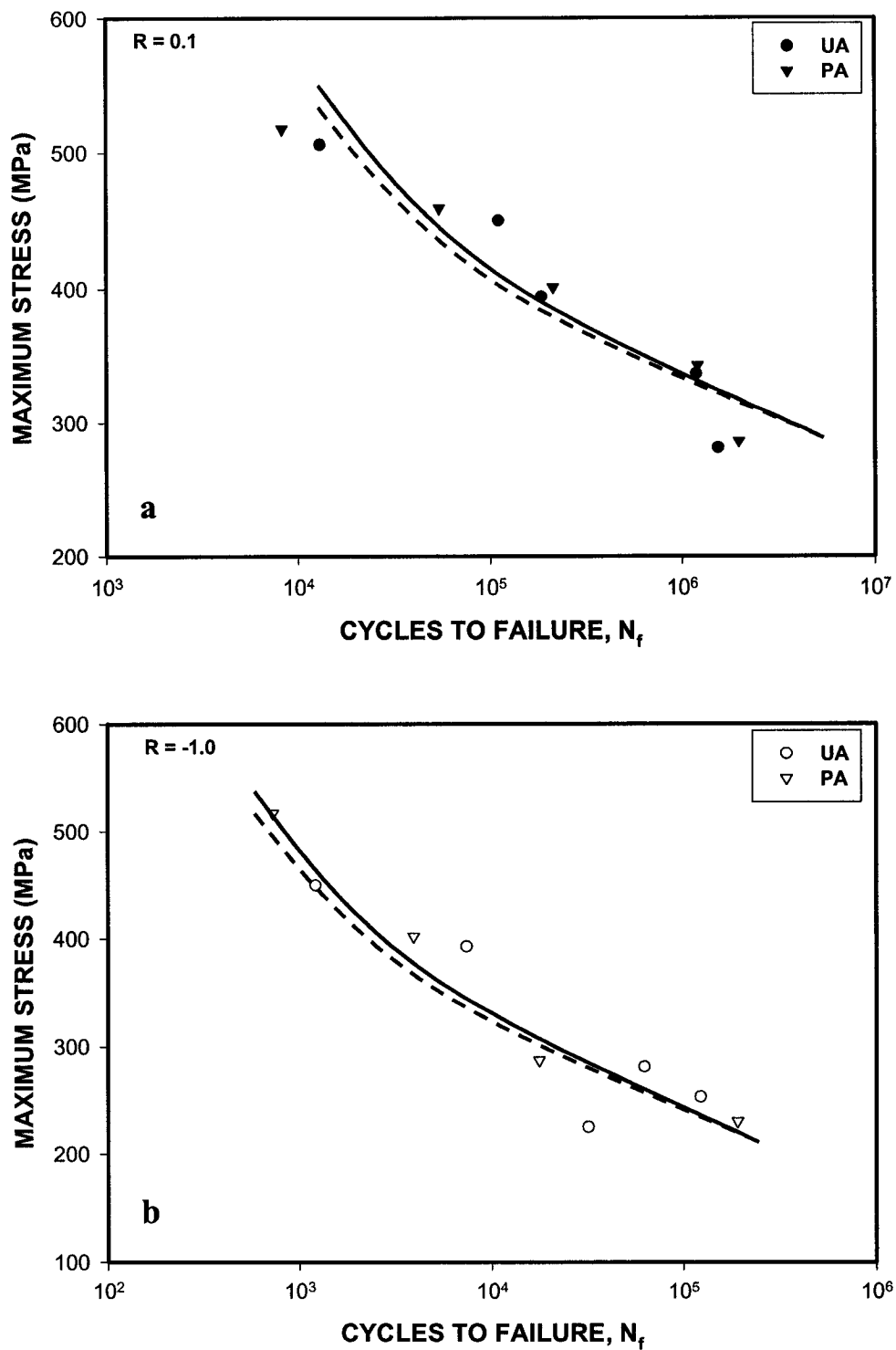
Figure 5.38: Influence of aging condition (UA versus PA) on high cycle fatigue response of 7034/SiC for: (a) R = 0.1 and (b) R = -1.0
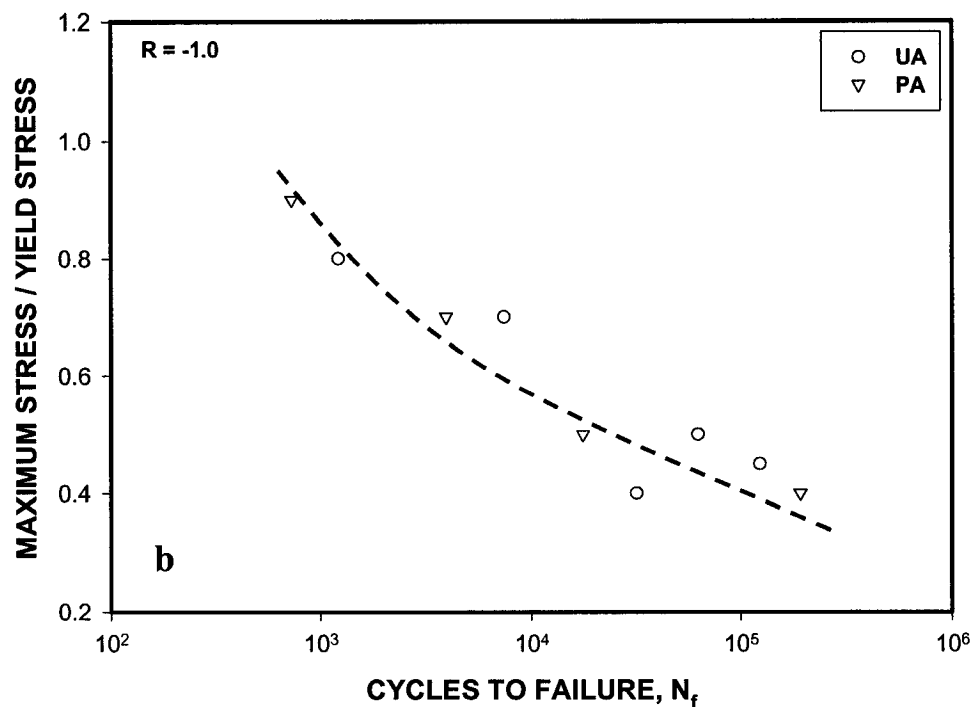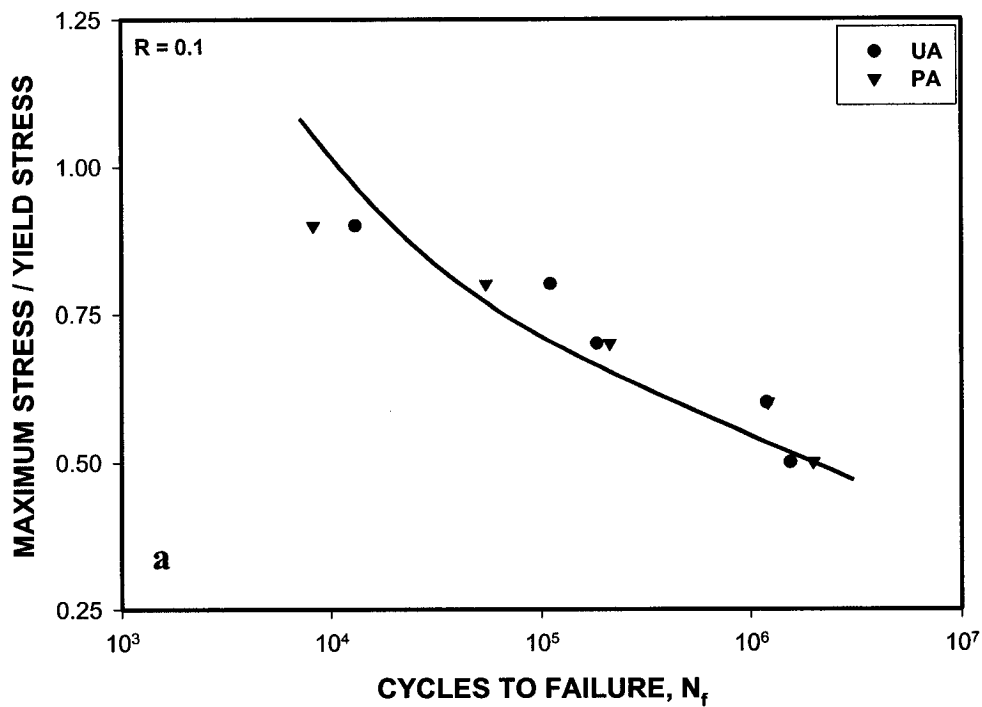
Figure 5.39: Variation of the ratio of maximum stress/yield
stress with fatigue life for:
(a) R = 0.1 and (b) R = -1.0.
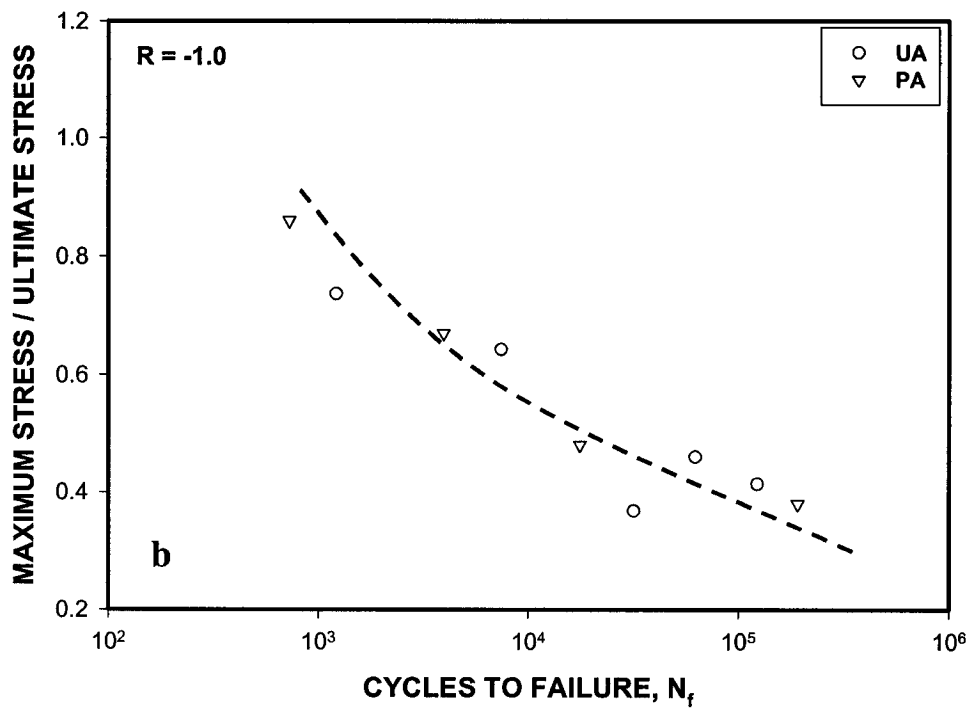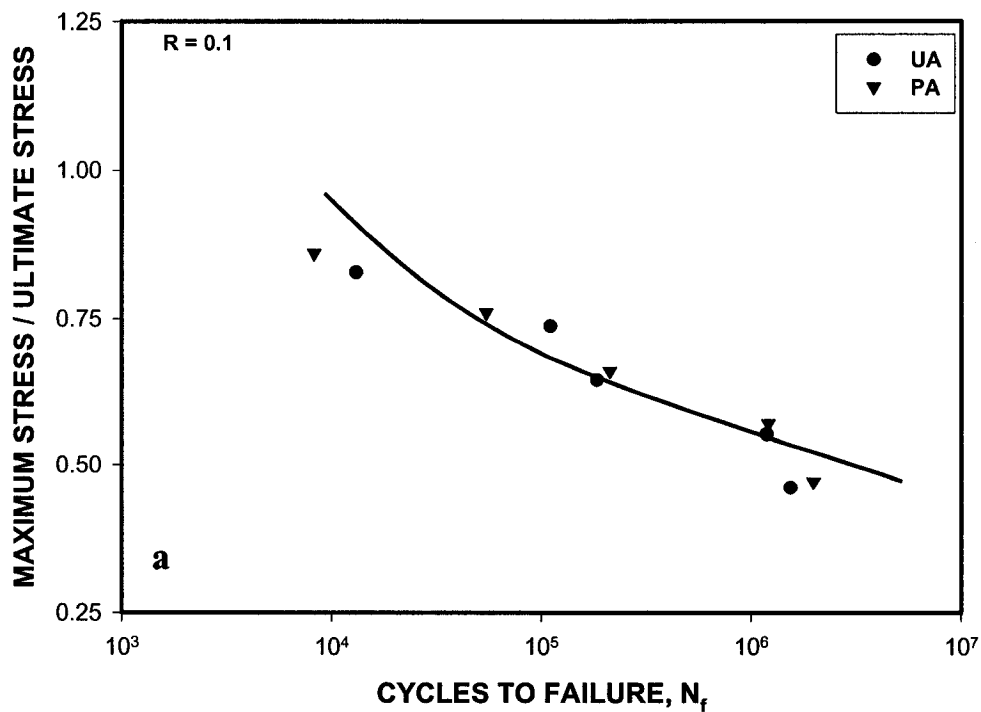
Figure 5.40: Variation of the ratio of maximum stress/ultimate strength with fatigue life for: (a) R = 0.1 and (b) R = -1.0.

5.2.3.1. <u>Cyclic Fatigue Fracture</u>

Examination of the fracture surfaces of the cyclically deformed fatigue specimens, in a JEOL scanning electron microscope, was done at: (a) low magnification to identify the regions of microscopic crack initiation, stable crack growth and final fracture (overload), and (b) at higher magnifications in the stable crack growth region to identify nature of damage initiation, nature of microscopic crack growth, and fine-scale fracture features in the overload region.

For a given aging condition and load ratio, the fatigue fracture surfaces of the 7034/SiC MMC revealed near similar topographies at the different values of maximum stress. However, on a microscopic scale, the nature and morphology of fatigue fracture features were found to vary with load ratio. Only representative fractographs of the fatigue fracture surfaces of the 7034/SiC/15p-UA and 7034/SiC/15p-PA composites, at the two load ratios, are shown in Figures 5.41-5.44 [116].

5.2.3.1.1 <u>Under-aged Condition</u>

At the higher load ratio ($R = \sigma_{min}/\sigma_{max} = 0.1$) and a maximum stress ($\sigma_{max}$) of 281 MPa, i.e., 50% of yield strength (σ_{ys}) of the composite, the macroscopic fracture

behavior was essentially normal to the far-field stress axis. Microscopic observations of the fatigue fracture surface revealed features reminiscent of brittle, i.e., (a) microscopic cracking in the matrix, and (b) particulate failure both by cracking and decohesion at matrix-particulate interfaces, and locally ductile (voids and dimples) mechanisms. The region of early microscopic crack growth comprised pockets of transgranular regions that were essentially featureless and an array of microscopic cracks (Figure 5.41a). The region of stable microscopic crack growth was rough and contained cracked SiC particles, ductile tear ridges (Figure 5.41b), randomly distributed microscopic voids (Figure 5.41c) and isolated pockets of very fine and shallow striations or ripples, evidence of localized micro-plastic deformation, covering the transgranular fracture regions (Figure 5.41d).

At the lower load ratio ($R = \sigma_{min.}/\sigma_{max} = -1.0$) and maximum stress of 253 MPa, the transgranular fracture regions were featureless. The region of transition from stable microscopic to rapid unstable microscopic crack growth and overload failure was distinctly evident (Figure 5.42a). Present in the region of early microscopic crack growth were (a) microscopic cracks (Figure 5.42b), (b)
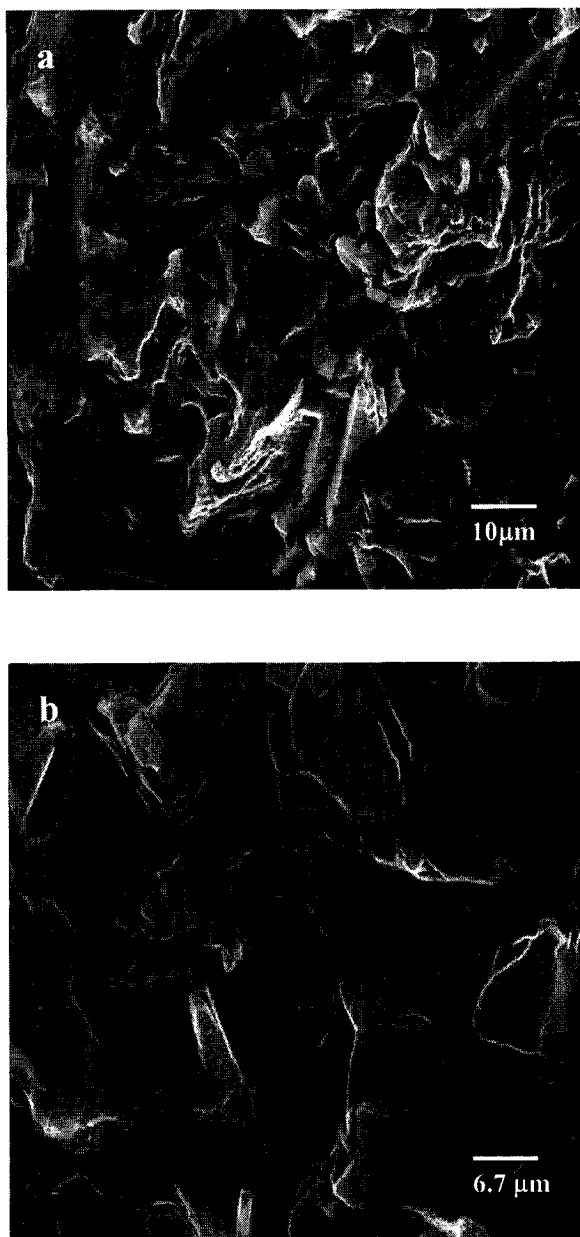
Figure 5.41: Scanning electron micrographs of the
7034/SiC/15p-UA composite; cyclically deformed
at 120 °C, at a load ratio of 0.10 and at max.
stress of 0.50 yield strength (max. stress =
281 MPa), showing: (a) overall morphology, (b)
cracked SiC particulates and tear ridges.
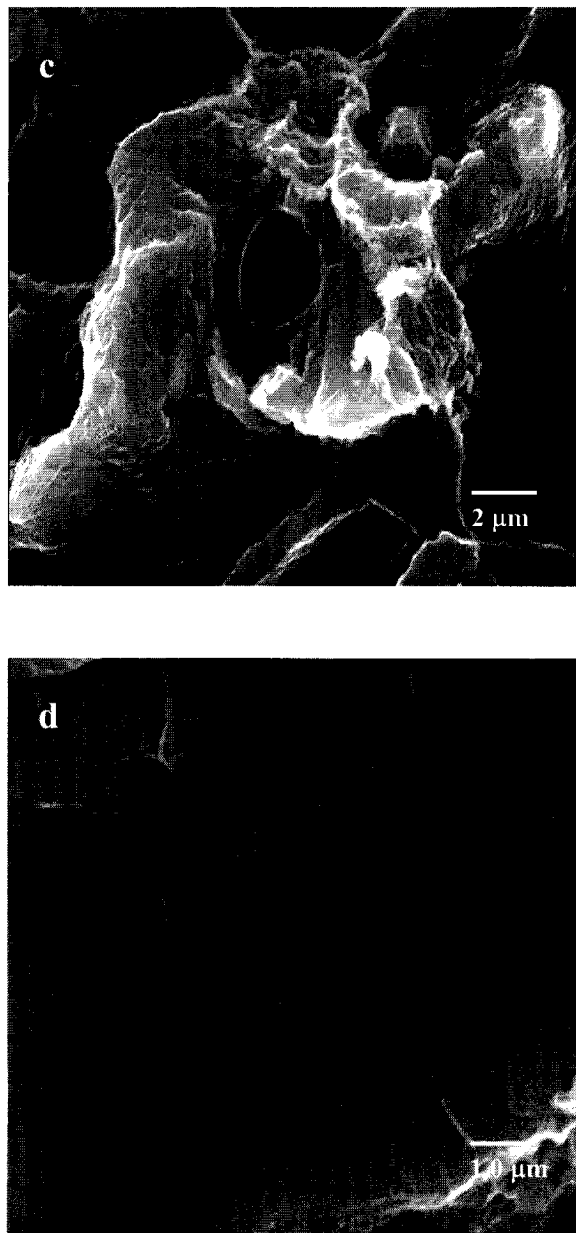
Figure 5.41 (Cont.): Scanning electron micrographs of the
7034/SiC/15p-UA composite; cyclically deformed at
120 °C, at a load ratio of 0.10 and at max. stress
of 0.50 yield strength (max. stress = 281 MPa),
showing: (c) microscopic voids, (d) fine shallow
striations on transgranular fracture surface in
the region of stable microscopic crack growth.
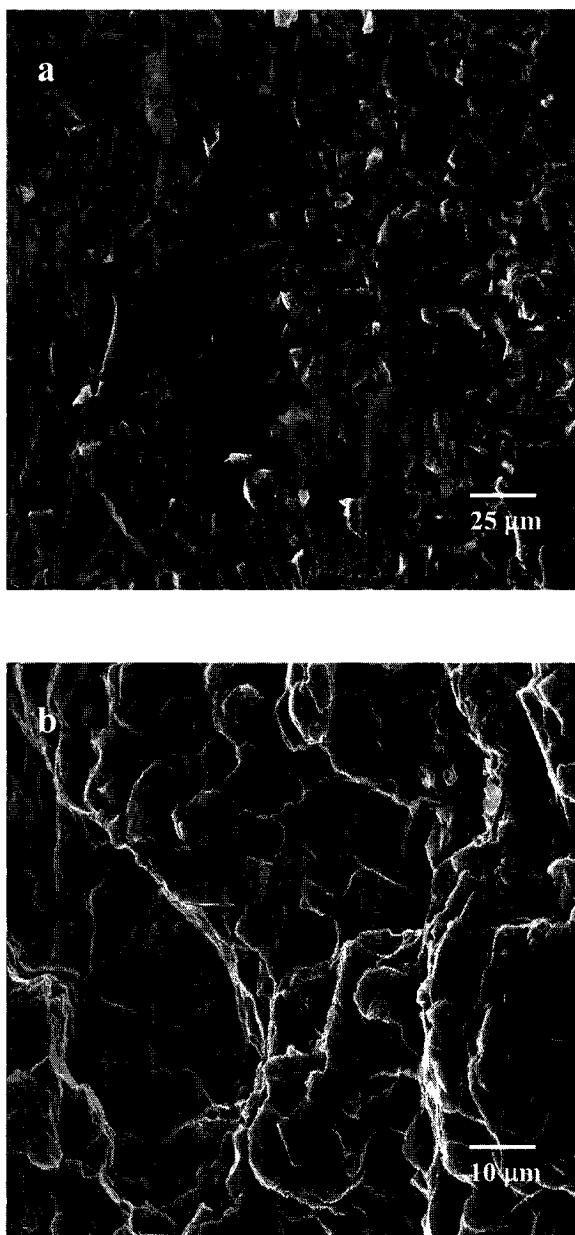
Figure 5.42: Scanning electron micrographs of the
7034/SiC/15p-UA composite; cyclically deformed
at 120 °C, at a load ratio of -1.0 and at max.
stress of 0.45 yield strength (max. stress =
253 MPa), showing: (a) region of early
microscopic crack growth, (b) ductile tear
ridges.

failure of the reinforcing SiC particulates both by cracking and separation at the matrix-reinforcement (particulate) interfaces, and (c) ductile tear ridges surrounded by pockets of shallow dimples (Figure 5.42c). Very fine and shallow striations were found covering the transgranular fracture surfaces in the region of early microscopic crack growth (Figure 5.42d) [116].

5.2.3.1.2 Peak-aged Condition

Macroscopic or low magnification observations of this composite material revealed microscopic fracture to be essentially similar at both high and low load ratios. At the load ratio of 0.1 the microscopic fracture surfaces of the sample, deformed at a maximum stress of 287 MPa, (50% of yield strength) were rough and covered with pockets of transgranular facet-like features (Figure 5.43a). The region of stable microscopic crack growth was small. Other features observed on the fracture surface were (a) failure of the reinforcing SiC_p through cracking, and presence of ductile tear ridges (Figure 5.43b), and (b) ensuing growth of the microscopic cracks through the microstructure (Figure 5.43c). At higher magnifications the transgranular fracture regions revealed pockets of fine striation-like features (Figure 5.43d) reminiscent of localized micro-plastic
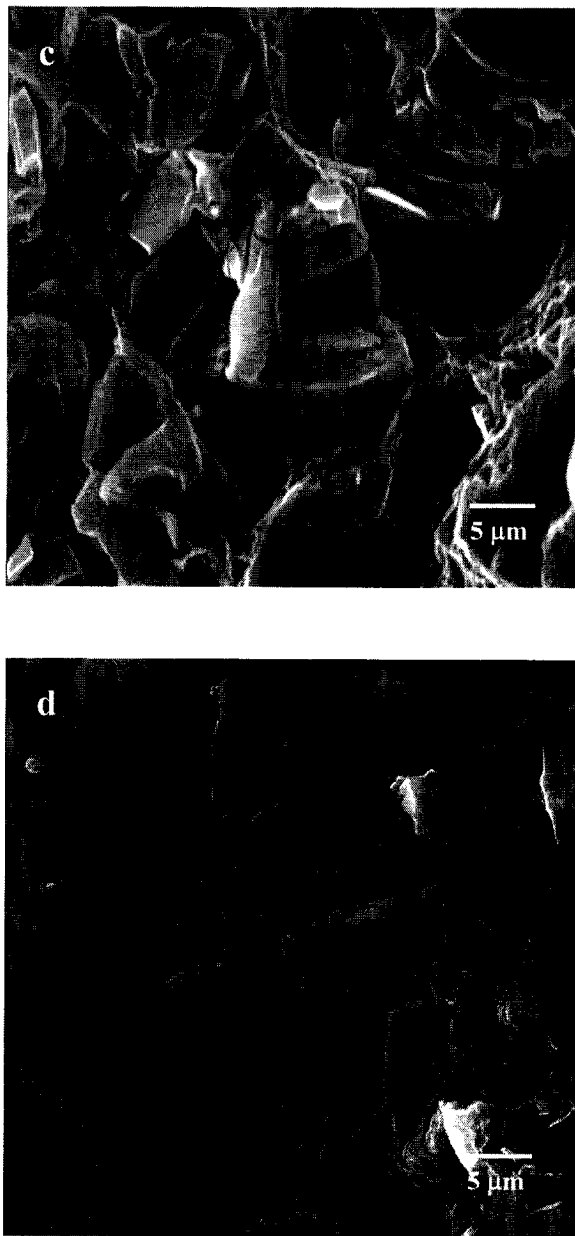
Figure 5.42 (cont.): Scanning electron micrographs of the
7034/SiC/15p-UA composite; cyclically deformed at
120 °C, at a load ratio of -1.0 and at max. stress
of 0.45 yield strength (max. stress = 253 MPa),
showing: (c) cracked SiC particulates and
failure at interfaces, (d) fine striations on the
transgranular fracture surface in the region of
stable crack growth.
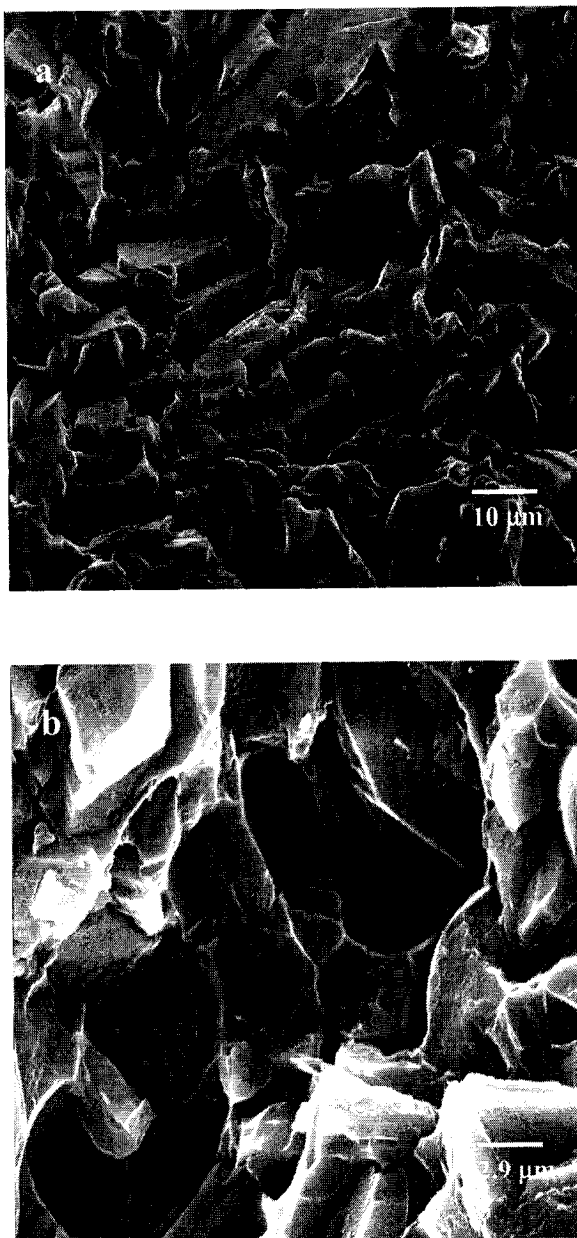
Figure 5.43: Scanning electron micrographs of the 7034/SiC/15p-PA composite; cyclically deformed at 120 °C, at a load ratio of 0.10 and at max. stress of 0.50 yield strength (max. stress = 287 MPa), showing: (a) transgranular fracture region: faceted, (b) cracking of the reinforcing SiC particulates.
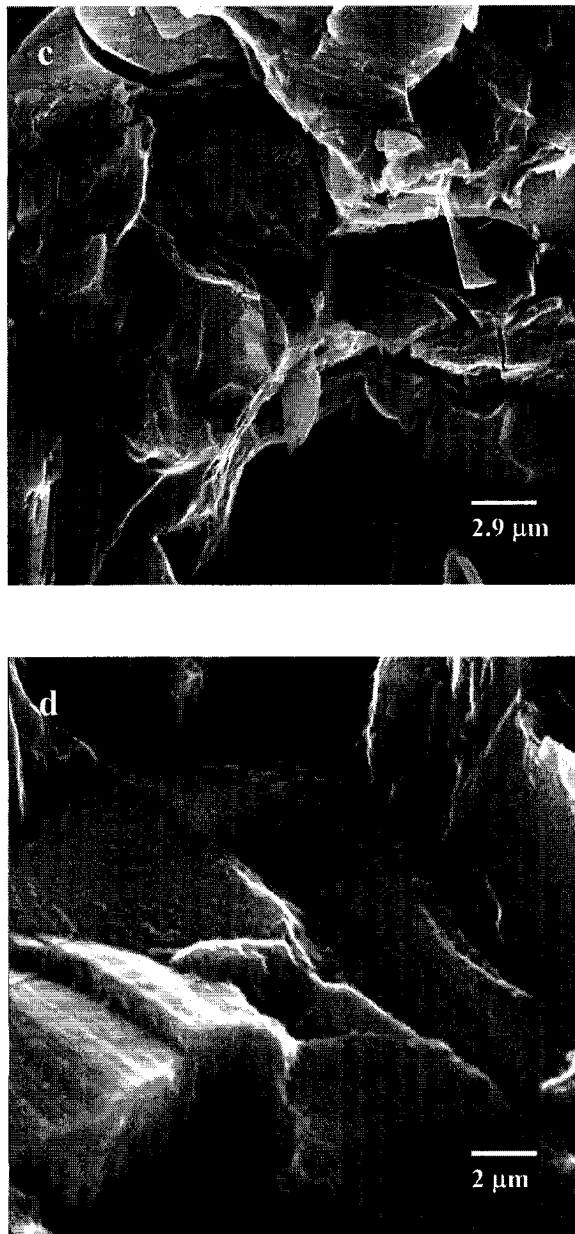
Figure 5.43 (cont.): Scanning electron micrographs of the
7034/SiC/15p-PA composite; cyclically deformed at
120 °C, at a load ratio of 0.10 and at max. stress
of 0.50 yield strength (max. stress = 287 MPa),
showing: (c) microscopic crack propagation
through the microstructure, (d) fine striations on
the transgranular fracture surface.

deformation and thus stable microscopic crack growth through the composite microstructure.

High magnification observations of a composite specimen cyclically deformed at maximum stress of 230 MPa, in fully-reversed loading ($R = -1.0$), and resultant degraded cyclic fatigue life, revealed (a) an overall rough fracture surface comprising distinct regions of microscopic crack growth and overload (Figure 5.44a), (b) evidence of localized brittle failure through failure of a large number of the reinforcing SiCp both by cracking and decohesion at its interfaces with the aluminum alloy metal matrix (Figure 5.44b), (c) isolated pockets of striation-like features (Figure 5.44c) reminiscent of stable microscopic crack growth, and (d) traces of brittle failure through failure of the reinforcing SiC particulates (Figure 5.44d) [116].

5.2.3.2. Mechanisms Governing Cyclic Fracture

A large mismatch in strain carrying capability exists between the hard, intrinsically brittle and elastically deforming reinforcing SiCp and the soft, ductile and plastically deforming aluminum alloy metal matrix. This results in a concentration of stress near the reinforcing SiC_p thus providing conditions conducive for them to crack
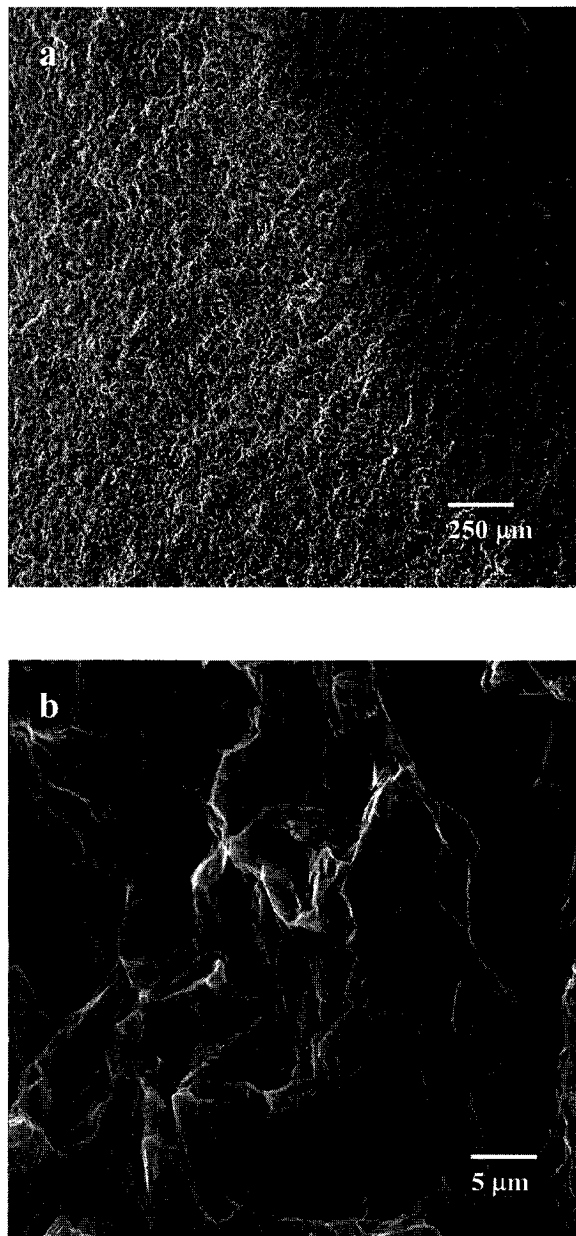
Figure 5.44: Scanning electron micrographs of the
7034/SiC/15p-PA composite; cyclically deformed
at 120 °C, at a load ratio of -1.0 and at max.
stress of 0.40 yield strength (max. stress =
230 MPa), showing: (a) overall morphology
showing two distinct regions on the
transgranular fracture surface, (b) shallow
dimples and ductile tear ridges.
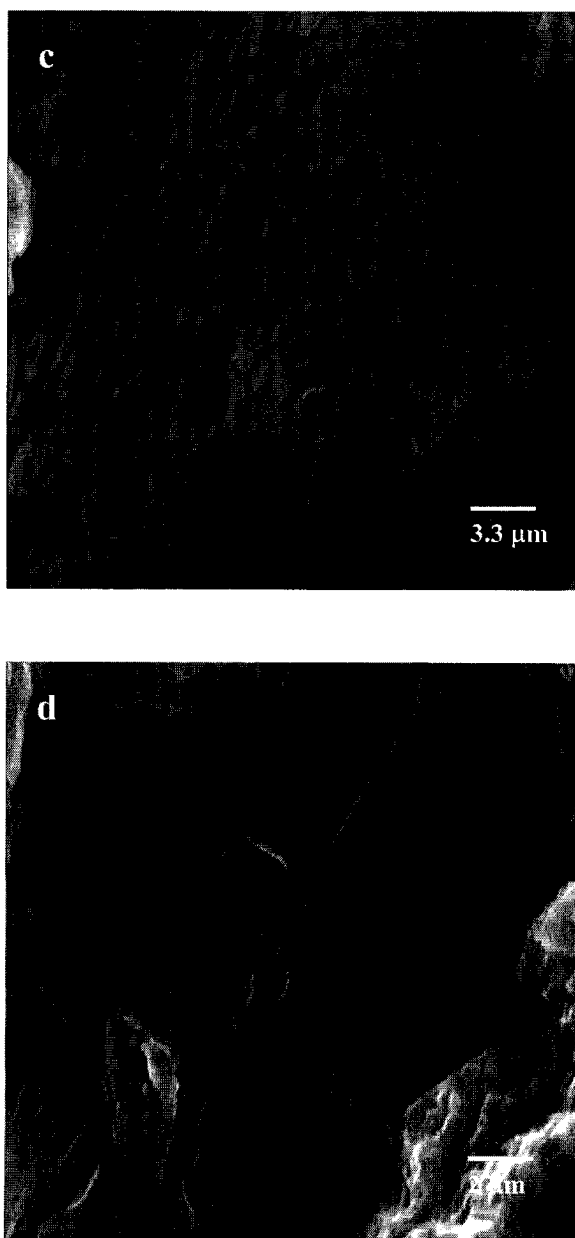
Figure 5.44 (cont.): Scanning electron micrographs of the
7034/SiC/15p-PA composite; cyclically deformed at
120 °C, at a load ratio of -1.0 and at max. stress
of 0.40 yield strength (max. stress = 230 MPa),
showing: (c) shallow striations ripple like
features on transgnular surface, (d) cracking of
the reinforcing SiC particulates.

and the adjacent matrix to fail by separation or decohesion. Failure through the conjoint influence of: (a) separation at the aluminum alloy matrix-reinforcing SiC particulate interfaces, referred to in this manuscript as decohesion, and (b) cracking of the reinforcing SiC_p suggests the exacerbation of micro-plastic deformation in regions containing a high concentration or agglomeration of the reinforcing SiC particulates [82]. Concurrent failure of the reinforcing SiCp and other coarse second-phase particles (i.e., the constituent particles) in the composite microstructure is governed by the competing influences of: (1) local plastic constraints, (2) particle size, and (3) degree of agglomeration, all other factors being held constant. The local plastic constraints are particularly important for the larger-sized particles and particle clusters during composite fracture [117,118]. An observation of the cyclic fatigue fracture surfaces of the two composites revealed that in excess of 25-30 percent of the reinforcing SiC_p had fractured during cyclic deformation. This indicates that not all of the reinforcing SiC_p were loaded to their fracture stress providing direct evidence for the non-uniform distribution of SiC particulates in the 7034 aluminum alloy metal-matrix, and (b) their orientation

with respect to the far-field stress axis. This situation is exacerbated by the mismatch strain and concomitant high compression stresses in the composite microstructure due to differences in the thermal expansion coefficient between constituents of the composite, the SiC particulates and the 7034 aluminum alloy matrix [1,14,116].

Microscopic cracks were found both ahead of and near the crack tip that was associated with regions of intense deformation. Crack propagation occurred by a process whereby coalescence of the fine microscopic cracks occurred through matrix failure ahead of the main crack tip [116,119,120]. Concurrently, the formation of additional microscopic cracks occurred ahead of the main crack tip. There was no evidence of crack branching suggesting that the damaged region ahead of the crack tip to be greatly reduced. Such reduction in the damage region suggests that the reinforcing SiC particles are loaded by shear forces caused by deformation of the matrix. Final fracture is achieved by fast fracture through the matrix between particulate clusters [116].

The microscopic voids ranged in size from the sub-micron scale to the tens of microns. The fine microscopic voids were associated with failure of the ductile metal matrix between the reinforcing particulates, whereas the

macroscopic voids were associated with the reinforcing SiC$_p$. The sources of macroscopic voids and resultant shallow dimples on the fracture surface are the critical events controlling fracture and decohesion of the reinforcing SiC particulates. The constraints induced by the presence of hard and brittle carbide (SiC) particulate reinforcements in the soft and ductile 7034 aluminum alloy metal-matrix and the resultant development of matrix triaxiality: (a) influences cyclic stress response of the composite during fully-reversed stressing [121-123], and (b) favors limited void growth. Failure of the reinforcing SiC particulates both by decohesion and cracking was evident on the fatigue fracture surfaces. This suggests the important role played by local plastic strains in governing damage initiation and propagation in this 7034/SiC/15p composite microstructure (UA and PA) [116].

5.2.4 Cyclic-Strain Controlled

The objective of this section is to document the influence of carbide particle reinforcement, aging conditions and test temperature on cyclic plastic strain response and final fracture (cyclic) behavior of MMCs based on aluminum alloy 7034 as the metal matrix.

5.2.4.1 <u>Cyclic Strain Resistance</u>

The effect of strain cycling on cyclic plastic strain response of this composite, for both the under-aged and peak-aged microstructural conditions, is shown in Figure 5.45. The variation of cyclic strain amplitude $(\Delta\varepsilon/2)$ with reversals-to-fatigue failure $(2N_f)$ can be viewed as an indication of the resistance of the composite microstructure to cyclic plastic deformation, stable crack growth and failure. Throughout fully reversed total strain amplitude $(\Delta\varepsilon_T/2)$-controlled testing no evidence of specimen buckling was observed to occur. For both aging conditions (UA and PA) it is observed that a significant portion of the total strain amplitude $(\Delta\varepsilon_T/2)$ is elastic strain amplitude $(\Delta\varepsilon_e/2)$. The variation of plastic strain amplitude $(\Delta\varepsilon_p/2)$ with reversals to fatigue life is linear and the Coffm-Manson relationship can be used to determine the fatigue behavior in the low- cycle fatigue regime (Nf < 10^4 cycles). The value of LCF parameters that satisfy the Basquin and Coffin-Manson relationships are summarized in Table 5.3. The fatigue-ductility exponent is around 0.15 for both microstructures. The fatigue-ductility coefficient (ε'_f) is 0.22% for the under-aged microstructure and 0.18%
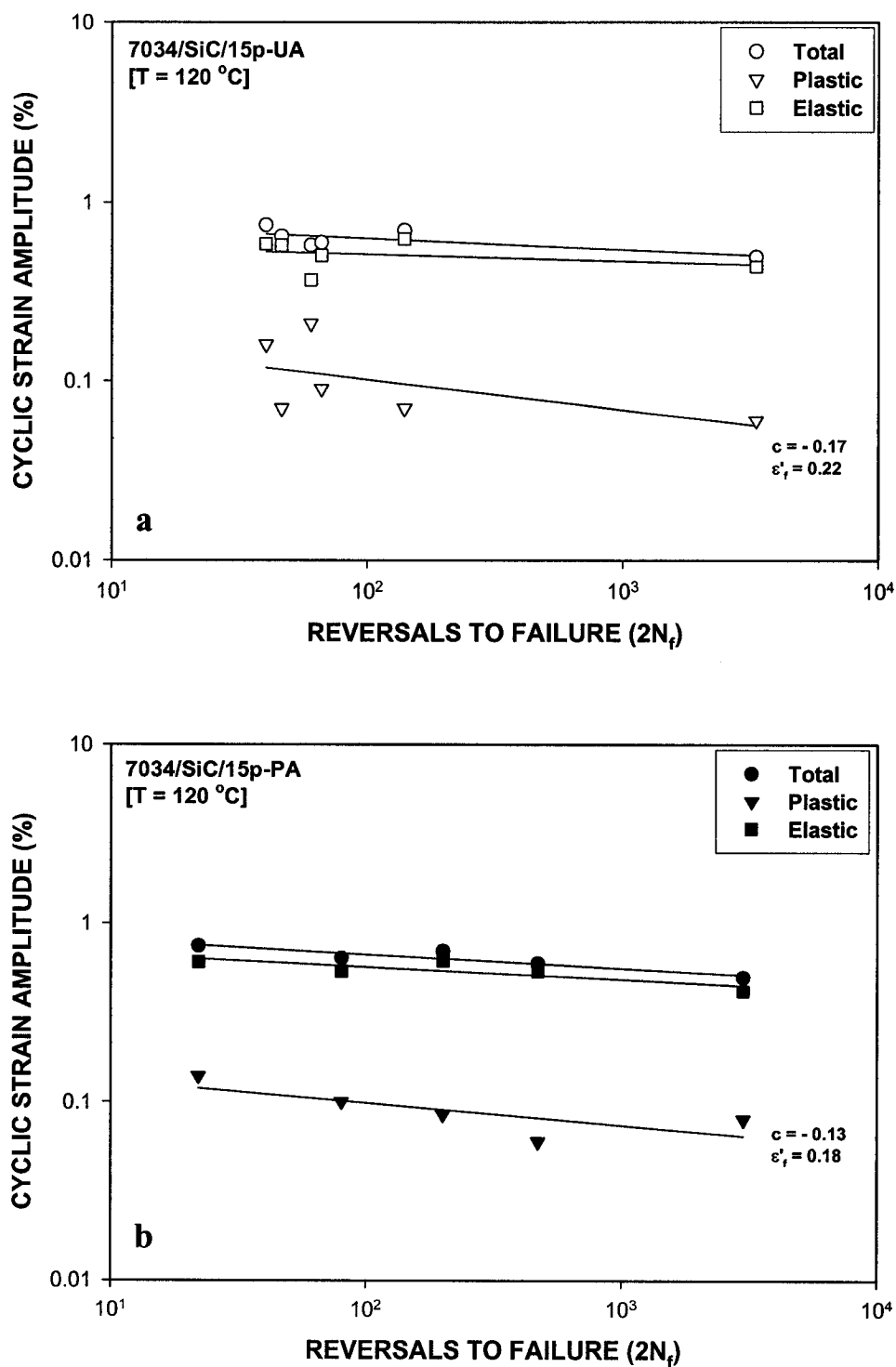
Figure 5.45: Cyclic strain amplitude-fatigue life response of
the 7034/SiC/15p composite at 120 °C:
(a) Under-aged, and (b) Peak-aged.

Table 5.3: Cyclic parameters of the 7034/SiC/15p material
at elevated temperature (120 °C).

Condition	Test Temperature (°C)	n	K		n`	K`		$\epsilon_f`$ (%)	C
			MPa	(Ksi)		MPa	(Ksi)		
PA	120	0.05	619	(90)	0.16	698	(101)	0.18	-0.13
UA	120	0.07	626	(91)	0.13	649	(94)	0.22	-0.17

n   : Monotonic Strain Hardening Exponent.
n`   : Cyclic Strain Hardening Exponent.
K   : Monotonic Strength Coefficient.
K`   : Cyclic Strength Coefficient.
ϵ'_f : Fatigue Ductility Coefficient.
C   : Fatigue Ductility Exponent.

for the peak-aged counterpart and does not accord well with the monotonic fracture ductility (ε_f).

A comparison of the influence of aging condition on cyclic strain-fatigue life response is shown in Figure 5.46. At equivalent plastic stain amplitudes little to no difference in cyclic plastic strain response of the two composites was evident. The plausible mechanisms and micro-mechanisms responsible for the minimal to no influence on cyclic strain resistance and LCF life of the two microstructural conditions are discussed in the following sections on cyclic stress response and fracture behavior. Under total strain amplitude-controlled conditions, the elastic strains in the composite matrix are much lower than they would be in the unreinforced metal matrix. This is because of the higher elastic modulus of the composite material. Thus, for a given total strain amplitude ($\Delta\varepsilon_T/2$), the average plastic strain, at the microscopic level, is significantly elevated in the composite microstructure than the unreinforced aluminum alloy metal matrix. The highly "localized" cyclic plastic strain dominates the development of fatigue damage resulting in a positive contribution to the overall inferior cyclic strain resistance of this aluminum alloy composite (7034/SiC/15p).
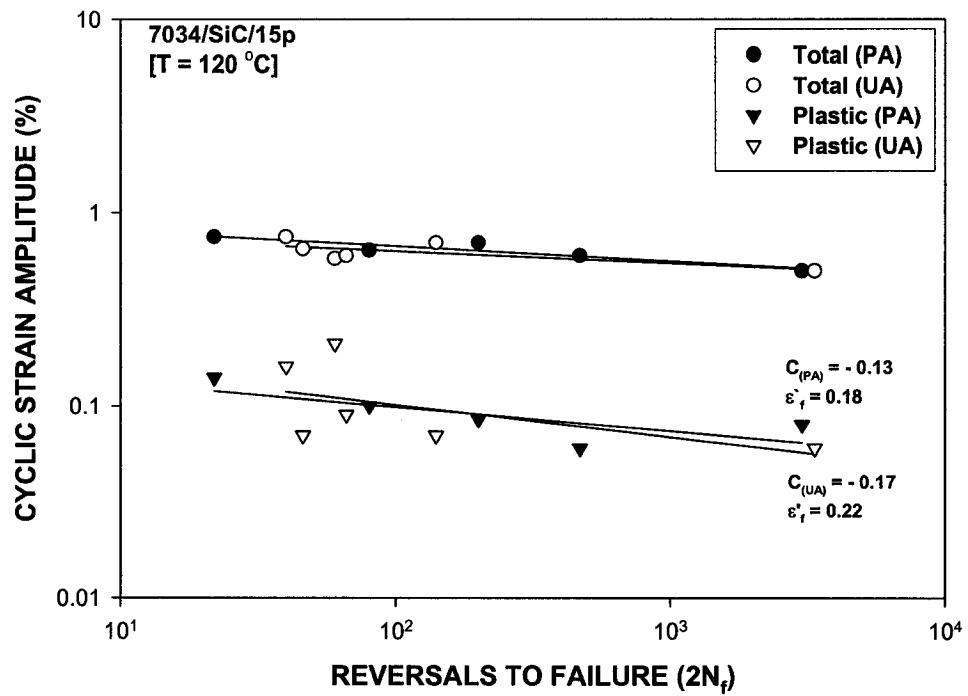
Figure 5.46: Comparison of the influence of aging condition on plastic strain-fatigue life response of the 7034/SiC/15p composites at 120 °C.

5.2.4.2 <u>Cyclic Stress Response</u>

An important feature of the low-cycle fatigue process is the variation of stress response with fully reversed strain cycling. A stress response curve, which was determined by monitoring the cyclic stress range during fully reversed total strain amplitude-controlled fatigue, provides useful information pertaining to the cyclic and overall mechanical stability of the material. Mechanical stability of the intrinsic microstructural features during fully-reversed ($R_\varepsilon/2 = -1$) cyclic straining coupled with an intrinsic ability of the 7034/SiC/15p composite microstructure to effectively distribute the plastic strain over the entire microstructural volume, are factors controlling cyclic stress response, resulting strain resistance, and overall stability of the MMC material [125-128,133]. The cyclic stress response curves, or cumulative glide plots, showing variation of cyclic stress-amplitude ($\Delta\sigma/2$) with the number of cycles (N), at fixed total strain-amplitudes ($\Delta\varepsilon_T/2$), illustrates the path taken by the material to its final level of stress during fully-reversed total strain-amplitude controlled deformation.

5.2.4.2.1 <u>Under-aged Condition</u>

The stress response curves for this composite, over a range of total strain amplitudes, are shown in Figure 5.47. Since cyclic plastic strain amplitude varied throughout testing, attaining a maximum value at the minimum stress and a minimum value at the maximum stress, the value at specimen half-life (N_f) was taken as the reference. At all cyclic strain amplitudes this composite showed evidence of initial hardening followed by stability for a fraction of fatigue life and terminating in gradual softening to failure. The rapid decrease in stress carrying capability for most of fatigue life is attributed to the formation and presence of a number of microscopic cracks, their progressive growth through the composite microstructure and eventual coalescence to form one or more macroscopic cracks. The softening effect is exacerbated by concurrent growth of the macroscopic and fine microscopic cracks through the composite matrix [133].

The degree of initial cyclic hardening was greater at the higher cyclic strain amplitudes and resultant short low-cycle fatigue life than at the intermediate and lower cyclic strain amplitudes and resultant enhanced fatigue life. The variation of normalized stress (σ_N/σ_1) with
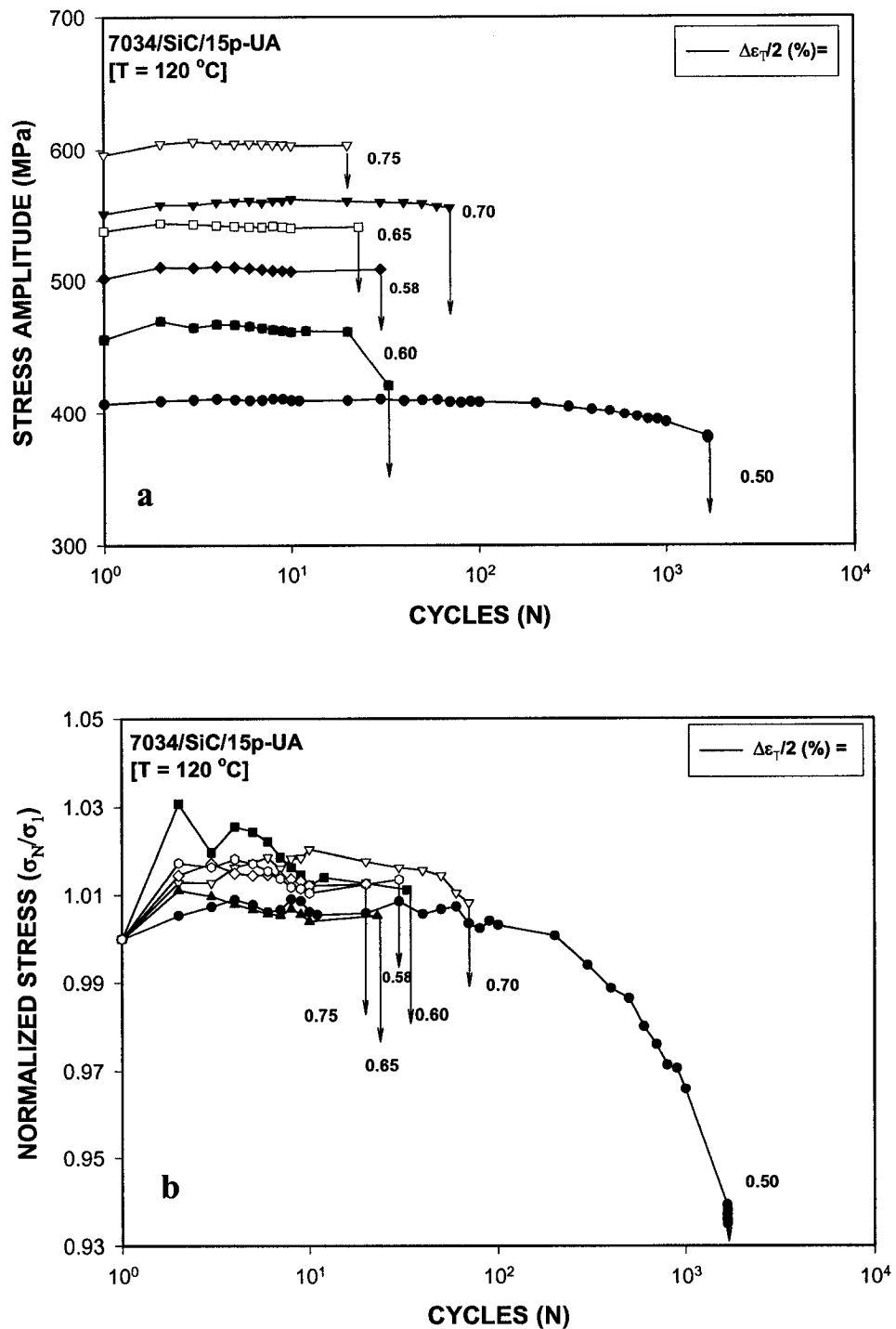
Figure 5.47: Cyclic stress response curves for the 7034/SiC/15p-UA composite at 120 °C, showing: (a) Variation of stress amplitude with cycles, and (b) variation of normalized stress with cycles.

fatigue cycles (N), where the stress amplitude at any cycle (σ_N) is normalized with respect to the cyclic stress amplitude of the first cycle (σ_1) shown in Figure 5.47b, confirms the observation of increased cyclic hardening at the higher cyclic strain amplitudes for this under-aged composite microstructure. It seems plausible that at the elevated test temperature there occurs intrinsic changes in microstructure with resultant changes in dislocation kinetics, that is: (i) dislocation-dislocation interactions, and (ii) dislocation-microstructural feature interactions, and thus contributions to softening. The loss in strength, or softening, with fully reversed cyclic straining arises from the mutually interactive influences of: (a) intrinsic microstructural changes, and (b) microscopic and macroscopic cracking. For most of low-cycle fatigue life, at both high cyclic strain and low cyclic strain amplitudes, the stress response comprised the tensile stress component being higher than the compressive stress component of a fatigue cycle (Figure 5.48a) [133].

5.2.4.2.2 Peak-aged Condition

The stress response curves at the two temperatures are shown in Figure 5.49. At all cyclic strain amplitudes ($\Delta\varepsilon_T/2$) this composite showed evidence of initial hardening
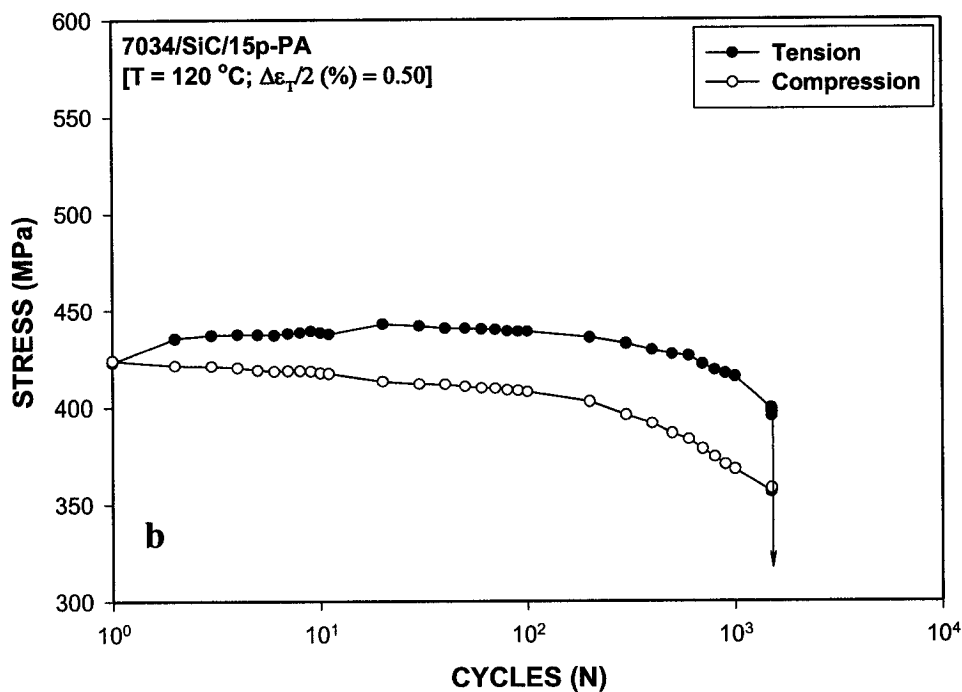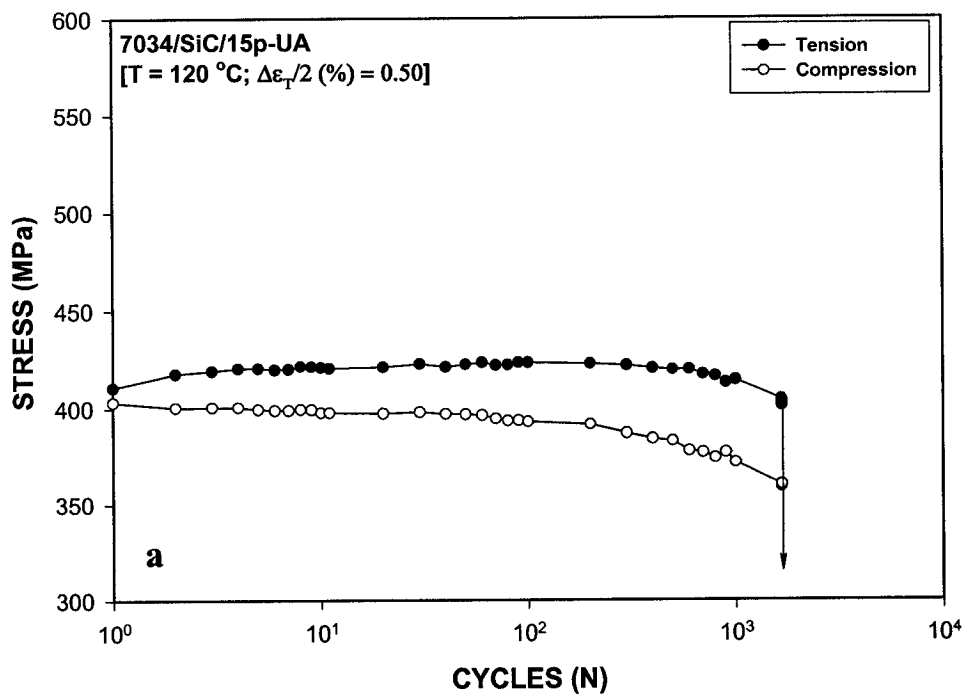
Figure 5.48: Stress response curves showing variation of tensile stress and compressive stress with fatigue cycles at 120 °C: (a) Under-aged condition, and (b) Peak-aged condition.
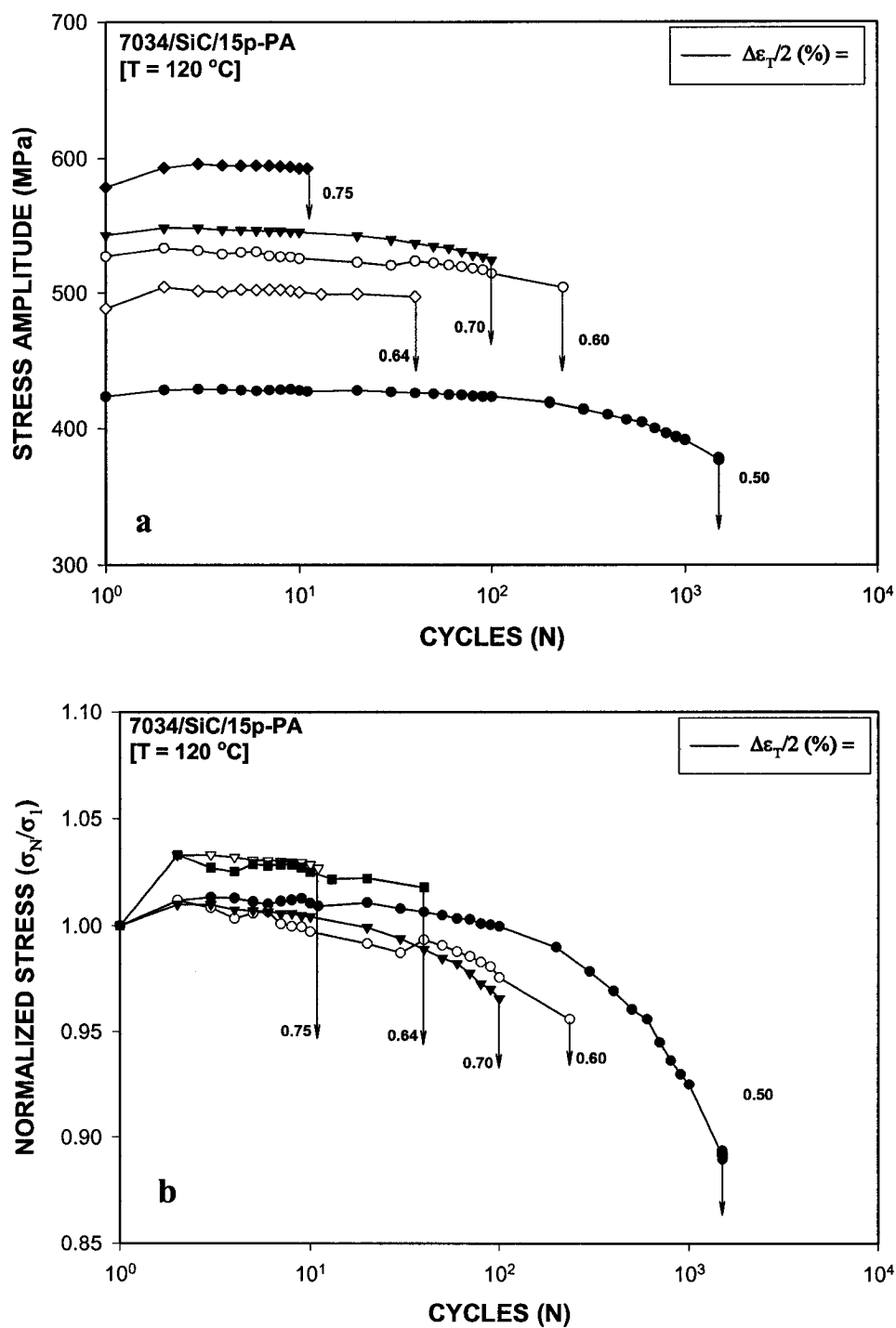
Figure 5.49: Cyclic stress response curves for the
7034/SiC/15p -PA composite at 120 °C, showing:
(a) Variation of stress amplitude with cycles, and
(b) variation of normalized stress with cycles.

during the first few cycles, followed by stability or saturation for the next 20-40% of life and culminating in gradual softening to failure (Figure 5.49b). The rapid softening observed immediately prior to failure is ascribed to the following:

(a) The formation and presence of multiple microscopic cracks.

(b) The growth of the microscopic cracks, through the composite matrix and eventual coalescence to form one or more macroscopic cracks.

(c) Ensuing unstable growth of both the macroscopic and fine microscopic cracks through the composite matrix.

For most of cyclic fatigue life, at high, intermediate and low cyclic strain amplitudes, the stress response comprised the tensile stress component to be higher than the compressive stress component (Figure 5.49b) [133].

5.2.4.3 Mechanisms Governing Cyclic Stress Response

At a given test temperature the intrinsic micro mechanisms controlling the variation of cyclic stress amplitude with fatigue cycling are dependent on the conjoint and mutually competitive influences of microstructure and cyclic strain range. The plausible micro

mechanisms controlling the initial hardening behavior can be ascribed to the competing and synergistic influences of the following:

- Load (stress) transfer between the plastically deforming aluminum alloy metal matrix and the hard, brittle and essentially elastically deforming carbide particle (SiC_p) reinforcement phase [129,130,133].

- A pre-existing high dislocation density in the aluminum alloy metal matrix caused by the presence of the hard and brittle ceramic particle (SiC) reinforcement phase [93,131,133].

- Hardening arising from constrained plastic flow and triaxiality in the plastically deforming aluminum alloy matrix due to the presence of brittle SiC_p reinforcements [94]. As a direct result of the elastically deforming particles resisting plastic flow of the matrix, an average internal stress or back stress (σ_p) is created.

- Residual stresses generated in the matrix and plastic strains introduced near the reinforcing particulates due to mismatch in thermal expansion coefficients (*CTE*) between constituents of the composite; the soft aluminum alloy metal matrix and the hard ceramic,

reinforcement phase [15,132]. For particulate

reinforcements the residual stress in the matrix is

assumed to be pure hydrostatic tension.

The interface-generated dislocations resulting from any one

or a combination of these mechanisms are distributed at

random through the matrix of the 7034-aluminum alloy/SiC$_p$

composite. Hardening or strengthening, during fully

reversed strain cycling, results from the conjoint action

of these plausible mechanisms [133]:

- An increase in the dislocation density already present

  in the composite microstructure.

- Dislocation multiplication.

- An increase in the mutual interaction of a dislocation

  with other dislocations Figure 5.50.

- An interaction of the mobile dislocations with the

  reinforcing particulates (SiC) coupled with an initial

  interaction of the dislocations with other second-

  phase constituents in the microstructure Figure 5.51.

The dislocation-dislocation interactions coupled with an

interaction of the mobile dislocations with the reinforcing

SiC particulates, distributed randomly in the aluminum

alloy metal matrix, dominates during the initial few cycles

of fully-reversed cyclic straining. Thus, the mechanisms,
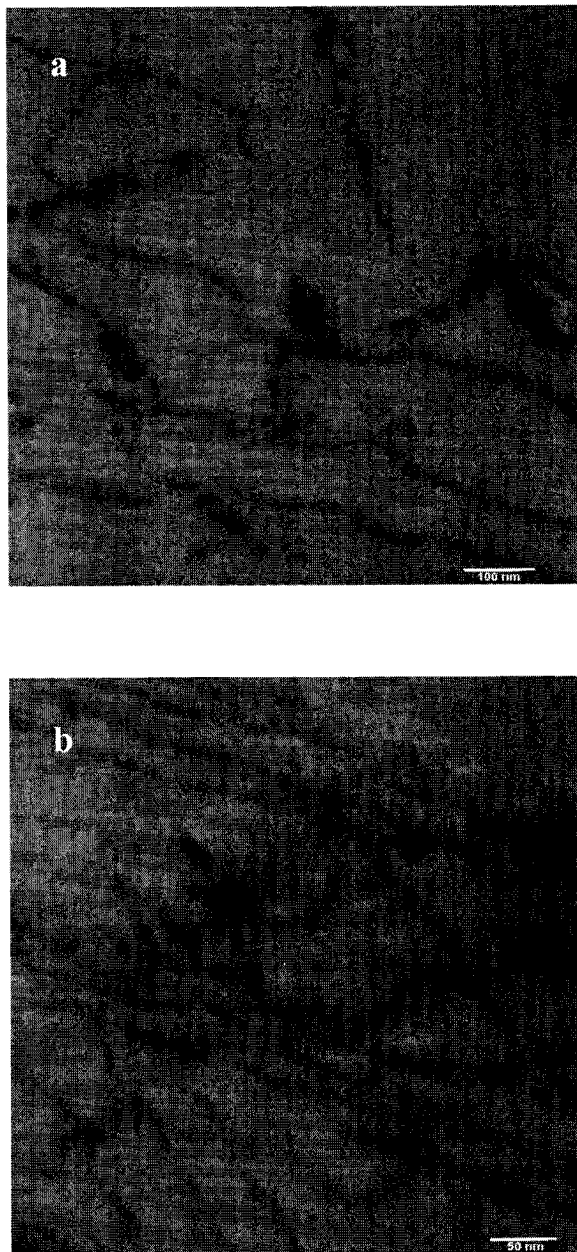
Figure 5.50:   Bright field transmission micrographs of the
cyclically deformed at 120 °C, and at total
strain amplitude of 0.5% for the
7034/SiC/15p composite showing: An
interaction of dislocations with other
second-phase constituents in the grain
interior for (a) Under-aged condition and
(b) Peak-aged condition.
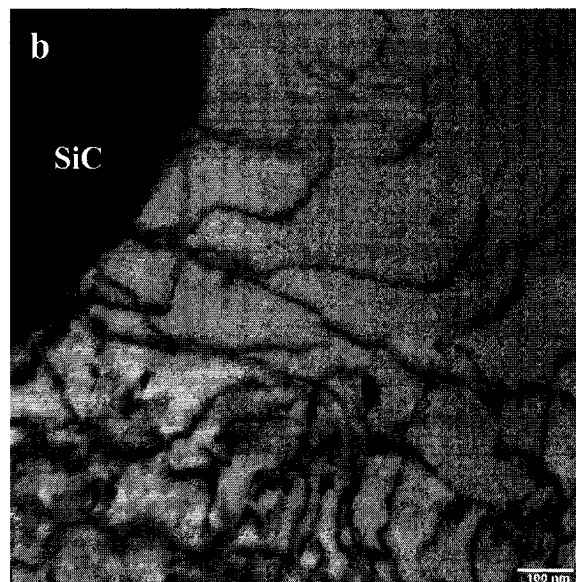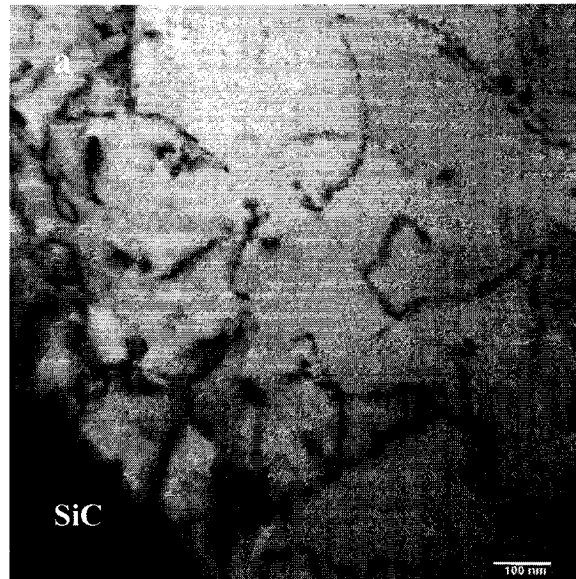
Figure 5.51:   Bright field transmission micrographs of the
                cyclically deformed at 120 °C, and at total
                strain amplitude of 0.5% for the
                7034/SiC/15p composite showing: An
                interaction of the mobile dislocations with
                the reinforcing particulates (SiC) for (a)
                Under-aged condition and (b) Peak-aged
                condition.

which are responsible for microscopic hardening, dominate. Once the stress response has reached the peak during initial hardening there occurs a dislocation configuration, which tries to change upon further cyclic straining. The onset of this dislocation rearrangement process provides an appealing rational for the initiation of softening. The softening effect due to the concurrent and mutually interactive influences of microstructural degradation and unstable crack propagation is dominant prior to failure [133].

Another plausible explanation for the softening is based on the formation of slip bands Figure 5.52. At a given cyclic strain amplitude, the amount of slip band formation reaches a saturation at the peak of initial cyclic hardening. From this point onward, no new slip bands appear on the surface during continued fully-reversed cyclic straining. Continued, cyclic deformation favors the occurrence of softening through an intensification of the slip bands. Also, when the local stress concentration caused by dislocation build-up at a reinforcing SiC particulate exceeds a critical value [say τ_c], microcrack initiation occurs through rupture of the hard, brittle and
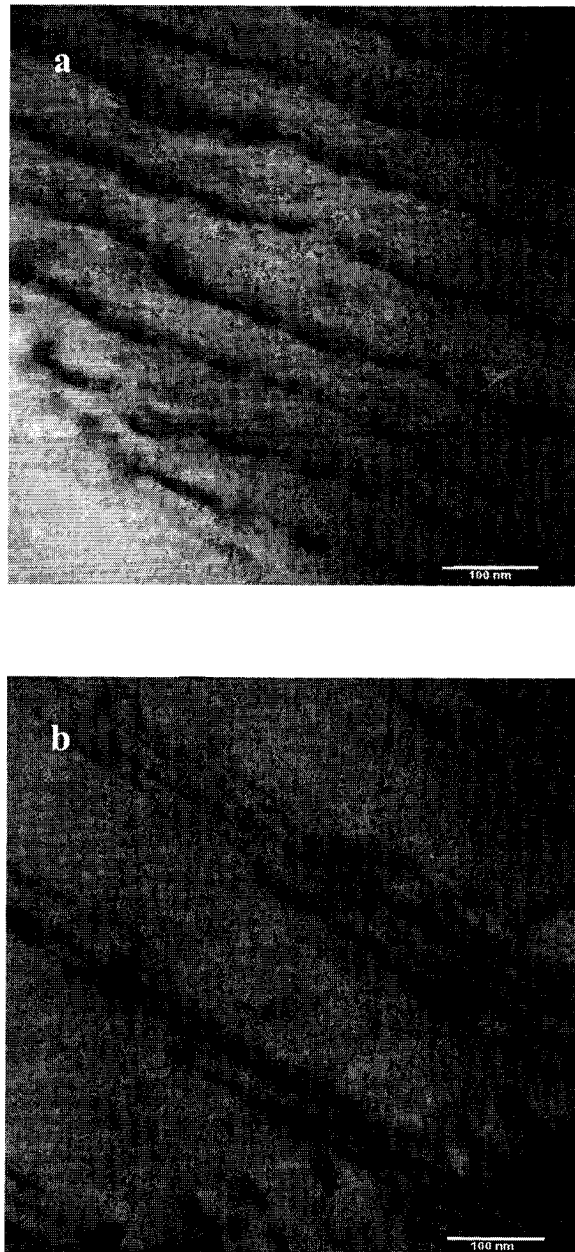
Figure 5.52:   Bright field transmission micrographs of the
               cyclically deformed at 120 °C, and at total
               strain amplitude of 0.5% for the
               7034/SiC/15p composite showing: Planar
               deformation bands in the matrix for (a)
               Under-aged condition and (b) Peak-aged
               condition.

elastically deforming particle (Figure 5.53). With continued cyclic straining numerous SiC particulates crack on account of [133]:

- Their intrinsic brittleness, that is, when the local stress concentration (say τ^*) exceeds the strength of the particulate ($\tau_{particulate}$) (Figure 5.53a).

- Decohesion occurring at the matrix-particulate interfaces (Figure 5.53b).

The theory behind the dependency of strength on grain size suggests that grain boundaries act as obstacles to dislocation motion and hence create dislocations pile-ups at the boundaries (Figure 5.54). For this aluminum alloy MMC having a fine-grained microstructure the dislocation pile-ups occur at numerous sites in the microstructure. An increase in dislocation density in the microstructure due to continued fully-reversed cyclic straining results in dislocation concentration, or build up, at locations of (a) second-phase inclusions in the microstructure, (b) reinforcing SiC particulates, (c) grain boundaries, and (d) grain boundary triple junctions. This results in a high local stress concentration in these regions. The high stress concentration facilitates the initiation of microscopic cracks at the grain boundary
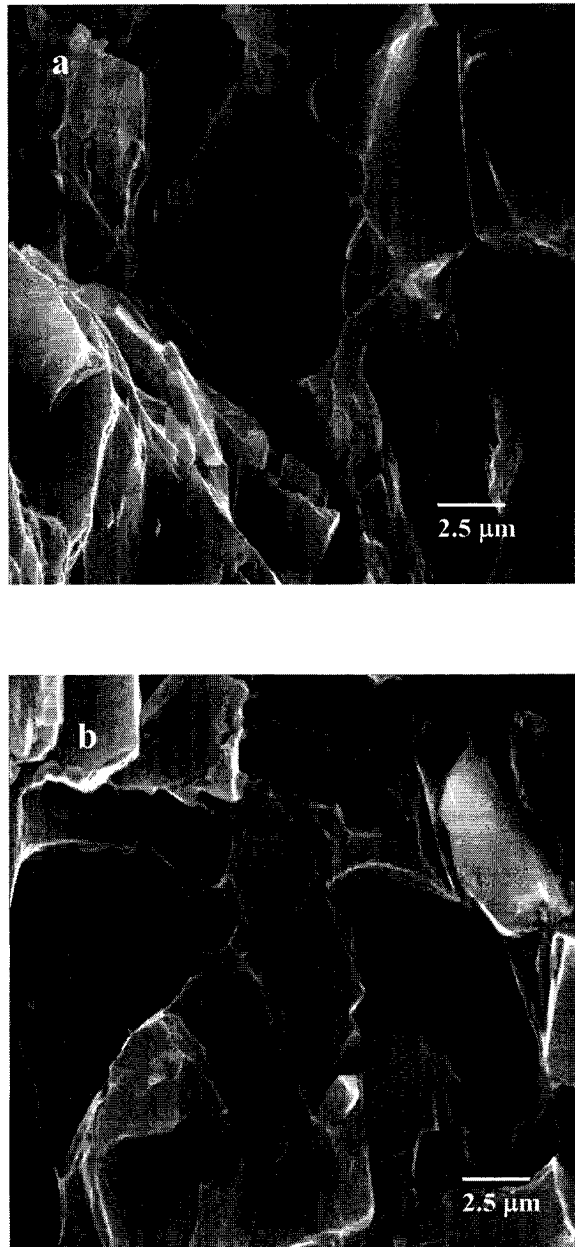
Figure 5.53: Scanning electron micrograph showing microscopic
cracks initiated in the reinforcing SiC particulate
of the composite specimen subjected to fully-
reversed cyclic deformation at 120 °C:
(a) Under-aged Condition, and (b) Peak-aged
Condition.
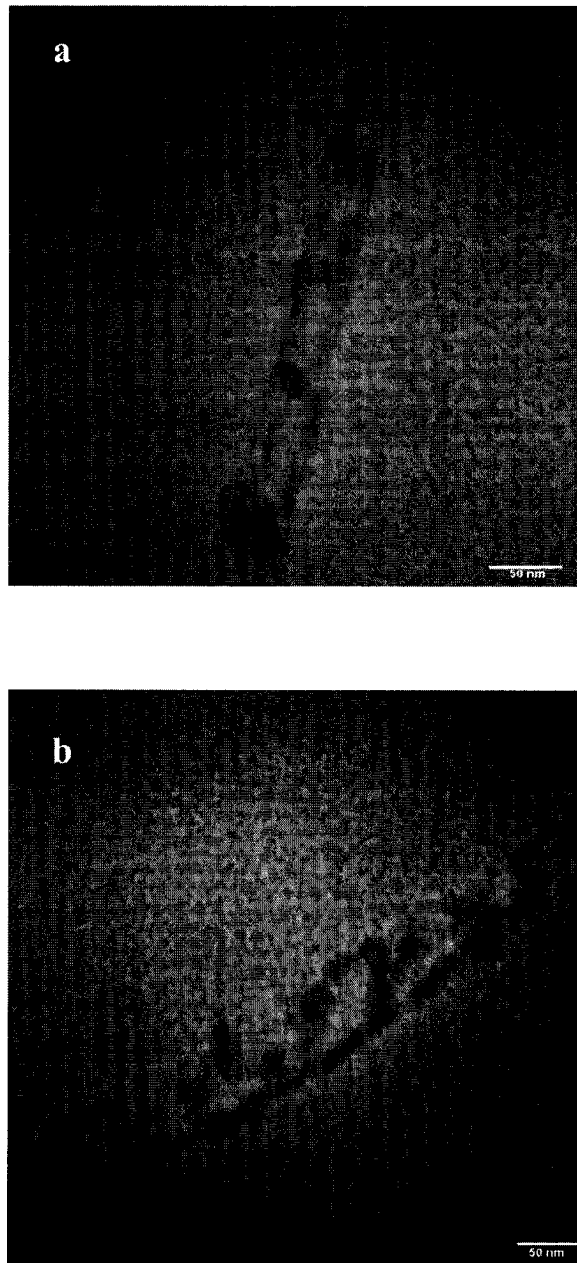
Figure 5.54:   Bright field transmission micrographs of the cyclically deformed at 120 °C, and at total strain amplitude of 0.5%, 7034/SiC/15p composite showing: dislocation pile-ups at the grain boundaries (a) Under-aged condition and (b) Peak-aged condition.

regions and is ably aided by cracking of the reinforcing

particulates [133].

5.2.4.4 Cyclic Fatigue Fracture

Fatigue fracture surfaces revealed nearly similar

topographies at the high cyclic strain-amplitudes (short

fatigue life), and low cyclic strain-amplitudes (long

fatigue life), for a given microstructural condition of the

aluminum alloy metal matrix. However, on a microscopic

scale, the fracture surface features were found to vary

with aging condition of the metal matrix. Representative

fractographs of the cyclic fatigue fracture surface

features are shown in Figures 5.55-5.58.

5.2.4.4.1 Under-aged Condition:

At high strain amplitude ($\Delta \varepsilon_T/2$= 0.75%, N_f = 20 cycles)

fracture on a macroscopic scale was normal, that is, at

about 90° to the major stress axis (Figure 5.55a).

Macroscopic or low magnification observations revealed

fracture to be flat (Figure 5.55b), relatively rough and

brittle (low cyclic ductility). The low-cycle fatigue

fracture was quite similar to the tensile fracture surface.

Numerous microscopic cracks were found in the sample. The

matrix of the composite revealed a non-linear crack profile
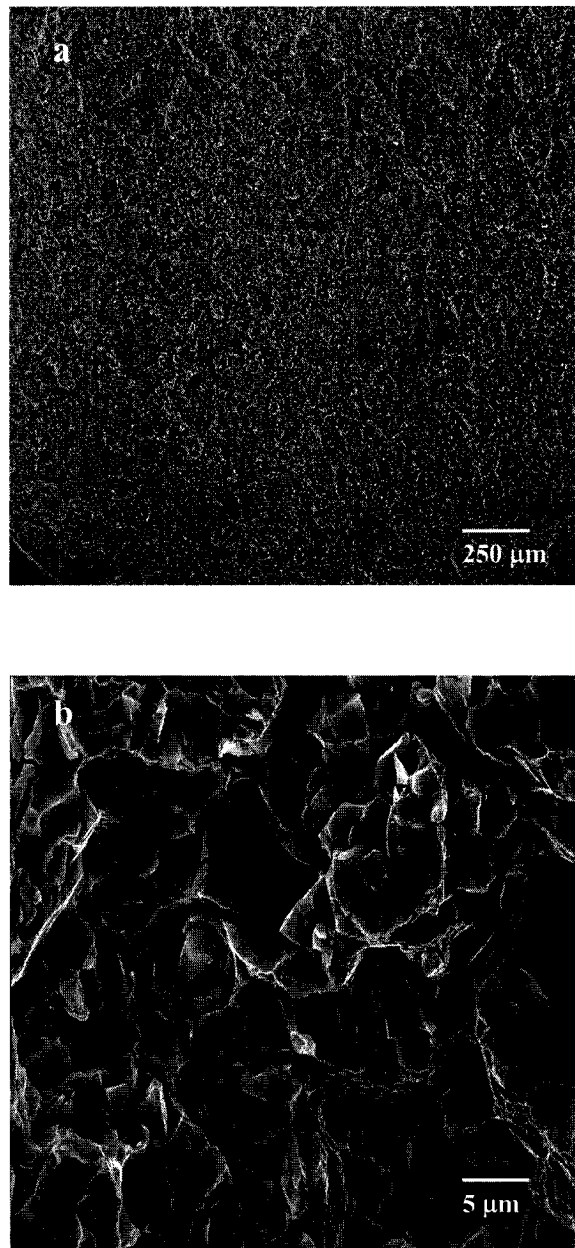
Figure 5.55: Scanning electron micrographs of the fatigue
sample of the 7034/SiC/15p-UA composite deformed
at 120 °C, at a total strain amplitude of 0.75%,
N_f = 20 cycles, showing: (a) Overall morphology
and (b) High magnification of (a) showing rough
fracture surface.

and isolated pockets of shallow dimples (Figure 5.55c), features reminiscent of locally brittle and ductile failure. Microscopic observations, at high magnification, revealed the fracture surface to comprise of multiple microscopic cracks and tear ridges (Figure 5.55d). Spatial arrangement of the carbide particulate reinforcements (SiCp) and the associated level of connectivity between the closely spaced particulates places constraints on the plastically deforming metal matrix and the resultant development of matrix triaxiality influences cyclic flow stress and void growth [133].

At a lower cyclic plastic strain amplitude and resultant long fatigue life ($\Delta\varepsilon_T/2$ = 0.50%, N_f = 1670 cycles) numerous macrocracks were evident covering the composite matrix (Figure 5.56b) with isolated particle cracking and decohesion occurring at the matrix-particulate interfaces (Figure 5.56c). Failure of the reinforcing particulates occurs when the cyclic tensile stress exceeds the fracture strength of the particle. A progressive increase in tensile stress, during the hardening that occurs during fully-reversed cyclic plastic deformation, causes a large number of microscopic cracks to initiate at the reinforcing SiC particles (Figure 5.56d) and
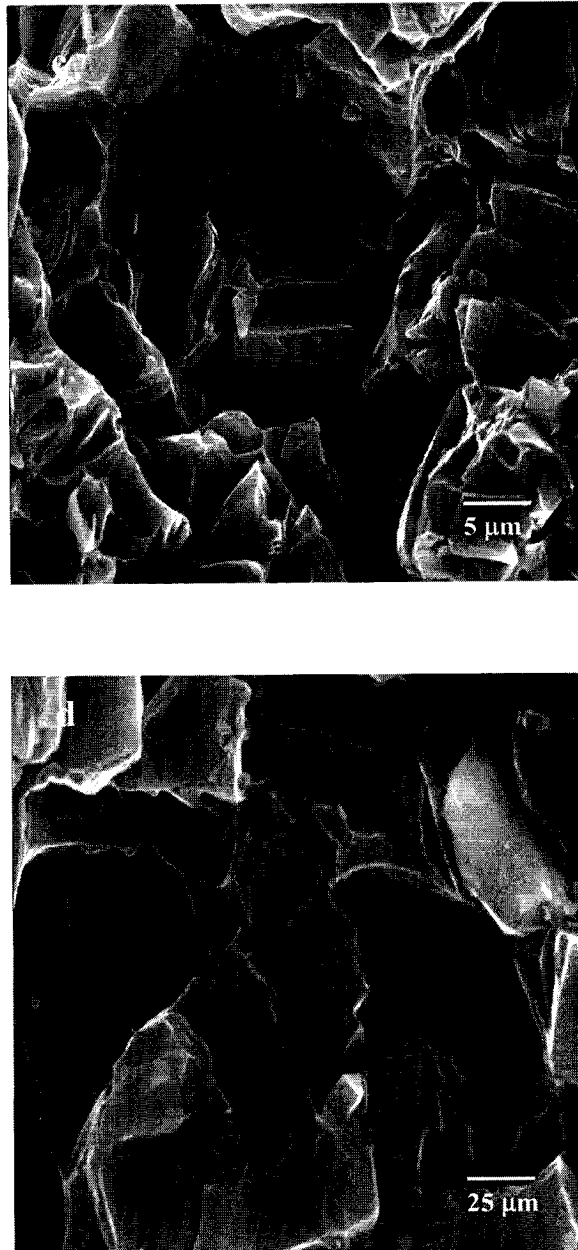
Figure 5.55(Cont.): Scanning electron micrographs of the
fatigue sample of the 7034/SiC/15p-UA composite
deformed at 120 °C, at a total strain amplitude of
0.75%, N_f = 20 cycles, showing: (c) Non-linear
cracks and pockets of shallow dimples and (d)
Cracked SiC particulates.
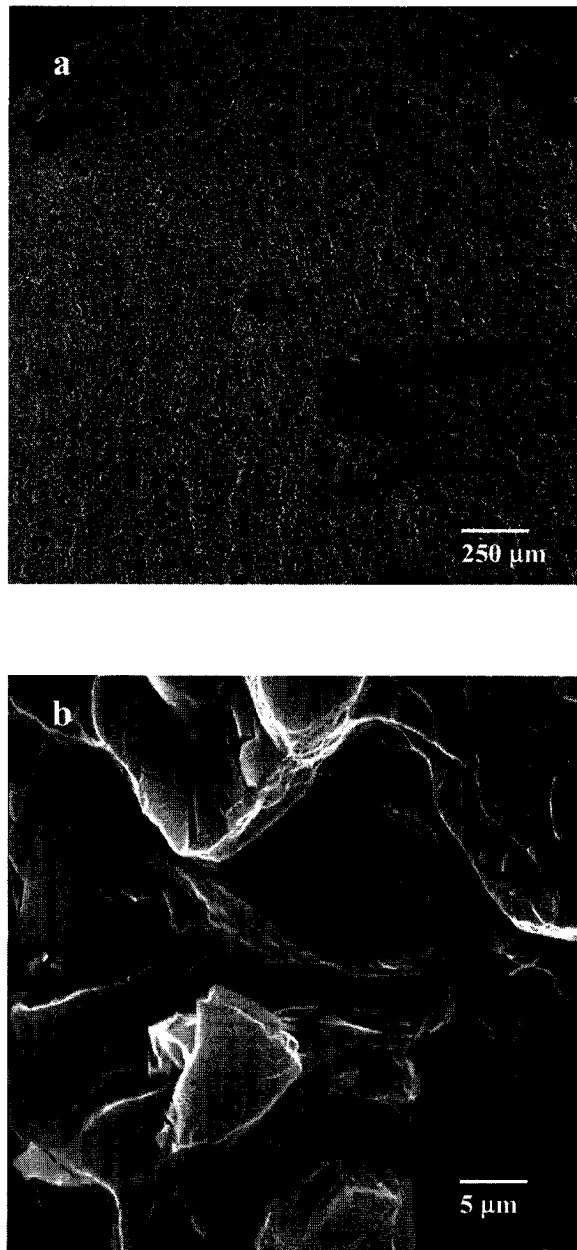
Figure 5.56: Scanning electron micrographs of the
7034/SiC/15p-UA composite fatigued to failure at
120 °C, at total strain amplitude of 0.50%, N_f =
1670 cycles, showing: (a) Overall morphology and
(b) Macroscopic cracks
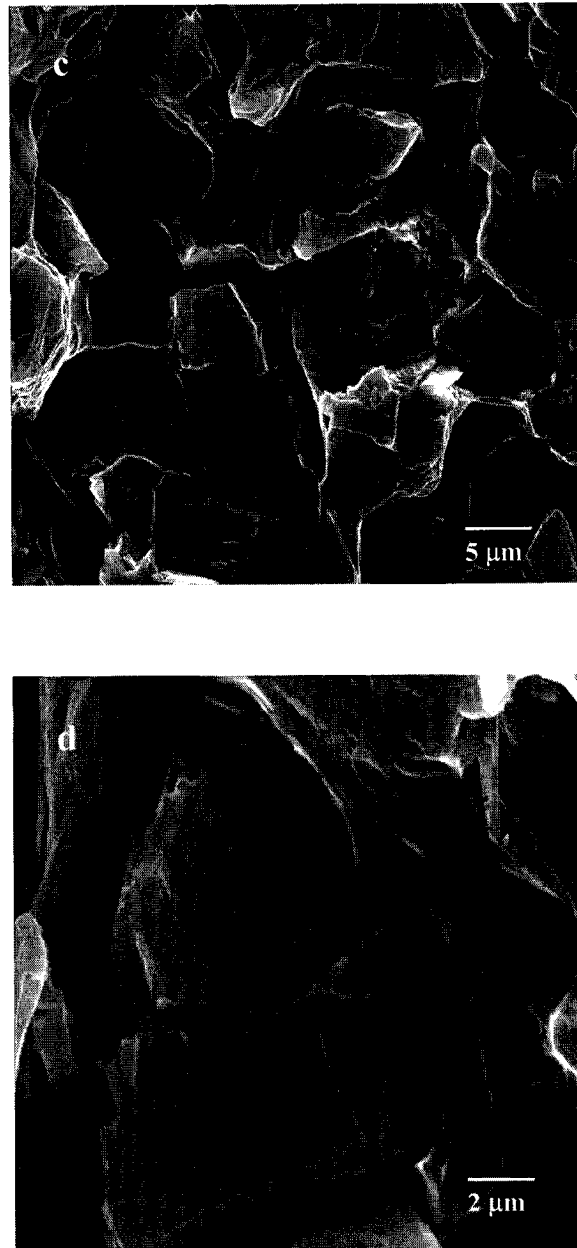
Figure 5.56(Cont): Scanning electron micrographs of the
7034/SiC/15p-UA composite fatigued to failure at
120 °C, at total strain amplitude of 0.50%, N_f =
1670 cycles, showing: (c) Particulate cracking and
decohesion at interfaces and (d) Cracked SiC
particulate.

decohesion at the matrix- particulate interfaces. The matrix between dispersed SiC particulates and SiC particulate clusters is subject to a high level of triaxial stress, which favors fracture of the matrix and concurrent microcrack initiation. The microscopic cracks grow through the SiC particulate clusters and link by fast fracture through the matrix to adjacent microscopic cracks resulting in a macroscopic crack. Concurrent propagation of the macroscopic and fine microscopic cracks occurs through the composite matrix. This results in a rapid drop in load carrying capability of the specimen prior to culminating in failure [133].

At lower cyclic strain-amplitudes and resultant longer low-cycle fatigue life, the fracture surfaces were quite similar to those observed at the higher cyclic strain amplitudes and short fatigue life. In addition to cracking of the reinforcing SiC particulates, decohesion was observed at the matrix-particulate interfaces. The larger SiC particulates tended to crack early during fully reversed cyclic deformation, while the smaller SiC particulates decohere from the soft and ductile aluminum alloy metal matrix to produce shallow dimples. The smaller SiC_p, do not crack easily, but on account of intrinsic

strain differences between the plastically deforming aluminum alloy metal matrix and the elastically deforming reinforcing particle, the process culminates in the occurrence of decohesion at the SiC particulate-matrix interfaces. The tendency for SiC particulate fracture is higher for the larger particulates and in regions containing a high local particulate volume fraction [133]. This arises from increased local stresses caused by a restriction of the plastic zone surrounding neighboring particles. Under the influence of a far-field applied cyclic stress the microscopic voids appeared to have undergone limited growth and coalescence, confirming a possible contribution from SiC particle constraint-induced triaxiality during deformation of the $AA7034/SiC_p$ composite. The limited growth of the microscopic voids during fully-reversed cyclic straining coupled with lack of their coalescence, as a dominant fracture mode, clearly indicates that the deformation properties of the soft and plastically deforming 7034 aluminum alloy metal matrix are significantly altered by the presence of hard and elastically deforming SiC particulates. Only a few of the fine microscopic voids coalescence and the halves of these

voids are the isolated pockets of shallow dimples observed on the fatigue fracture surface (Figure 5.55c) [133].

5.2.4.4.2 Peak-aged Condition:

At high cyclic plastic strain amplitude ($\Delta\varepsilon_T/2$ = 0.75%, N_f = 11 cycles) fracture was rough on a macroscopic scale. High magnification revealed the region of stable crack growth to be short and near featureless (Figure 5.57a). The overload region revealed macroscopic voids (Figure 5.57b), decohesion at the matrix-particulate interfaces (Figure 5.57c) and isolated pockets of shallow dimples (Figure 5.57d).

At the lower cyclic strain amplitude ($\Delta\varepsilon_T/2$ = 0.50%, N_f = 1504 cycles) the overall fracture was normal to the far field stress axis (Figure 5.58a). High magnification observations in the region of stable crack growth was near featureless (Figure 5.58b) with cracked particulates, feature reminiscent of locally brittle failure (Figure 5.58c). The overload region revealed numerous microscopic cracks and isolated pockets of shallow dimples (Figure 5.58d). The growth of voids is a cavity enlargement process, which is enhanced by localized plastic deformation. The coalescence of macroscopic voids is aided by the fine microscopic voids in the microstructure
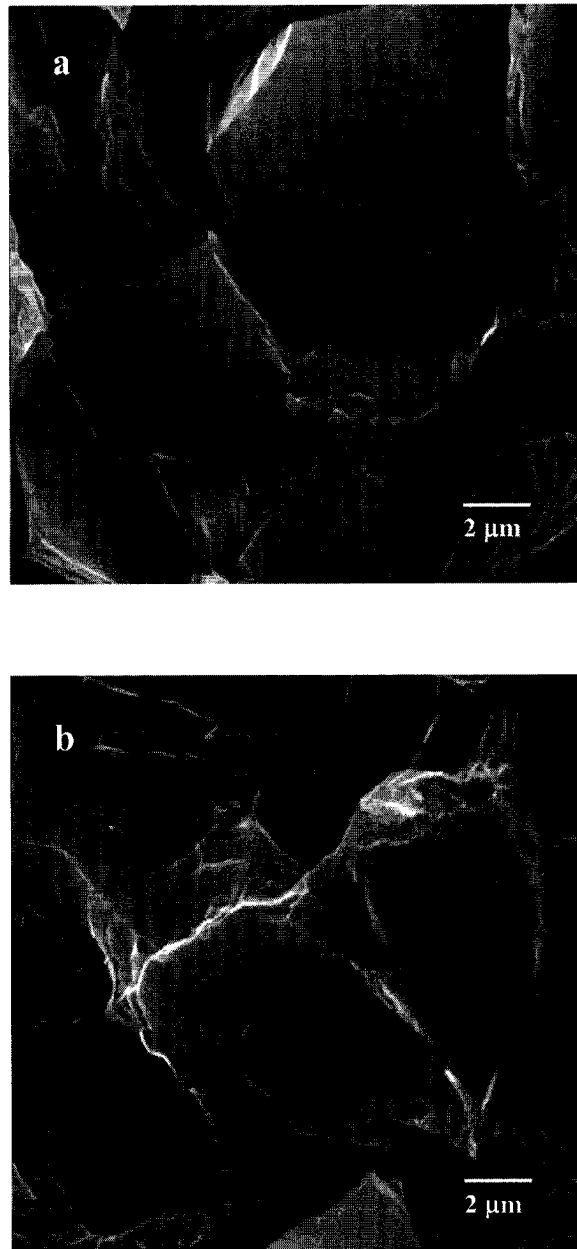
Figure 5.57: Scanning electron micrographs of the
7034/SiC/15p-PA composite fatigued to failure at
120 °C, at total strain amplitude of 0.75%, N_f = 11
cycles, showing: (a) Region of stable crack growth
and (b) Macroscopic voids
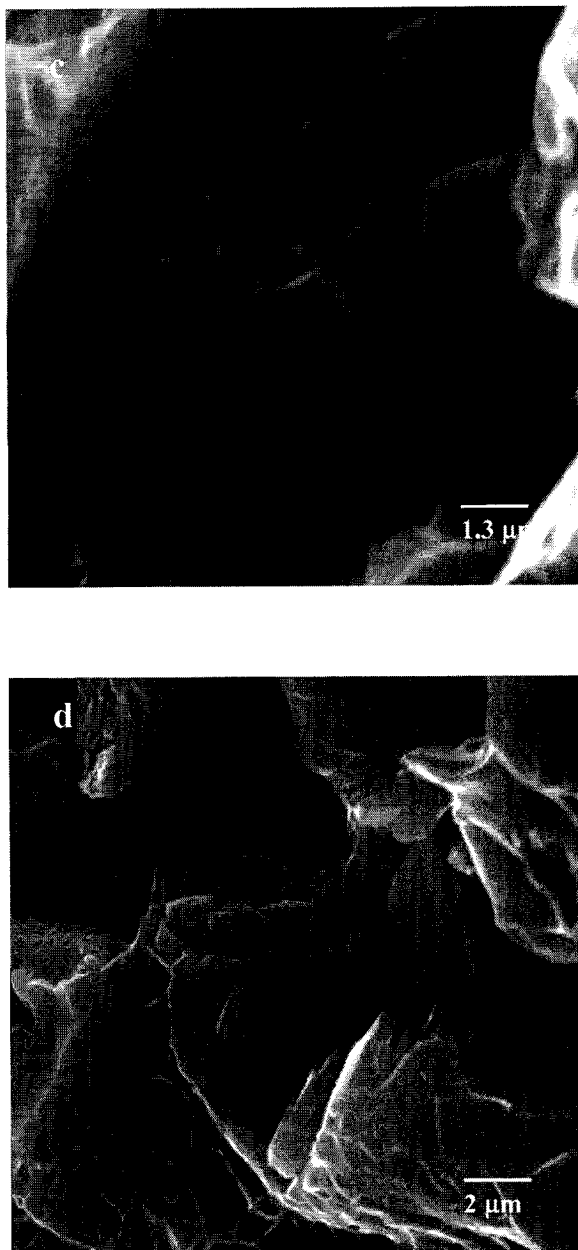
Figure 5.57(Cont.): Scanning electron micrographs of the
7034/SiC/15p-PA composite fatigued to failure at
120 °C, at total strain amplitude of 0.75%, N_f = 11
cycles, showing: (c) Decohesion at matrix-
particulate interfaces and (d) Isolated pockets of
shallow dimples.
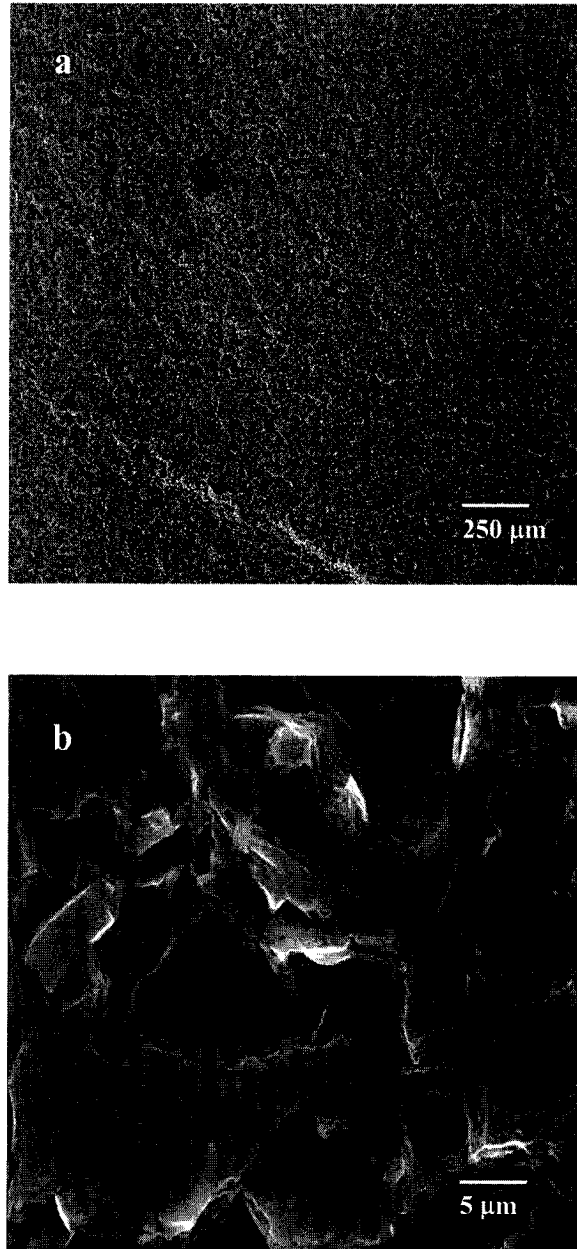
Figure 5.58: Scanning electron micrographs of the
7034/SiC/15p-PA composite fatigued to failure at
120 °C, at total strain amplitude of 0.50%, N_f =
1504 cycles, showing: (a) Overall morphology: flat
and normal and (b) Region of stable crack growth.
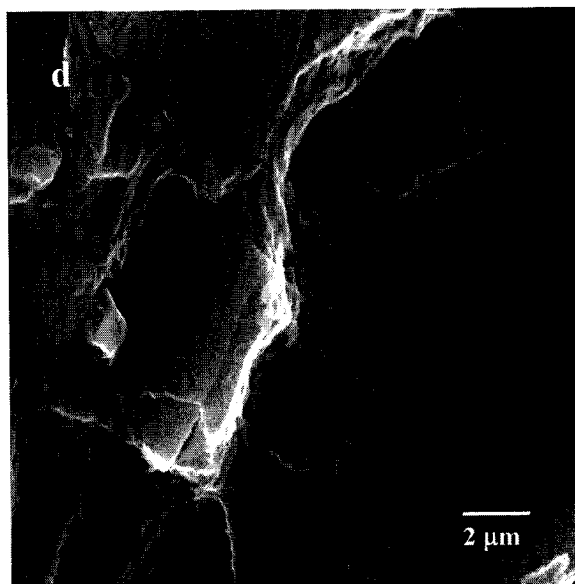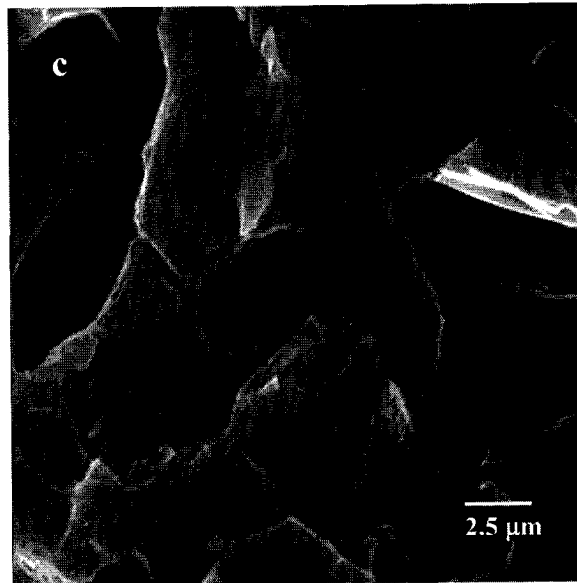
Figure 5.58(Cont.): Scanning electron micrographs of the
7034/SiC/15p-PA composite fatigued to failure at
120 °C, at total strain amplitude of 0.50%, N_f =
1504 cycles, showing: (c) Cracked SiC particulates
and (d) Microscopic cracks and shallow dimples in
the region of overload.

(Figure 5.58d). The void nucleation, decohesion at the matrix-particulate interfaces, and cracking of the reinforcing SiC particulates suggests that local plastic strains dominate in regions containing a high volume fraction of the SiC particulate reinforcement and is partially responsible for the inferior cyclic strain resistance and low-cycle fatigue life of this composite microstructure when compared to the unreinforced counterpart [133].

5.3. Mg-6%Zn Matrix Composite

The objective of this section is to record the influence of discontinuous particulate reinforcement on high cycle fatigue properties and fracture (quasi-static and cyclic) behavior of a magnesium-zinc alloy reinforced with particulates of silicon carbide (referred to as SiC_p). The fatigue response and final fracture behavior of the composite are discussed in light of concurrent and mutually interactive influences of composite microstructural effects, matrix deformation characteristics, test temperature and cyclic stress amplitude.

5.3.1. <u>Initial Microstructure</u>

Figure 5.59 is an optical micrograph showing microstructure of the Z6/SiC/20p composite. The silicon carbide particulates (SiC), in the Z6 magnesium alloy metal matrix, were generally of near-uniform size, although a few irregularly shaped particulates were found dispersed randomly between the near uniform shaped particulates. An agglomeration or clustering of the SiC_p was observed. An agglomerated site consisted of a few larger SiC particulates intermingled with the smaller, uniform and more regularly shaped particles. Alignment of the reinforcing SiC particulates was observed in the extrusion direction. Such an alignment has been documented in other extruded aluminum alloy-based MMCs [119,134,135]. No attempt was made, in this study, to determine the particle size distribution for the MMC material. The etched composite microstructure revealed the matrix to consist of very fine grains, which could not be easily resolved in the optical microscope at low magnifications (<1000 X).

5.3.2. <u>Tensile Deformation and Fracture</u>

The tensile properties of the Z6/SiC/20p-F composite, at the two test temperatures, are summarized in Table 5.4. The results are the mean values based on duplicate tests. At

40 μm
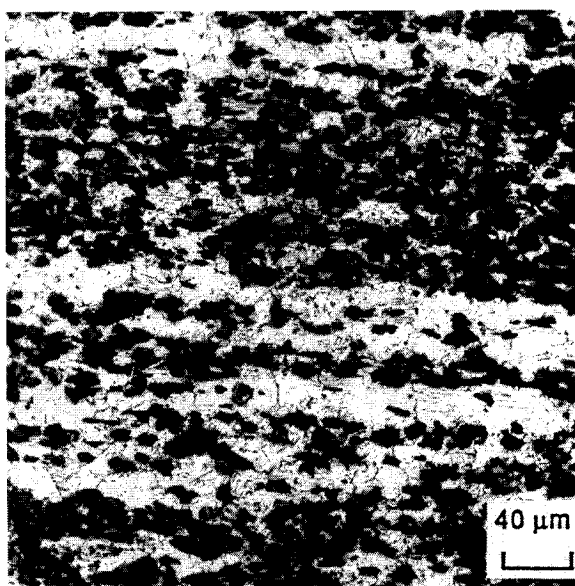
Figure 5.59: Optical micrograph illustrating microstructure
of the Z6/SiC/20p-F composite.

Table 5.4: Tensile Properties of the Magnesium Alloy / SiC Composite.

Test Temperature (°C)	E (GPa)	0.2%Offset Yield Strength MPa	(Ksi)	Ultimate Tensile Strength MPa	(Ksi)	Elongation (%)	Reduction In Area (%)
27	66	307	(44.5)	379	(55)	2.0	3.0
150	48	166	(24)	186	(27)	19	19

ambient temperature (27 °C), the composite material revealed limited ductility, quantified in term of both elongation-to-failure (ε_f) and reduction-in-area (RA). Increase in test temperature resulted in a decrease of yield strength (σ_{ys}) by 46% and ultimate tensile strength (σ_{uts}) by as much as 51% with a concomitant improvement in elongation-to-failure (ε_f) by over 800%, and reduction in area by 500%. It is evident that the degradation in strength had a profound influence on tensile ductility of this composite [99,137].

The tensile fracture surfaces provide valuable information pertaining to microstructural effects on tensile ductility and fracture properties of this composite. It is fairly well documented by researchers that fracture of unreinforced monolithic alloys is associated with events of microscopic void nucleation and growth, with nucleation essentially occurring at the coarse intermetallic particles and other insoluble phases in the microstructure [96,97,100]. An essential requirement for void nucleation at a reinforcing particle and other coarse second-phase particles present in the microstructure is the development of a critical normal stress across particulate-matrix interfaces [98]. In the unreinforced metal matrix, the nucleation of cavities and voids is favored to occur by the

influences of: (1) cracking of the hard and brittle SiC_p inclusions that deform elastically, and (2) decohesion at interfaces between the reinforcing particulate and the soft magnesium alloy metal matrix. The Z6/SiC/20p-F composite examined exhibited limited ductility at ambient temperature, with fracture, on a macroscopic scale, occurring on a plane normal to the far-field stress axis. High magnification observations of the tensile fracture surface revealed microscopic features reminiscent of locally ductile and brittle mechanisms [137]. Representative fractographs of the tensile fracture surface at the two temperatures are shown in Figures 5.60-5.62.

5.3.2.1. <u>Test Temperature = 27 °C</u>

Tensile fracture of the Z6/SiC/20p-F MMC at this temperature was flat, near featureless and essentially on a plane normal to the far field stress axis when viewed on a macroscopic scale (Figure 5.60a). Microscopic observations revealed cracking parallel to the major stress axis (Figure 5.60b). The macroscopic cracks were surrounded by cracked particulates and ductile regions, which are referred to as tear ridges. Isolated tear ridges were evident on the tensile fracture surface (Figure 5.60c). The matrix was covered with numerous microscopic cracks (Figure 5.60d) and cracked SiC particulates (Figure 5.61a). The overload region
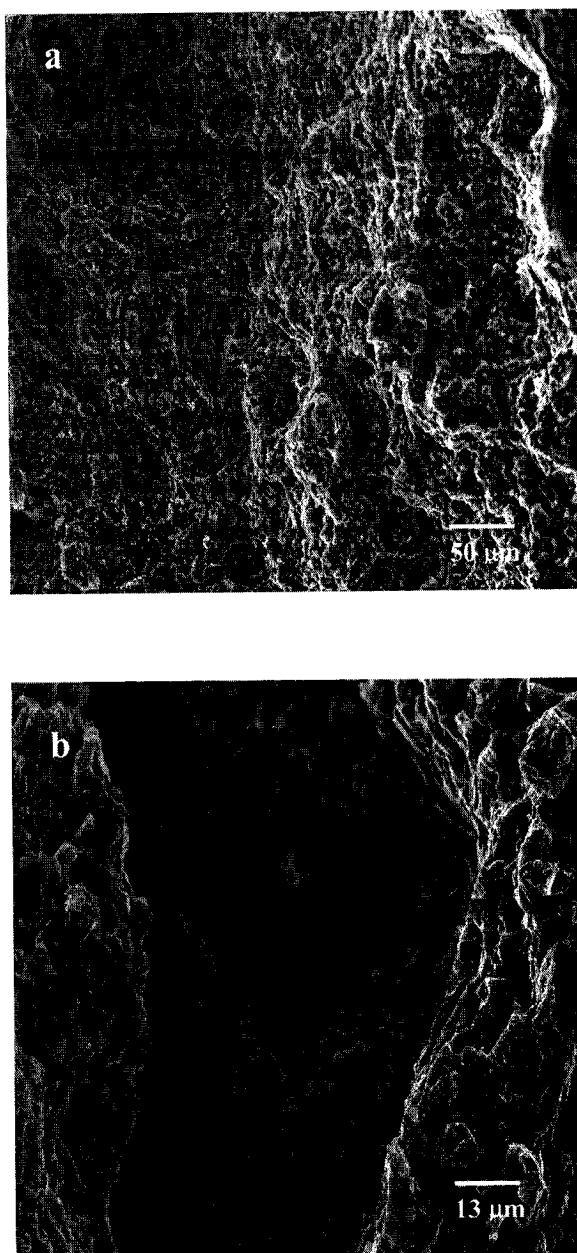
Figure 5.60:Scanning electron micrographs of the tensile
fracture surface of the Z6/SiC/20p-F composite at
ambient temperature (27 °C) showing: (a) Overall
morphology, and (b) Cracking parallel to the major
stress axis.
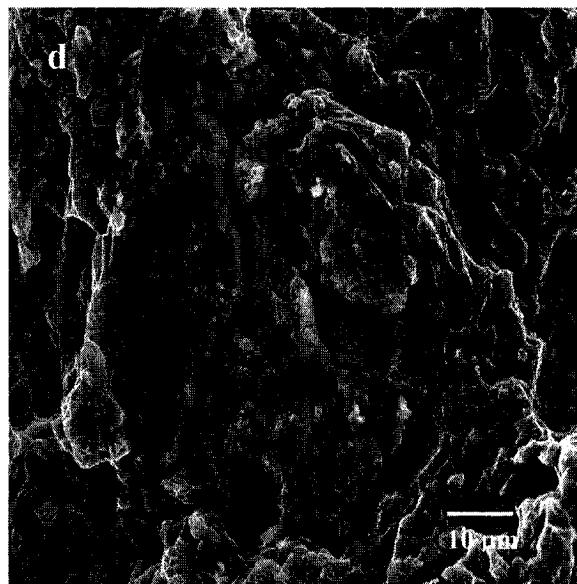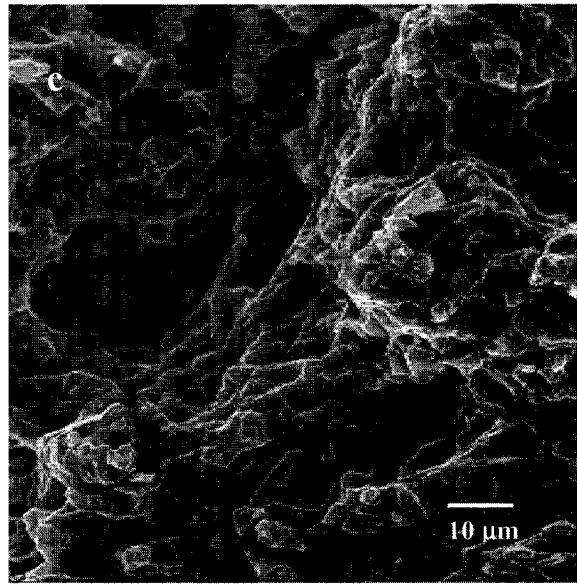
Figure 5.60 (Cont.): Scanning electron micrographs of the
tensile fracture surface of the Z6/SiC/20p-F
composite at ambient temperature (27 °C) showing:
(c) Isolated tear ridges and (d) numerous
microscopic cracks
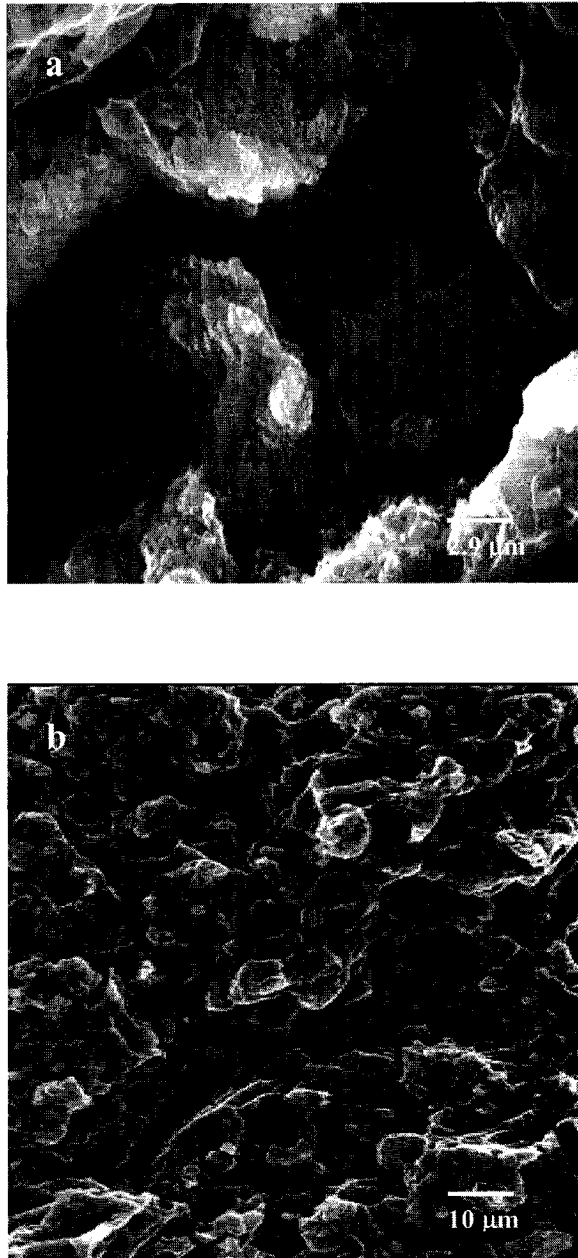
Figure 5.61:Scanning electron micrographs of the tensile
fracture surface of the Z6/SiC/20p-F composite
showing: (a) cracked SiCp, and (b) fine microvoids
and isolated shallow dimples.

revealed a population of microscopic voids of varying

size and shapes intermingled with ductile dimples (Figure

5.61b), features reminiscent of locally ductile fracture.

5.3.2.2. Test Temperature = 150 °C

On a macroscopic scale, tensile fracture surface of the

Z6/SiC/20p-F MMC deformed at the elevated temperature (150

°C) was flat and similar to ambient temperature fracture

surface but relatively rough when viewed on a microscopic

scale (Figure 5.62a). Numerous macroscopic cracks were found

oriented along the major stress axis (Figure 5.62b). The

fracture surfaces revealed the presence of cracked SiC

particulates surrounded by a population of shallow dimples.

The matrix of composite was covered with a population of

microscopic voids of a wide range of sizes (Figure 5.62c).

The voids were distributed throughout the fracture surface

and were intermingled with dimples (Figure 5.62d).

The constraints in mechanical deformation caused by the

hard, brittle and elastically deforming SiCp in a relatively

soft and ductile magnesium alloy metal matrix coupled with

the concurrent development of a triaxial stress state in the

matrix of the Z6/SiC$_p$ composite is a factor that aids in

limiting flow stress of the composite microstructure, while

concurrently placing constraints on microscopic void

nucleation and growth. As a direct consequence of the
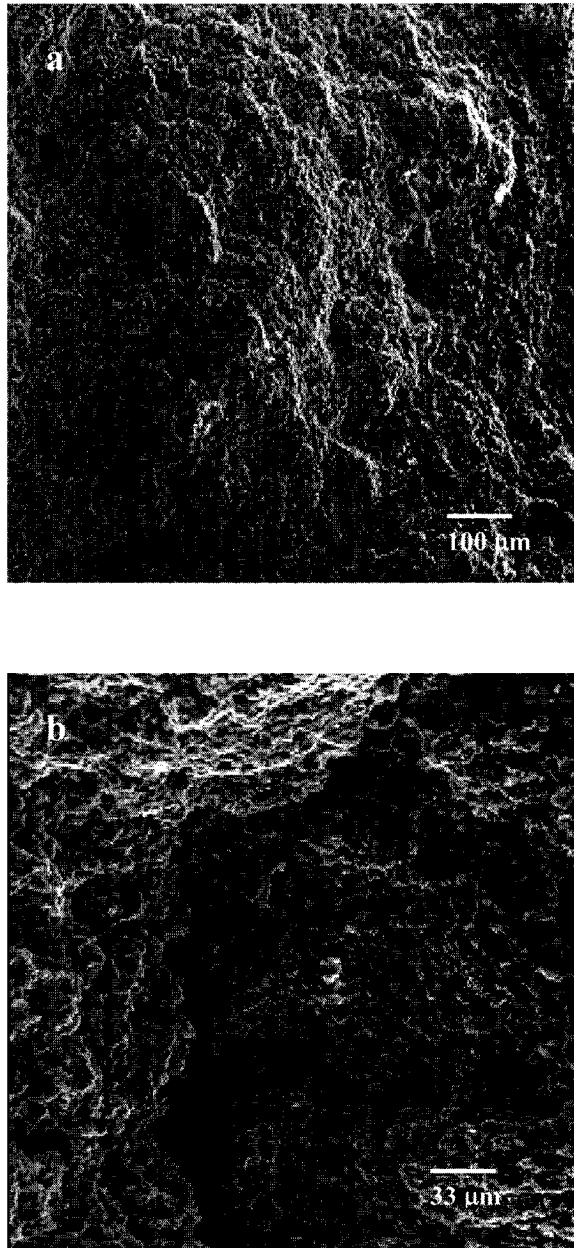
Figure 5.62:Scanning electron micrographs of the tensile
fracture surface of the Z6/SiC/20p-F composite at
elevated temperature (150 °C) showing: (a) Overall
morphology, (b) Numerous macroscopic cracks along
the major stress axis.
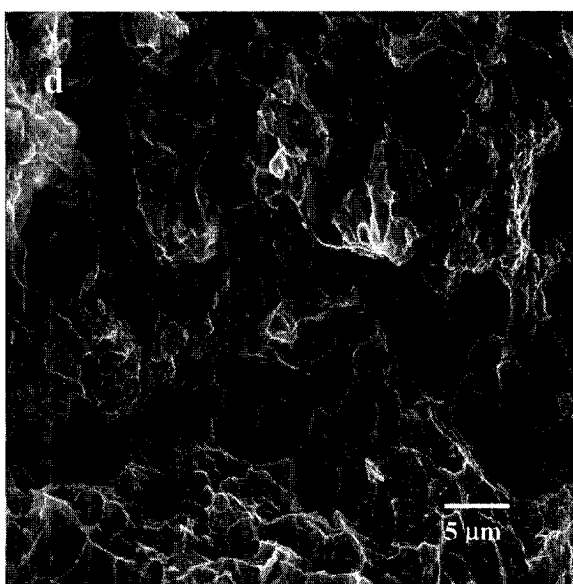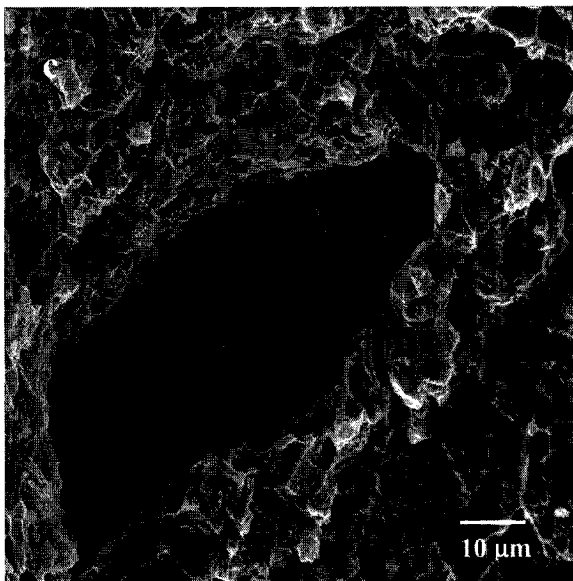
Figure 5.62(Cont): Scanning electron micrographs of the
tensile fracture surface of the Z6/SiC/20p-F
composite at elevated temperature (150 °C)
showing: (c) population of microscopic voids and
(d) Voids intermingled with dimples

deformation constraints induced by the discontinuous SiC particulates, a higher applied stress is required to initiate plastic deformation in microstructure of the composite. This translates to a higher elastic stiffness and yield strength of the Z6/SiC/20p-F composite [55].

Failure of the reinforcing SiC particulate in the magnesium alloy metal matrix can be essentially attributed to the mutually interactive influences of: (a) local plastic constraints, (b) particle size, and (c) particle agglomeration. The local plastic constraints are particularly important for the larger-sized SiC particles and particle clusters during composite fracture [58,90,136]. Examination of the tensile fracture surfaces revealed that damage associated with fracture to be highly localized at the discontinuous SiC_p reinforcements with little evidence of void formation away from the fractured SiC particulates. Fracture of the hard and brittle SiC_p was found to be greater in regions of particle clustering. This is attributed due to: (1) enhanced local stresses resulting from restriction of plastic deformation, and (2) an intrinsic brittleness of the reinforcing SiC_p with the propensity for it to fracture due to localized deformation. It is the two concurrent and competitive factors that result in particulate cracking and aided by decohesion, or separation at its interfaces, with the metal matrix being

the dominant damage modes. The damage of the composite microstructure, during uniaxial loading, arising from the synergistic influences of particle cracking and decohesion at the matrix-particulate interfaces results in a detrimental influence on tensile ductility. Furthermore, assuming that the metal matrix-reinforcement particle interfaces are strong, the triaxial stresses generated during far-field tensile loading favors limited growth of the microscopic voids in the matrix of the composite. Under the influence of an applied tensile load, the microscopic voids appeared to have undergone limited growth confirming a possible contribution from SiC particle constraint-induced triaxiality on deformation and failure of the composite matrix. The limited growth of the voids coupled with lack of their coalescence, as a dominant fracture mode for the Z6/SiC/20p-F6 composite, suggests that the deformation properties of the magnesium alloy metal matrix are significantly altered by the presence of discontinuous SiC_p reinforcements [23,137].

Fracture of the brittle SiC particulates aided by failure or decohesion at the interface results in the formation of voids. Few of the fine microscopic voids coalesce and the halves of these voids are the shallow dimples observed on the tensile fracture surface (Figure 5.61b). The lack of formation of dimples, as a dominant

fracture mode, is attributed to the constraints in plastic flow in the composite matrix caused by the presence of discontinuous SiC_p reinforcement phase and not to limited ductility of the Z6 magnesium alloy matrix. The constraints in plastic flow tend to favor the formation of fine tear ridges between the SiC particulates in the magnesium alloy metal matrix [137].

5.3.3. Cyclic-Stress Controlled

The stress amplitude-controlled high-cycle fatigue test provides information pertinent to the existence of an endurance limit. In the high cycle, low stress amplitude fatigue of Mg MMC the property changes are expected to be confined to occur at and around the vicinity of the fracture process zone at the tip of the advancing crack, while the material in the far field remains essentially unaffected during fatigue cycling. The results of the axis stress amplitude controlled tests are shown in Figure 5.63 as the variation of stress amplitude ($\Delta\sigma/2$) with fatigue life (cycles N_f). The stress amplitude ($\Delta\sigma/2$)-fatigue life (N_f) curve exhibits the general trend shown by non-ferrous metals. At equivalent stress amplitudes an increase in test temperature resulted in degradation in HCF life by at least an order of magnitude. To understand and establish the potential reasons for such degradation in life the stress
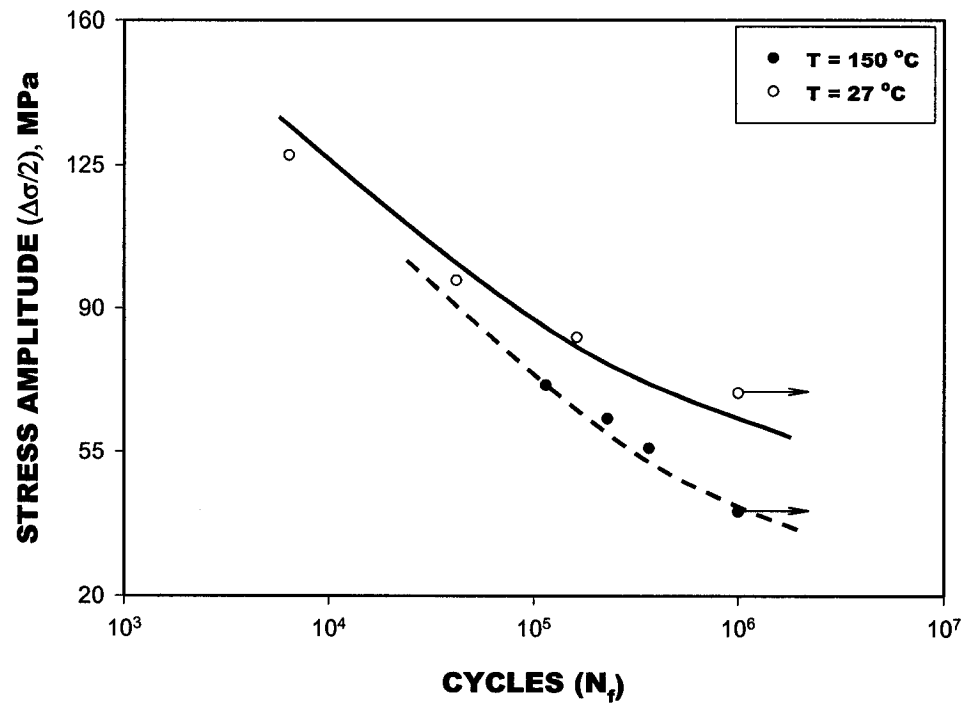
Figure 5.63:Influence of temperature on cyclic stress
amplitude ($\Delta\sigma/2$)-fatigue life (N_f) response of the
Z6/SiC/20p-F composite.

amplitude-fatigue life data are replotted in terms of elastic strain amplitude in the manner suggested by Hassen and co-workers [103], where the elastic strain amplitude $(\Delta\varepsilon_e/2)$ is the stress amplitude $(\Delta\sigma/2)$ normalized by elastic modulus (E). Variation of elastic strain amplitude with fatigue life is shown in Figure 5.64. This is done in order to account for the decrease in stiffness of the Z6/SiC/20p-F composite material with an increase in test temperature. Little to no difference in behavior is observed at the two test temperatures suggesting that the demonstrated degradation in cyclic fatigue life with increase in test temperature is a reflection of the lower elastic modulus (48 GPa) of the Z6/SiC/20p-F composite material at the higher test temperature when compared with the modulus (66 GPa) at ambient temperature. To further examine the influence of temperature on high-cycle fatigue response, the stress-life data are replotted to account for differences in strength of the composite material at the two temperatures. In Figure 5.65a the stress amplitude has been normalized by the uniaxial yield strength (σ_{ys}), while in Figure 5.65b the cyclic stress amplitude has been normalized by the ultimate tensile strength (σ_{uts}). In both cases the normalized stresses are plotted against the number of cycles-to-failure. In both situations the Z6/SiC/20p-F composite
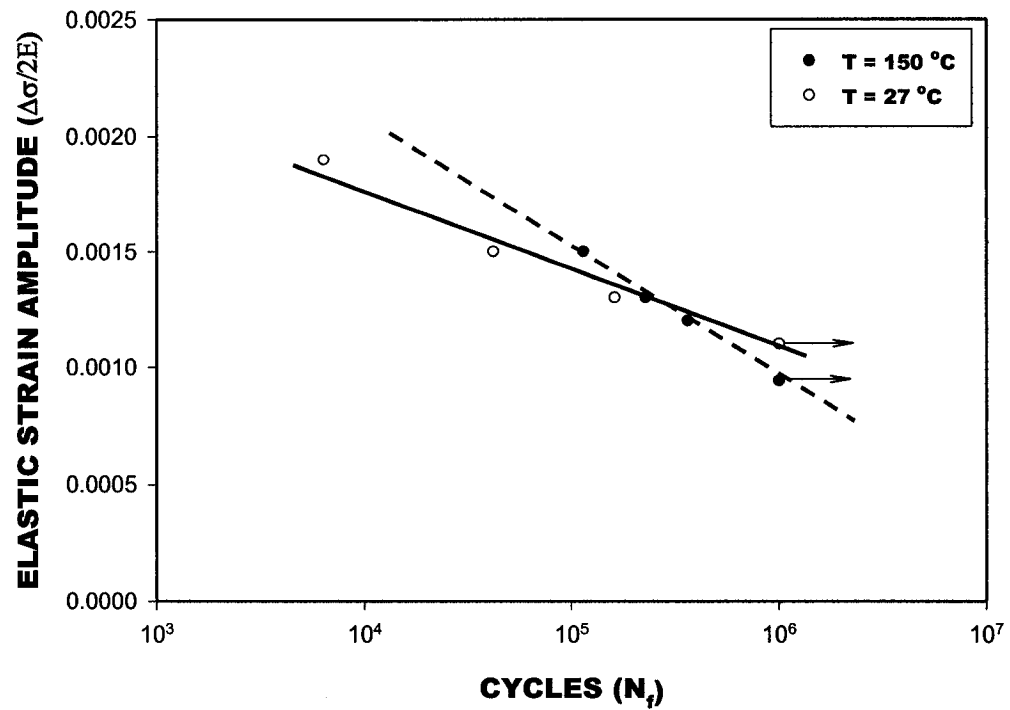
Figure 5.64: Elastic strain amplitude ($\Delta\varepsilon/2$)-fatigue life (N_f) response of the Z6/SiC/20p-F composite.
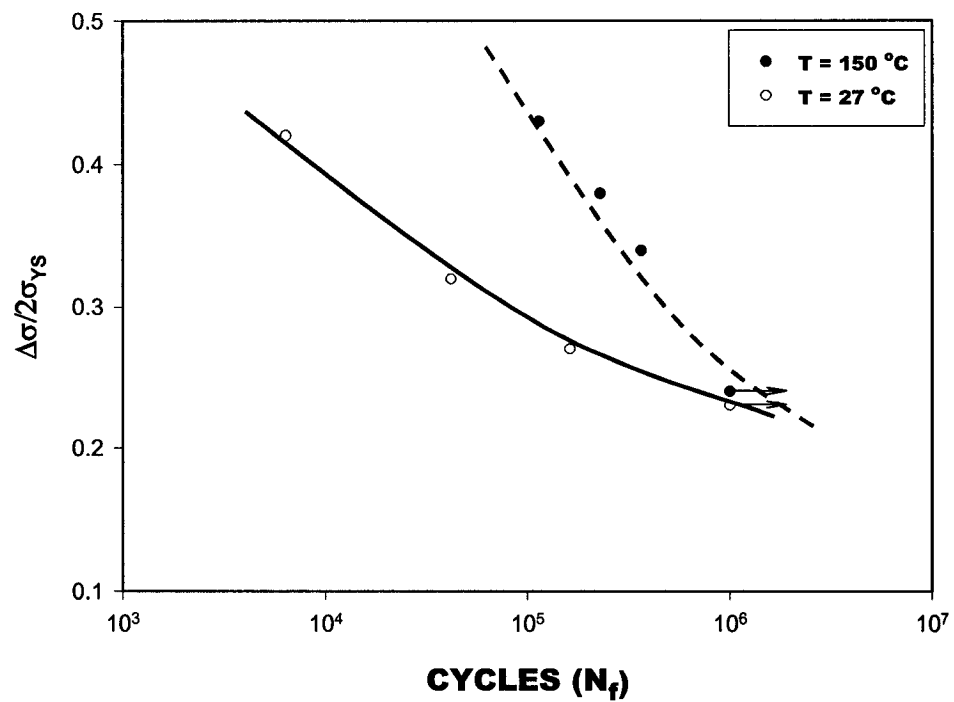
Figure 5.65:Variation of (a) cyclic stress amplitude
          normalized with yield strength (σ_{ys}) Versus
          fatigue life (N_f) response of the Z6/SiC/20p-F
          composite at the two temperatures.
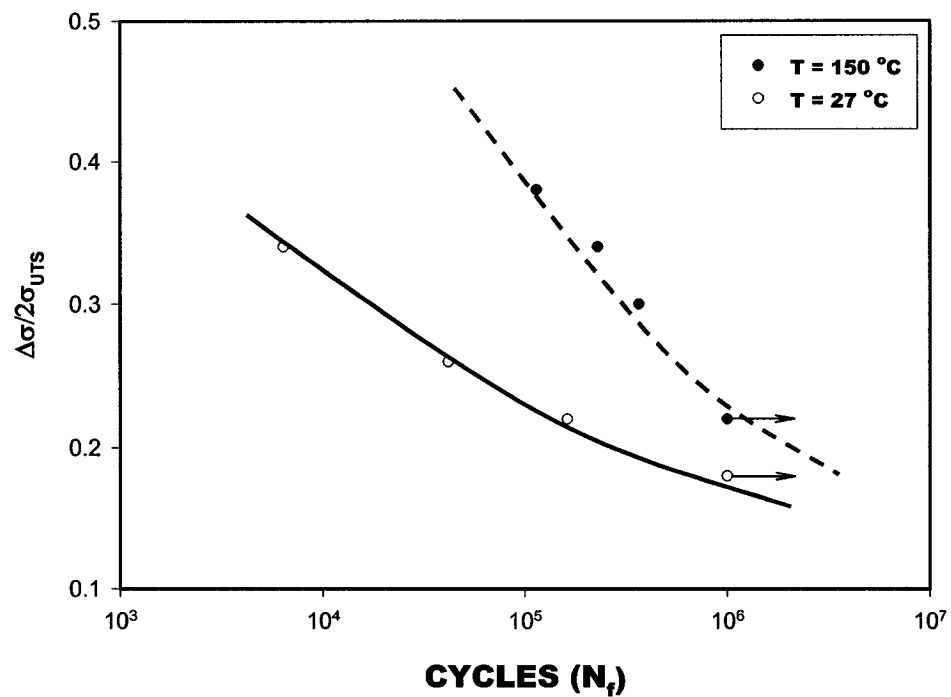
Figure 5.65 (Cont.):Variation of (b) cyclic stress amplitude
normalized with ultimate tensile strength
(σ_{uts}) Versus fatigue life (N_f) response of
the Z6/SiC/20p-F composite at the two
temperatures.

material reveals improved high cycle fatigue life at the higher test temperature. The improvement is greater at the higher ratios of stresses and resultant low fatigue life than at the lower ratios of stresses and resultant enhanced fatigue life. The beneficial effects of elevated temperature on cyclic fatigue resistance at the higher ratios of stress is an indication of superior crack initiation and/or crack growth resistance of this composite material at the elevated temperature. Details are discussed in the following section on cyclic fracture [137].

5.3.3.1. Cyclic Fracture Behavior

Examination of the fracture surfaces of the cyclically deformed fatigue specimens, in a JEOL scanning electron microscope, was done at: (a) low magnification to identify the regions of fatigue initiation and final fracture (overload), and (b) at higher magnifications in the fatigue region to identify the regions of microcrack formation and early microscopic crack growth, and the overload region to identify the fine-scale fracture features. Representative fracture features of the Z6/SiC/20p-F composite are shown in Figures 5.66-5.69.

5.3.3.1.1. Test Temperature = 27 °C

High cycle fatigue fracture of the composite sample deformed at the maximum cyclic stress of 283 MPa (N_f = *6369 cycles*) revealed fracture to have occurred on a plane that is normal to the far-field stress axis. The fracture surface revealed a small region of fatigue, about the size of a thumbnail, and a large portion to be overload-failure (Figure 5.66a) with little evidence of gross cyclic ductility. Low magnification observations revealed randomly distributed microscopic cracks in the region of early crack growth (Figure 5.66b), features reminiscent of locally brittle failure. The microscopic cracks were common in test specimens deformed at the higher cyclic stress and resultant short fatigue life. There was little to no evidence of crack branching suggesting that the damaged region ahead of the crack tip is greatly reduced. High magnification observations of the overload region revealed: (a) a population of fine microscopic voids of varying size and shapes, (b) shallow dimples (Figure 5.66c), and (c) cracked SiC particulates (Figure 5.66d), features reminiscent of locally ductile and brittle failure. The voids were distributed through the fracture region with the occurrence of microvoid coalescence. The macroscopic voids were intermingled with the fine microscopic voids. The composite sample cyclically deformed at the lower stress of 184 MPa
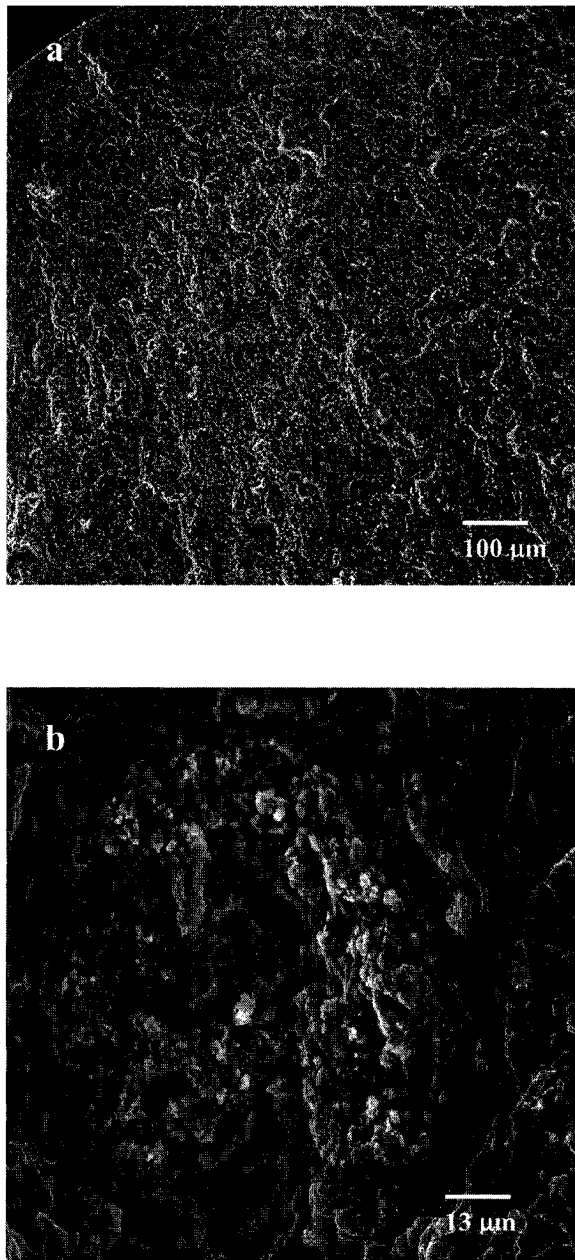
Figure 5.66:Scanning electron micrographs showing HCF
        fracture surface features of the Z6/SiC/20p-F
        composite deformed at cyclic stress amplitude of
        283 MPa, N_f = 6369 cycles, showing: (a) overall
        morphology, (b) array of varying microscopic
        cracks.
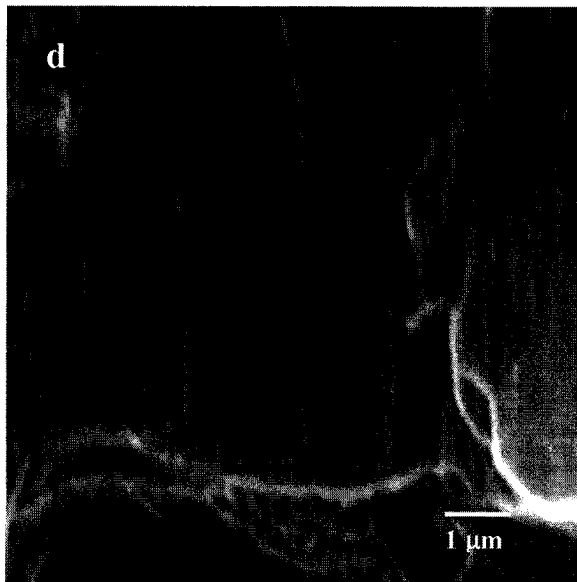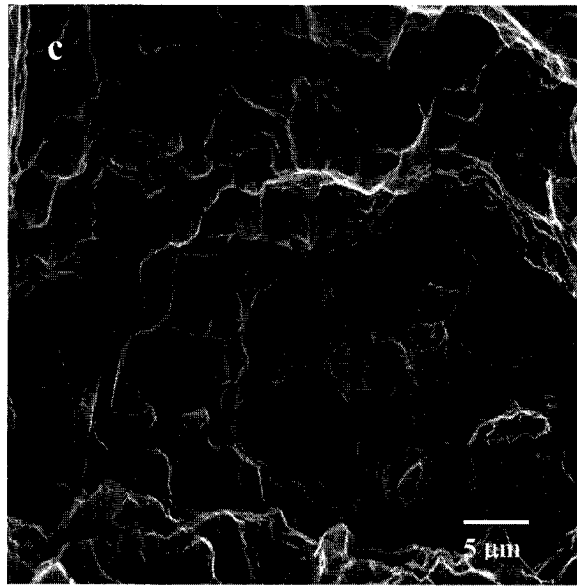
Figure 5.66 (Cont.): Scanning electron micrographs showing
    HCF fracture surface features of the Z6/SiC/20p-F
    composite deformed at cyclic stress amplitude of
    283 MPa, N_f = 6369 cycles, showing: (c) voids of
    varying size and shallow dimples on the overload
    fracture surface, and (d) cracked SiC particulate.

(N_f =162,197 cycles) revealed distinct regions of stable crack growth and overload (Figure 5.67a). High magnification observations in the region of stable crack growth revealed it to be flat and near featureless (Figure 5.67b). The overload region revealed microscopic cracks, isolated pockets of shallow dimples and microscopic voids (Figure 5.67c), all features reminiscent of brittle and ductile failure. The randomly distributed voids revealed evidence of microvoid coalescence (Figure 5.67d). The microscopic voids ranged in size from submicron to the tens of micron.

5.3.3.1.2. <u>Test Temperature = 150 °C</u>

At this temperature the fatigue fracture surface of the composite sample cyclically deformed at the lower stress amplitude and resultant longer fatigue life (Figure 5.69) was quite similar to those observed at the higher stress amplitude and short fatigue life (Figure 5.68). In addition to cracking of the reinforcing particulates, decohesion or separation was evident at the matrix-particulate interfaces. The larger SiC particulates tended to crack early than the smaller SiC particulates. This is because the larger particulates and particulate clusters are more likely to contain inherent discontinuities than the smaller particulates. Typically, these discontinuities are sharp corners and re-entrant angles that act as potential stress
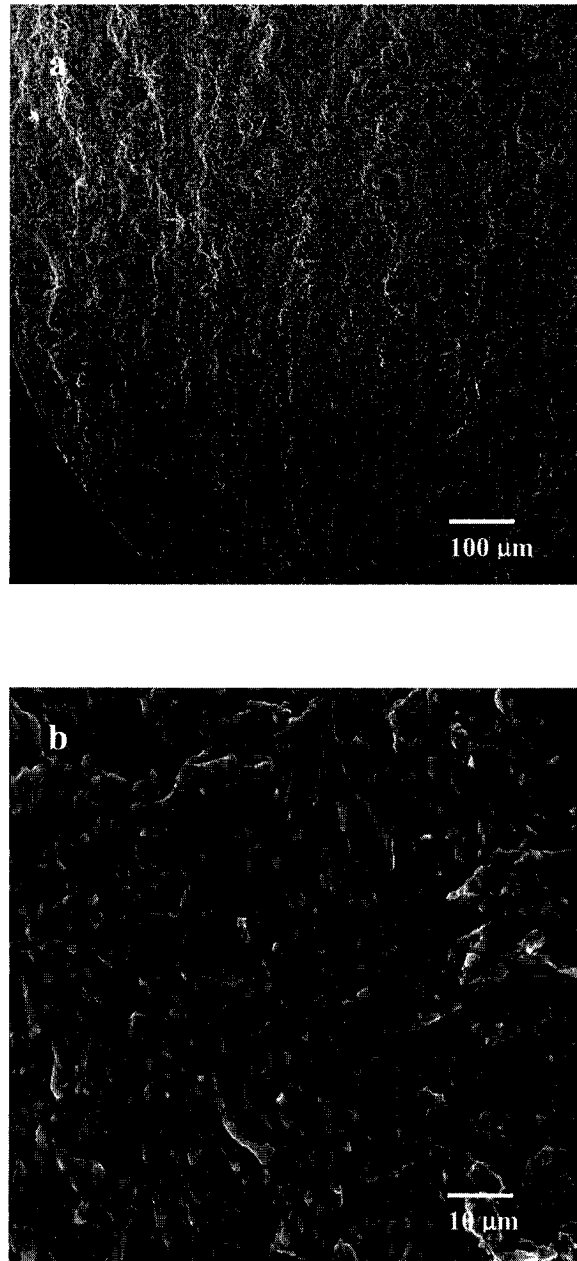
Figure 5.67:Scanning electron micrographs showing HCF
          fracture surface features of the Z6/SiC/20p-F
          composite deformed at cyclic stress amplitude of
          184 MPa, N_f = 162,197 cycles, showing: (a) overall
          morphology, (b) randomly distributed microscopic
          cracks on transgranular fracture surface.
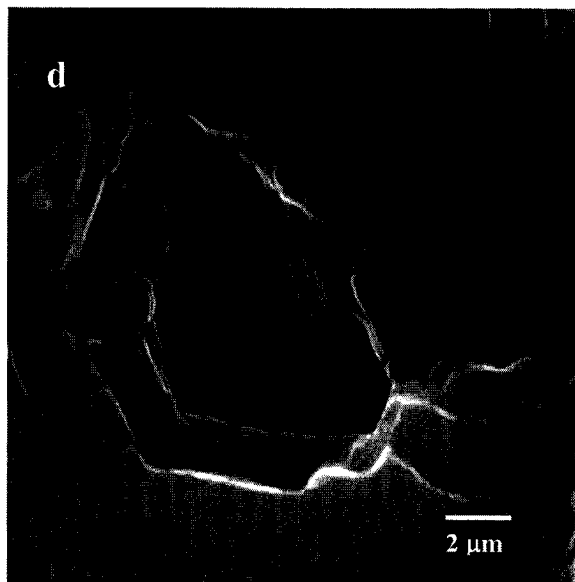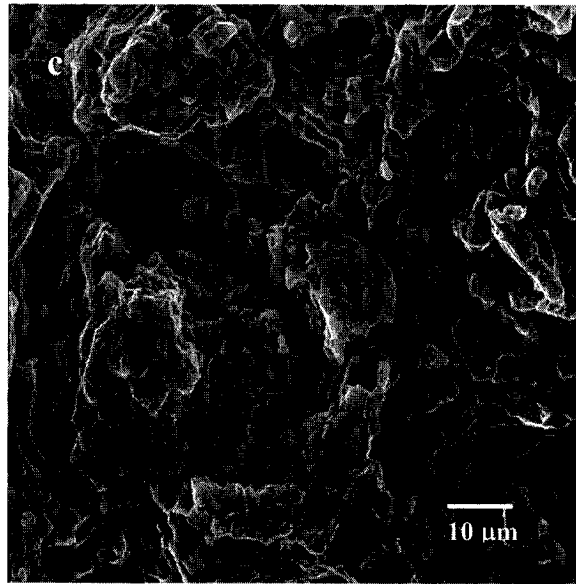
Figure 5.67 (Cont.): Scanning electron micrographs showing
HCF fracture surface features of the Z6/SiC/20p-F
composite deformed at cyclic stress amplitude of
184 MPa, N_f = 162,197 cycles, showing: (c)
microcrack, dimples and voids, (d) void
coalescence.
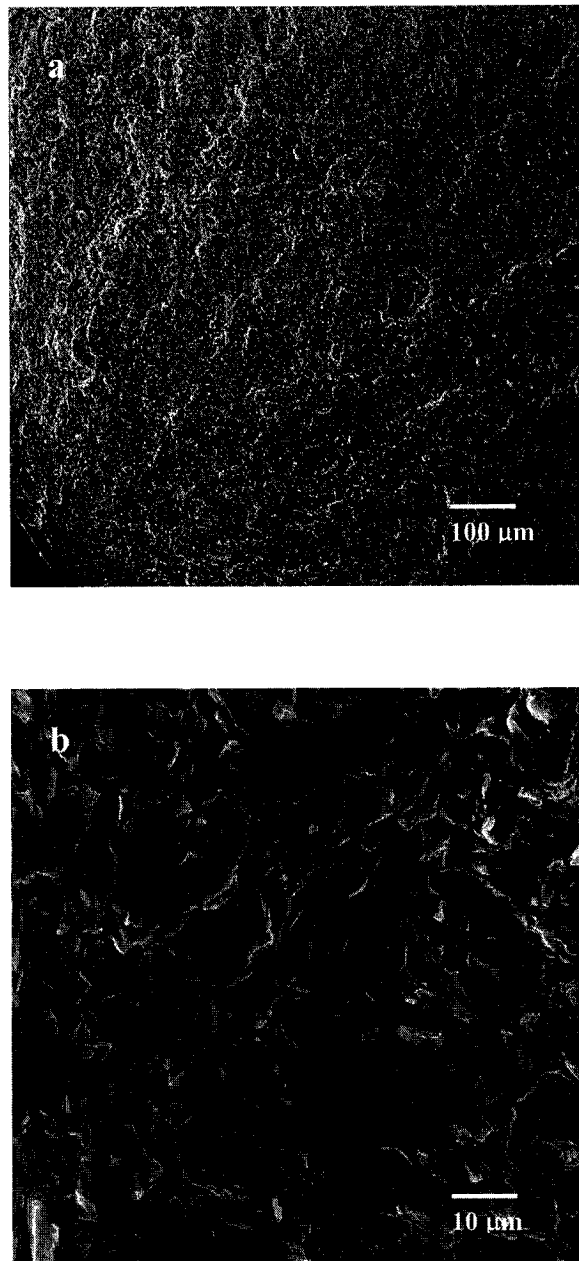
Figure 5.68:Scanning electron micrographs of the fatigue
           fracture surface features of the Z6/SiC/20p-F
           composite deformed at cyclic stress amplitude of
           151 MPa, N_f = 114,490 cycles at 150 °C, showing:
           (a) overall morphology, and (b) microscopic cracks
           in transgranular fracture surface.
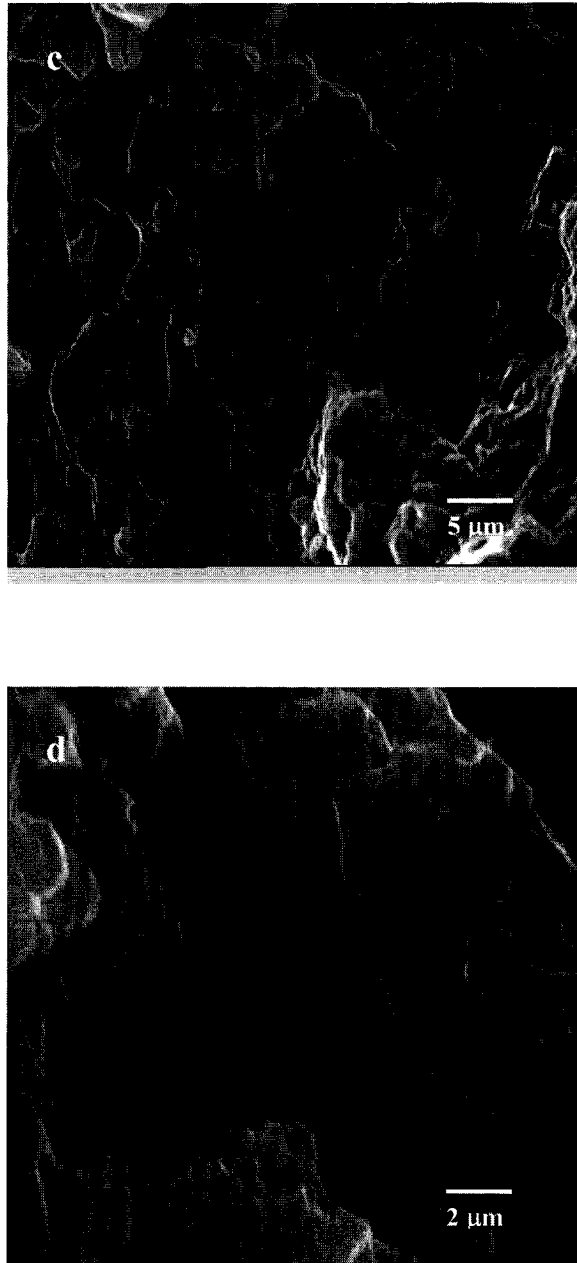
Figure 5.68 (Cont.): Scanning electron micrographs of the
fatigue fracture surface features of the
Z6/SiC/20p-F composite deformed at cyclic stress
amplitude of 151 MPa, N_f = 114,490 cycles at 150
°C, showing: (c) voids shallow dimples and
microcracks, and (d) SiC particulate cracking.

concentrators in the magnesium alloy metal matrix. The larger dimensions of the reinforcing SiC$_p$ facilitate a greater degree of stress transfer from the plastically deforming magnesium alloy metal matrix to the elastically deforming SiC particulate. The smaller SiC$_p$ do not crack easily. However, on account of intrinsic strain differences between the plastically deforming metal matrix and elastically deforming SiC particle, the process culminates in the occurrence of separation, or decohesion, at its interfaces with the metal matrix. The tendency for SiC particulate fracture is higher in regions containing a high local particulate volume fraction. This arises from increased local stresses caused by a restriction of the plastic zone surrounding neighboring particles. Also, the short interparticle distance associated with SiC particulate clustering facilitates rapid linkage between neighboring voids. The coalescence of the fine microscopic voids results in pockets of shallow dimples observed on the fatigue fracture surface (Figure 5.68c) [137].

At a lower cyclic stress amplitude of 124 MPa (N_f = 364,874 cycles) the region of detectable crack formation and early growth was rough on a microscopic scale (Figure 5.69a) and revealed evidence of a population of macroscopic and microscopic voids (Figure 5.69b). Progressive void growth with continued cyclic stressing, and eventual coalescence
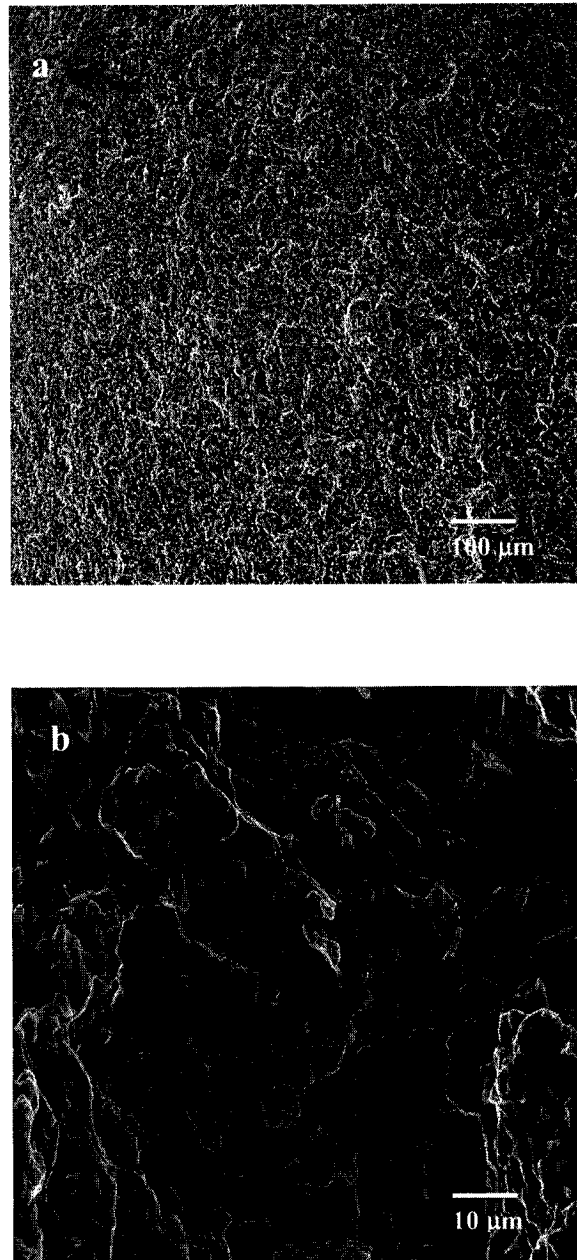
Figure 5.69:Scanning electron micrographs of the fatigue
fracture surface features of the Z6/SiC/20p-F
composite deformed at cyclic stress amplitude of
124 MPa, N_f = 364,874 cycles, showing: (a) overall
morphology, and (b) high magnification of (a)
showing population of microscopic voids.

of the macroscopic and microscopic voids culminates in fracture. The growth of voids is essentially a cavity enlargement process, which is enhanced by localized plastic deformation. The coalescence of the macroscopic voids is aided by the fine microscopic voids in the microstructure (Figure 5.69d). The overload fracture surface revealed evidence of SiC_p cracking (Figure 5.69c) and numerous microscopic cracks (Figure 5.69d). The fracture surfaces revealed features reminiscent of locally ductile and brittle failure mechanisms, namely, microscopic voids, dimples, SiC particulate cracking, and microscopic cracks. During cyclic deformation the large mismatch in strain that exists between the hard, brittle and elastically deforming particle and the soft, ductile and plastically deforming metal- matrix results in a concentration of stress at and near the reinforcement particle causing it to fail by cracking (Figure 5.69c). The void nucleation and cracking of the SiC_p suggests that local plastic strains dominate in regions containing a high volume fraction of the particulate reinforcement [137].

Fracture of the reinforcing SiC_p, in the plastic zone ahead of an advancing crack, generates conditions conducive for crack tip extension, which in turn aids in enhancing the crack propagation rate. For a constant volume fraction of the SiC_p reinforcement the tendency for it to fracture is
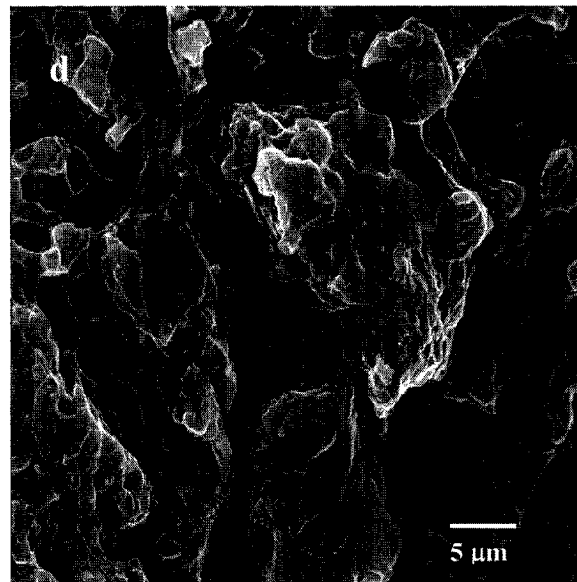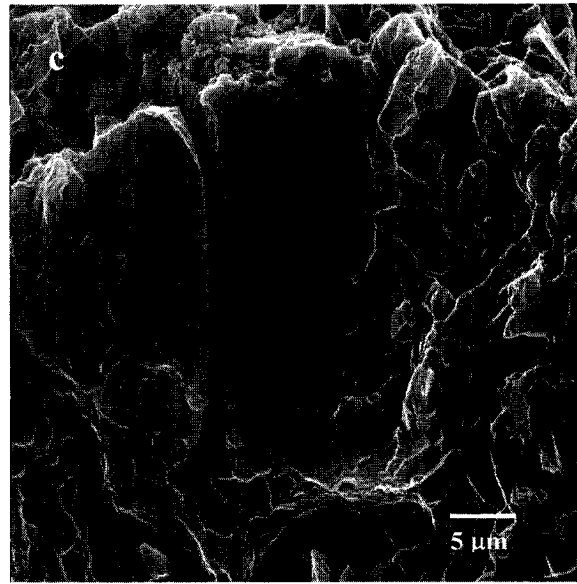
Figure 5.69 (Cont.): Scanning electron micrographs of the
        fatigue fracture surface features of the
        Z6/SiC/20p-F composite deformed at cyclic stress
        amplitude of 124 MPa, N_f = 364,874 cycles,
        showing: (c) cracked SiC particulate, and
        (d) region of overload showing microscopic cracks
        and dimples.

greatest when the tensile stress exceeds the fracture strength of the particle. A progressive increase in localized stress concentration causes the initiation of micro-cracking at the SiC_p either individually dispersed or in clusters, while concurrently favoring decohesion at their interfaces with the metal matrix [137].

Numerous microscopic cracks are formed at the reinforcing SiC particulates. Besides, the matrix between particulate clusters is subjected to high triaxial stresses, which favors fracture of the matrix and exacerbates microscopic crack initiation at the reinforcing SiC particulates [137]. The microscopic cracks grow through the particulate clusters and link by fast fracture through the matrix to adjacent SiC particles resulting in a macroscopic crack. Rapid propagation of the macroscopic cracks along with the microscopic cracks is responsible for the inferior cyclic stress resistance at ambient temperature (27 °C). Particulate fracture aided by decohesion at interfaces with the metal matrix, void nucleation, growth and coalescence serves to increase the rate of crack growth by providing conditions conducive for crack-tip extension. For a constant reinforcement volume fraction, the probability of the reinforcing particle to fracture increases at the higher cyclic stress amplitudes and concomitant short fatigue life [137].

CHAPTER VI

MODELING TECHNIQUES

6.1 <u>Outline</u>

In the first section, finite element simulations using

the ABAQUS software, were computed using the periodical

unit cell model with the objective of illustrating and

confirming clustering and distribution effects of the

particulate reinforcement on mechanical properties of

aluminum metal matrix composites.

For cyclic fatigue, two types of modeling schemes were

evaluated. The fatigue damage evolution model was used to

predict the cyclic-stress controlled response. In, the last

section, is demonstrated a methodology of incorporating

microstructural parameters determined from experimental

investigation for simulating the cyclic-plastic strain

controlled response.

6.2 <u>Quasi-Static Prediction Model</u>

The complete analysis of a material system with the

matrix and reinforcement phase represented separately and

using realistic reinforcement geometries and distribution

255

is currently beyond computational capabilities, many
descriptions of composite are based on periodic unit cell
approaches. In the periodic unit cell approach the
microstructural geometry is divided into unit cells that
are periodically repeating. However this does limit the
investigation without greatly altering the overall
generality.

6.2.1 Periodic Unit Cell

The finite element analysis of composite materials has
traditionally been based on the unit cell model. In this
model the reinforcement is assumed to be symmetrical in
shape, and distributed periodically in the metal matrix.
Morphology of the reinforcement has an influence on
mechanical properties of the composite. A composite
material reinforced with angular particles tends to fail by
cracking of the particles, while the composite material
reinforced with spherical particles tends to fail by a
combination of void nucleation, growth, and coalescence in
the metal matrix adjacent to the reinforcing particles
[138]. The effect of particle corners in promoting damage
is different for different composites. Experimental
evidence has convincingly shown that in some composite
materials, the voids nucleate preferentially at the corners

of particles [139]. Slip band initiation and concentration occur at the corners of particles in a region of agglomeration of particles [131]. The unit cell model containing cubic or rectangular particles has been used to analyze the detrimental influence of particle corners [140]. The composite material reinforced with spherical-shaped particles exhibits a lower yield strength and work hardening rate, but considerably higher ductility than the metal matrix reinforced with angular particles [82]. Shen [68] found the square unit cylinder to have the highest average axial stress compared to the double-cone, sphere truncated cylinder.

It is for this reason having cylindrical morphology particles are considered more realistic than those, which are spherical since optical micrographs of the composite reveal the particles to have sharp corners. However, in this study the effects of particle morphology are not considered.

For particulate-reinforced metal matrix composites (PMMCs) a change in fatigue crack initiation site from coarse intermetallic inclusions and particulate clusters at ambient temperature to the matrix at the higher temperature is best explained from the numerical results of Llorca

[141]. He represented the composite material as a three-dimensional array of hexagonal prisms, with each prism containing one ceramic particle at its center (Figure 6.1). The ceramic reinforcements were considered to be cylindrical in the shape, with the cylinder axis being parallel to the prism axis, and the cylinder length equal to the diameter. This geometry has been recognized to be a good approximation of particles having irregular shape and sharp corners. Due to periodic distribution of the reinforcement, the overall composite response under uniaxial deformation is obtained from an analysis of one prism and using periodic boundary conditions. The hexagonal prism is approximated to be a cylinder, whose behavior is studied using finite element analyses of an axisymmetric unit cell (Figure.6.1).

6.2.2 Model Theory

The basic equations for the elastic-plastic response model provided in ABAQUS [142] have the same general form based on the theory of incremental plasticity. The plasticity models are taken to be rate-independent. When deformation is small, (ε_{ij}) the response is elastic and stress (σ_{ij}) in an isotropic solid is given by
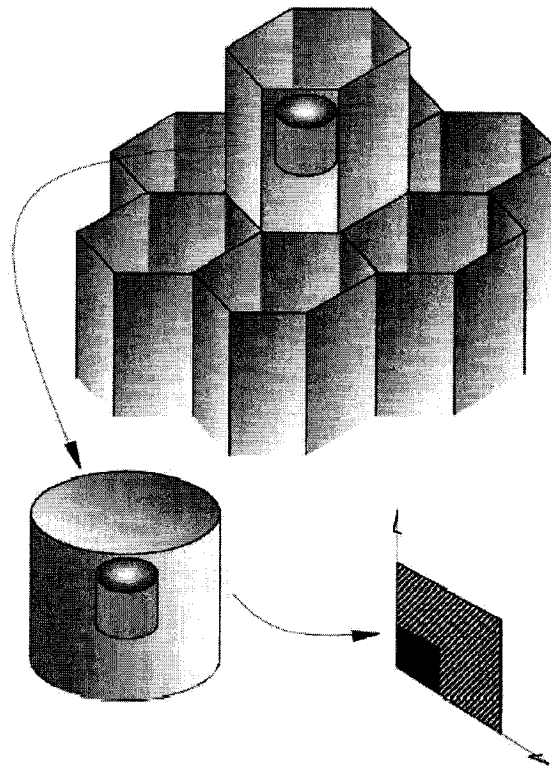
Figure 6.1:Composite idealization as a three-dimensional
array of hexagonal prisms, each containing a
cylinder oriented in the prism axis at the
center. Each hexagonal prism can be approximated
by a cylindrical cell, whose deformation under
uniaxial loading can be analyzed in two
dimensions owing to the axial symmetry of the
cell and of the boundary conditions [141].

$$\sigma_{ij} = \frac{E}{1+v}\left(\varepsilon_{ij} + \frac{v}{1-2v}\varepsilon_{kk}\delta_{ij}\right) \qquad (6.1)$$

where E is Young's modulus and v is Poisson's ratio. The flow theory (J_2) is used to determine the general elastic-plastic stress state. The deviatoric stress (S_{ij}) is defined as:

$$S_{ij} = \sigma_{ij} - \frac{1}{3}\delta_{ij}\sigma_{kk} \qquad (6.2)$$

For an isotropic material [142]

$$d\sigma_{ij} = \frac{E}{1+v}\left(d\varepsilon_{ij} + \frac{v}{1-2v}d\varepsilon_{kk}\delta_{ij} - \frac{3}{2q^2}\frac{S_{ij}S_{kl}d\varepsilon_{kl}}{\left[1+\frac{2}{3}(1+v)(E_t/E-E)\right]}\right) \qquad (6.3)$$

where the Von Mises stress say (q) is defined by the stress invariant

$$q = \sqrt{\frac{3}{2}S_{ij}S_{ij}} \qquad (6.4)$$

and E_t is the tangent modulus. The equivalent plastic strain is given by the expression [142]

$$d\varepsilon_p = \sqrt{\frac{2}{3}d\varepsilon_{ij}^p d\varepsilon_{ij}^p} \qquad (6.5)$$

$$\varepsilon_{ij}^p = \varepsilon_{ij} - \varepsilon_{ij}^e$$

$$\varepsilon_{ij}^e = \left[(1+v)\sigma_{ij} - v\sigma_{kk}\delta_{ij}\right]/E \qquad (6.6)$$

where ε_{ij}^p is the plastic strain and the elastic strain is ε_{ij}^e

The increment in plastic strain components is expressed as [142]

$$d\varepsilon_{ij}^p = \frac{3}{2}\frac{S_{ij}}{q}d\varepsilon_p \qquad (6.7)$$

Furthermore, the increment plastic strain is determined using the flow rule [142]

$$d\varepsilon_{ij}^p = \frac{\partial f}{\partial \sigma_{ij}}d\lambda \qquad (6.8)$$

where f is the yield function and

$$d\lambda = \frac{d\varepsilon_p}{2\sqrt{f}} \qquad (6.9)$$

The equivalent stress for an isotropic material is given by as:

$$\sigma_e = \sqrt{f} \qquad (6.10)$$

6.2.3 <u>Model Implementation</u>

The particulate-reinforced metal matrix composite (PMMC) is modeled using a periodic array of unit cells, each cell containing elastically deforming SiC particles and an elastic-plastic aluminum matrix. The elastic constants for SiC were obtained from materials handbook [143]. The elastic and plastic properties of the aluminum alloy matrix were determined from the calculated true

stress-true strain curve obtained from the tensile data at room temperature. The interface between the metal matrix and the reinforcing particles is assumed to be perfectly bonded.

In the unit cell model, the effect of modeling two-dimensional (2D) using plane strain elements was considered. A preliminary simulation was done using the experimental stress-strain test data as input properties. The simulation used generalized plane strain deformation. The finite element analysis was applied to one quadrant of the unit cell. The finite element mesh over the quadrant was generated using the ABAQUS pre-processor and 2139 8-noded biquadrilateral elements having reduced integration were used to mesh the geometry with the volume fraction of 15% and is shown in Figure 6.2.

The boundary conditions are implemented by constraining the bottom and left edge of the quadrant in the axial direction to have zero displacement (Figure 6.2). Uniform displacements are applied to the top edge (U_2) to cause axial straining of the cell and the outer edge is constrained to remain straight by using uniform solution dependent displacement (U_1), which keeps nodes on a same straight line while allowing facilitating relative movement
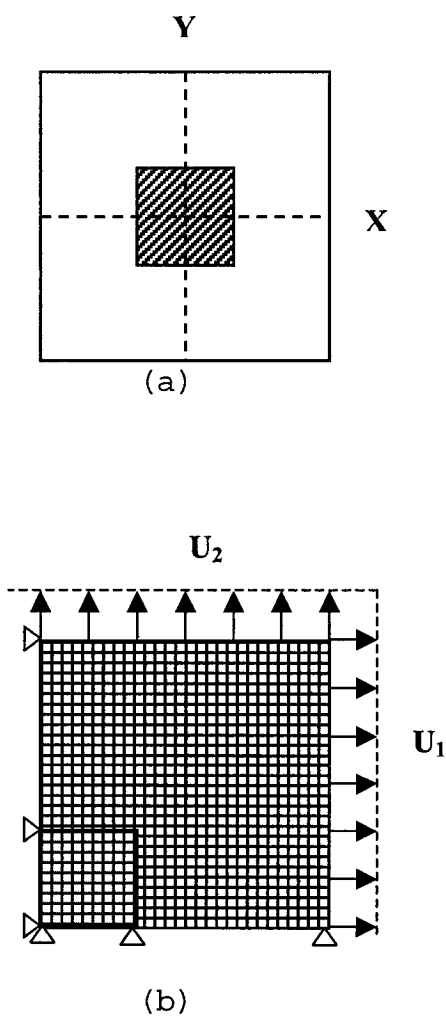
Figure 6.2: Two-dimensional (2D) (a) unit cell with a square reinforcing particle with lines of symmetry and (b) one quadrant of the 2D unit cell for modeling [68].

along the line. This is not a complete implementation of the boundary conditions since the outer edge, although straight, can rotate in the plane of the quadrant resulting in the possibility of the quadrant becoming non-rectangular in shape during deformation. This is a relaxation of constraint and hence results in a softer stress-strain response [65,144] and the softening effect is expected to be small. The applied cell boundary displacements determine the average tensile strain. The boundary reaction forces were averaged over the top boundary to calculate the average tensile stress of the material.

6.2.3.1 Uniformly Distributed Particles

The equivalent plastic strain for a 2D unit cell quadrant for a square particle model is shown in Figure 6.3. The plastic deformation patterns were characterized by bands of plastic strain in the matrix, oriented at 45° to the loading direction. The plastic strain was localized at the particle-matrix interfaces and reached the highest intensity at the sharp corner of the particle. The corners of the reinforcing particle play a significant role in constraining plastic flow in the metal matrix that has or exerts a critical influence on overall composite strength. The effect on global stress-strain curve is shown in
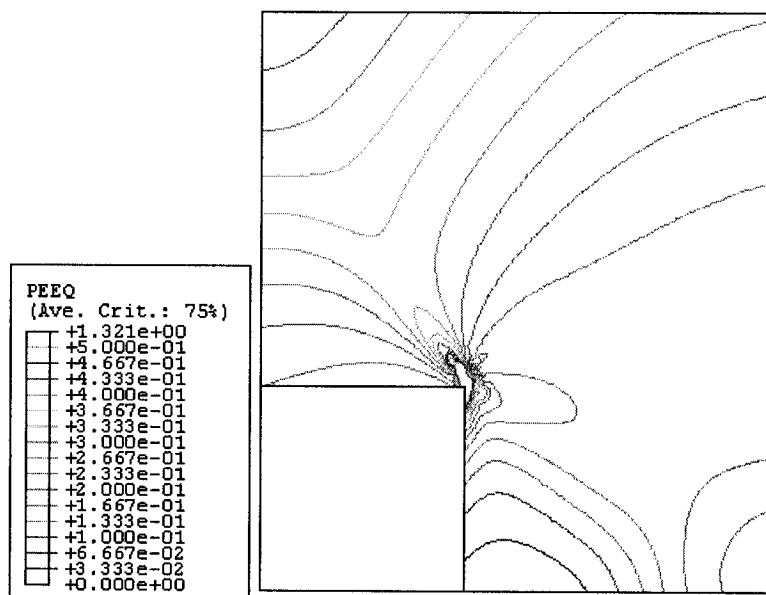
Figure 6.3: The contour plot of equivalent plastic strain for a two-dimensional (2D) square particle for the 2009/SiC/15p composite.

Figure 6.4. This model provided reasonable prediction of the tensile response of the particle-reinforced metal matrix composite, with a deviation of about 11% between the predicted value and experimental measurement of flow stress.

6.2.3.2 Effect of Clustering Particulate

This section focuses on an evaluation of the performance of the model considered in the first section but for different reinforcement distribution. Christman [144] in his study showed that clustering resulted in a radical decrease in flow stress of the composite containing whiskers but had has little influence when the reinforcing particles are considered as unit squares. Corbin [145] suggested that a composite material containing clustered spheres has much higher flow stress than a composite having homogeneous distribution of particles. So the role of particle distribution a lot of data and analysis exist in the published literature showing the clusters to impose additional constraints on plastic flow and the flow stress of a composite having particulate clusters to be higher than the flow stress of a composite having uniform distribution of the reinforcement.
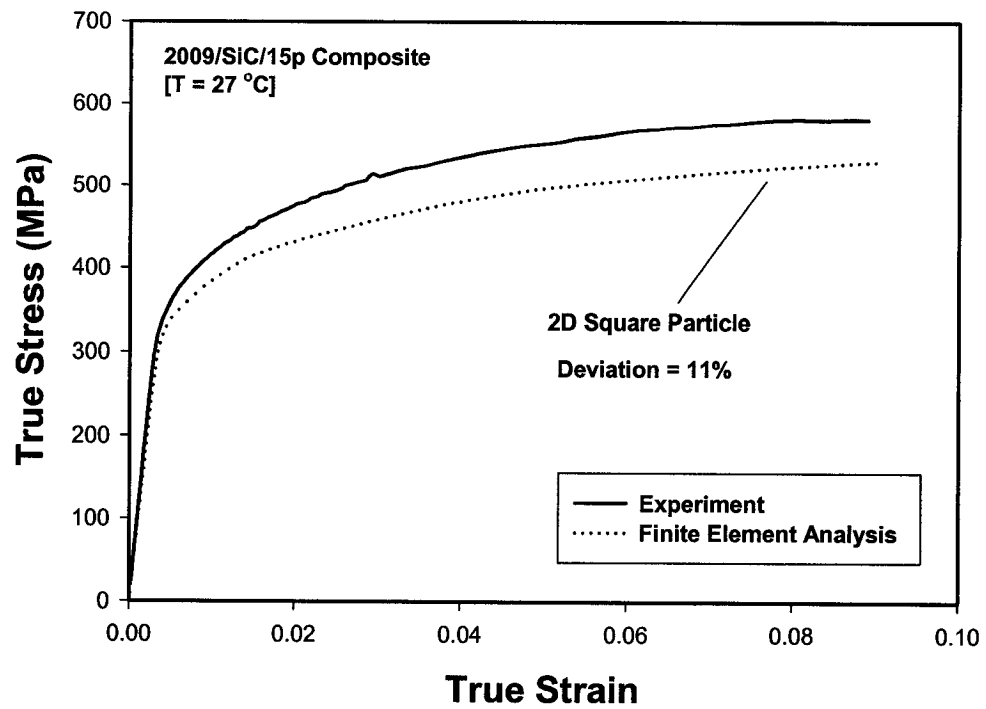
Figure 6.4: A comparison of the finite element prediction
model with unit cylinder and experimental results
of the response of 2009/SiC/15p composite.

The model introduced by Shen, Finot, Needleman, and Suresh [68] was used to study the effects of spatial distribution of the reinforcement. The plane strain formulation is sufficient for capturing the trends associated with clustering of the particulate reinforcement. The particle shape is taken to be square, in order to reflect the two-dimensional (2D) geometry of a unit cylinder, and two sizes of the reinforcement are considered to exist in the composite material.

The two configurations for uniformly dispersed particles are shown in Figure 6.5. The dashed lines represent the unit cell and quadrants analyzed numerically. The configurations considered are obtained by changing the relative size of the two groups of particles while keeping the overall particle area fraction constant, as shown in Figure 6.6. The particles are equal in size in Figure 6.6 (d) and (h). Figure 6.1b and Figure 6.6h represent different unit cells for the same square packing arrangement. The diagonal packing arrangement is shown in Figure 6.6d. Figures 6.6(a), (b), (c) and (d) are obtained from Figure 6.5 configurations a, while Figures 6.6(e), (f), (g) and (h) are obtained from Figure 6.5 configurations b [68].
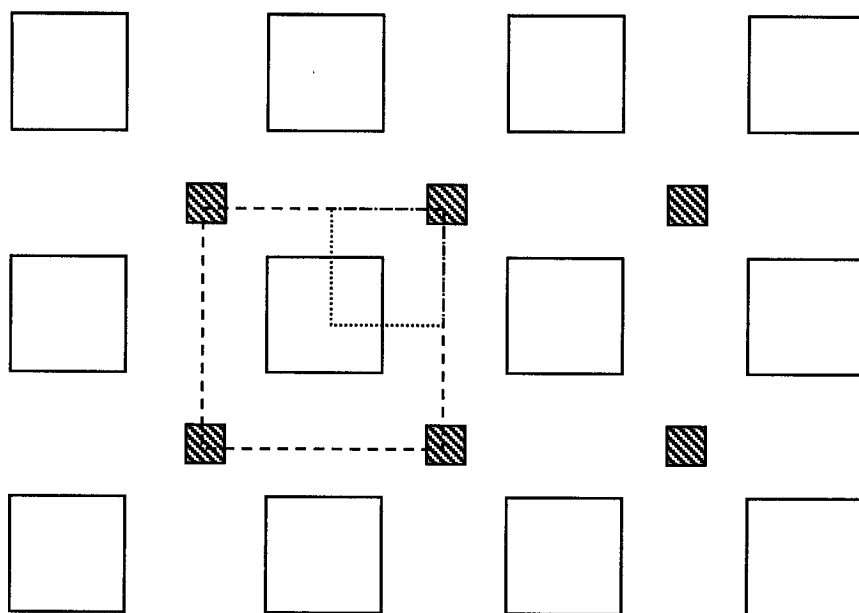
(a)
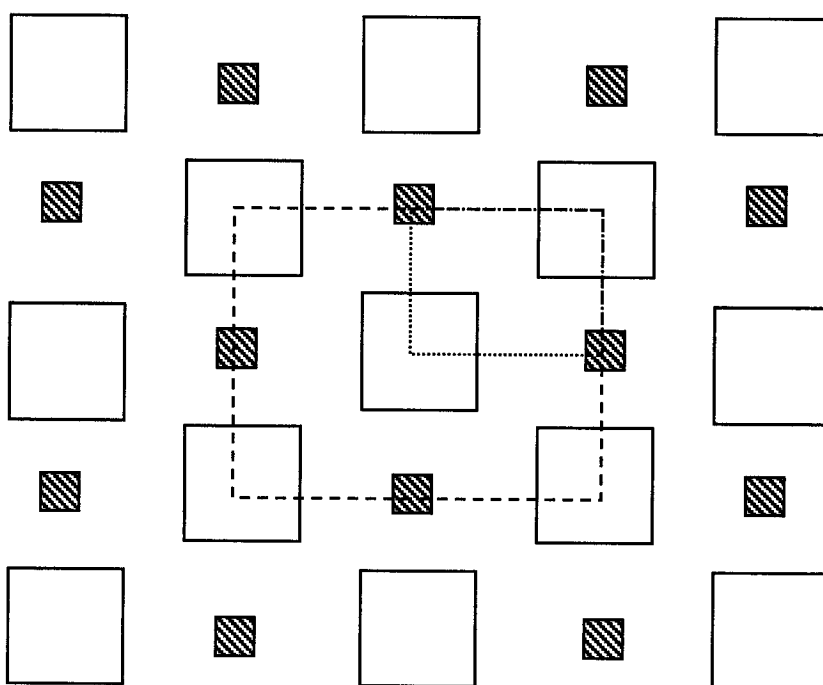
(b)

Figure 6.5: Schematic diagram showing two configurations of
uniformly dispersed particles. Two different
sizes of particles are considered to exit in the
composite. The dash lines represent the unit
cells and the quadrants used for finite element
modeling [68].

h/H = 1/4

(a)   (e)

h/H = 1/2

(b)   (f)

h/H = 3/4

(c)   (g)

h/H = 1.0

(d)   (h)
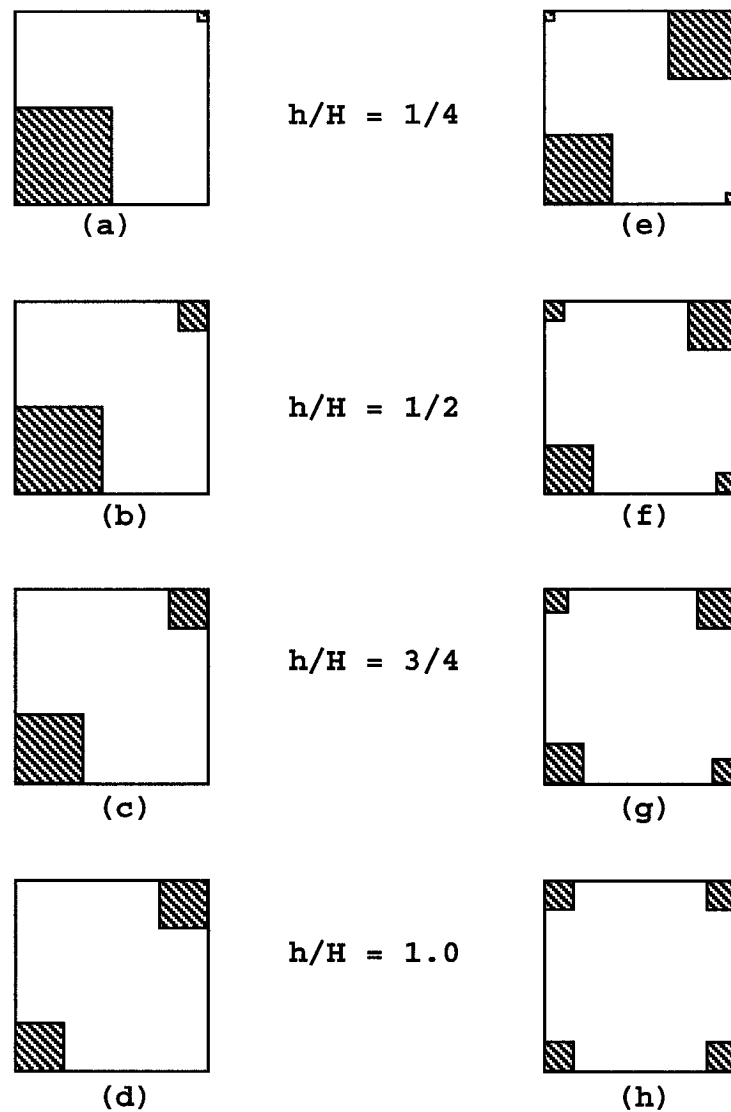
h: side length of small particles
H: side length of large particles

Figure 6.6: Schematic diagram showing configurations associated with different sizes and spatial distributions of the particles [68].

The influence of particle size and spatial distribution on tensile stress-strain response is shown in Figure 6.7. The effect of particle distribution on overall strength of the composite was found to follow similar trend for both configurations (a) and (b). A near equal size of the reinforcing particles demonstrates the pronounced effect of clustering on macro-response of the composite Figure 6.8.

The contour plots depicting effective plastic strain in the composite matrix for different distribution of the unit cylinders are shown in Figure 6.9 and Figure 6.10. In Figure 6.3 the concentration of deformation occurs near the particle corner and at corners of the unit cell. A equivalent pattern of band distribution in the unit cell having smaller concentration value of maximum plastic strain is shown in Figure 6.9d and Figure 6.10h. These broaden of matrix plastic flow leads to influence the overall response of the composite. The deformation zone in Figures 6.9a,b and c is wider than the deformation zone in Figure 6.3. A similar analysis is made for Figure 6.10e, f and g having a significant concentration of deformation near the corner of a large reinforcing particle, while plastic deformation is small near the corner of a small
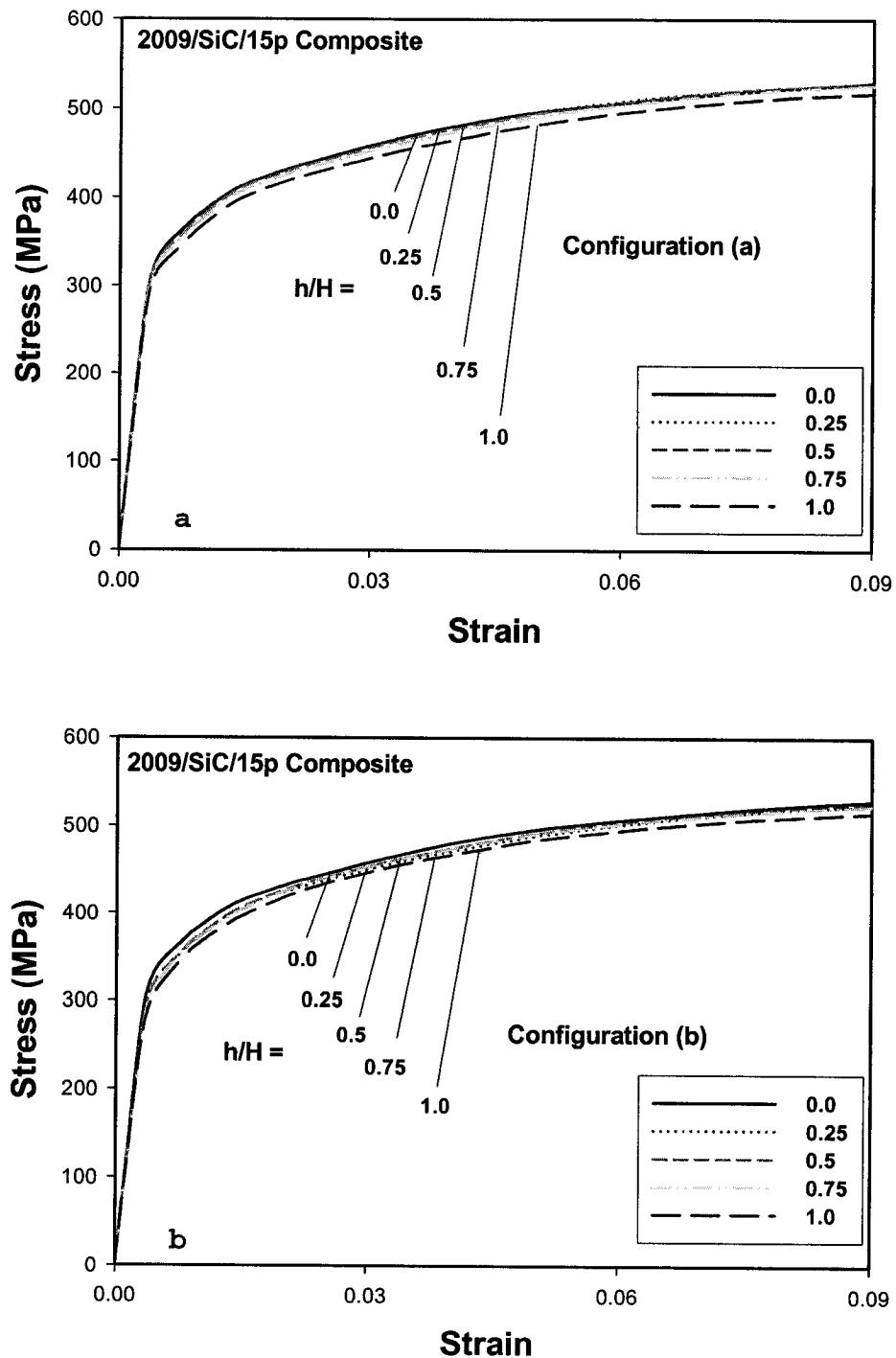
Figure 6.7: Finite element predictions of the effects of
different particles distribution on the
constitutive behavior of 2009/SiC/15p unit
cell:

(a) Configuration (a) (b) Configuration (b)
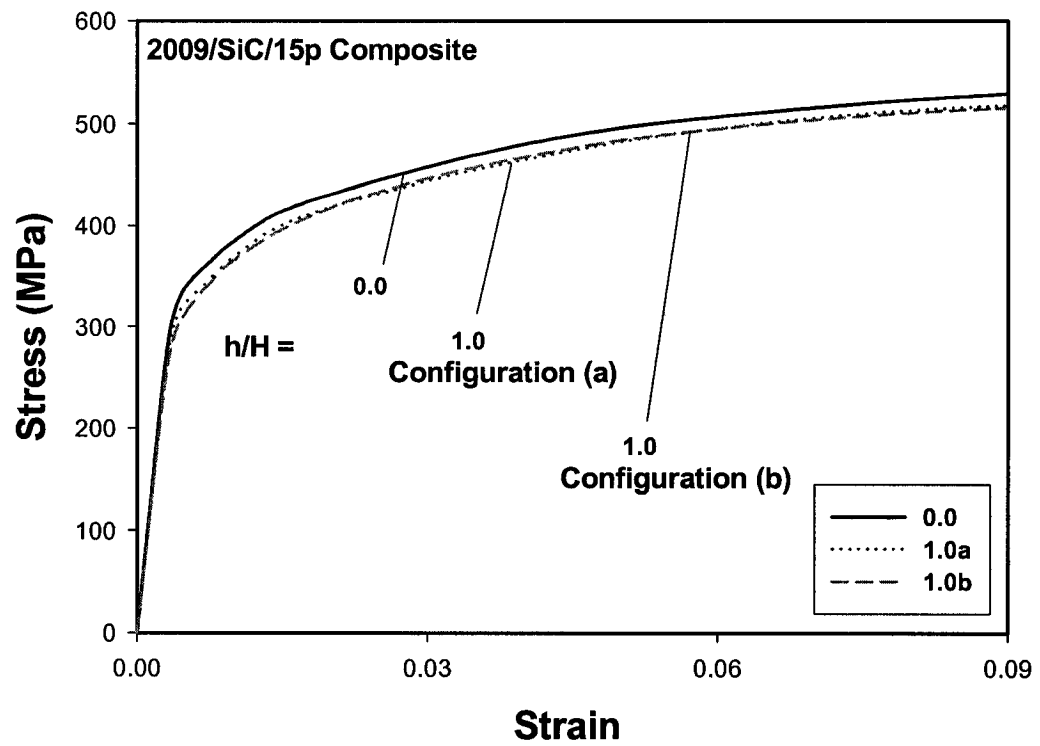
Figure 6.8:Finite element predictions of the effects of
particles distribution with size ratio of 1.0
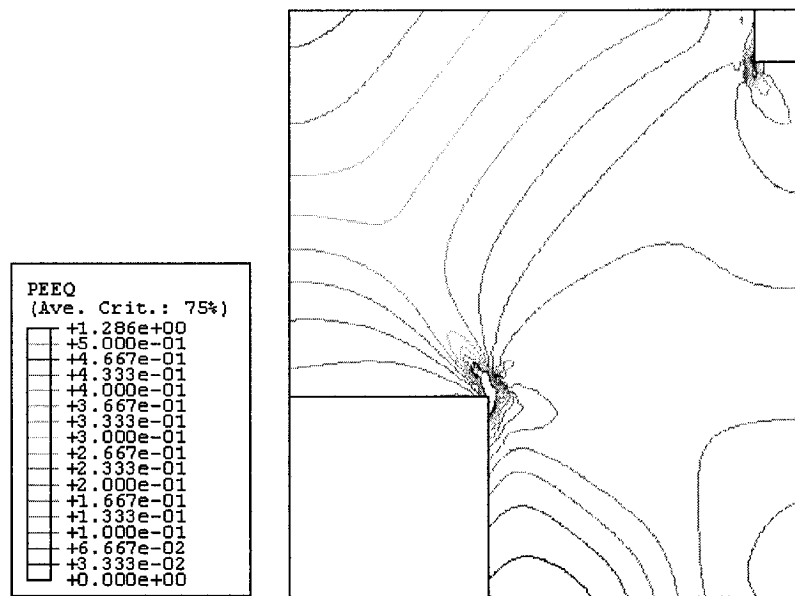
(a)
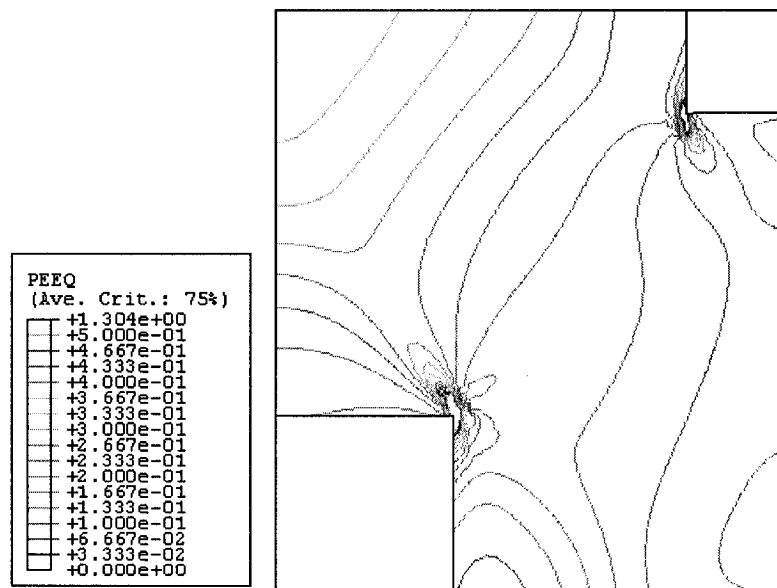
(b)

Figure 6.9:Contours plot of equivalent plastic strain for
2D at different particles configurations (a)
(a) h/H = 1/4   (b) h/H = 1/2
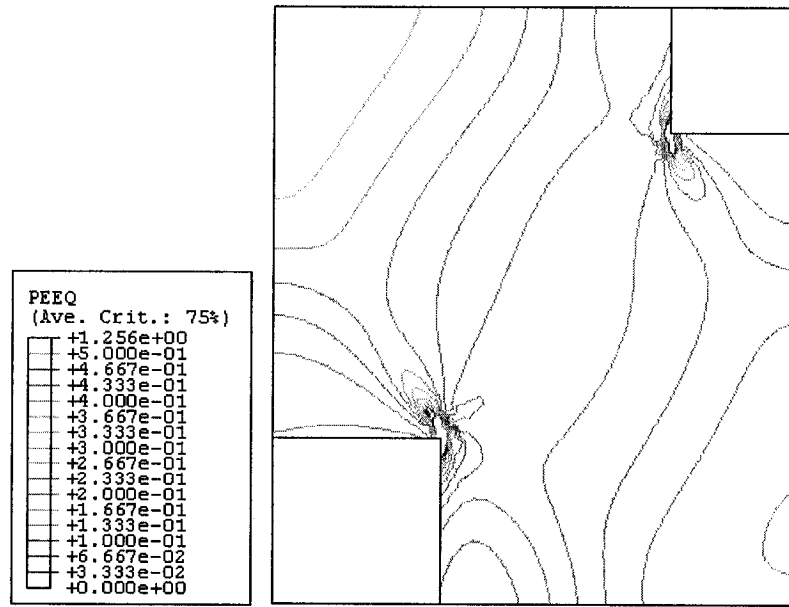
(c)
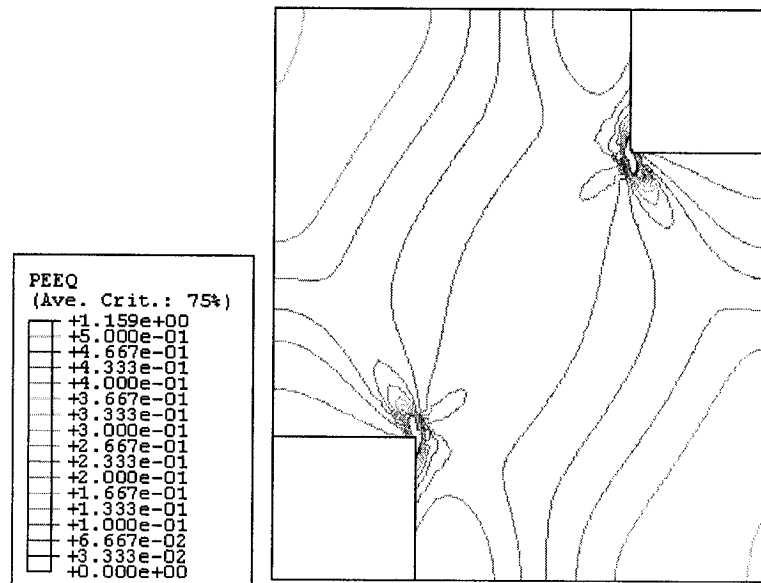
(d)

Figure 6.9 (Cont.): Contours plot of equivalent plastic
strain for 2D at different particles
configurations (a) (c) h/H = 3/4   (d) h/H = 1.0

(e)

(f)
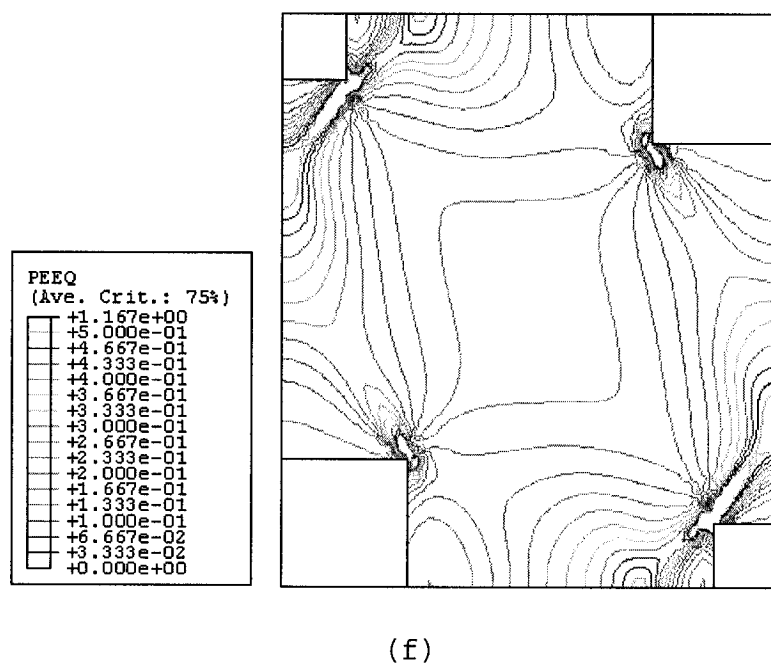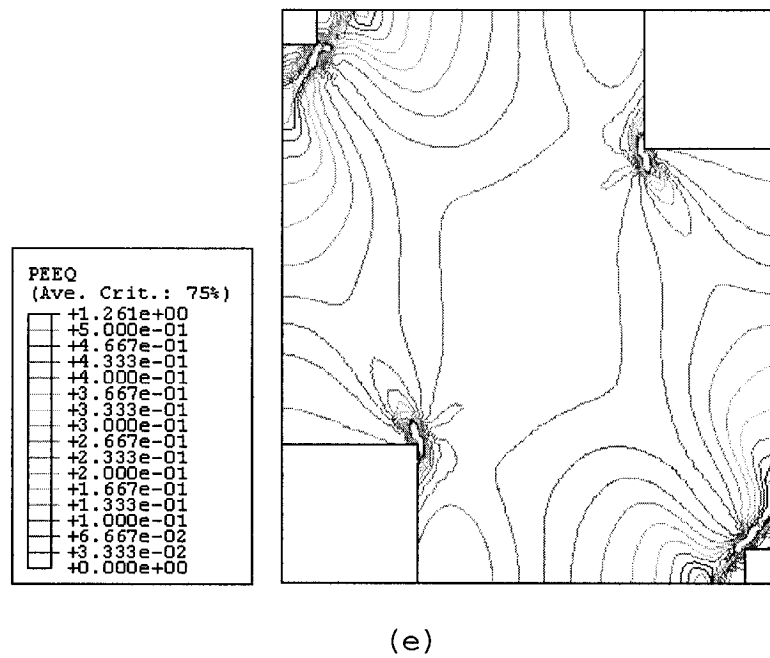
Figure 6.10: Contours plot of equivalent plastic strain for
2D at different particles configurations (b)
(e) h/H = 1/4   (f) h/H = 1/2
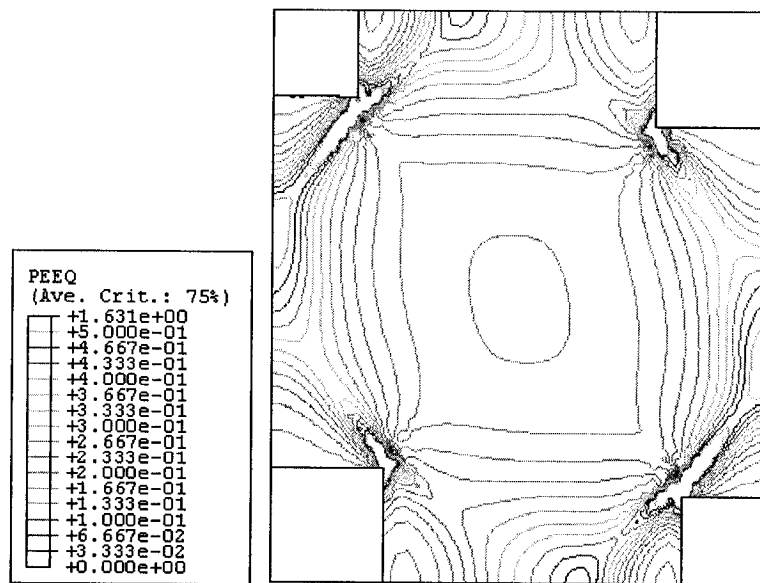
(g)
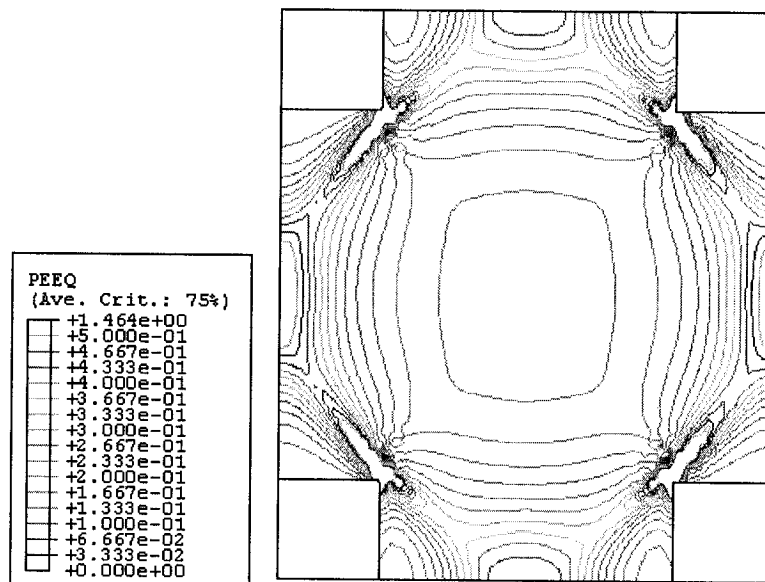
(h)

Figure 6.10 (Cont.): Contours plot of equivalent plastic
strain for 2D at different particles
configurations (b) (g) h/H = 3/4   (h) h/H = 1.0

particle. The small particles essentially make minimal

contribution to strengthening when the size difference

between the two families of reinforcing particles is

sufficiently large. A lack of significant changes in matrix

constraint due to size differences seems to produce overall

plastic response, which is very similar to the composite

having a uniformly distributed unit cell.

6.2.4 Model Discussion

By using the periodic unit cell model a reliable

prediction of the mechanical response in tension of the

particle-reinforced metal matrix composite is achieved. The

effects of thermal residual stresses can be considered by

altering the stress-strain relationships of the matrix

[68]. However, it is difficult to experimentally obtain the

local residual stress field. For this reason an analysis of

the thermal residual stress is not considered in this model

and a study detailed representation of the matrix a

polycrystalline structure (microscale model did not

translate into significant changes in macroscale flow

stress level [146]) is of secondary importance. The

mechanical properties of the candidate composite material

can be improved if the reinforcing particle has a square

shape. This is because to the fact that if the aspect ratio

is equal to 1.0 and the reinforcing particles are uniformly distributed in the metal matrix, the void volume fraction spreads through the matrix and disperses into the area losing a wide range of its carrying capacity. Thus, it improves the load carrying capacity in these areas and concurrently increases the fracture strain [147].

The numerous effects of reinforcement particle distribution on overall stress-strain behavior of the composite material are noticeably less pronounced for the square unit cylinder approach, primarily because of a lack of significant changes in matrix triaxiality.

6.3 Cyclic-Stress Controlled Prediction Model

The statistical method, as an alternative approach to the deterministic method, has been extensively used after Weibull [148]. In this method Weibull applied the probabilistic model to predict failure of materials. Since then, many different approaches, such as: (a) the probability fracture mechanics model [149], (b) the non-equilibrium statistical fracture mechanics theory [150,151], and (c) the fractal statistical model [152-154] have been developed and tried.

The objective of this section is to present statistical model of fatigue damage evolution for particulate-reinforced metal-matrix composites (MMCs) by taking into consideration both: (a) the initial damage distribution, and (b) the effect of particulate-reinforcement on fatigue damage development during fatigue [154]. The process of fatigue failure in particulate-reinforced MMCs is one in which a large number of microscopically damaged regions, such as micro-cracking and voids, initiate and grow continuously in bulk of the composite under the influence of an applied cyclic stress, and the most critical flaw, propagates rapidly, terminating or causing catastrophic failure of the composite [154-155]. The growth of microscopically fatigue-damaged regions in particulate reinforced MMCs is considered to be a stochastic process, and both the non-equilibrium statistical method and minimum strength principle are used to establish an equation for the evolution of fatigue damage [154].

The key points in this development are:

- The microstructures of all MMCs have near uniform particle distributions.

- The fatigue damage events that occur in particulate-reinforced MMCs are (a) cracking of the particulate and/or intermetallic inclusion, cracking of the matrix, which includes hardening or softening of the matrix, and (b) interfacial decohesion at the matrix-particulate interfaces [5,156-165].

- For most particulate-reinforced MMCs, the macroscopic fatigue crack propagation law is described by the Paris law,

$$\frac{da}{dN} = A\Delta K^n \qquad (6.11a)$$

  The Paris equation was determined through experimental analysis [9,57,156-157,163-172]. A schematic plot depicting fatigue crack growth behavior is shown in Figure 6.11.

- An important feature of fatigue crack growth behavior for particulate-reinforced MMCs is that crack growth essentially occurs over a narrow range of ΔK. It is reported [9,57,156-157,163-172], that fatigue crack growth behavior is associated with the material matrix, but also, influenced by other factors, such as: (a) the properties of the particle, (b) particle morphology, (c) distribution of
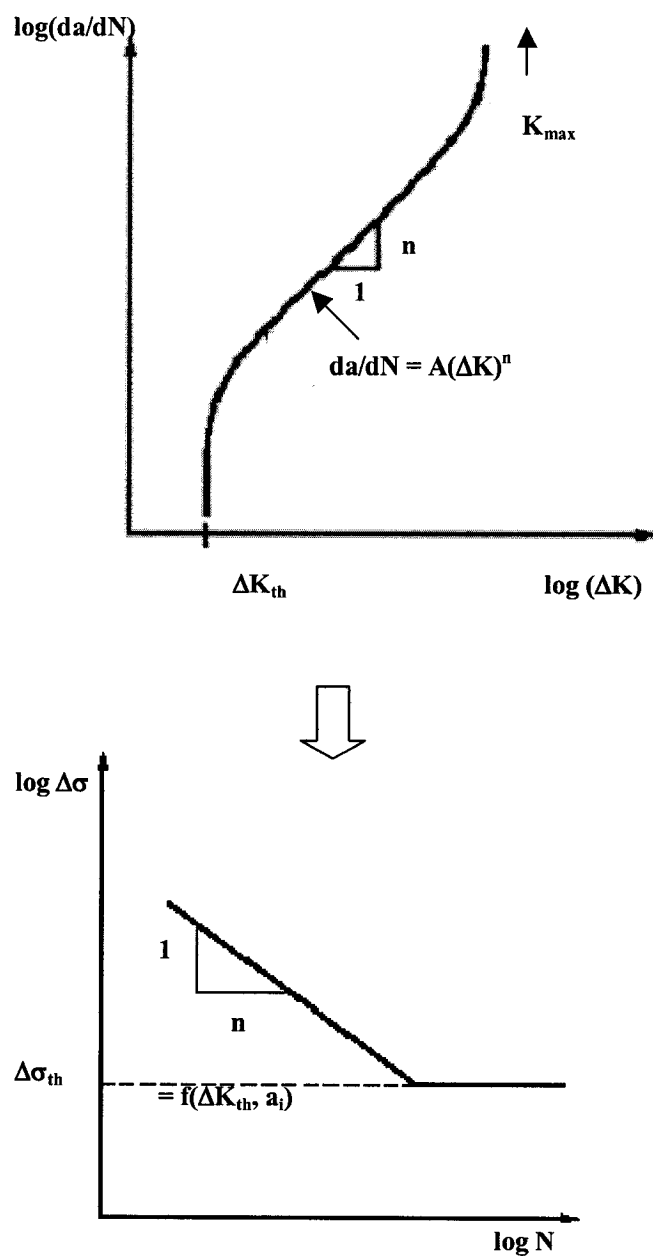
Figure 6.11: Typical plot of (a) fatigue crack growth
curve [154] and (b) S-N curve for monolithic and
particulate reinforced metal matrix composites.

particles, (d) volume fraction, and (e) nature of
loading condition.

- The development of damage in particulate-reinforced
  MMCs during fatigue loading is a cycle-dependent
  dynamic process caused by microscopic structural
  damage of different modes. The behavior of fatigue
  damage development is random and deterministic. Thus
  residual strength and life of the composite are
  essentially statistical in nature. Fatigue damage
  initiation and propagation in particulate-reinforced
  MMCs cannot be adequately addressed without an
  incorporation of geometric and material randomness
  [164-168].

The deterministic approach equation for the rate of
change of a given fatigue-damage region is made stochastic
by the addition of a random term, (i.e., it is assumed that
the equation governing macroscopic fatigue crack growth
rate is approximate). During actual service, individual
fatigue-damaged regions depart from this behavior in an
unpredictable way. The factors responsible for the observed
randomness are the microstructure inhomogeneity of the
particulate-reinforced MMCs, which causes a variability in
the resistance of a material to fatigue crack growth along

the path of the crack, coupled with the random nature of the stresses during fatigue, which dominates the probabilistic approach to the problem in most applications. Therefore, the predicted cyclic growth rate of the fatigue-damaged region (a) is expressed in a unified form as [151,173-174].

$$da/dN = K(a) + \beta(a)\eta(N) \qquad (6.11)$$

Here $K(a)$ is the deterministic migration growth rate, which is determined by the average structure background of the particulate-reinforced MMCs and applied cyclic stress, $\eta(N)$ is the fluctuation function, which is related to the stochastic fluctuation of microstructure and applied cyclic stress, and $\beta(a)$) is a fluctuation magnifying function. The growth of the fatigue-damaged region is path-dependent, and depends entirely on the applied cyclic stress and intrinsic microstructure of the composite at that cycle and during its very recent past history. The term $\eta(N)$ is assumed to obey the Gauss distribution, which satisfies:

$$\langle\eta(N)\rangle = 0; \quad \langle\eta(N)\eta(N')\rangle = Q\delta(N-N') \qquad (6.12)$$

where Q is the fluctuation coefficient, which characterizes the effect of microstructure fluctuation on growth of the fatigue-damaged regions.

Taking equations (6.11) and (6.12) as the base and using the standard methods of stochastic equations [175], it was shown that the generalized approach equation (6.11) in conjunction with a well-known Stratonovich option [152] results in a partial differential equation that governs the distribution of fatigue-damaged region [P(a, N)] as [154].

$$\frac{\partial}{\partial N}P(a,N) = -\frac{\partial}{\partial a}\left[\left(K(a) + \frac{Q}{2}\beta(a)\frac{\partial\beta(a)}{\partial a}\right)P(a,N)\right]$$
$$+ \frac{Q}{2}\frac{\partial^2}{\partial a^2}\left[\beta^2(a)P(a,N)\right] \qquad (6.13)$$

Here, P(a, N) da is the probability that a fatigue-damaged region grows to a size between a and a+da following N cycles of cyclic loading.

Once the evolution of the fatigue-damaged region is definite, then, when it size reaches a critical value, the fatigue-damaged region will initially deform propagate culminating in failure. However, before real failure occurs, the microstrucural inhomogeneity in particulate-reinforced MMCs makes evolution of the fatigue-damaged region to be stochastic. Therefore, a large number of microscopically fatigue-damaged regions are considered, and fatigue failure probability of the particulate-reinforced MMCs is obtained from the minimum strength principle [154].

$$F\left[a(\Delta\sigma/_2),N\right]=1-\left[1-\int_{a(\Delta\sigma/_2)}^{\infty}P(a,N)da\right]^{\rho V} \qquad (6.14)$$

Here $a(\Delta\sigma/2)$ is the critical size of the fatigue-damaged region, which is monotonically decreasing of the applied cyclic stress amplitude $(\Delta\sigma/2)$, ρ is the density of the fatigue-damaged region, and V is the material volume. $F[a(\Delta\sigma/2),N]$ is then understood as the fatigue failure probability for the particulate-reinforced MMCs being under the action of applied cyclic stress amplitude between 0 and $(\Delta\sigma/2)$ for N cycles. Fatigue failure probability determined using equation (6.14) correlates with the mechanism of microstructural evolution while also characterizing the statistical representation of structure degradation. Therefore, the probability of failure due to fatigue or the fatigue damage parameter D, is expressed as [152-153],

$$D(\Delta\sigma/_2,N)\equiv F\left[a(\Delta\sigma/_2),N\right]=1-\left[1-\int_{a(\Delta\sigma/_2)}^{\infty}P(a,N)da\right]^{\rho V} \qquad (6.15)$$

This equation is applicable to different processes for the evolution of fatigue damage in various materials as long as the micromechanisms governing initiation and growth behavior of the microscopically fatigue-damaged regions are known [154],

$$\int_{a_o}^{\infty} P(a,N)da = 1 \qquad\qquad (6.15b)$$

From this we inform that $D(\Delta\sigma/2 = 0, N) = 0$, and $D(\Delta\sigma/2 \to \infty, N) = 1$.

Substituting equation (6.15) into equation (6.13), the equation evolution of fatigue damage can be obtained as [154]:

$$\frac{\partial D}{\partial N} = -\frac{1}{\rho}\frac{d\rho}{dN}(1-D)\ln(1-D) - \left[K(a)\frac{\partial D}{\partial a}\right]_{a(\Delta\sigma/2)}$$
$$+ \left\{\frac{Q\beta(a)}{2}\left[\frac{\partial\beta(a)}{\partial a}\frac{\partial D}{\partial a} + \beta(a)\frac{\partial^2 D}{\partial a^2}\right]\right\}_{a(\Delta\sigma/2)} \qquad (6.16)$$

From this equation a change in fatigue damage rate with the cycles is determined by the initiation, growth or fluctuation of microscopically fatigue-damaged regions, which are characterized by the terms $d\rho/dN$ (density of critical fatigue-damaged region), $K(a)$ (deterministic migration growth rate), $\beta(a)$ (fluctuation magnifying function) and Q (fluctuation coefficient). Also, equation (6.16) can not only characterize the kinetic processes dictating or governing fatigue damage evolution, but also set up a relationship between the mechanisms of fatigue damage growth of microscopically damaged regions and the overall result of fatigue damage, i.e., degradation of mechanical properties of particulate-reinforced MMCs. Most

importantly, the fatigue damage parameter is obtained by solving equation (6.16) when $\frac{d\rho}{dN}$, $K(a)$, $\beta(a)$ and Q, are known.

To relate fatigue crack growth rates to the underlying mechanism, it is assumed that the law governing growth of the microscopic fatigue-damaged region growth retains the features of the laws governing macro-crack propagation and is similar to the Paris equation.

$$\frac{da}{dN} = K(a) = A\Delta K^n = A(\frac{Y\Delta\sigma}{2})^n a^{n/2} \qquad (6.17)$$

Here: (a) $\Delta K = Y(\Delta\sigma/2)\sqrt{a}$ is the applied stress intensity factor range, (b) $\frac{\Delta\sigma}{2}$ is the cyclic stress amplitude, (c) A and n are material constants and (d) Y is the geometric factor of the fatigue crack.

The fracture toughness of the particulate-reinforced MMCs is calculated using the failure criterion proposed by Rice and Johnson [176]:

$$K_{Ic} = (2\sigma_{ys}E \times CTOD)^{1/2} \qquad (6.18)$$

Where the linear dimension of crack tip opening displacement (CTOD), has been replaced by size of the unbroken ligament between cracked particles. By assuming all particles in the vicinity of a crack-tip to either

rupture or decohere, equation (6.18) gives the relation [154]:

$$K_{Ic} = \left[2\sigma_{ys} E(\pi/6)^{1/3} d_p \right]^{1/2} f_p^{-1/6}$$ (6.19)

Here σ_{ys} is yield strength of the matrix, E is the Young's modulus of the matrix, d_p is the average size of the particulate reinforcement and f_p is the volume fraction of the reinforcement. The critical condition for the unstable propagation of fatigue cracks is [154]:

$$a(\Delta\sigma/2) = \left(\frac{K_{Ic}}{Y\Delta\sigma/2} \right)^2 = \frac{2\sigma_{ys} E\left(\pi/6\right)^{1/3} d_p}{\left(Y\Delta\sigma/2\right)^2 f_p^{1/3}}$$ (6.20)

For the growth of fatigue-damaged region given by equation (6.17) and the critical condition defined by equation (6.20), the fluctuation magnifying function is $\beta(a) = a^{n/2}$. Substituting in the fatigue damage rate equation (6.16) gives.

$$\frac{\partial D}{\partial N} = -\frac{1}{\rho}\frac{d\rho}{dN}(1-D)\ln(1-D) - \left[A\left(Y\Delta\sigma/2\right)^n a^{\frac{n}{2}}\frac{\partial D}{\partial a} \right]_{a(\Delta\sigma/2)}$$
$$+ \left\{ \frac{Q}{2}\left[\frac{n}{2}a^{n-1}\frac{\partial D}{\partial a} + a^n \frac{\partial^2 D}{\partial a^2} \right] \right\}_{a(\Delta\sigma/2)}$$ (6.21)

with $a(\Delta\sigma/2)$ given in equation (6.20). This is the equation for the evolution of fatigue damage in particulate-reinforced MMCs that was developed by combining (a) the

fatigue damage mechanisms, (b) evolution of fatigue-damaged region, (c) statistical nature, and (d) macromechanical properties of the material.

For the given initial damage distribution function $D[(a\Delta\sigma/2), N = 0]$ the damage due to fatigue of the particulate-reinforced MMCs for any number of cycles is calculated using equation (6.21). However, for purposes convenience in calculation, only two simplistic assumptions are considered:

- The fatigue damage mechanism in particulate-reinforced MMCs is slow growth of pre-existing cracks, and a fluctuation in growth rate of the fatigue-damaged regions is negligibly small (the scatter observed in fatigue strength and number of cycles-to-failure is entirely attributed to initial damage distribution).

- The total number of fatigue-damaged regions that reaches to critical size during the later stages of a fatigue test is constant, $dp/dN = 0$. The experimental aspect behind this simplification is that microcrack concentration at failure is independent of the mechanical loading conditions [155]. As observed by Allison and Jones [155], the last stage during processes governing fatigue damage development in

particulate-reinforced MMCs is characterized by the

initiation of a single dominant crack, which once

initiated, leads rapidly to material failure.

With these two simplified assumption, the fatigue damage

rate equation (6.21) reduces to the simplest form,

$$\frac{\partial D}{\partial N} = -\left[A(Y\Delta\sigma/2)^2 \, a^{n/2} \, \frac{\partial D}{\partial a} \right]_{a(\Delta\sigma/2)} \qquad (6.22)$$

with $a(\Delta\sigma/2)$ by equation (6.20). The initial condition is

assumed to be the two-parameter Weibull function [148,154]:

$$D(\Delta\sigma/2, N = 0) = 1 - \exp\left\{ -\rho V \left(\frac{\Delta\sigma}{\Delta\sigma_o} \right)^m \right\} \qquad (6.23)$$

where m and $\Delta\sigma_o/2$ are the Weibull modulus and scale

parameter, respectively. In fact, $\Delta\sigma_o/2$ is the stress

amplitude corresponding to the smallest fatigue-damaged

region for the crack size (a_o). Solving equations (6.22) and

(6.23) the fatigue damage parameter is obtained as:

$$D(\Delta\sigma/2, N) = 1 - \exp\left(-\rho V \left(\frac{\Delta\sigma}{\Delta\sigma_o} \right)^m \right.$$

$$\times \left\{ 1 + \frac{(n-2)A(Y\,\Delta\sigma/2)^2}{2 f_p^{(n-2)/6}} \times \left[2\sigma_{ys} E\left(\frac{\pi}{6}\right)^{1/3} d_p \right]^{(n-2)/2} N \right\}^{m/(n-2)} \right) \qquad (6.24)$$

Using the approximation

$$\frac{(n-2)A(Y\Delta\sigma/2)^2}{2f_p^{(n-2)/6}}\left[2\sigma_{ys}E\left(\frac{\pi}{6}\right)^{1/3}d_p\right]^{(n-2)/2}N\rangle\rangle 1$$

Equation (6.24) reduces to [154],

$$D\left(\Delta\sigma/2,N\right)=1-\exp\left(-\frac{\rho V}{(\Delta\sigma_o/2)^m}\left\{\frac{(n-2)AY^2}{2f_p^{(n-2)/6}}\right.\right.$$

$$\left.\left.\times\left[2\sigma_{ys}E\left(\frac{\pi}{6}\right)^{1/3}d_p\right]^{(n-2)/2}\left(\frac{\Delta\sigma}{2}\right)^n N\right\}^{m/(n-2)}\right)$$
(6.25)

For a given value of $D\left(\Delta\sigma/2,N\right)$ (i.e., a given fatigue

damage), the fatigue strength $\Delta\sigma/2$ is calculated from

equation (6.25):

$$\frac{\Delta\sigma}{2}=\left[\frac{2f_p^{(n-2)/6}}{(n-2)AY^2}\right]^{1/n}\left[2\sigma_{ys}E\left(\frac{\pi}{6}\right)^{1/3}d_p\right]^{-(n-2)/2n}$$

$$\times\left[\frac{(\Delta\sigma_o/2)^m[-\ln(1-D)]}{\rho V}\right]^{(n-2)/mn}N^{-1/n}$$
(6.26)

The average fatigue strength (σ_f) of the particulate-

reinforced MMCs is calculated to be [154]:

$$\sigma_f=\int_0^\infty\left[(\Delta\sigma/2)\frac{\partial D}{\partial(\Delta\sigma/2)}\right]d(\Delta\sigma/2)=\int_0^\infty(1-D)d(\Delta\sigma/2)$$
(6.27)

Substituting equation (6.25) into equation (6.27) gives

$$\sigma_f = \left[\frac{f_p^{(n-2)/6}}{2(n-2)AY^2}\right]^{1/n} \left[2\sigma_{ys}E\left(\frac{\pi}{6}\right)^{1/3} d_p\right]^{-(n-2)/2n}$$

$$\times \left[\frac{(\Delta\sigma_o/2)^m}{\rho V}\right]^{(n-2)/mn} \Gamma\left(1+\frac{n-2}{mn}\right)N^{-1/n} \qquad (6.28)$$

Here Γ is the Gamma function. Using equation (6.28) the fatigue damage parameter can be rewritten in a simpler form

$$D(\Delta\sigma/2, N) = 1 - \exp\left\{-\left[\Gamma\left(1+\frac{n-2}{mn}\right)\frac{\Delta\sigma}{\sigma_f}\right]^{mn/(n-2)}\right\} \qquad (6.29)$$

These equations are dependent upon an initial distribution of fatigue damage and a law governing growth of the fatigue-damaged region. All of these expressions show how cumulative fatigue damage and fatigue strength change with related material parameters.

6.3.1 Model Validation and Discussion

The predicted average fatigue strengths of the particulate-reinforced metal matrix composites (MMCs) are compared with the trends observed from experiments. The model predicts a cumulative fatigue damage equation (6.25) and a average fatigue strength equation (6.28) for a particulate-reinforced MMC. According to these predictions, the cumulative fatigue damage and the average fatigue strength of the particulate-reinforced MMCs are

qualitatively in good agreement with the existing experimental observations.

2009/SiCp/15p-T42 and 7034/SiC/15p metal matrix composites are chosen for quantitative comparison. The crack growth parameters n and A are obtained by re-analyzing the experimental data in terms of the Paris' equation (6.17).

6.3.1.1 2009 Aluminum Matrix Composite

The mechanical and material data used in the calculations are given in Table 6.1.
The cumulative fatigue damage predicted using equation (6.25) is plotted as a function of the number of cycles for a given cyclic stress ($\Delta\sigma/2$ = 250 MPa) as shown in Figure 6.12, at two different test temperatures. The statistical model predictions reveal cumulative fatigue damage to increase with an increases of test temperature. However, differences in cumulative fatigue damage diminish at lower number of cycles, i.e., below 10^4 cycles.

In Figure 6.13, the fatigue damage value $D = 0.40$, $D= 0.45$, $D = 0.50$, $D = 0.55$ and $D = 0.60$ are plotted with the experimental results. The experimental fatigue data lies between the fatigue damage values $D = 0.40$ and $D = 0.60$.

Table 6.1: Mechanical properties and material parameters for 2009/SiC/15p-T42 composite [104].

T (°C)	27	150
d_p (μm)	5	5
f_p (%)	15	15
σ_{ys} (MPa)	367	360
E (GPa)	100	91
n	12.7	9
A m/cycle X (MPa $\sqrt{m}$)$^{-n}$	$5.39*10^{-19}$	$3.96*10^{-16}$
Y	1.5	1.5
a_o (μm)	15	15
$\Delta\sigma_o/2$ (MPa)	4061.5	3843.8
m	3	3
ρV	10	10

T	:	Test Temperature
d_p	:	Average size of reinforcing particles
f_p	:	Volume fraction of reinforcing particles
σ_{ys}	:	Yield strength
E	:	Young's modulus
n, A	:	Material constants of Paris law
Y	:	Geometric factor of fatigue crack
a_o	:	Initial crack size
$\Delta\sigma_o/2$	:	Cyclic stress amplitude at a_o
m	:	Weibull shape parameter
ρ	:	Density of fatigue-damage region
V	:	Material volume

$$D\left(\Delta\sigma/2, N\right) = 1 - \exp\left(-\frac{\rho V}{\left(\Delta\sigma_o/2\right)^m}\left\{\frac{(n-2)AY^2}{2f_p^{(n-2)/6}}\right.\right.$$

$$\left.\left.\times\left[2\sigma_{ys}E\left(\frac{\pi}{6}\right)^{1/3}d_p\right]^{(n-2)/2}\left(\frac{\Delta\sigma}{2}\right)^n N\right\}^{m/(n-2)}\right) \qquad (6.25)$$

Figure 6.12: The cumulative fatigue damage versus number of cycles for 2009/SiC/15p composite at stress amplitude of 250 MPa.
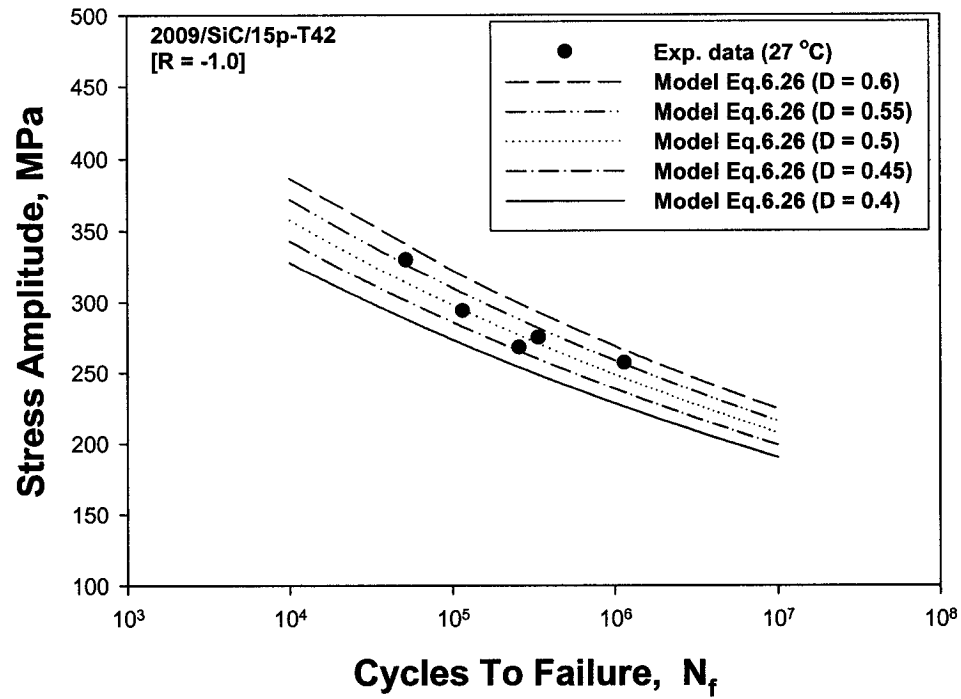
$$\frac{\Delta\sigma}{2} = \left[\frac{2f_p^{(n-2)/6}}{(n-2)AY^2}\right]^{1/n}\left[2\sigma_{ys}E\left(\frac{\pi}{6}\right)^{1/3}d_p\right]^{-(n-2)/2n}$$

$$\times\left[\frac{(\Delta\sigma_o/2)^m\left[-\ln(1-D)\right]}{\rho V}\right]^{(n-2)/mn}N^{-1/n} \qquad (6.26)$$

Figure 6.13: Predicated fatigue damage values for 2009/SiC/15p-T42 composite at: (a) 27 °C.
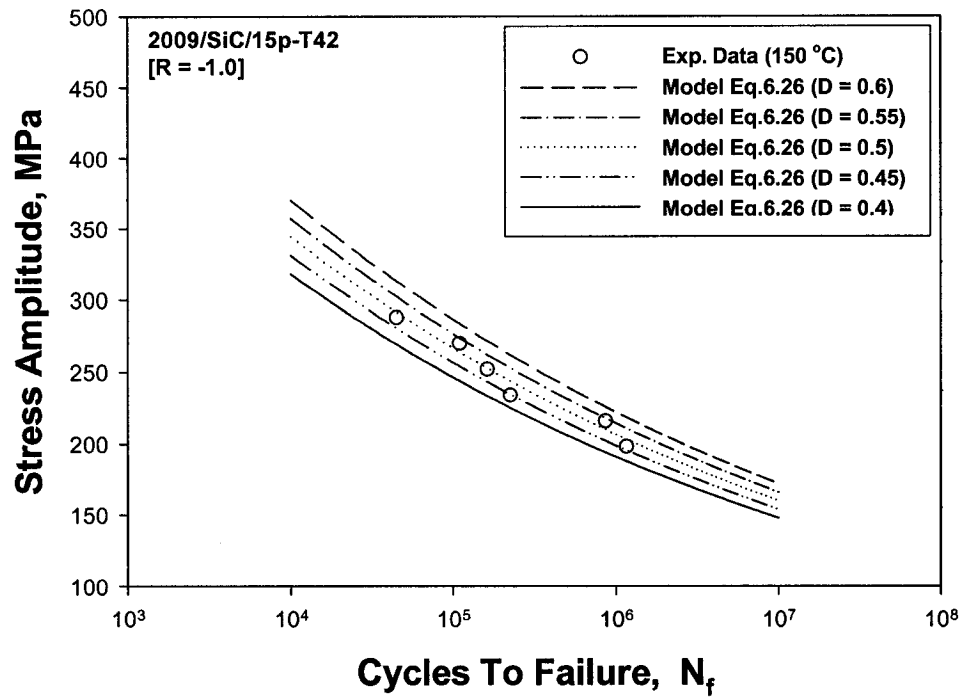
$$\frac{\Delta\sigma}{2} = \left[\frac{2f_p^{(n-2)/6}}{(n-2)AY^2}\right]^{1/n} \left[2\sigma_{ys}E\left(\frac{\pi}{6}\right)^{1/3}d_p\right]^{-(n-2)/2n}$$

$$\times\left[\frac{(\Delta\sigma_o/2)^m[-\ln(1-D)]}{\rho V}\right]^{(n-2)/mn} N^{-1/n} \qquad (6.26)$$

Figure 6.13 (Cont.): Predicated fatigue damage values for 2009/SiC/15p-T42 composite at: (b) 150 °C
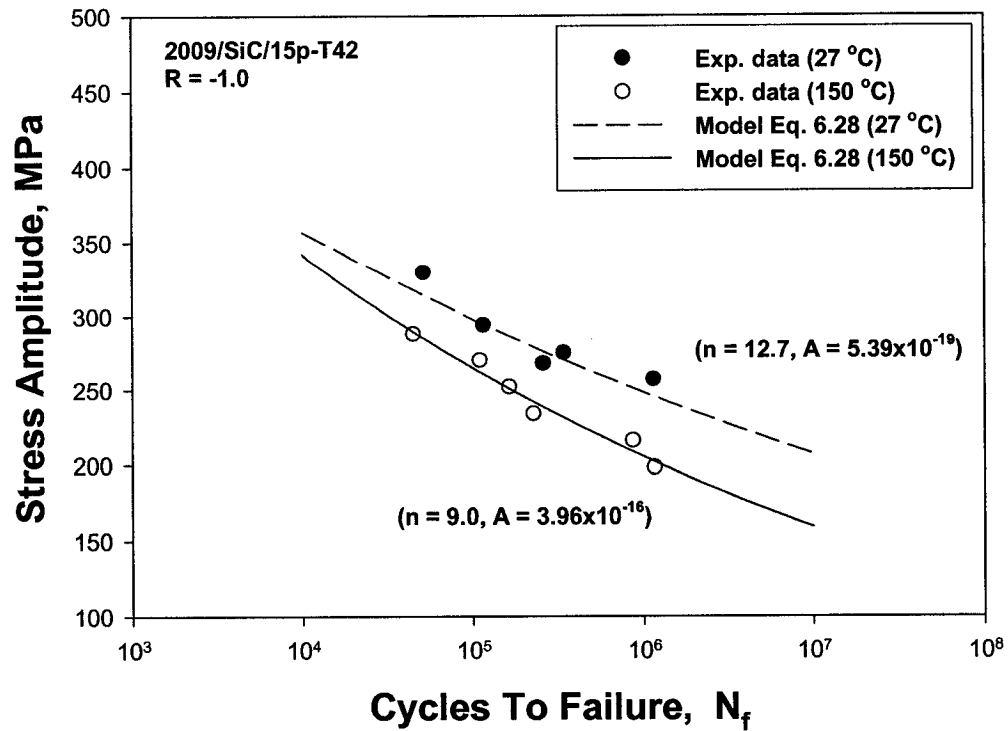
$$\sigma_f = \left[\frac{f_p^{(n-2)/6}}{2(n-2)AY^2}\right]^{1/n}\left[2\sigma_{ys}E\left(\frac{\pi}{6}\right)^{1/3}d_p\right]^{-(n-2)/2n}$$

$$\times\left[\frac{(\Delta\sigma_o/2)^m}{\rho V}\right]^{(n-2)/mn}\Gamma\left(1+\frac{n-2}{mn}\right)N^{-1/n} \qquad (6.28)$$

Figure 6.14: Comparison of the predicated model with experimental fatigue data of 2009/SiC/15p-T42 composite at two temperatures 27 and 150 °C.

Predicted stress amplitude versus cycles-to-failure (S-N) curves are compared with the experimental fatigue data in Figure 6.14. The solid lines represent the prediction model. In Figure 6.14, the effect of test temperatures on fatigue strength and life of 2009/SiC/15p composites is well predicted and in good agreement.

According to equation (6.26) and equation (6.28), $\sigma_f \sim (1/V)^{(n-2)/(mn)}$, the average fatigue strength increases with a decrease in sample volume (V), thus showing a size-effect. For the 2009/SiC/15p-T42 composite, the average fatigue strength is found to be $\sigma_f \sim (1/V)^{0.3}$. This size-effect is a reflection of the nature of fatigue damage in particulate-reinforced metal matrix composites. Due to limited experimental data, it is difficult to compare the predicted size-effect with experimental results.

6.3.1.2 <u>7034 Aluminum Matrix Composite</u>

The mechanical and material data used in the calculations are given in Table 6.2. The cumulative fatigue damage predicted by equation (6.25) is plotted as a function of the number of cycles for a given cyclic stress ($\Delta\sigma/2 = 300$ MPa) and is shown in Figure 6.15, for two aging conditions. The model predictions show the cumulative

Table 6.2: Mechanical properties and material parameters for 7034/SiC/15p composite [116].

Aging	Under-aged	Peak-aged
d_p (μm)	5	5
f_p (%)	15	15
σ_{ys} (MPa)	574	562
E (GPa)	86	90
n	7.15	6.8
A m/cycle X (MPa $\sqrt{m}$)$^{-n}$	$1.18*10^{-14}$	$1.74*10^{-14}$
Y	1.5	1.5
a_o (μm)	15	15
$\Delta\sigma_o/2$ (MPa)	4716.4	4768.1
m	3	3
ρV	10	10

d_p	: Average size of reinforcing particles
f_p	: Volume fraction of reinforcing particles
σ_{ys}	: Yield strength
E	: Young's modulus
n, A	: Material constants of Paris law
Y	: Geometric factor of fatigue crack
a_o	: Initial crack size
$\Delta\sigma_o/2$	: Cyclic stress amplitude at a_o
m	: Weibull shape parameter
ρ	: Density of fatigue-damage region
V	: Material volume

$$D\left(\Delta\sigma/_2, N\right) = 1 - \exp\left(-\frac{\rho V}{\left(\Delta\sigma_o/2\right)^m}\left\{\frac{(n-2)AY^2}{2f_p^{(n-2)/6}}\right.\right.$$

$$\left.\left.\times\left[2\sigma_{ys}E\left(\frac{\pi}{6}\right)^{1/3}d_p\right]^{(n-2)/2}\left(\frac{\Delta\sigma}{2}\right)^n N\right\}^{m/(n-2)}\right) \qquad (6.25)$$

Figure 6.15: The cumulative fatigue damage versus number of cycles for 7034/SiC/15p composite at stress amplitude of 300 MPa.

fatigue damage to slightly decrease as the aging condition alters from the under-aged (UA) to the peak-aged (PA) conditions. The difference in cumulative fatigue damage is uniformly distributed through all fatigue cycles.

Using equation (6.26) all experimental fatigue damage points lie between the fatigue damage values (a) *D = 0.20* to *D = 0.60,* and (b) D = 0.3 to D = 0.55 for both the under-aged and peak-aged conditions (Figure 6.16).

The effect of aging condition on fatigue strength and life of 7034/SiC/15p composites is well-predicted using equation (6.28) (Figure 6.17). Significantly little to-no-influence of aging condition for all fatigue cycles. For the 7034/SiC/15p composite, the average fatigue strength is found to be $\sigma_f \sim (1/V)^{0.25}$.

The results suggest that the scatter observed in fatigue of particulate-reinforced metal matrix composites can be well described by the statistical model.

6.4 Cyclic-Strain Controlled Prediction Model

The low-cycle fatigue (LCF) failure mechanism in particulate-reinforced metal matrix composites is essentially a matter of crack growth [177,178]. The prediction model for particulate-reinforced metal matrix composites (MMCs) is based on (a) specific microstructural
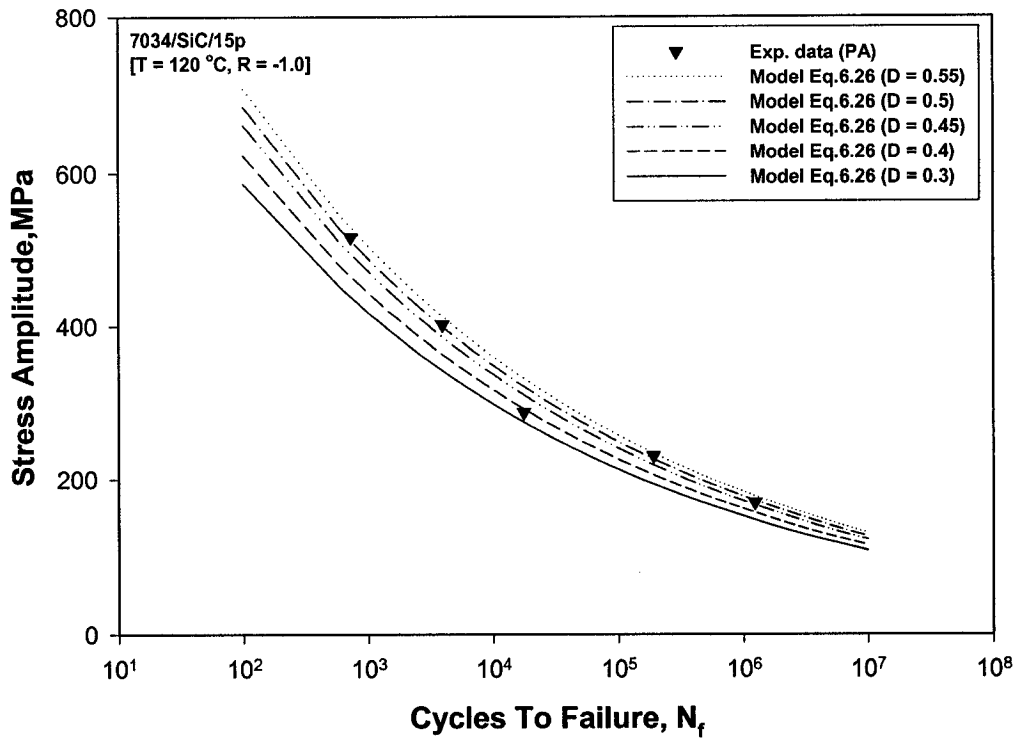
$$\frac{\Delta\sigma}{2} = \left[\frac{2f_p^{(n-2)/6}}{(n-2)AY^2}\right]^{1/n} \left[2\sigma_{ys}E\left(\frac{\pi}{6}\right)^{1/3}d_p\right]^{-(n-2)/2n}$$

$$\times \left[\frac{(\Delta\sigma_o/2)^m[-\ln(1-D)]}{\rho V}\right]^{(n-2)/mn} N^{-1/n} \qquad (6.26)$$

Figure 6.16: Predicated fatigue damage values for 7034/SiC/15p composite at:(a) Peak-aged (PA) condition.
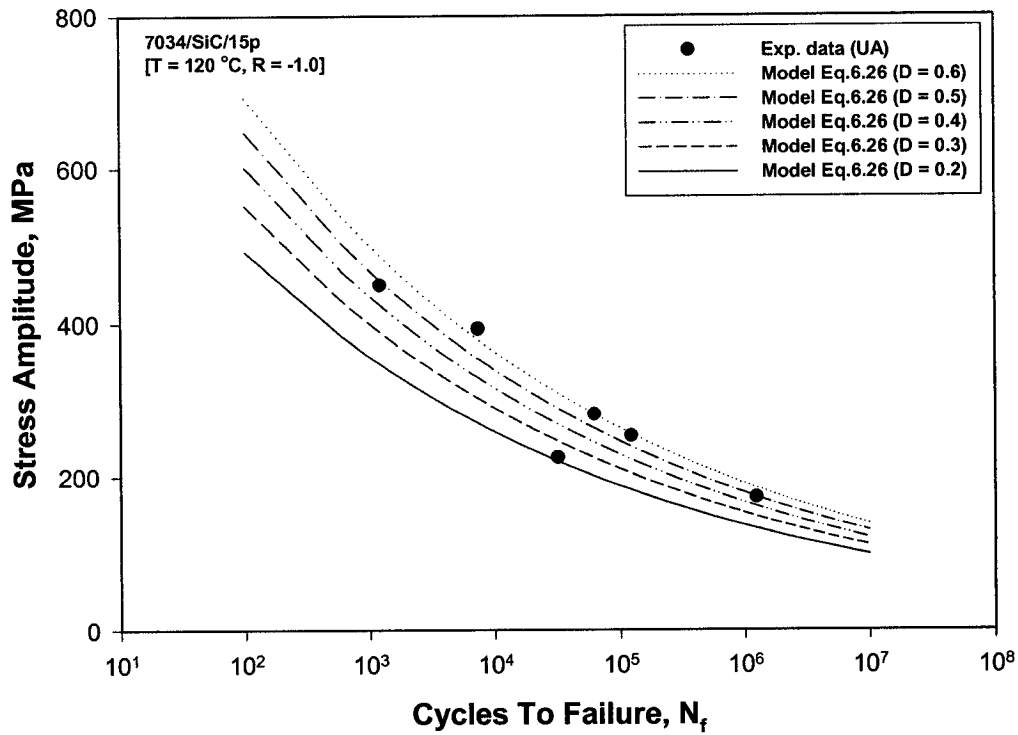
$$\frac{\Delta\sigma}{2} = \left[\frac{2f_p^{(n-2)/6}}{(n-2)AY^2}\right]^{1/n}\left[2\sigma_{ys}E\left(\frac{\pi}{6}\right)^{1/3}d_p\right]^{-(n-2)/2n}$$

$$\times\left[\frac{(\Delta\sigma_o/2)^m[-\ln(1-D)]}{\rho V}\right]^{(n-2)/mn} N^{-1/n} \qquad (6.26)$$

Figure 6.16 (Cont.): Predicated fatigue damage values for 7034/SiC/15p composite at: (b) Under-aged (UA) condition.
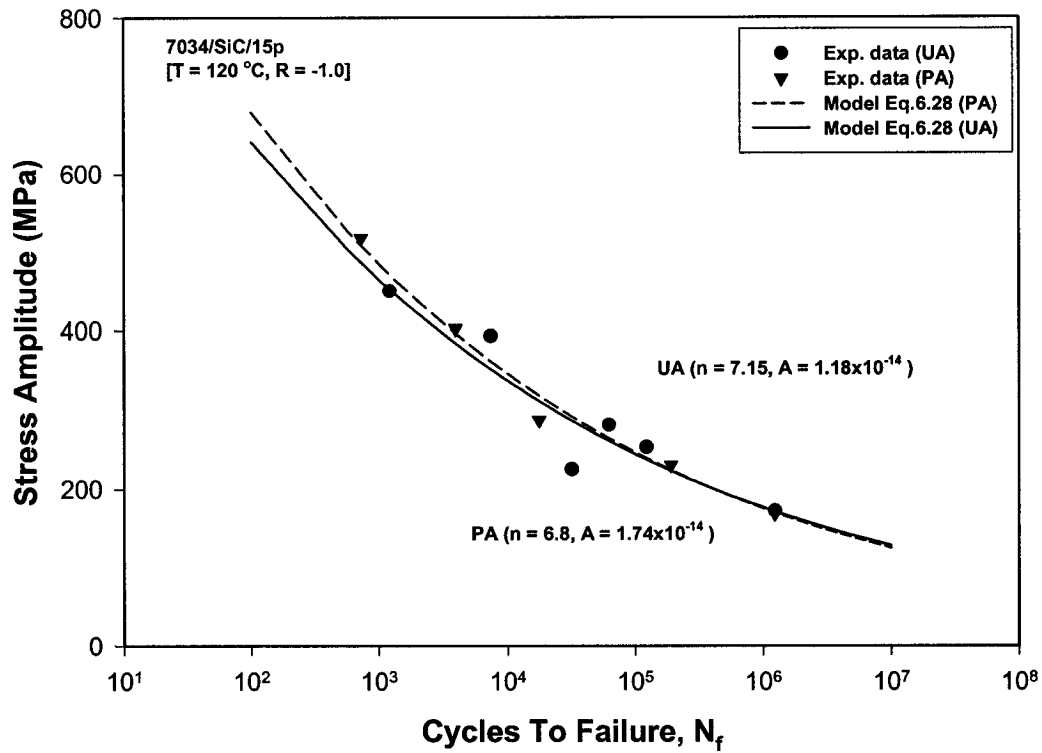
$$\sigma_f = \left[\frac{f_p^{(n-2)/6}}{2(n-2)AY^2} \right]^{1/n} \left[2\sigma_{ys}E\left(\frac{\pi}{6}\right)^{1/3} d_p \right]^{-(n-2)/2n}$$

$$\times \left[\frac{(\Delta\sigma_o/2)^m}{\rho V} \right]^{(n-2)/mn} \Gamma\left(1 + \frac{n-2}{mn}\right) N^{-1/n} \qquad (6.28)$$

Figure 6.17: Comparison of the predicated model with experimental fatigue data of 7034/SiC/15p composite at two aging conditions PA and UA.

mechanisms, (b) material properties, and (c) loading conditions [178]. The low-cycle fatigue behavior of particulate-reinforced MMCs is treated as a localized damage development (i.e., crack growth) phenomenon that is activated by applied cyclic loading. The localized cyclic stress and strain concentration, and fatigue damage evolution in the microstructural elements, within the fatigue-damaged zone (*FDZ*) very near the crack tip, is considered to dominate the LCF process. In high-strain low-cycle fatigue, the FDZ is a region in which the local stress level approaches the ultimate tensile strength of the composite and within which actual degradation of the composite material occurs. The fatigue crack growth rate is correlated with the range of the crack tip opening displacement (*CTOD*), and LCF life is calculated from the number of cycles required for crack growth to failure. For modeling crack growth during LCF and faigue life of particulate-reinforced MMCs the following assumptions are considered:

- The local plastic strain around the crack tip plays an important role in governing damage initiation and propagation (i.e., crack growth process) in particulate-reinforced MMCs [159,177,179-181].

- The microstructures of MMCs have relatively uniform particle distributions (the particles are aligned in the direction of extrusion with near uniform distribution, except for a few agglomeration sites).

- The microstructure influences strength, stiffness, crack initiation and growth behavior in MMCs. Volume fraction of the reinforcement phase is a significant factor in determining the yield strength and effective matrix stress intensity range, experienced at the crack tip [57].

- The LCF life of the particulate-reinforced MMCs follows the Coffin-Manson relationship. However, LCF endurance of particulate-reinforced MMCs is generally lower than that of the unreinforced matrix for a wide range of plastic strain amplitudes [158,182-186].

The strengthening effect of the particulate phase reinforcement on the matrix is attributed to two factors: (1) the modified shear lag model [4], which attributes the entire strengthening effect to the load bearing capability of the reinforcement particles, and (2) dislocation density model [32], which attributes strengthening to the enhanced strength of the matrix resulting from an increase in dislocation density in the matrix by a few orders of

magnitude. Nardone and Prewo provided a formula to relate

yield strength of particulate-reinforced MMCs ($R_{p,C}$) with the

yield strength of the matrix alloy ($R_{p,M}$). This express as

[4]:

$$R_{p,C} = R_{p,M}\left(f_p(s+2)/2 + f_m\right)$$ (6.30)

where f_p and $f_m=1-f_p$ are the volume fraction of the

reinforcing particles and the matrix, respectively; and s

is the length-to-diameter aspect ratio of the reinforcing

particles. Davidson and McClung [187] developed a technique

for experimentally assessing the local level of constraint

from the measured response of at a crack tip. They defined

the constraint C_ε in terms of strain as [187],

$$C_\varepsilon = \left|\varepsilon_{mean}\right|/\varepsilon_{eff} = \left[\left(\frac{\Delta\sigma_1}{2} + \frac{\Delta\sigma_2}{2}\right)/\frac{\Delta\sigma_{eff}}{2}\right]/4$$ (6.31)

where ε_{mean} is the in-plane mean strain and ε_{eff} is, the

effective strain, both of which are computed from the

displacements measured on the surface of the material, $\Delta\sigma_1/2$

and $\Delta\sigma_2/2$ are the principal stress amplitudes while $\Delta\sigma_{eff}/2$

is the effective stress amplitude. Constraint is defined

to have the bounds $0 \leq C_\varepsilon \leq 0.5$, with a higher value denoting

higher constraint. For aluminum alloy matrix composites,

constraint in the matrix between reinforcing particles is

low ($C_\varepsilon = 0.1-0.3$) compared to constraint near the particle

($C_\varepsilon \geq 0.4$). On the crack plane the principal stress amplitudes $\Delta\sigma_1/2$ and $\Delta\sigma_2/2$ are equal and act in the X and Y directions and cyclic stress amplitude ($\Delta\sigma_2/2$) is defined as a principal stress. By using this definition of constraint, i.e., equation (6.31), the effective stress is calculated for particulate-reinforced MMCs [178].

$$\frac{\Delta\sigma_{eff}}{2} = \frac{1}{2C_\varepsilon}\left(\frac{\Delta\sigma}{2}\right) \qquad (6.32)$$

During fatigue loading the cyclic-plastic zone ahead of the crack tip includes a FDZ (fatigue damage zone) in front of the fatigue crack tip within which local shearing processes take place during crack growth [188-189]. The size of the cyclic plastic zone (D_C) is estimated using the linear elastic fracture mechanics (LEFM) approach. The standard theoretical estimation of D_C was put forth by Rice [190] and is derived using the LEFM concept as the expression [190],

$$D_C = \lambda\left(\frac{\Delta K}{2R_p}\right)^2, \qquad (6.33)$$

where ΔK is the applied stress intensity factor range, R_p is the cyclic yield strength, and λ is the cyclic plastic zone correction factor, which is a dimensionless constant and represents the best-fit proportionality factor between the cyclic plastic zone size D_C and ($\Delta K /2R_p)^2$.

In metal matrix composites the FDZ is considered to be a combination of matrix-particulate interface decohesion, failure of the reinforcing particle by a cracking, and matrix damage, which includes the matrix hardening or softening and complex interactions between them. With plastic strain localization in the vicinity of reinforcement particles in the FDZ, the local stress increases and approaches the ultimate tensile strength of the specimen, and favors the initiation of secondary microcracks. The growth of these microcracks, and there eventual coalescence with the main crack, the main crack advances. In MMCs, the effective stress intensity range in the matrix governs fatigue crack growth behavior of the composite [57]. Therefore, cyclic plastic zone size (D_C) depends on the value of $(\Delta K_{eff} / 2R_{p,M})^2$ for the particulate-reinforced MMCs, and D_C is calculated using the expression [178]

$$D_C = \lambda \left(\frac{\Delta K_{eff}}{2R_{p,M}} \right)^2, \qquad (6.33a)$$

where ΔK_{eff}, λ and $R_{p,M}$ are the effective matrix stress intensity range, the cyclic plastic zone correction factor and the matrix cyclic yield strength. This assumption is consistent with the fact that only the matrix deforms

plastically. Substituting equation (6.30) into equation (6.33a) gives,

$$D_C = \frac{\lambda}{4} \left(f_p(s+2)/2 + f_m \right)^2 \left(\frac{\Delta K_{\mathit{eff}}}{R_{p,C}} \right)^2, \qquad (6.34)$$

During LCF, an important control parameter to determine is size of the cyclic plastic zone in the plastic strain range ($\Delta\varepsilon_{pl}$) as well as the crack length (a), rather than the stress intensity range (ΔK_{eff}). In terms of the effective stress ($\Delta\sigma_{\mathrm{eff}}/2$) determined using equation (6.32), the effective matrix stress intensity range (ΔK_{eff}) is determined to be [178],

$$\Delta K_{\mathit{eff}} = \frac{\Delta\sigma_{\mathit{eff}}}{2}\sqrt{\pi a} = \frac{1}{2C_\varepsilon}\left(\frac{\Delta\sigma}{2}\right)\sqrt{\pi a}, \qquad (6.35)$$

where (a) is the crack length. The average steady-state cyclic stress amplitude in bulk of the composite ($\Delta\sigma/2$) is determined using the following cyclic stress-strain relationship

$$\frac{\Delta\sigma}{2} = K'\left(\frac{\Delta\varepsilon_{pl}}{2}\right)^{n'} \qquad (6.36)$$

where $\Delta\varepsilon_{pl}/2$ is the cyclic plastic strain amplitude of the composite, n' and K' are the cyclic stress–strain hardening exponent and hardening coefficient, respectively.

Substituting equation (6.35) and (6.36) into equation (6.34), the size of the cyclic plastic zone of the particulate-reinforced MMCs can be obtained as

$$D_C = \frac{\lambda\pi}{16C_\varepsilon^2}\left(f_p(s+2)/2 + f_m\right)^2\left(\frac{K'}{R_{p,C}}\right)^2\left(\frac{\Delta\varepsilon_{pl}}{2}\right)^{2n'}a, \qquad (6.37)$$

According to Rice [190], the stress and strain distribution within the cyclic plastic zone of particulate-reinforced MMCs can also be described as

$$\sigma(r) = \frac{\Delta\sigma}{2}\left(\frac{D_C}{r}\right)^{n'/(n'+1)}, \qquad (6.38)$$

$$\varepsilon_{pl}(r) = \frac{\Delta\varepsilon_{pl}}{2}\left(\frac{D_C}{r}\right)^{1/(n'+1)}. \qquad (6.39)$$

The size of the FDZ, (D_{FDZ}) is calculated using equation (6.38) by using the condition that local cyclic stress level approaches ultimate tensile strength of the composite ($R_{m,C}$), i.e.,

$$D_{FDZ} = D_C\left(\frac{\Delta\sigma}{2R_{m,C}}\right)^{(n'+1)/n'}. \qquad (6.40a)$$

Substituting equations (6.36) and (6.37) into equation (6.40a)

$$D_{FDZ} = \frac{\lambda\pi}{16C_\varepsilon^2}\left(f_p(s+2)/2 + f_m\right)^2\left(\frac{(K')^{3+1/n'}}{R_{m,C}^{1+1/n'}(R_{p,C})^2}\right)\left(\frac{\Delta\varepsilon_{pl}}{2}\right)^{3n'+1}a. \qquad (6.40b)$$

The increased volume fraction of reinforcement particles results in an increased size of the FDZ. By using

equations (6.39) and (6.40b), the accumulated average

plastic strain, (ε_{pl}^{*}), in the FDZ, is calculated to be [178]

$$\varepsilon_{pl}^{*} = \frac{1}{D_{FDZ}} \int_{0}^{D_{FDZ}} \varepsilon_{pl}(r) dr = \frac{n'+1}{n'} \left(\frac{R_{m,C}}{K'} \right)^{1/n'},$$ (6.41)

Crack growth during LCF is correlated with the cyclic

J integral (referred to as ΔJ) [191-193]. The ΔJ parameter

has demonstrated excellent versatility in the correlation

of fatigue crack growth for tests with various total strain

or plastic strain amplitudes [192,194-195]. Therefore, it

is reasonable to consider ΔJ as the local driving force for

crack growth during LCF of particulate-reinforced MMCs.

Rice [191] has shown that the integral J is the rate

of change of potential energy (V) (with respect to crack

advance) for nonlinear elastic solid and J is calculated

using the expression [191],

$$J = -\frac{\partial V}{\partial r}$$ (6.42)

In view of crack growth during low-cycle fatigue being

controlled by FDZ around the crack tip, it is assumed that

the potential energy (V) in the J integral equation (6.42)

is equal to the interaction energy (V_{int}) between the FDZ

and the crack tip stress-strain field. So, the local crack

tip driving force acting on the FDZ is merely the local

driving force for fatigue crack growth. The interaction

energy (V_{int}) is calculated as [196].

$$V_{int} = -\int_V \sigma^* \varepsilon_{pl}^* du, \qquad (6.43)$$

where σ^* is the local cyclic stress amplitude and ε_{pl}^* is the

average accumulated plastic strain. The integral is taken

over fatigue-damage zone volume (FDZ). In determining the

size of the crack tip fatigue-damage zone, by assuming that

within the FDZ the local cyclic stress is uniform and

$\sigma^* = R_{m,C}$. The average plastic strain ε_{pl}^* is determined using

equation (6.41). Therefore, equation (6.43) simplifies to

[178]

$$V_{int} = -\int_V \sigma^* \varepsilon_{pl}^* du = -R_{m,C} \varepsilon_{pl}^* \int_V du \qquad (6.43a)$$

and the interaction energy per unit size, along the

direction that is perpendicular to the crack plane, is

$$V_{int} = -R_{m,C} \varepsilon_{pl}^* S, \qquad (6.43b)$$

where the area of the FDZ is $(S = \pi(D_{FDZ}/2)^2)$. Substituting

equation (6.43b) into equation (6.42) the cyclic J integral

is calculated and is,

$$\Delta J = -\frac{\partial V_{int}}{\partial D_{FDZ}} = \pi R_{m,C} \varepsilon_{pl}^* (D_{FDZ}/2). \qquad (6.44)$$

Here ΔJ depends on both size of the FDZ and the accumulated

average plastic strain within it. By substituting equations

(6.40) and (6.41) in equation (6.44), the ΔJ for particulate-reinforced MMCs is described as,

$$\Delta J = \frac{\lambda \pi^2}{32 C_\varepsilon^2} \left(f_p (s+2)/2 + f_m \right)^2 \left(\frac{n'+1}{n'} \right) \left(\frac{(K')^3}{(R_{p,C})^2} \right) \left(\frac{\Delta \varepsilon_{pl}}{2} \right)^{3n'+1} a. \qquad (6.45)$$

The cyclic J integral is related to the range of crack tip opening displacement $(\Delta CTOD)$ and in its general form, the relation is [190]

$$\Delta J = \omega R_{p,C} \Delta CTOD. \qquad (6.46)$$

Here, ω is between 1 and 2. For purposes of convenience calculation, the numerical factor is taken as $\omega \approx 1.5$. By combining equations (6.45) and (6.46), $\Delta CTOD$ is determined as [178]

$$\Delta CTOD = \frac{\lambda \pi^2}{48 C_\varepsilon^2} \left(f_p (s+2)/2 + f_m \right)^2 \left(\frac{n'+1}{n'} \right) \left(\frac{K'}{R_{p,C}} \right)^3 \left(\frac{\Delta \varepsilon_{pl}}{2} \right)^{3n'+1} a. \qquad (6.47)$$

The crack growth rate (da/dN) during low-cycle fatigue, is related to the local driving force acting on the FDZ, and the range of crack tip opening displacement $(\Delta CTOD)$. Tomkins [188] in his study suggested that an upper bound to fatigue crack growth can be determined by assuming the crack to extend each cycle by an amount equal to one-half of the crack tip opening displacement. Using this argument, the crack growth rate (da/dN) during low-cycle fatigue of

particulate reinforced MMCs can be predicted using equation

(6.47) and is [178],

$$\frac{da}{dN} = \frac{1}{2} \Delta CTOD = \frac{\lambda \pi^2}{96 C_\varepsilon^2} \left(f_p (s+2)/2 + f_m \right)^2 \left(\frac{n'+1}{n'} \right) \left(\frac{K'}{R_{p,C}} \right)^3 \left(\frac{\Delta \varepsilon_{pl}}{2} \right)^{3n'+1} a. \quad (6.48)$$

The LCF crack growth model is applied to (a) determine

the life of a particulate-reinforced MMC, and (b) to

analyze the influence of reinforcement particle volume

fraction on fatigue life. In view of the microscopic

mechanism governing damage during LCF, the number of

fatigue crack growth cycles-to-failure is calculated by

integrating equation (6.48) from an assumed initial crack

size (a$_i$) to a critical crack size (a$_f$). The fatigue life is

[178],

$$N_f = \left[\frac{96 C_\varepsilon^2}{\lambda \pi^2} \left(f_p (s+2)/2 + f_m \right)^{-2} \left(\frac{n'}{n'+1} \right) \left(\frac{R_{p,C}}{K'} \right)^3 \ln \left(\frac{a_f}{a_i} \right) \left(\frac{\Delta \varepsilon_{pl}}{2} \right)^{-(3n'+1)} \right] \quad (6.49)$$

This equation (6.49) is written in the form

$$\frac{\Delta \varepsilon_{pl}}{2} = \left[\frac{192 C_\varepsilon^2}{\lambda \pi^2} \left(f_p (s+2)/2 + f_m \right)^{-2} \left(\frac{n'}{n'+1} \right) \left(\frac{R_{p,C}}{K'} \right)^3 \ln \left(\frac{a_f}{a_i} \right) \right]^{1/(3n'+1)} \left(2 N_f \right)^{-1/(3n'+1)}. \quad (6.50)$$

This is similar to the empirical Coffin-Manson law [108-109]

$$\frac{\Delta \varepsilon_{pl}}{2} = \varepsilon'_f \left(2 N_f \right)^c. \quad (6.51)$$

From equations (6.49) and (6.50), the fatigue ductility coefficient (ε'_f) and the fatigue ductility exponent *(c)* can be obtained and are

$$\varepsilon'_f = \left[\frac{192C_\varepsilon^2}{\lambda \pi^2} \left(f_p(s+2)/2 + f_m \right)^{-2} \left(\frac{n'}{n'+1} \right) \left(\frac{R_{p,C}}{K'} \right)^3 \ln\left(\frac{a_f}{a_i} \right) \right]^{1/(3n'+1)} \qquad (6.52a)$$

$$c = -1/(3n'+1) \qquad (6.52b)$$

6.4.1 Model Validation

For (a) 2009/SiC/15p-T42 composite in the temperature range between T = 27 and 150 °C, and (b) 7034/SiC/15p composite in the under-aged and peak-aged conditions during total-strain controlled fatigue. The mean size of the SiC particulate reinforcement is about 10-15 µm for both the composites. The cyclic stress-strain data and mechanical parameters of the 2009/SiC/15P-T42 composite and the 7034/SiC/15p composite are listed in Tables 6.3 and 6.4, respectively. In conformance with the monotonic yield stress, the composite's cyclic yield strength *(Rp,c)* is regarded as the stress amplitude for a plastic strain amplitude *(Δεp1/2)* of 0.2% [197], i.e., $R_{p0.2,c}$ = *K'*(0.002)*n'*, determined from the cyclic stress-strain curve.

Low cycle fatigue (*LCF*) life is predicted based on crack growth only. For quantitative calculations, the

initial crack size *(a$_i$)* is taken to be 15 μm for both composites, i.e., the mean particle size. The critical crack size *(a$_f$)* is considered to 2 mm, which is the crack at the final fracture surfaces. The value of constraint *(C$_\varepsilon$)* is taken 0.20 [187].

6.4.1.1. 2009 Aluminum Matrix Composite

The cyclic plastic zone correction factor (λ) is a unique value for 2009/SiC/15p-T42 samples by using the data obtained at room temperature and equation (6.49). The value of cyclic plastic zone correction factor (λ) for 2009/SiC/15p-T42 composite is 0.55. A comparison of model predictions with experimental data at the two test temperatures (27 °C and 150 °C) is shown in Figure 6.18. The LCF prediction model correlates well with the experimental test data at both test temperatures.

6.4.1.2 7034 Aluminum Matrix Composite

For the 7034/SiC/15p composite the value of correction factor is λ$_{(PA)}$ = 3.9 and λ$_{(UA)}$ = 4.3. There is minimal variation in the value of λ for the two aging conditions. The experimental test data for the composite at the two aging conditions are shown in Figure 6.19. The model

Table 6.3:Cyclic stress-strain data and model
parameters of the 2009/SiC/15p-T42 composite [111].

T (°C)	$R_{p0.2,c}$ (MPa)	n'	K' (MPa)	ε'_f (exp.)	C (exp.)	ε'_f	C	λ	C_ε
27	229.1	0.15	582	5.9	-0.59	0.12	-0.69	0.55	0.2
150	180.8	0.17	520	2.2	-0.40	0.11	-0.66	0.55	0.2

$R_{p0.2,c}$:   Cyclic yield strength
n' :   Cyclic strain hardening exponent
K' :   Cyclic strength coefficient
ε'_f :   Fatigue ductility coefficient
C   :   Fatigue ductility exponent
λ :   Cyclic plastic zone correction factor
C_ε :   Constraint parameter

Table 6.4:Cyclic stress-strain data and model
parameters of the 7034/SiC/15p composite [133].

Aging	$R_{p0.2,c}$ (MPa)	n'	K' (MPa)	ε'_f (exp.)	C (exp.)	ε'_f	C	λ	C_ε
UA	289	0.13	649	0.22	-0.17	0.032	-0.72	4.3	0.2
PA	258	0.16	698	0.18	-0.13	0.030	-0.68	3.9	0.2

$R_{p0.2,c}$:   Cyclic yield strength
n' :   Cyclic strain hardening exponent
K' :   Cyclic strength coefficient
ε'_f :   Fatigue ductility coefficient
C   :   Fatigue ductility exponent
λ :   Cyclic plastic zone correction factor
C_ε :   Constraint parameter
UA   :   Under-aged condition
PA   :   Peak-aged condition
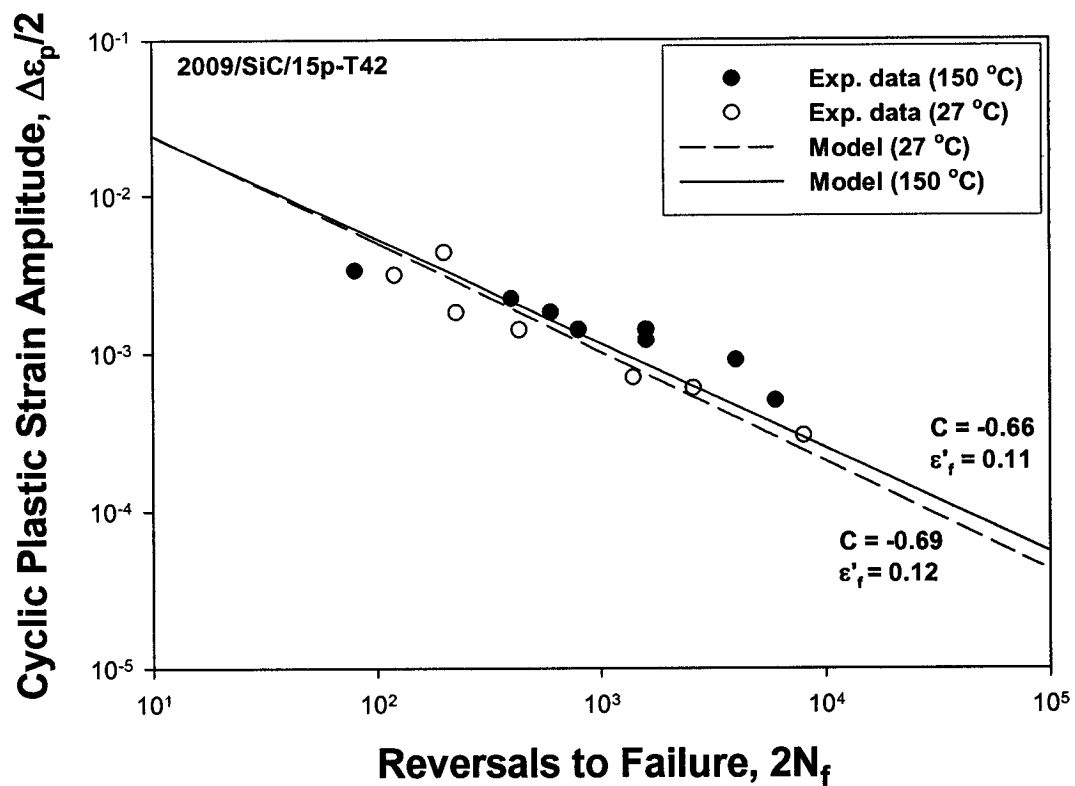
Figure 6.18: Comparison of experimental fatigue data with
the predication model of 2009/SiC/15p-T42
composite at two temperatures 27 and 150 °C.
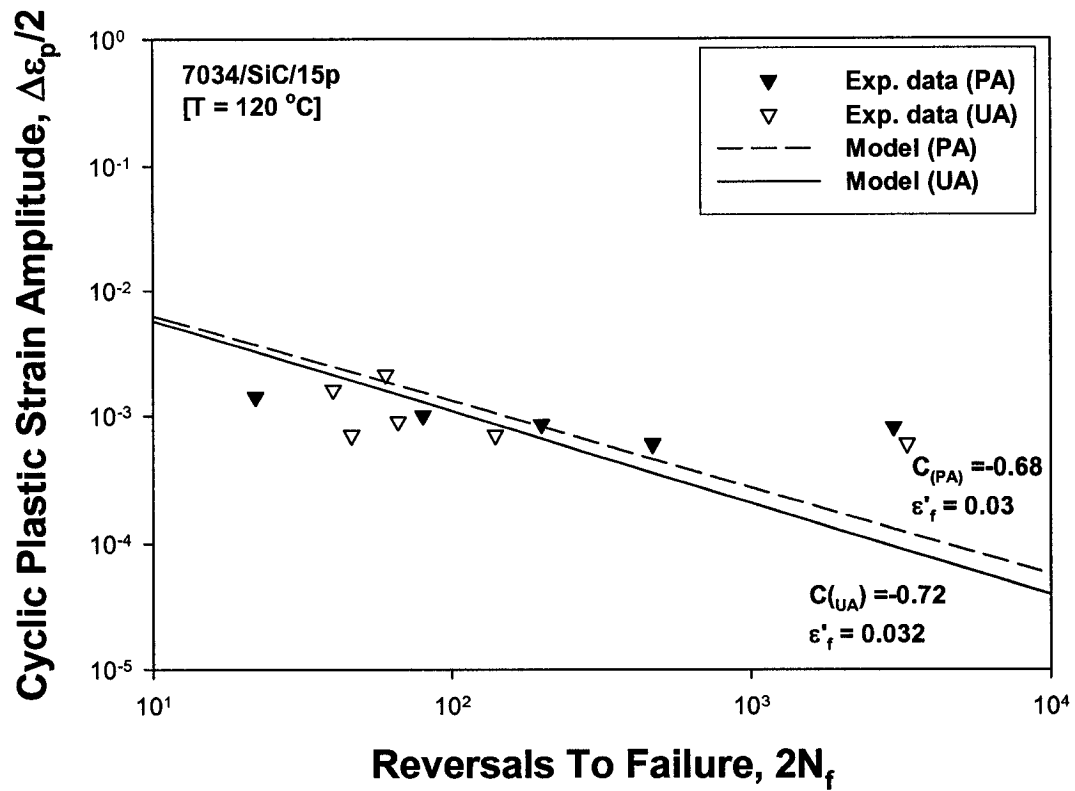
Figure 6.19: Comparison the experimental fatigue data with
the predication model of 7034/SiC/15p
composite at two aging conditions PA and UA.

perditions follow the trend of the experimental data, with a larger deviation.

In terms of a model, cyclic plastic deformation at the crack tip FDZ is the mechanical driving force for crack growth under strain-controlled cyclic loading, and crack growth rate during LCF is directly correlated with the range of crack-tip opening displacement. This in turn is a function of the following (a) cyclic plastic strain amplitude, (b) the crack length and (c) reinforcement particle constraint. The quantitative comparison presented (Figures 6.18 and 6.19) shows clearly that model predictions are in good agreement with the experimental data over a wide range of plastic strain amplitudes.

6.4.2 Justification of the Model

The model is essentially a LCF crack growth model. A theoretical analysis of the Low cycle fatigue crack growth model for particulate-reinforced MMCs is to consider damage evolution of the microstructural elements within the fatigue damage zone (FDZ) close to the crack tip. The LCF behavior of particulate-reinforced MMCs is treated as a localized damage development phenomenon at the crack tip FDZ, which is activated by applied cyclic loading. The localized cyclic stress, strain concentration and fatigue

damage evolution of the microstructural elements within the FDZ close to the crack tip, dominate the LCF processes in particulate-reinforced MMCs [178]. Successive crack growth corresponds to an accumulation of fatigue damage. Once ultimate tensile strength of the composite is exceeded, the FDZ adjacent to the main crack tip induces a microcrack, and advance of the main crack occurs by coalescence of the microcracks with the main crack [178]. This process stops when the local cyclic stress level reduces to $(\Delta\sigma/2) < R_{m,c}$. The matrix-particulate interface decohesion, cracking of the particulate and matrix damage by void formation or complex interactions between them, have been proposed as the dominant fatigue damage processes occurring at the crack tip fatigue damage zone (FDZ).

In this model $\Delta CTOD$ is used as the correlating parameter to rationalize the dependence of crack growth rate during LCF on both microstructural and mechanical variables in particulate-reinforced MMCs. Since crack opening near the tip in essence controls deformation of the material, it is reasonable to expect the kinetics of fatigue crack growth of particulate-reinforced MMCs to be directly related to $\Delta CTOD$. This argument has been used to derive the Paris law and to also explain the dependence of

fatigue crack growth on elastic modulus for a wide range of materials [188,198]. Since an experimental evaluation of $\Delta CTOD$ for the low cycle fatigue (LCF) cracks is difficult, an analytical model for evaluating the actual value of $\Delta CTOD$ based on global variables, such as: (a) applied plastic strain amplitude, (b) crack length, (c) yield strength, and (d) volume fraction of reinforcement particles, is desirable [178].

An advantage of the approach used is that few parameters are required to establish a relationship between microscopic and the macroscopic process of fatigue failure during LCF. All of the parameters can be determined experimentally. Among the few parameters are the cyclic plastic zone correction factor λ, and constraint C_ε. It is noted that λ is a material-dependent characteristic constant (independent of temperature and plastic strain amplitude, as shown in Figures 6.18-6.19) for each composite. In fact, the situation is more complicated, and determination of λ also depends on: (a) the yield criterion used and (b) the thickness of the material of interest, since this influences the state of the stress at the crack tip [178]. In metals, Edmunds and Willis [199] have shown that λ is a function of the hardening exponent of the material. For the

Dugdale yielding model and a perfectly plastic material satisfying the von Mises yield criterion in conjunction with non-hardening plane strain conditions, they showed that λ = 0.076 [199]. Similarly, Sham [200] derived λ = 0.1 for a non-hardening material. Rubiolo [201] used the finite element method (FEM) to conduct an elastic-plastic analysis for a propagating fatigue crack under cyclic loading at a constant stress intensity factor range. He found the value of λ to be 0.168. Harmain and Provan [202] identified λ to depend on (a) Poisson's ratio, (b) load ratio (defined as the ratio of applied stress to yield strength), and (c) shape ratio (defined as the plasticity affected height to the plasticity affected range of the plastic zone) [178]. An application of the model to 2009/SiC/15p-T42 and 7034/SiC/15p aluminium matrix composites provided the results λ =0.55 and $\lambda \approx$ 4.0, respectively. When compared to the case of metals without a reinforcing phase values of λ are large. However, it is noted that high-strain LCF changes the size of the cyclic plastic zone and the value of λ, since the small scale yielding condition becomes invalid in this case [178]. These results also provide a valuable insight into the effect of reinforcement particles on the development of cyclic plastic zone. The

reinforcement particles enhance the level of cyclic plastic deformation and size of the cyclic plastic zone ahead of the crack tip under strain-controlled LCF. For MMCs comprising two dissimilar components, a fatigue crack located at the interface between the two materials will be subject to local mixed-mode loading. The presence of mixed-mode conditions at the fatigue crack tip results in (1) pronounced changes in the effective crack tip driving force (2) the size of crack tip plastic zone (3) the rate of crack propagation, and (4) the microscopic mechanisms governing damage [66, 178]. In addition, the constraint (C_ε) closely relates to microstructure of the composite and is a important parameter introduced in this study to explore the effects of microstructural factors on fatigue life of the MMCs.

Davidson and McClung [187] have shown the constraint levels in particulate-reinforced MMCs depend on proximity of the crack tip to the reinforcement particles. Constraint is high when the fatigue crack tip plastic zone size is small. Deformation relaxes constraint as the stress intensity factor is increased and the plastic zone expands. Under high-strain cyclic loading, most constraint is relaxed because of intensive cyclic plastic deformation in

the plastic zone and fatigue damage zone (*FDZ*) and the average value of constraint levels will be low.

There are some limitations in the experiments are carried out in total strain control, and a certain amount of cyclic hardening and cyclic softening occurred during the individual fatigue tests. In particular, cyclic softening was found at larger strain amplitudes, starting after about 10% of the fatigue lives. Another factor is the choice of the appropriate values for the initial and the critical crack sizes (a_i and a_f). In the model, the mean particle size is taken as the initial crack size (a_i) in a first approximation. The critical crack size a_f is estimated from the surface measurement of fractured specimens. Also, the values of a_i and a_f as well as constraint C_ε are unchanged for the cyclic plastic strain amplitude range and in the whole tested temperature range [178]. This explains why the model predictions show a deviation from the corresponding experimental data for 7034/SiC/15p at different aging conditions.

These results are indicating that the proposed modeling approach is generally applicable to the low cycle fatigue (LCF) life prediction of particulate-reinforced MMCs.

CHAPTER VII

CONCLUSIONS

7.1. 2009 Aluminum Matrix Composite

Based on the results of an investigation on the effect of SiC particulate reinforcement content on mechanical (tensile and fatigue) behavior of 2009 aluminum alloy composite, the following are the observations:

1. The SiC reinforcement particulates in the 2009 aluminum alloy metal matrix were of near-uniform size. However, few of the particles were found to be irregularly shaped and these were dispersed randomly through the matrix. At regular intervals a clustering or agglomeration of the reinforcing SiC_p was observed in the longitudinal orientation of the billet. An agglomerated site consisted of a few larger SiC particles intermingled with smaller, uniform and more regularly shaped particles.

2. An increase in test temperature decreased the elastic modulus and strength of the 2009/SiC/15p

330

composite and increased ductility, quantified both by elongation-to-failure and reduction-in-area.

3.   The increased strength of the discontinuously-reinforced composites is rationalized in terms of mechanisms based on: (a) an increase in dislocation density in the matrix due to the presence of discontinuous SiC particulate reinforcement phase, (b) misfit strains and resultant misfit stresses due to differential thermal contraction at the Al/SiC_p interfaces, and (c) constrained plastic flow due to presence of discontinuous SiC particulate reinforcements in the aluminum alloy metal matrix.

4.   The presence of hard, brittle and elastically deforming SiC particles in the soft, ductile and plastically deforming metal matrix caused fine microscopic cracks to initiate at low values of applied stress. Fractography revealed limited ductility on a macroscopic scale, but microscopically features were reminiscent of locally ductile and brittle mechanisms. Fracture of the matrix between particle clusters coupled with particle cracking and decohesion of the matrix surrounding particles allows the microscopic cracks

to grow rapidly and link by fracture of the ductile
metal matrix resulting in macroscopic failure and
resultant low tensile ductility.

5. The composite exhibited a linear trend for the
    variation of elastic strain amplitude ($\Delta\varepsilon_e/2$) with
    reversals-to-failure ($2N_f$) and plastic strain
    amplitude ($\Delta\varepsilon_p/2$) with reversals-to-fatigue failure
    ($2N_f$). At equivalent plastic strain amplitudes
    ($\Delta\varepsilon_p/2$) an increase in test temperature enhanced
    cyclic plasticity and improved low cycle fatigue
    life. The improvement in cyclic strain resistance
    and resultant low cycle fatigue life was noticeable
    at the lower cyclic strain amplitudes.

6. Cyclic stress response of the discontinuous
    particulate-reinforced 2009 composite revealed
    hardening to failure from the onset of fully-
    reversed cyclic deformation at all strain
    amplitudes, at both the ambient and elevated test
    temperatures. The hardening, or an increase in
    stress amplitude with cycles, was more pronounced at
    the higher test temperature. At a given test
    temperature, the degree of hardening was greater at
    higher cyclic strain amplitudes and concomitant

higher response stress resulting in shorter cyclic fatigue life.

7. For the volume fraction of the SiC particulate reinforcement phase (15 vol.%) in the 2009 aluminum alloy metal matrix, fracture morphology was essentially similar over the range of cyclic strain amplitudes. Macroscopic observations revealed fracture to be essentially brittle but microscopically features reminiscent of locally ductile and brittle mechanisms.

7.2. 7034 Aluminum Matrix Composite

A study of the tensile, high cycle fatigue, low cycle fatigue and final fracture behavior of 7034/SiC/15p-UA and 7034/SiC/15p-PA metal-matrix composites provides the following key observations:

1. The initial microstructure of the 7034/SiC_p MMCs revealed the reinforcing SiC particulates were non-uniform in size, irregularly shaped and randomly dispersed. At regular intervals, a clustering or agglomeration of the SiC_p, of varying sizes, was observed resulting in SiC_p-rich and SiC_p-depleted regions. An agglomerated site consisted of the smaller SiC_p intermingled with larger SiC_p.

2. The modulus and strength of the two composite microstructures decreased with an increase in temperature. The ductility, quantified in terms of elongation-to-failure and reduction in area decreases with an increase in temperature

3. At equivalent values of maximum cyclic stress the degree of degradation in fatigue life was in the range 200 to 300 percent. The degradation in cyclic fatigue life was more pronounced for the under-aged (UA) microstructure than the peak-aged (PA) microstructure. Also, for a given aging condition, increasing the load ratio resulted in higher fatigue strength (taken as the highest stress at which a composite specimen survived 10^6 cycles). Further for a given load ratio, the variation of maximum stress with fatigue life reveals minimal to no influence of aging condition (i.e., UA versus PA) of the7034/SiC/15p composite. This observation is consistent with the near identical yield strength (σ_{ys}) and ultimate tensile strengths (σ_{uts}) of the two microstructures.

4. For a given volume fraction of the reinforcing phase in the 7034 aluminum alloy metal matrix, aging

condition and load ratio, fracture morphology was observed to be essentially similar at the different values of maximum stress. Macroscopic observations revealed the fracture surface to be brittle, that is: low cyclic ductility but microscopically features reminiscent of locally ductile (voids and dimples) and brittle (microscopic and macroscopic cracks) mechanisms. With a decrease in load ratio fracture of the composite was dominated by failure of the reinforcing SiC particulate both by cracking and decohesion at the particulate-matrix interfaces. This results from constraints in deformation induced in the metal matrix by the hard and brittle SiC_p reinforcement phase coupled with local stress concentration effects. Fracture of the plastically deforming matrix occurred through the formation, growth and coalescence of the voids.

5. Cyclic stress response of the ceramic particle reinforced aluminum alloy metal matrix revealed rapid initial hardening in the first few cycles of cyclic straining followed by stability for fraction of fatigue life and culminating in rapid softening to failure at the high cyclic strain amplitudes. At

the lower cyclic strain amplitudes the initial hardening during straining was low, followed by stabilization for most of fatigue life and culminating in gradual softening to failure

6. The possible mechanisms contributing to hardening of the composite matrix during fully-reversed cyclic straining are ascribed to the conjoint influence of an increase in dislocation density during fully-reversed cyclic straining, mutual interaction of dislocations with other dislocations, dislocation multiplication, and dislocation-silicon carbide particulate interactions. Growth and coalescence of the microscopic cracks to form one or more macroscopic cracks causes the load carrying and thus the stress-carrying capability of the structure to decrease and the material soften to failure.

7. The aluminum alloy/SiC composites followed the Basquin and Coffin-Manson relationships for strain-reversals to fatigue life response. The cyclic ductility (ε'_f) of the composite microstructure is inferior to the true monotonic fracture ductility (ε_f).

8. For a given volume fraction of the SiC particulate reinforcement phase in the aluminum alloy matrix, fracture morphology was found to be essentially similar over the entire range of cyclic strain amplitudes. Macroscopic observations revealed the fracture surface to be essentially brittle, at high, intermediate, and low cyclic strain amplitudes, but microscopically features reminiscent of locally ductile and brittle mechanisms. For both aging conditions overall fracture was dominated by cracking of the reinforcing SiC particulates coupled with decohesion at the matrix-particle interfaces. Constraints in mechanical deformation, induced in the plastically deforming aluminum alloy metal matrix, by the hard, brittle and elastically deforming SiC_p reinforcement phase, coupled with local stress concentration effects at the matrix-particulate interfaces promotes SiC particulate failure through the conjoint influences of cracking and decohesion at its interfaces. Final failure occurs by fast fracture through the composite matrix.

7.3. Mg-6%Zn Matrix Composite

A study of the mechanical response and fracture behavior of Z6/SiC, metal-matrix composite provides the following key observations:

1. The initial microstructure of the Z6/SiC/20p-F MMC revealed a near-uniform distribution of the reinforcing SiC particulates in the longitudinal direction of the extruded composite plate. An agglomeration or clustering of the SiC particulates was observed.

2. The presence of hard, brittle and elastically deforming SiC particulates in a soft, ductile and plastically deforming magnesium alloy metal matrix causes fine microscopic cracks to initiate at low values of applied stress. Fractography revealed limited ductility on a macroscopic scale, but microscopically features were reminiscent of locally ductile and brittle mechanisms. Fracture of the matrix between the dispersed SiC particulates and particulate clusters coupled with failure of the reinforcement particulate by cracking allows the microscopic cracks to grow rapidly and coalesce by

fracture through the ductile metal matrix resulting in macroscopic failure and low tensile ductility.

3. Influence of temperature on stress amplitude-fatigue life response revealed degradation in cyclic fatigue life with an increase in test temperature. However, when the cyclic stress amplitude is normalized with respect to yield strength and ultimate tensile strength of the material at the test temperature, the variation with fatigue life reveals improved cyclic stress resistance at the higher test temperature. The improvement in cyclic fatigue life is more pronounced at the higher ratios of stress than at the lower ratios of stresses.

4. At a given temperature, cyclic fracture morphology was found to be essentially similar over the range of cyclic stress amplitudes. Macroscopic observations revealed the fracture surface to be brittle, i.e., low cyclic ductility, at all cyclic stress amplitudes, but microscopically features reminiscent of locally ductile and brittle mechanisms. Constraints in mechanical deformation, induced in the metal matrix, by the hard, brittle and elastically deforming SiC reinforcement phase

coupled with local stress concentration effects at the matrix-reinforcement particle interfaces promote failure through the conjoint influences of particle cracking and fast fracture through the matrix. Fracture of the plastically deforming matrix occurred through the formation, growth and coalescence of the voids.

7.4 Modeling Techniques

Based on an outcome of modeling simulations of the distribution effects on particulate reinforced aluminum metal matrix composites mechanical properties and two types of modeling schemes are evaluated to predict the cyclic-stress control and the cyclic-plastic strain control response with the following key interpretation:

1. The model shows that by using periodic unit cell model a good prediction of actual tensile mechanical behavior of the particle reinforced metal matrix composite is achieved.

2. The effects of particle distribution on overall stress-strain behavior of the composite is noticeably less pronounced for the unit cylinders, due to a lack of significant changes in the matrix triaxiality.

3. The result of cyclic stress-control modeling reveals that the scatter in fatigue test data of the particulate-reinforced metal matrix composites can be well described by statistical model.

4. The results of cyclic plastic-strain control indicate that the proposed modeling approach is applicable to low cycle fatigue (LCF) life prediction of particulate-reinforced MMCs. For the 2009/SiC/15p-T42 composite the prediction model is correlates well with the experimental fatigue data for both test temperatures. However, for the 7034/SiC/15p composite the model prediction follows the trend of the experimental test data, but with a larger deviation.

REFERENCES

1. J.M. Papazian, Metallurgical Transactions A. 19, 2945 (1988).

2. S.J. Harris, H.W. Gai, P.C. Weatherbern, Advanced Composites 93, International Conference on Advances in Composite Materials, (T. Chandra, A.K. Dhingra, ed), The Minerals, Metals and Materials Society, 1993.

3. G. E Dieter, "Mechanical Metallurgy", McGraw-Hill Book Co. New York, 1986.

4. V. Nardone and K. Prewo, Scripta Metallurgica. 20, 43 (1986).

5. T. Clyne and P. Withers, "An introduction to metal matrix composites", Cambridge University Press, Cambridge, 1993.

6. D. Lloyd, International Materials Review. 39, 1 (1994).

7. B. Maruyama, "Advanced Materials and Processes Technology", The AMPTIAC Newsletter, 2, 1 (1998).

8. W. Harrigan Jr., Materials Science and Engineering A, 244, 75 (1998).

9. I. Dutta and D. L. Bourell, Materials Science and Engineering.A, 112, 67 (1989).

10. T. Christman and S. Suresh, Acta Metallurgica, 36,1691 (1988).

11. R. J. Arsenault, Materials Science and Engineering A, 64, 171 (1984).

12. L.F. Mondolfo, "Aluminum Alloys: Structure and Properties", Butterworth, Londan, 1976.

342

13. C.H. Davis, N. Roghunathan and T. Sheppard, Materials Science and Technology, 8, 977 (1992).

14. T. G. Nieh and R. F. Karlak, Scripta Metallurgica, 18, 25 (1984).

15. M. Taya and T. Mori, Acta Metallurgica, 35, 155 (1987).

16. H. Ribes, M. Suery, G. Lsperance, and T. G. Legoux, Metallurgical Transactions A, 21, 2489 (1990).

17. L. N. Thanh and M. Suery, Scripta Metallurgica Materialia, 25, 2781 (1991).

18. A. Weiland, L. Hultman, U. Wahlstroe, C. Persson and T. Johannohannesson, Acta Metallurgica, 46, 5271 (1998).

19. L. Jae-chul, B. Ji-young and O. Chang, Acta Metallurgica Materialia, 45, 5303 (1997).

20. H.J. Rack, Dispersion strengthened aluminum alloys, (Y.W. Kim, W.M. Griffith,ed), The Minerals, Metals and Materials Society, PA, 649 (1988).

21. S. V. Kamat, A. D. Rollet and J. P. Hirth, Scripta Metallurgica, 25, 27 (1991).

22. K. Vijay, Y. Mahajan and V. Kutumbarao, Scripta Metallurgica, 37, 485 (1997).

23. A. P. Sannino, H. J. Rack, Journal of Materials Science, 30, 4316 (1995).

24. W. S. Miller and F. J. Humphreys, Scripta Metallurgica, 25, 33 (1991).

25. C. H. Davies, Journal of Materials Processing and Technology, 62, 225 (1996).

26. I. Dutta and D. L. Bourell, Materials Science and Engineering A, 112, 67 (1989).

27. H. J. Rack, in Proc. ICCMDVI, (F. L. Matthews, N. C. R. Buskell, J. M. Hodgkinson and J. Morton, ed). Elsevier "Applied Science", London, 2, 382 (1987).

28. S.J. Harris, H.W. Gai, P.C. Weatherbern, "Advanced Composites Materials 93", (T. Chandra, A.K. Dhingra, ed), The Minerals, Metals and Materials Society,PA, 1993.

29. D. L. McDanels, Metallurgical Transactions A, 16, 1105 (1985).

30. D. J. Towle and C. M. Friend, Journal of Materials Science, 27, 2781 (1992).

31. C. M. Friend, I. Horsfall, S. D. Luxton, and R. J. Young, "Advances in Cast Reinforced Metal Composites", (S. G. Fishman and A. K. Dhingra, ed), ASM International, Metals Park, Ohio, 309, 1988.

32. R.J. Arsenault, N. Shi, Materials Science and Engineering A, 81, 175 (1986).

33. B. A. Mikuki, S. O. Shook, W. E. Mercer and F. G. Green, "International Magnesium Association (IMA)", McLean, VA, 1986.

34. A. Luo, M. O. Pekguleryuz, AFS Transactions, 102, 313 (1994).

35. A. Luo, Canadian Metallurgical Quarterly, 35, 375 (1996).

36. A. Luo, Metallurgical and Materials Transactions A, 26, 2445 (1995).

37. R. A. Saravanan and M. K. Surappa, Materials Science and Engineering A, 276, 108 (2000).

38. M. Gupta, M.O. Lai, D. Saravanaranganathan, Journal of Materials Science, 35, 2155 (2000).

39. Gu. Mingyuan, Wu Zhengan, Jin Yanping and K. Mustafa, Materials Science and Engineering A, 272, 257 (1999).

40. P.K. Chaudhury, H.J. Rack, Journal of Materials Science, 26, 2893 (1991).

41. Y.X. Chen, D.X. Li and G.D. Zhang, Scripta Metallurgica Materialia, 43, 337 (2000).

42. Hu Lianxi and Wang Erde, Materials Science and Engineering A, 278, 267 (2000).

43. R. Mehrabian, T. Riek and M. Flemings, Metallurgical Transactions A, 5, 1899 (1974).

44. B. Lux, Cast Metal Research Journal, 18, 25 (1972).

45. T. C. Willis, Metals and Materials, 4, 485 (1988).

46. R. Gardiner and B. Viney, "Electron Beam Melting and Refining", British Materials, 116 (1992).

47. J. Llorca, S. Suresh and A. Needleman, Metallurgical Transactions A, 23, 919 (1992).

48. P. Singh and J. Lewandowski, Metallurgical Transactions A, 24, 2531 (1993).

49. J.J. Lewandowski, C. Liu and W.H. Hunt, Jr., Materials Science and Engineering A, 107, 241 (1989).

50. M. Vedani and E. Gariboldi, Acta Metallurgica, 44 3077 (1996).

51. M. Manoharan and J. Lewandowski, Acta Metallurgica, 38, 489 (1990).

52. F. Zhang, P. Sun, X. Li and G. Zhang, Materials Science and Engineering A, 300, 12 (2001).

53. M. Ashby D. Jones, "Engineering Materials II", Pergamon Press, Oxford, 1986.

54. N. Ravi Kumar and E. Dwarakadasa, Composites A, 31 1139 (2000).

55. A. Martin and Llorca, Materials Science and Engineering A, 12, 77 (1995).

56. B. Chua, L. Lu and M. Lai, Composites Structure, 47, 595 (1999).

57. J. Allison, J. Jones, "Fundamentals of meal matrix composites", (S. Suresh, A. Mortensen and A. Needleman, ed), Butterworth-Heinemann, 269 (1993).

58. D. Lloyd, Acta Metallurgica, 39, 59 (1991).

59. V. Varma, S. Kamat, Y. Mahajan, and V. Kutumbarao, Scripta Materialia, 38, 1571 (1998).

60. K. Tokaji, H. Shiota and K. Kobayasi, Fatigue Fracture of Engineering Materials Structure, 22, 281 (1999).

61. C. Masuda and Y. Tanaka, Journal of Materials Science, 27, 413 (1992).

62. A. Vaidya and J. Lewandowski, Materials Science and Engineering A, 220, 85 (1996).

63. D. Lloyd, International Materials Review, 1, 39 (1994).

64. J. Hashim and S. Shtrikman, Journal of Mechanical Physics, 11, 127 (1963).

65. T. Christman, A. Needleman and S. Suresh, Acta Metallurgica, 37, 3029 (1989).

66. S. Suresh, "Fatigue of Materials", University Press, Cambridge, 1996.

67. S. Manson, Experimental Mechanics, 5, 193 (1965).

68. Y. Shen, M. Finot, A. Needleman and S. Suresh, Acta Metallurgica, 43, 1701 (1995).

69. V. Tvergaard, Acta Metallurgica. Materialia, 38, 185 (1990).

70. R. McMeeking and M. Jain, Acta Metallurgica. Materialia, 39, 117 (1991).

71. M. Jain, S. MacEwen and L. Wu, Materials Science and Engineering A, 183, 111 (1994).

72. G. Bao, R. McMeeking and J. Hutchinson, Acta Metallurgica. Materialia, 39, 1871 (1991).

73. P. Thomason, "Ductile Fracture of Metals", Pergamon Press, Oxford, 1990.

74. A. Gurson, ASME Journal of Engineering Materials Technology, 99, 2 (1977).

75. V. Tvergaard, International Journal of Fracture, 17, 389 (1981).

76. V. Tvergaard and A. Needleman, Acta Metallurgica, 32, 157 (1984).

77. P. Thomson, Acta Metallurgica, 33, 1087 (1985).

78. V. Tvergaard, Computational Mechanics, 20, 184 (1997).

79. T. Siegmud, E. Werner and F. Fischer, Computational Materials Science, 1, 234 (1993).

80. L. Xia, C. Shih, Journal of Mechanical Physics Solids, 43, 1953 (1995).

81. H. Anderson, Journal of Mechanical Physics Solids, 25, 217 (1997).

82. J. Llorca, A. Needleman and S. Suresh, Acta Metallurgica, 39, 2317 (1991).

83. S.L. Couling, Use of Air/CO /SF Mixtures For Improved Protection of Molten Magnesium, "Magnesium", Oslo, Norway, 54, 1979.

84. ASTM E-8, "American Society of Testing and Materials", Race Street, Philadelphia, PA, 1995.

85. ASTM E-466, "Stress Amplitude Controlled Fatigue of Metallic Materials," ASTM, American Society of Testing and Materials, Philadelphia, PA, 1993.

86. ASTM E-606, "Strain Amplitude Controlled Fatigue of Metallic Materials," ASTM, American Society of Testing and Materials, Philadelphia, PA, 1993.

87. N. Hansen, Acta Metallurgica, 25, 9863 (1977).

88. M. Vogelsang, R. Arsenault and R. Fisher, Metallurgical Transactions A, 17, 379 (1986).

89. K. K. Chawla and M. Metzger, Journal of Materials Science, 17, 34 (1972).

90. T. Mochida, M. Taya and D. Lloyd, Materials Transactions A, 32, 931 (1991).

91. M. Ashby, Philosophical Magazine, 8, 399 (1970).

92. T. S. Srivatsan, Meslet Al-Hajri and X. Gao, The Tensile Deformation and Fracture Characteristics of 2009 Aluminum Alloy-SiC Particulate Metal Matrix Composite, "Affordable Metal Matrix Composites for High Performance Applications III", (A. Pandey, K. Kendig and T. Watson, ed), The Minerals, Metals and Materials Society, PA, 210, 2001.

93. R. Arsenault, "Metal Matrix Composites: Mechanisms and Properties", (R. Everett and R. Arsenault, ed) Academic Press, San Diego, CA, 79 (1991).

94. T. Butler and D. Drucker, Journal of Applied Mechanics, 40, 780 (1973).

95. T. Christman, A. Needleman, S. Nutt and S. Suresh, Materials Science and Engineering A, 107, 49 (1989).

96. F. McClintock, "Ductility", American Society for Metals, Materials Park, Ohio, USA, 256 (1968).

97. R. VanStone, T. Cox, J. Low Jr., and J. Psioda, International Metals Reviews, 30, 157 (1995).

98. A. Argon, J. Im and R. Safoglu, Metallurgical Transactions A, 6, 825 (1975).

99. J. Bonnen, J. Allison and J. Jones, Metallurgical Transactions A, 22, 1007 (1991).

100. T. S. Srivatsan and Meslet Al-Hajri, Aluminum Transactions A, (In Review).

101. N. Sorensen, S. Suresh, V. Tvergaard and A. Needleman, Materials Science and Engineering A, 197, 1 (1995).

102. T. S. Srivatsan and T. A. Place, Journal of Materials Science, 14, 1543 (1989).

103. D.F. Hassen, C.R. Crowe, J.S. Ahearn and D.C. Cooke, "Failure Mechanisms in High Performance Materials", (J.G. Early, T.R. Shives and J.H. Smith, ed), Cambridge University Press, Cambridge, United Kingdom, 147 (1985).

104. T. S. Srivatsan, Meslet Al-Hajri, and C. Smith, The High Cycle Fatigue and Fracture Behavior of a Silicon Carbide Particulate Reinforced 2009 Aluminum Alloy Metal Matrix Composite, "Modeling The Performance of Engineering Structural Materials II" (D. Lesuer and T. S. Srivatsan, ed), The Minerals, Metals and Materials Society, PA, 119 (2001).

105. Y. Sugimura and S. Suresh, Metallurgical Transactions A, 23, 2231 (1992).

106. T. S. Srivatsan and J. Mattingly, Journal of Materials Science, 28, 611 (1993).

107. E.A. Starke, Jr., and G. Lutjering, "Fatigue and Microstructure", (M. Meshii, ed), ASM International, Metals Park, Ohio, 205, 1979.

108. L.F. Coffin, Jr., Transactions ASM, 76, 931 (1954).

109. S.S. Manson, NASA Technical Note,6, 2933 (1954).

110. B.I. Sandor, "Fundamentals of Cyclic Stress and Strain", University of Wisconsin Press, Madison, Wisconsin, 1972.

111. T.S. Srivatsan, Meslet Al-Hajri and V. Vasudevan, International Journal of Fatigue, 2003 (In Press).

112. T.S. Srivatsan, Meslet Al-Hajri and M. Petraroli, The Quasi Static Fracture Behavior of 7034 Aluminum Alloy Reinforced with Silicon Carbide Particulates, "10th International Congress on Fracture" (R.O. Ritchie and K. Ravi-Chandar, ed), Elsevier Limited, Oxford, UK, 2001.

113. P.F. McGuire, Machine Design, 64, 71 (1992).

114. W. H. Hunt, Jr., C.R. Cook and R. R. Sawtell: "Cost Effective High-Performance Powder Metallurgy Aluminum Matrix Composites for automotive applications," Annual SAE Congress, Paper No. 910834, Detroit, Michigan, 1991.

115. M.J. Koczak, S.C. Khatri, J.E. Allison and M.G. Bader, "Fundamentals of Metal Matrix Composites", (S. Suresh, A. Mortensen and A. Needleman, ed), Butterworth- Heinemann, Boston, MA, 297, 1993.

116. T. S. Srivatsan and Meslet Al-Hajri, Composites Engineering B, 33, 391 (2002)

117. L. M. Brown and W. Stobbs, Philosophical Magazine, 23, 1185 (1971).

118. D. A. Koss and S. M. Copley, Metallurgical Transactions A, 2, 1557 (1971).

119. J. K. Shang, and R. O. Ritchie, Metallurgical Transactions A, 20, 897 (1989).

120. J. K. Shang and R. O. Ritchie, Acta Metallurgica, 37, 2267 (1989).

121. P.K. Liaw and W.A. Logsdon, Engineering Fracture Mechanics, 24, 637 (1986).

122. J. J. Bonnen, J. E. Allison and J. W. Jones, Metallurgical Transactions A, 22, 1007 (1991).

123. T. S. Srivatsan, International Journal of Fatigue, 14, 355 (1992).

124. T. S. Srivatsan and R. Auradkar, International Journal of Fatigue, 14, 173 (1992).

125. T.S. Srivatsan, K. Yamaguchi, and E.A. Starke, Jr., Materials Science and Engineering A, 83, 87 (1986).

126. T.S.Srivatsan, and E.J. Coyne, Jr., international Journal of Fatigue, 8, 201 (1986).

127. T.S. Srivatsan, and E.J. Coyne, Jr, Materials Science and Technology, 5, 548 (1989).

128. T. S. Srivatsan, R. Auradkar and A. Prakash, Engineering Fracture Mechanics, 2, 277 (1991).

129. J. Cho, and J. Gurland, Metallurgical Transactions A, 19, 2027 (1989).

130. V.C. Nardone, and K.M. Prewo, Metallurgical Transactions A, 26, 43 (1986).

131. R.J. Arsenault, L. Wang, and C.R. Feng, Acta Metallurgica Materialia, 39, 47 (1991).

132. M. Taya, K.E. Lulay, and D.J. Lloyd, Acta Metanurgica, 39, 73 (1991).

133. T. S. Srivatsan, Meslet Al-Hajri and V. Vasudevan, Material Science and Engineering A, 2003 (In Press).

134. T. M. Osman, J. J. Lewandowski and W. H. Hunt Jr.: Microstructure-property relationships for an Aluminum/SiCp composite with different deformation histories, "Processing and Fabrication of Fiber-Reinforced MMCs", American Society for Materials International, Materials Park, Ohio, USA, 209, 1990.

135. T. S. Srivatsan, Influence of Secondary Processing on Cyclic Fracture Behavior of an Aluminum-Ceramic Particle Composite, "Processing and Fabrication of Advanced Materials III", (V. A. Ravi, T. S. Srivatsan and J. J. Moore, ed), The Minerals, Metals and Materials Society: TMSD, Warrendale, PA, 699, 1994.

136. B. Derby and P.M. Mummey, "in Fundamentals Of Metal-matrix Composites", (S. Suresh, A. Mortensen and A. Needleman, ed), Butterworth-Heinemann Publishers, MA, 251, 1992.

137. T.S. Srivatsan, Meslet Al-Hajri and P. C. Lam, Composite Engineering B, 2003 (In Press).

138. C. Gonzalez and J. Llorca, Scripta Materialia, 35, 91 (1996).

139. S. Song, N Shi, G. Gray and J. Roberts, Metallurgy Materials Transactions A, 27, 3739 (1996).

140. D. Watt, X. Xu and D. Lloyd, Acta Materialia, 44, 789 (1996).

141. J. Llorca, Acta Materialia, 42, 151 (1994).

142. ABAQUS Theory manual, RI HKS (2002).

143. ASM Handbook,9 (2001)130.

144. P. Mchugh, R. Asaro and C. Shih, Acta Materialia, 41, 1489 (1993).

145. S. Corbin and D. Wilkinson, Acta Metallurgica, 42, 1311 (1994).

146. J. Harfer, International Journal of Plasticity, 6, 605 (1999).

147. M. Gen and M. Kikuchi, Acta Materialia, 46, 3125 (1998).

148. W. Weibull, "A statistical theory of the strength of materials", Stockholm, Sweden, 1939.

149. K. Sobczyk, Engineering Fracture Mechanics, 24, 609 (1986).

150. X. S. Xing, Engineering Fracture Mechanics, 26, 393 (1987).

151. X. S. Xing, Engineering Fracture Mechanics, 55, 699 (1995).

152. H. Z. Ding, X. S. Xing and H. S. Zhu, Journal of Materials Science Letter, 13, 636 (1994).

153. H. Z. Ding, X. S. Xing and H. S. Zhu, Journal of Materials Science Letter, 14, 916 (1995).

154. H. Z. Ding, H. Biermann, H. Mughrabi, Fatigue and Fracture of Engineering of Materials Structure, 23, 847 (2000).

155. J. E. Allison and J. W. Jones, Fatigue behavior of discontinuously reinforced metallic composites, "International Fatigue Congress 96", (G. Luetjering and H. Nowack, ed), Pergamon, Oxford, UK, 1439, 1996.

156. Z. G. Wang, S. Li and L. Sun, Key Engineering Materials, 104, 729 (1995).

157. Z.Wang, Key Engineering Materials, 104, 765 (1995).

158. J. N. Hall, J. W. Jones and A. L. Sachdev, Materials Science and Engineering A, 183, 69 (1994).

159. T. S. Srivatsan,. International Journal of Fatigue, 17, 183 (1995).

160. M. Papakyriacou, H. R. Mayer, S. E. Tschegg-Stanzl and M. Groschl, Fatigue and Fracture of Engineering Materials Structure, 18, 477 (1995).

161. P. Poza and J. Llorca, Metallurgical Materials Transactions A, 26, 3131 (1995).

162. H. Biermann, G. Beyer and H. Mughrabi, Materials Science and Engineering A, 234, 198 (1997).

163. S. Kumai, J. E. King and J. F. Knott, Fatigue and Fracture of Engineering Materials Structure, 13, 511 (1990).

164. S. Kumai, J. E. King and J. F. Knott, Materials Science and Engineering A, 146, 317 (1991).

165. C. S. Li and F. Ellyin, Fatigue and Fracture of Engineering Materials Structure, 18, 1299 (1995).

166. J. K. Shang, W. Yu and R. O. Ritchie, Materials. Science and Engineering A, 102, 181 (1988).

167. J. K. Shang and R. O. Ritchie, Fatigue of discontinuously reinforced metal composites. "Metal Matrix Composites: Mechanisms and Properties", (R. J. Arsenault and R. K. Evertt, ed), Academic Press, Boston, MA, 255, 1991.

168. M. J. Hadianfard and Y.W. Mai, Journal of Materials Science, 30, 5335 (1995).

169. M. Papakyriacou, H. R. Mayer, S. E. Tschegg-Stanzl and M. Groschl, International Journal of Fatigue, 18, 475 (1996).

170. T. Christman and S. Suresh, Materials Science and Engineering A, 102, 211 (1988).

171. D. L. Davidson, Metallurgical Materials Transactions A, 22, 97 (1991).

172. Z. Wang and R. J. Zhang, Acta Metallurgica. Materialia, 42, 1433 (1994).

173. X. S. Xing, Engineering Fracture Mechanics, 37, 1099 (1990).

174. X. X. Diao, X. S. Xing and H. Z. Ding, Engineering Fracture Mechanics, 52, 289 (1995).

175. G. van Kampen, "Stochastic Process in Physics and Chemistry", Amsterdam, Netherlands, 1992.

176. J. R. Rice and M. A. Johnson, "Inelastic Behavior of Solids", McGraw-Hill. New York, 1970

177. M. Levin, B. Karlsson, International Journal of Fatigue, 15, 377 (1993).

178. H.-Z. Ding, O. Hartmann, H. Biermann, H. Mughrabi, Materials Science and Engineering A, 333, 295 (2002).

179. N.L. Han, Z.G. Wang, W.L. Wang, G.D. Zhang, C.X. Shi, Composites Science and Technology, 59, 147 (1999).

180. M. J. Hadianfard, Y. W. Mai, Journal of Materials Science, 35, 1715 (2000).

181. N.L. Han, J. M. Yang, Z.G. Wang, Scripta Materialia, 43, 801 (2000).

182. T.S. Srivatsan, International Journal of Fatigue, 14, 173 (1992).

183. C.C. Perng, J.R. Hwang, J.L. Doong, Composite Science and Technology, 49, 225 (1993).

184. N.L. Han, Z.G. Wang, L. Sun, Scripta Metallurgica Materialia, 33, 781 (1995).

185. G.M. Vyletel, D.C. Van Aken, J.E. Allison, Metallurgy Materials Transactions A, 26, 3155 (1995).

186. P.C. Cheng, S.J. Lin, M.T. Jahn, Journal of Materials Science, 32, 4153 (1997).

187. D.L. Davidson, R.C. McClung, International Journal of Fracture, 84, 81 (1997).

188. B. Tomkins, Philosophical Magazine, 18, 1041 (1968).

189. J.O. Yong, W.N. Soo, Journal of Materials Science, 27, 2019 (1992).

190. J.R. Rice, "ASTM STP 415", ASTM, Philadelphia, PA, 247 (1967).

191. J.R. Rice, Journal of Applied Mechanics, 35, 379 (1968).

192. N.E. Dowling, "Cyclic stress-strain and plastic deformation aspects of fatigue crack growth", ASTM STP 637, ASTM, Philadelphia, PA, 97, 1997.

193. C. Wuethrich, International Journal of Fracture, 20, 35 (1982).

194. K. T. Rie, H. Wittke, Fatigue and Fracture of Engineering Materials Structure, 19, 975 (1996).

195. A. Jung, H. J. Maier, H.J. Christ, "Thermo-mechanical Fatigue Behavior of Materials", (H. Sehitoglu and H. J. Maier, ed), 3, ASTM STP 1371, ASTM, Philadelphia, PA, 167, 2000.

196. J.D. Eshelby, Proc. Royal Society London, 241, 376 (1957).

197. J. Polak, "Cyclic Plasticity and Low Cycle Fatigue Life of Metals", Elsevier, Amsterdam, 1991.

198. H.W. Liu, Theoretical Applied Fracture Mechanics, 16, 91 (1991).

199. T.M. Edmunds, J.R. Willis, Journal of Mechanical Physics Solids, 25, 423 (1977).

200. T.L. Sham, "Elastic-Plastic Fracture: Second Symposium, Inelastic Crack Analysis", (C.F. Shih and J.P. Gudas ed), 1, 152, ASTM STO 803, 1984.

201. G.H. Rubiolo, J.C. Rios, P. Gargano, Engineering Fracture Mechanics, 60, 447 (1998).

202. G.A. Harmain, J.W. Provan, Theoretical Applied Fracture Mechanics, 26, 63 (1997).